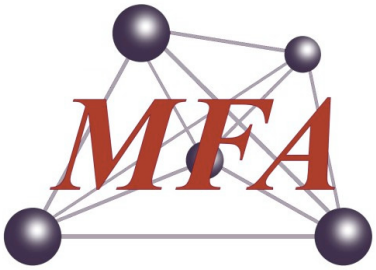

Yearbook

2011

Research Institute for Technical Physics and Materials Science

Hungarian Academy of Sciences

http://www.mfa.kfki.hu/
http://www.ttk.mta.hu/

Research Institute for Technical Physics and Materials Science
Hungarian Academy of Sciences

Director: Prof. István Bársony, corr. member of HAS

Address: Konkoly-Thege Miklós út 29-33,
H-1121 Budapest, Hungary
Postal: P.O.Box 49, H-1525 Budapest, Hungary
Phone: +36-1-392 2225
Fax: +36-1-392 2226
E-mail: info@mfa.kfki.hu, info@ttk.mta.hu
URL: http://www.mfa.kfki.hu/
http://www.ttk.mta.hu/

MTA MFA Yearbook 2011

Editors: Miklós Menyhárd and Csaba S. Daróczi
Published by: MTA MFA, Budapest, Hungary, 2011

CONTENT

DIRECTOR'S FOREWORD

2011 was the last year of operation of MTA MFA as an independent research institution! Therefore, this yearly accounting of the life and achievements of the Research Institute for Technical Physics and Materials Science of the Hungarian Academy of Sciences – MFA will also be the last of its kind in the series of Yearbooks, which started in 2004. The strategy of following the selected four major directions of strong multidisciplinary character: *nanoscience and - technology, physics, photonics* and *microtechnology* proved to be successful.

The scientific progress in the six scientific departments in an unchanged organisatory scheme was reviewed by the External Advisory Board (EAB) appointed by the president of HAS in 2010, composed of professors *Lars Hultman* (Linköping University), *Lothar Frey* (FhG IISB, Erlangen), *Árpád Csurgay* (HAS), *József Gyulai* (HAS), *Gábor Szabó* (University of Szeged) and *János Kertész* (BUTE) as chairman. The Board stated in its evaluation (early 2011) that

> *"The profile of MFA corresponds both to its mission declaration and to the international trends. The research carried out at the Institute is of high average level, with internationally recognized peaks…**Once more, it should be emphasized that there are top quality groups, which would be beneficial to any research institute.**"*

The above quote from the EAB is underlined by the *unprecedented success of the MFA in the network of research institutes of the HAS in 2011*. The highest scientific distinction of the Hungarian Academy of Sciences, the *Academy Prize* was awarded by both supervising scientific departments, the Engineering Department and the Physics Department of HAS to the scientific advisors of MFA: deputy director *Béla Pécz* and head of department *László P. Biró*.

The achievements of MFA are to be measured beyond the scientometric parameters in a more complex fashion, i.e. also by the patents applied for, the success in Ph.D. training and other educational activities, the services and advisory activities and last but not least by the efficiency of industrial utilization of the scientific results.

Other scientific distinctions provided to MFA staff, two of our senior researchers, *Miklós Serényi* and *Attila Szolnoki* obtained the title Dr. of HAS. One Ph.D. degree was granted for *Péter Kozma*, who also received the "Excellent Young Researcher Award of the Academic Committee of Veszprém". *Anita Pongrácz* obtained the Junior Academy Prize, *Krisztina Szakolczai* the Distinction by the Secretary General of HAS, *Péter Nemes-Incze* the Dr. György Frenczi Memorial Award; *Zoltán Juhász* the Jenő Szervatiusz Award; *György Kádár* became Research Professor Emeritus; *Éva Denkné Horváth* got the MFA Prize for Excellent Science

Support, *Zoltán Fekete* the MFA Prize for Ph.D. students; *Anita Pongrácz*, and *Krisztián Kertész* the MFA Prize for Postdocs, and *János Volk* the MFA Research Prize.

A primary scientific event of the Hungarian EU presidency in 2011 was the international conference and exhibition EuroNanoForum 2011. MFA and the MFA-led IMNTP played a determining role as organizer and participant of the scientific programmes alike. An MFA initiative connected to the conference was the *creation of a mobile exhibition displaying the potential and possible dangers associated with nanotechnology exploitation*. This interactive exhibition, financed by project support, sponsor contributions and the efforts of MFA, was installed in a reconstructed large Ikarusz-type city bus. Ideas of young participants of the Nano-Demo Contest of MFA, as well as the enthusiastic scientific/technical contribution of coworkers of the Institute were used for the interactive experiments. The Nanobus (**www.mfa.kfki.hu/hu/nanobusz**) was introduced to the press and transferred to the operating institution, the Palace of Miracles. The Nanobus will tour the countryside, and appeared already at several popular scientific events in 2011 (Bridge of Science, Night of Researchers in Miskolc, inauguration of the Visitor Center of the sponsoring company GE-Tungsram) with great success.

The *MFA Summer School for secondary high school students* from all over the Carpatian basin is already a four years old tradition **http://alag3.mfa.kfki.hu/mfa/nyariiskola/** . In 2011 again 24 youngsters spent a week getting an insight into scientific research in the experimental laboratories of MFA. Reports by two children from Transylvania even obtained a special prize in the physics contest of secondary school students in Kolozsvár. Last year the *Open Day of MFA* offered again 120-150 visitors, (interested tax payers) the chance get acquainted with research at MFA. Referring to the EAB again:

> *„It is questionable if the performance of MFA can be compared to leading institutes of similar scope. The research carried out here depends very much on materials and equipment, finally on finances. Therefore, it depends on the parameter we ask for. Certainly, neither the global scientometric parameters nor the number of implemented patents can be compared to the Fraunhofer Institute or to Ris?.* ***If, however, we take the cost per article, MFA certainly wins.*** *The human resources with high and broad level of expertise and intellectual capacity is another quality of the MFA. Taking into account the given circumstances, MFA shows a good and improving performance."*

Being an institute of experimental research the biggest load for MFA is still the operation, maintenance and development of its large infrastructure occupying ca 5000 m2 including preparative clean-rooms, and big analytical facilities. The ISO quality assurance system introduced 8 years ago, enforces the administrative discipline required for successful research and collaboration. Our Accredited Characterization Laboratory for ellipsometry passed successful revision of its accreditation in 2011.

The working conditions at MFA were improved also in 2011 by the installation of a *new ceramics research laboratory* and the purchase of a key instrument, a Heidelberg-type *laser pattern generator*, with a substantial grant from the Telecommunication Foundation and additional support of the HAS.

Economically, the year 2011 was as critical as the one before with more *serious liquidity problems*. For the last 14 years, i.e. from its foundation MFA suffers from a *chronic shortage in subsidy* amounting to a yearly 180 MFt. This has been duly acknowledged by each reigning leadership of the HAS.

In 2011 eight FP7 European projects were conducted (most of them finished) at MFA including an ENIAC JTI 1st Call project granted in 2008. The audits for all FP7 and domestic projects ended with a flawless acceptance of the accounts. In the 2nd call of ENIAC in 2009 support for CAJAL4 was also granted, but the co-financing contract was only signed by the Hungarian authority (NIH) at the end of 2011. The government also delayed payments for already prefinanced, fulfilled R&D contracts. The funding for new domestic R&D project financing schemes as well as for co-financing of joint technology initiatives of the EC (ENIAC JTI after this first two calls) dried up in 2011. Thereby even the chances for mobilization of international financial resources also became dim.

Thanks to the exceptionally disciplined financial management of MFA and the trust of the staff in the direction of the institute, *the year of 2011closed with a turnover of HUF 1.5 Billion and without any debts to record.*

By the end of the year it became obvious, however, that due to further decreasing subsidy, lack of domestic competitive R&D calls and accessible industrial R&D resources the institute will hardly be able to survive 2012! A crisis and even bankruptcy seems to be preprogrammed. This situation was further aggravated by the consequences of the decision of the General Assembly of HAS concerning the „*renewal of the research network*" in December, which requires *MFA to become part of the Research Centre for Natural Sciences (MTA TTK)*. For the time being this meant *solely an administrative unification* of the Research Centre of Chemistry and three formerly independent flexible research institutes *in the new centre with a staff of 650. Each having completely different scientific strategies, research culture, and levels of organization they further operate at four or five different sites*. By experience any *centralized administrative operation* has a greater inertia and is thus *less efficient* and *more expensive* as well.

In a generally *unfavourable research support atmosphere*, due to the imposed budget cuts and additional costs for the new *centralized operation*, the year 2012 does not promise benefit for us! *The exceptionally dynamic development, which characterized the 14 years of MFA from its foundation until the loss of independence is seemingly going to come to an end.* Unless…

Budapest, February 2012.

István Bársony
corr. member of HAS, director HAS RCNS Institute MFA

GENERAL INFORMATION

Organization

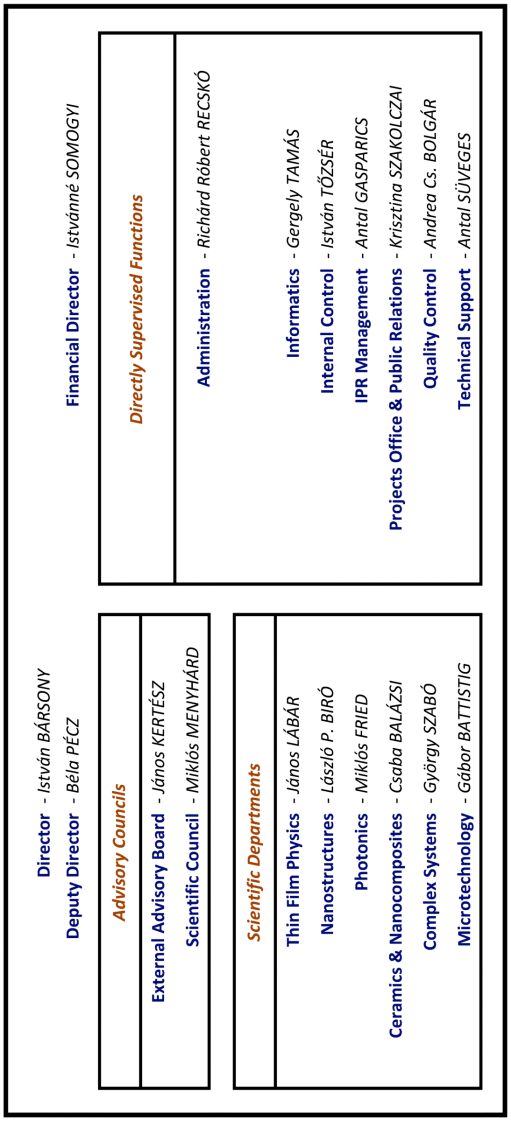

External Advisory Board

János KERTÉSZ
ordinary member of the HAS
(president)

BME TTK Fizikai Intézet, Elméleti Fizika Tanszék
1111 Budapest, Budafoki út 6-8., Hungary
kertesz@planck.phy.bme.hu

Árpád CSURGAY
ordinary member of the HAS

PPKE Információs Technológia Kar
1083 Budapest, Práter u. 50/A, Hungary
University of Notre Dame, Center for Nano Sci. &Technology, France
acsurgay@itk.ppke.hu
acsurgay@nd.edu

Lothar FREY
Univ. Prof.

FhG IISB, Erlangen
91058 Erlangen, Schottkystrasse 10., Germany
lothar.frey@iisb.fraunhofer.de

József GYULAI
ordinary member of the HAS

MTA MFA
1121 Budapest, Konkoly-Thege M. út 29-33., Hungary
gyulai@mfa.kfki.hu

Lars HULTMAN
Univ. Prof.

Thin Film Physics Division, Linköping University, Sweden, **IFM** Linköping University, S-581 38 Linköping, Sweden
larhu@ifm.liu.se

Gábor SZABÓ
corresponding member of the HAS

SZTE TTK Optikai és Kvantumelektronikai Tanszék
6720 Szeged, Dóm tér 9.
gszabo@physx.u-szeged.hu

Key Financial Figures

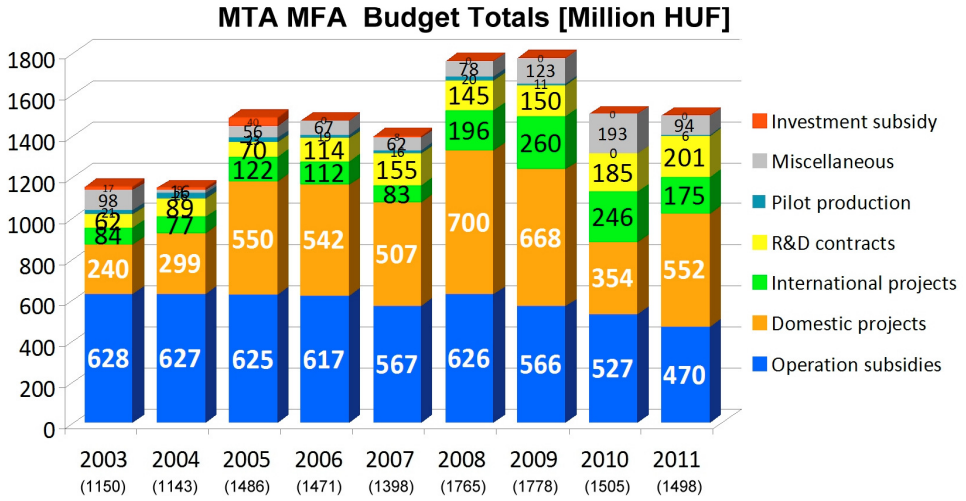

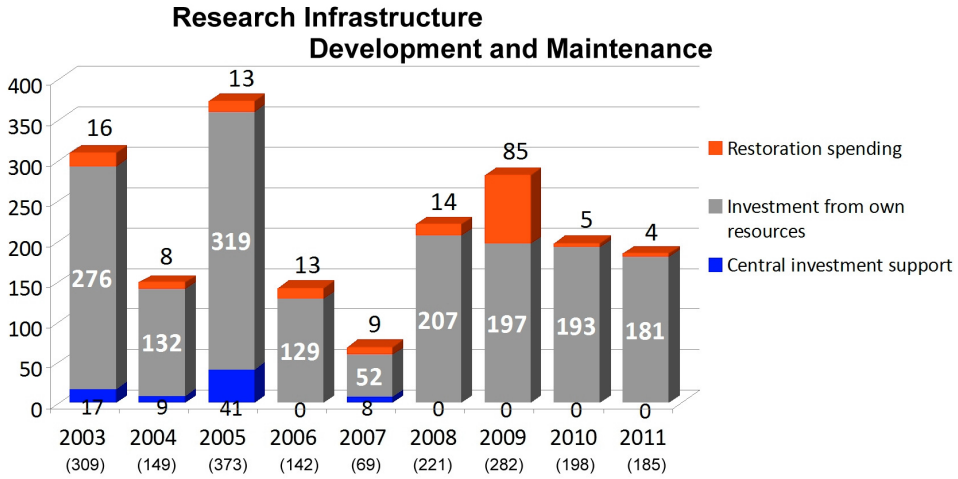

Publications & Citations of MFA

According to the WoS and MTMT databases, the institute has kept an average publication activity of over 100 scientific journal papers per year in the past decade.

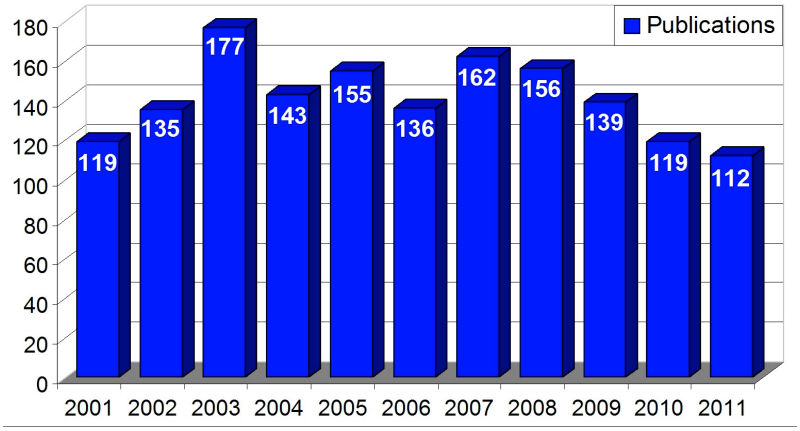

The complete 2011 publication list of MFA – with considerably more titles than listed by ISI Web of Science –is included at the end of this yearbook.

A good measure of the recognition of MFA's scientific activity is the h-index value of 49, and the steady growth of the number of independent citations.

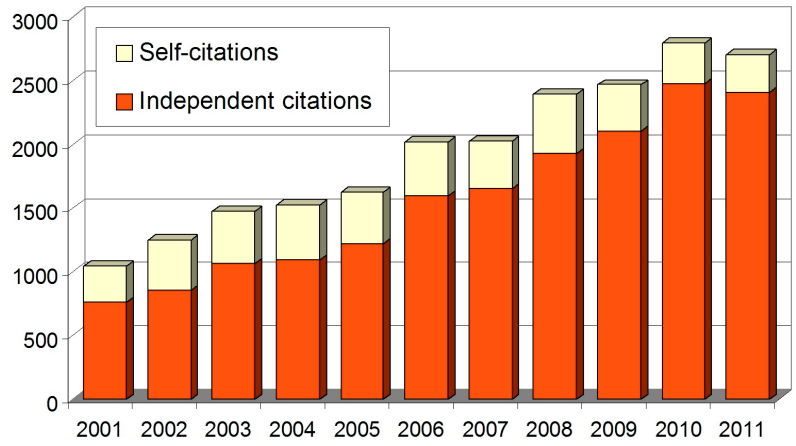

Honoures and Awards

In 2011 the highest scientific prize of the Hungarian Academy of Sciences (HAS) was given to 2 scientists of the MFA (László P. Biró and Béla Pécz), by the Physics and the Engineering Sections of the HAS. This is an unparalleled scientific achievement!

Prof. Dr. László P. Biró (**www.researcherid.com /rid/A-3057-2010**), winner of the **Physical Prize of the Hungarian Academy of Sciences (HAS) 2011**, has a longstanding expertise in the field of nanoscale materials science. He obtained his Diploma in Physics (with distinction) from the Babes-Bolyai University, Cluj-Napoca (1979), and his Ph.D. (summa cum laude) in Physical Engineering from the Technical University of Budapest (1997) for his achievements in in-situ defect engineering during ion implantation. Following the Ph.D. he became the founding head of the Nanostructures Department in MFA (**www.nanotechnology.hu**). His research was focused on carbon nanotubes (CNTs) and CNT type complex nanoarchitectures. In 2005 he got the title of Doctor of the HAS for his achievements in the field.

Since 2003 he became interested in photonic nanoarchitectures of biologic origin - particularly in photonic crystal type structures occurring in butterfly scales - and published several ground breaking papers and invited reviews in the field. Since 2005 he is interested in graphene research. In 2008 he and his group published the first paper reporting the atomic precision lithography of the graphene with crystallographic orientation control. Later they developed the first oxidation process allowing the production of atomically precise zig-zag edges in graphene nanoarchitectures. In the past decade Prof. Biró has been the supervisor of 8 Ph.D. dissertations, and 2 of his Ph.D. students won the most prestigious Hungarian scientific prizes for young scientists (Junior Prima Prize). Prof. Biró has authored/co-authored more than 220 peer reviewed papers, 3 books, 10 book chapters, has received more than 2500 WoS citations, and has a Hirsch-index of 29.

Dr. Béla Pécz, winner of the **Academy Prize 2011** (Engineering section), was awarded for his achievements in transmission electron microscopy, for his results in the research of semiconducting materials. He obtained his Diploma in Physics from the Roland Eötvös University, Budapest (1985) and got his Ph.D. (C.Sc.) from the HAS (1993) for his results in the field of Au/AIIIBV contacts. In 2004 he got the title Doctor of the HAS in the field of wide bandgap semiconductors. He was the head of the Thin Film Physics Laboratory (MFA) from the beginning of 2000 and became the deputy director of MFA from 2004 March.
He is interested in the structural research of semiconducting materials. He made valuable research experiments in the ion beam synthesis of wide bandgap semiconductors. He initiated new experiments in the crystal growth of nitrides. He was the Hungarian principal investigator of seven EU projects. He is the president of the Hungarian Society for Microscopy. His publications in international journals received more than 1000 independent citations and resulted in a Hirsh-index of 20.

Krisztina Szakolczai, Ph.D*, the leader of the IMNTP office received* ***Certificate of Merit*** *from Tamás Németh, the main secretary of the HAS, in her outstanding services for HAS.*

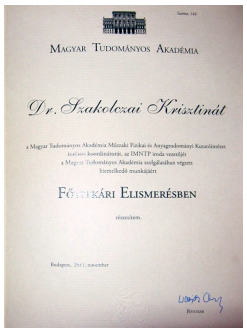
MAGYAR TUDOMÁNYOS AKADÉMIA

Dr. Szakolczai Krisztinát

FŐTITKÁRI ELISMERÉSBEN

Anita Pongrácz, Ph.D.*, obtained the* ***Academy Prize for Young Scientists*** *in 2011 from Tamás Németh, the main secretary of the HAS for her work in the field of: "Epitaxial growth of cubic SiC nanocrystals on Si surface".*

Péter Kozma, Ph.D.*, received the* ***"Outstanding Young Scientist of VEAB"*** *prize from the Veszprém local committee of the HAS (left and below).*

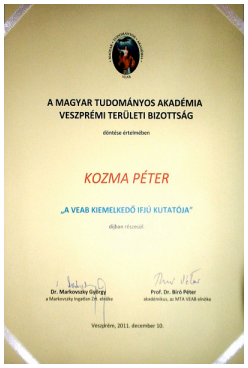
A MAGYAR TUDOMÁNYOS AKADÉMIA
VESZPRÉMI TERÜLETI BIZOTTSÁG

KOZMA PÉTER

„A VEAB KIEMELKEDŐ IFJÚ KUTATÓJA"

***Péter Nemes-Incze, Ph.D.**, postdoc received the **Ferenczi György prize 2011**.*

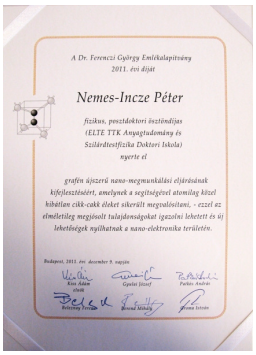
A Dr. Ferenczi György Emlékalapítvány
2011. évi díját

Nemes-Incze Péter

fizikus, posztdoktori ösztöndíjas
(ELTE TTK Anyagtudomány és
Szilárdtestfizika Doktori Iskola)
nyerte el

grafén újszerű nano-megmunkálási eljárásának
kifejlesztéséért, amelynek a segítségével atomilag közel
hibátlan cikk-cakk éleket sikerült megvalósítani, - ezzel az
elméletileg megjósolt tulajdonságokat igazolni lehetett és új
lehetőségek nyílhatnak a nano-elektronika területén.

***Zoltán Juhász, Ph.D.**, senior research fellow of MFA received the **Szervatiusz Jenő prize 2011**, as an excellent folk musician and teacher (left).*

***Zsolt Czigány, Ph.D.**, received the "**European Materials Society Outstanding Paper Award 2011**" in the category of materials science (among 28 other candidates) for his paper: "Interpretation of electron diffraction patterns from amorphous and fullerene-like carbon allotropes"* Ultramicroscopy 110, 815–819 (2010)*, by Zsolt Czigány and Lars Hultman.*

- **Zoltán Fekete** received the **MFA youth prize** for his help for students.
- **Anita Pongrácz, Ph.D.,** received the **MFA postdoc prize** for her international micromechanical technological achivements.
- **Krisztian Kertész, Ph.D.**, received the **MFA postdoc prize** for his achivements in photonic nanoarchitectures and mentoring students.
- **János Volk, Ph.D.**, received the **MFA research prize**, for creating his research group, delivering excellent lectures, and for organizing international conference.
- **Andrea Németh**, first place in the XXX. OTDK competition in bio-physics.
- **Éva Denkné-Horváth** received the **MFA prize** for her decades long services for the MFA

HIGHLIGHTS

Punishing strategies in structured populations

(OTKA K-73449)

György Szabó, Attila Szolnoki, and Lilla Czakó

The evolutionary game theory provides a general framework for the quantitative analysis of large self-organizing living systems composed of several members. In the corresponding models the players can represent viruses, microbes, plants, animals, human individuals or even their groups (firms, countries). According to the basic concept of payoff matrix, it is used to describe the interactions between the players who can modify their own strategies by following an evolutionary rule to increase their personal income or fitness. The fundamental problem is to identify the main mechanisms to avoid the "*tragedy of the commons*" by maintaining cooperation among selfish players. According to earlier studies, the punishment of antisocial behavior seems necessary for a stable society. This can be done via peer (individual) or pool (institutional) punishment.

The novelty of our proposed model was that it considered the limited interactions of members regarding the institution of pool punishment [149]. This feature can be modeled as an additional strategy increasing the complexity in the spatial system.

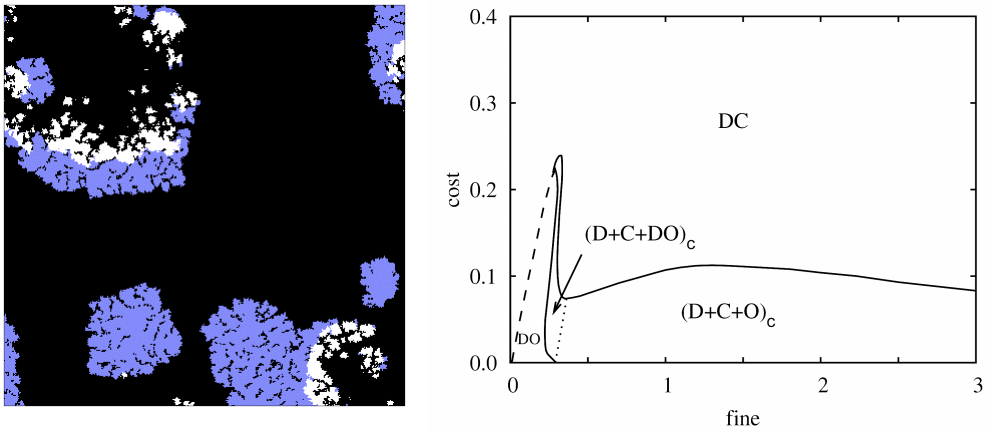

Figure 1. *(Left) Typical distribution of strategies within the (D+C+DO)c phase (strategies are marked by different colors, as indicated). (Right) The full fine-cost phase diagram for r=3.8 synergy factor. Solid (dashed) lines indicate continuous (discontinuous) phase transitions. The dotted line represents the analytical continuation of phase boundary separating the pure D and O phases in the absence of cooperators.*

Indeed, such a multi-strategy complex system can be characterized by the presence of strong fluctuations, unpredictable and non-linear dynamics, multiple scales of space and time, and frequently some forms of emergent structure. As an example, Fig. 1. shows a typical pattern where rock-paper-scissors type cyclic dominance can emerge where one strategy in the cycle can be an alliance of two strategies. It should be noted that, because of the mentioned complexity, such a solution can only be obtained by careful and intensive numerical simulations, where the stability analysis based on the concept of competing associations is required. The full phase diagram, shown in Fig. 1, suggests that for high fines the system paradoxically evolves into a self-organizing spatio-temporal pattern where another type of cyclic dominance helps the coexistence of all three strategies.

Further important question is to compare the efficiency of pool and peer punishment strategies within the framework of a spatial public goods game [148]. In striking contrast to the well-mixed condition where everybody interacts with everybody else, the solutions in a structured population may depend sensitively on the parameter values that characterize the relation of punishment strategies as it is demonstrated in Fig. 2. In many cases the peer punisher strategy seems to be more efficient, but there are parameter regions where both types of punishment coexist, sometimes together with the (pure) cooperators weakening the efficiency of punishment. More interestingly, there are parameter regions where the competition between the different types of punishment help defectors prevail over the whole system. This can happen via a new type of mechanisms what has not been identified earlier.

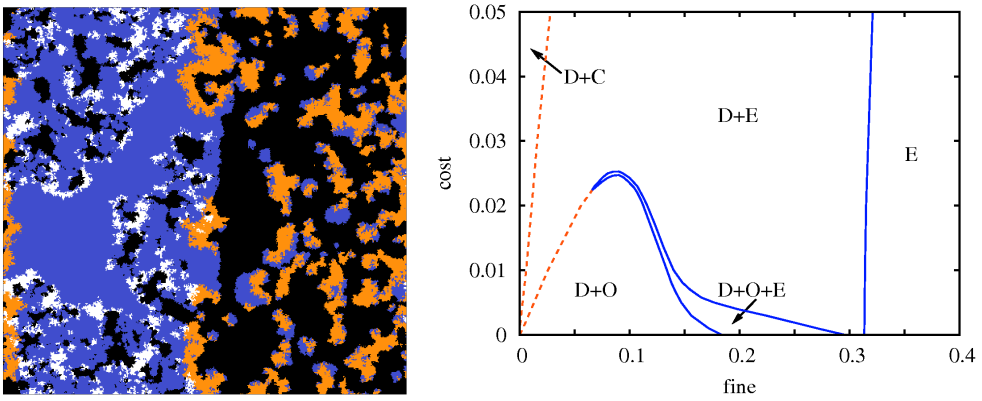

Figure 2. *(Left) Typical arrangement of cooperators (white), defectors (black), and peer punishers (orange) when we study the spatial competition between two different associations of strategies.*

(Right) The full fine-cost phase diagram for r=3.8 synergy factor in the four-strategy system at low noise limit. Blue solid (red dashed) lines indicate continuous (discontinuous) phase transitions.

The snapshot in Fig. 2 illustrates how the strategy association D+O+E invades the territory of another assocation composed from D, C, and O strategies. For the present parameters both types of associations can be considered as a particular solution of the subsystems where one of the strategies are missing. By determining the direction of invasion we could identify the stable solution.

Real-life situations can not only be reached by increasing the number of possible strategies as exemplified in the mentioned studies. An alternative approach is when instead of pure strategies players can adopt an emotional profile from one of their neighbors. Now we have supposed that the emotional profile of each player is determined by two privotal factors only, namely how it behaves towards the less and how towards the more successful neighbors [150]. As a result, the proposed imitation rule can promote cooperation but also allows players to form a role-separating configuration in snow-drift game quadrant which state is unreachable by traditional strategy imitation rules.

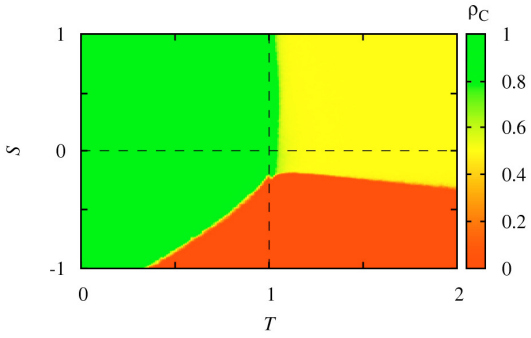

Figure 3. *Color map depicting the final probability of cooperative behavior on the temptation (T) – sucker's payoff (S) parameter plane. This plot reveals that replacing the imitation of strategies with the imitation of emotional profiles promotes cooperation in all spatial social-dilemma games.*

Our works were partly made in strong collaboration with Swiss, Sloven and Chinese scientists and we hope that such strong connections will be extended to other English and US partners in the near future.

Dual Channel Grating coupled interferometer configuration for high resolution label-free optical sensing

(EU FP7 OPTIBIO, OTKA PD 73084)

Daniel Patko, Kaspar Cottier*, András Hámori, and Róbert Horváth

*Creoptix GmbH, Wädenswil, Switzerland

Sensitively measuring biological interactions at the nanometer length scale has increasing importance both in basic biological research and in modern industrial applications. Devices capable to conduct such measurements find intense applications in the diverse areas of genomics, proteomics, basic cell biological research; and in the food, health and military areas. When biochemical interactions are monitored, today, the widely used and well accepted technique is the ELISA (Enzyme Linked Immunosorbent Assay) assay. ELISA is a sensitive technology based on labelling. This means that it uses fluorescently (or radioactivaly) labelled molecules to monitor the interactions. The advantage of ELISA is its high sensitivity and the massive and solid knowledge behind it. But, in several applications this additional labelling is a disturbing factor affecting the state of the molecules or living cells under investigation. Label-free technologies are under intense research and development today. In these systems the molecules are detected through their inherent properties; such as mass, charge or refractive index. Among these the optical techniques are the most sensitive. The integrated optical waveguide-based systems are especially promising. They offer high sensitivity, cost effective miniaturization and possible parallelization of various sensing units. Moreover, the sensing surface can be coated with basically any type of transparent material suitable for the application. The key element of all waveguide based method is a thin high refractive index dielectric film (typically 100-200 nm thick) deposited on a solid support. Light can be guided in such a film by total internal reflections, creating an evanescent wave above the film (see Fig. 1.). Any material deposited in the evanescent field affect the properties (such as intensity, phase) of the guided light which can be measured using an appropriate interrogation unit.

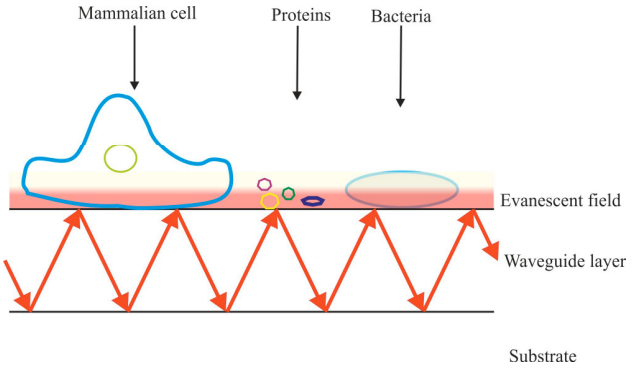

Figure 1. *The evanescent field of the waveguide mode interacts with the analytes.*

Grating Coupled Interferometry (GCI) is a waveguide based cost effective and label-free optical sensing method introduced recently [P. Kozma, A. Hamori, S. Kurunczi, K. Cottier, R. Horváth: Applied Physics B, Volume 97 (2009), Issue 1, Page 5]; [71]. This fundamentally novel measurement strategy combines the simplicity of grating coupled planar optical waveguides with the excellent resolution of interferometric measurements.

Our recent work focused on the development of a novel GCI configuration which outperforms the previous ones in terms of stability, easy of usage and reproducibility of the measurements. Now we use high quality waveguides with two incoupling and one outcoupling grating areas to increase and precisely control the mode interaction length with the sample; and to make the sensor more suitable for plate-based multiplexing. Moreover, the introduced referencing sensor channel and a built in peltier based temperature stabilizing system gives excellent device stability, easy of operation and low sensor drifts making GCI suitable for high resolution label-free measurements.

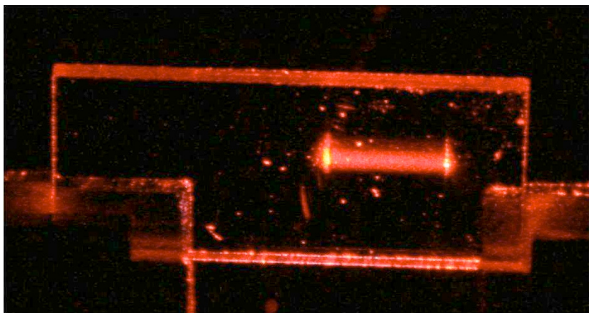

Figure 2. *The high quality sensor chip.*

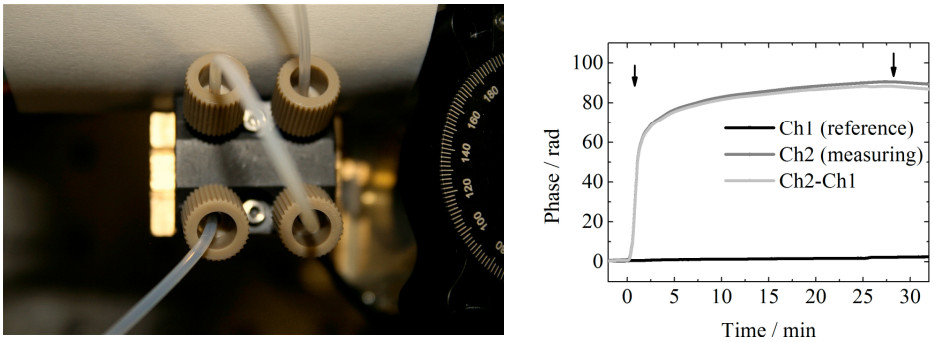

Figure 3. *The flow through cuvette (left) and the measured phase signals in the two channels (right) when solutions with various RIs (1,33115; 1,33207; 1,33676) were flowed over the sensing areas.*

Public outreach

EuroNanoForum

The **EuroNanoForum** (**ENF'11**, http://euronanoforum2011.eu/) conference and exhibition was held in 2011 as the largest nanotechnology conference and exhibition in Europe. ENF'11 was proposed to be organized by the Hungarian National Innovation Office (NIH, http://www.nih.gov.hu), and was prominently featured in the Hungarian EU Presidency program during 2011. The ENF'11 attracted more than 1100 visitors to Budapest from all over Europe between May 30-June 1.

MFA's substantal participation in the organization of the event:

EuroNanoForum 2011 Budapest

Budapest, May 30-June 1 (2011)

- Prof. László P. Biró invited plenary speaker at the press conference (top left).
- The IMNTP-MFA stand to promote the Nanobus concept and to present the scaled-down paper model (left).
- Final accord of the workshop "Under the umbrella of NANO*futures*" (right).

Nanobus

NIH and the Local Organizing Committee of the ENF'11 supported the idea of **setting up a mobile nanotechnology exhibition for Hungary**, and run it for several years to increase the nano-awareness in the country. The project called "**NanoMiracles - on the Move**" (a.k.a. **Nanobus**) was one of the accompanying programs of ENF'11. The project was initiated and lead by MFA and the Hungarian Technology Platform for Integrated Micro/Nanosystems (IMNTP). The idea inspired and mobilized the Hungarian nanotechnology oriented companies, institutes, universities and persons.

The aim of the mobile nanotechnology exhibition is to demonstrate the potential applications and the socio-economic benefits of the use of nanotechnology. The roadshow would welcome thousands of visitors and also give the opportunity to high-school groups and university students, as well as the general public to get directly in touch with nanotechnologies, nanomaterials and the related products.

MFA opened a call for proposals (**NanoDemo**) in January 2011 soliciting ideas for toys and demonstrators, enhancing nanotechnology awareness. The best accepted

Jury and winners of the NanoDemo call, March 2011.

interactive games had been constructed and tested in the **Palace of Miracles,** Budapest (PM). The NanoMiracles exhibition officially opened on the eve of the opening of ENF'11 on 30th May 2011. After that over 58.000 visitors tested the exhibits for 3 months. The testing period was successful; the selected interactive demonstrations were placed in the nanobus.

Due to (mainly) Hungarian projects' financing problems, the nanobus was not ready for ENF'11. The downscaled model, however, was shown to the participants and the press at the exhibition. After evaluating the options, a Hungarian bus (Ikarusz 288) was bought and refurbished. 20 square meters of scientific, educational posters, product showcase, cleanroom technology demonstration, 40 videos, a microscope and a nanomanipulator serve the visitors. There are 9 interactive games on the bus, including a lotus effect labyrinth game, a solar control capsule, an AFM model and a nano-treadmill shown. The exhibit focuses on the basic knowledge of nanoscience, the benefits and potential, and also the risks associated with nanotechnology. It provides a multimedia illustration of the state-of-the-art in nanotechnology today. The implementation includes Hungarian "nano" products, too. The Hungarian versions of nanotechnology videos made available via PM and YouTube channels.
Estimated total cost of the nanobus is ca. 100k EUR (net value). It was financed by an FP7 program, by national fund and also from sponsorship and support of IMNTP members and other Hungarian institutions. The nanobus roadshow was officially kicked off on 12th September, 2011 by Dr. József Pálinkás, the president of HAS. An official address on the inauguration was also presented by Dr. György Mészáros, president of NIH, and Dr. István Bársony, director of MFA. The nanobus is going to be operated by PM. The mobile exhibition is expected to visit about 50 larger towns within the next 3 years. It already appeared at the festival "Bridge of Science" (Budapest, Chain Bridge) and at the Researcher's Night event (Miskolc).

Prof. József Pálinkás, president of the HAS officially inaugurates the Nanobus.

MFA Open Day

We do our best at popularizing natural sciences among the wider audience, to make it tangible what and why we make from the money that the goverment spends on research institutes like ours. For this purpose, we organize laboratory viewing excursions for groups of visitors throughout the year, but we keep also an official open day (open for everybody older than 18), usually in the first half of November, associated with the **Science Day in Hungary** on November 3. In 2011 it was held on **November 18,** with lots of interesting labors open, and with four exciting oral presentations ("Scanning Electron Microscopy" by Attila L. Tóth, "Music research Using Artificial Intelligence" by Zoltán Juhász, "The Nature of Co-operation" by György Szabó, and "Travels by Tuneling Effect" by Péter Vancsó).

Labor viewing and speaches at the official MFA Open Day, November 18 (2011).

MFA Summer School

We have organized the **MFA Summer School** in 2001 (June 27–July 1) already the 4th time, devoted to secondary school students. Our "scientific camp" (as the youngsters like to call it) is open for applicants from the whole Carpathian basin, for the Hungarian speaking high school students, especially for the younger ones! (Details from: **Csaba S. Daróczi**) This year we hosted 23 pupils. MFA fully financed their participation (travelling, subsistence, social programs, etc.). Previously we offered **21 scientific subjects** for the fellowship to choose from, and during the week we provided professional guidence.

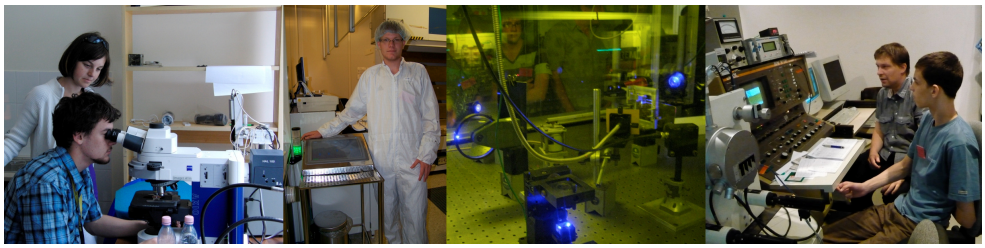

During the regular working hours the enthusiastic students were fully absorbed in scientific research, everybody in her/his chosen subject (selected from more than 20).

After the working hours we always find the time to make excursions to the beautiful places of the neighborhood.

The participants of the MFA Summer School 2011 (June 27–July 1), Csillebérc.

The proof of the long-term positive effect of the summer school is the success of our 2 participants (**Ágota Z. Farkas**, and **Áldor E. Kenéz**) at the scientific student conference **TUDEK**, where they received special prizes in physics.
Another two participants (**Ervin Hábel**, and **Kata Ferenc**) from the earlier years received special prizes of the **NanoDemo** competition.

Social events

MFA sport day

In our traditional sport day everyone can challenge herself/himself at least in some not so common, but in Hungary always popular sports, like wine glass lifting (down, left), mass feeding (down, center), endurance sitting (top, left). Others tried bread lining (down, right), archery (top, right), football, tennis, table tennis, badminton, or running.

Santa Claus party

We have always popular meetings/parties at santa claus and before christmas eve.

2011. Christmas celebration of MFA with invited guests and staff.

SCIENTIFIC REPORTS

Nanostructures Department

Head: Prof. László Péter BIRÓ, D.Sc., scientific advisor

Research Staff

- Zsolt Endre HORVÁTH, Ph.D., Deputy Head of Department
- Prof. József GYULAI, Member of the HAS (Professor Emeritus)
- Antal Adolf KOÓS, Ph.D. (on leave)
- Géza István MÁRK, Ph.D.
- Zoltán OSVÁTH, Ph.D. (on leave)
- Levente TAPASZTÓ, Ph.D.
- Krisztián KERTÉSZ, Ph.D
- Enikő HORVÁTH, Ph.D (maternity)
- Zofia VÉRTESY, Ph.D.

Ph.D. students / Diploma workers

- Gergely DOBRIK, Ph.D. student
- Péter NEMES-INCZE, Ph.D. student
- Péter Lajos NEUMANN, Ph.D. student (on leave)
- Bernadeth PATAKI, Ph.D. student
- István TAMÁSKA, Ph.D. student
- Péter VANCSÓ, Ph.D. student

- Gábor MAGDA, diploma worker
- Vince OBRECZÁN, diploma worker
- Gábor PISZTER, diploma worker

Technical Staff

- Zoltánné SÁRKÁNY, technician

The Nanostructures Department has an almost two decades expertise in the production and characterization of various nanostructures. In recent years in the focus of work were various carbon nanostructures (CNTs, graphene and few layer graphite) their nanoarchitectures, bioinspired photonic nanoarchitectures and their applications. The most relevant results in 2011 are detailed below:

We showed for the first time by STM/STS that the grain boundary regions separating the crystallites of CVD graphene have strikingly different electronic properties as compared with the crystallites.

We developed an AFM based, quick and widely accessible method for revealing the grain size and relative grain orientation in CVD graphene.

The wings of nine polyommatine, Blue butterflies were demonstrated to exhibit selective chemical detection, using the spectral analysis of the reflected light.

It was shown by detailed structural and spectral analysis that both the wing nanoarchitecture and the reflectivity of the investigated nine polyommatine, Blue butterflies is species characteristic.

The tunneling processes into a thin sheet of jellium and those into single sheet of graphene and the charge propagation in a defect free layer of graphene and a sheet with a grain boundary were compared by wave packed dynamical calculations.

Carbon nanotube (CNT)/polymer composites were investigated by optical, electron microscopy complemented by conductive AFM (C-AFM) measurements. The C-AFM was able to reveal the distribution of interconnected CNTs. For more details, please feel free to visit the web page of the Nanostructures Department (link: **http://www.nanotechnology.hu/**).

Mapping the electronic properties of individual graphene grain boundaries

(JKHLN 2010K000980, OTKA PD8424, OTKA K0677934)

L. Tapasztó, P. Nemes-Incze, G. Dobrik, K. Yoo (KRISS, Korea),
C. Hwang (KRISS. Korea), and L. P Biró

Grain boundaries, the characteristic topological defects of CVD graphene samples are expected to substantially alter the electronic properties of the unperturbed graphene lattice. The CVD synthesis method is of high practical relevance, as it allows the growth of wafer-scale continuous single layer samples. However, a fundamental challenge of this technique is that the electrical quality (conductivity, charge carrier mobility) of the as-grown graphene samples falls behind by about an order of magnitude as compared to mechanically exfoliated graphene. There is growing evidence that the presence of grain boundaries is responsible for the degradation of the intrinsic electronic performance of these samples. However, very little is known about the underlying mechanism, which is of particular importance in our efforts towards understanding and ultimately controlling electronic transport in the presence of GBs.

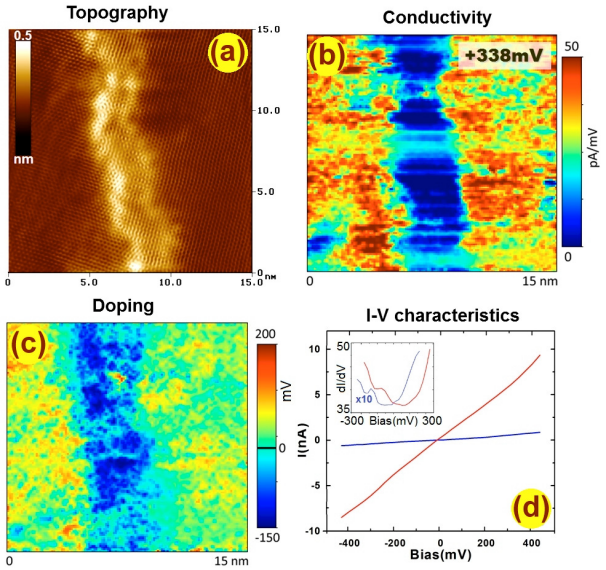

Figure 1. ***a)*** *Atomic resolution constant current topographic STM image (100 mV, 1 nA) of a 29º graphene grain boundary, with the boundary region displaying a bright contrast.* ***b)*** *Spatially resolved tunneling conductivity map revealing a markedly suppressed conductivity at the grain boundary region.* ***c)*** *Spatial map of the Dirac-point position relative to the Fermi energy, indicating the local doping.* ***d)*** *Representative individual current-voltage characteristics acquired at the grain boundary (blue) and over the unperturbed graphene lattice (red). The corresponding numerical derivatives (differential conductance) are shown in the inset.*

In this work, we employed local probe methods, namely, scanning tunneling microscopy (STM) and spectroscopy (STS) measurements, which allow us to locally explore the electronic behavior of individual graphene grain boundaries at the nanometer scale. From the map in Fig. 1b it is apparent that the conductivity is markedly suppressed at the grain boundary within a region of a few nanometers. This implies that from the electrical point of view, the interconnected grain boundary network divides the graphene sample into highly conductive single crystalline islands delimited by more resistive interface regions of a few nanometer widths.

We have also mapped the spatial distribution of the tunneling conductivity (LDOS) minima position, relative to the Fermi energy, which is indicative of the local doping. A striking difference has been revealed in the position of the Dirac point at the grain boundaries and over the defect free graphene lattice, as apparent form Fig 1.c. According to these results, the GBs of CVD graphene form n-doped inversion channels within the overall p-doped graphene lattice.

Moreover, these properties of grain boundaries have been found to be universal and robust against disorder. In order to illustrate this in Fig. 2 we show a grain boundary triple junction consisting of three distinct grain boundaries with tilt angles of 27°, 21° and 12°. As can be seen the conductivity maps and doping profiles are quite similar for all three GBs, underscoring the universal character of the reported phenomena, which is a huge advantage from the applications point of view.

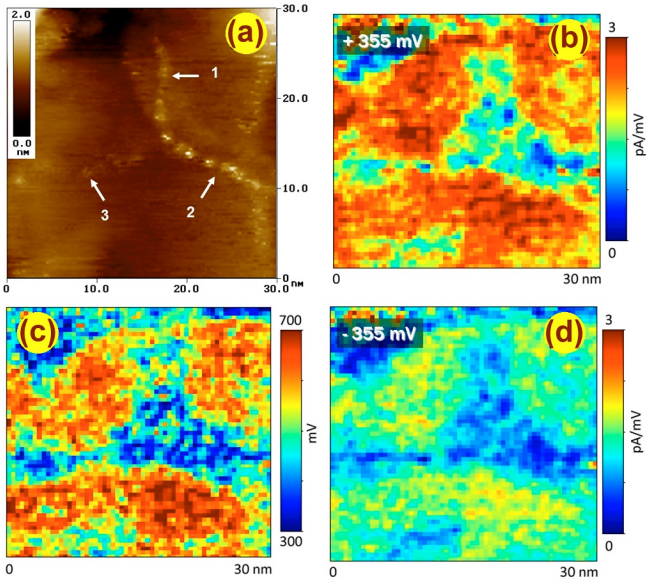

Figure 2. a) *STM image (100mV, 2 nA) of a graphene grain boundary triple junction consisting of three grain boundaries with relative angles of 27°, 21°, and 12°.* ***b)*** *Local conductivity map showing the suppression of conductivity on all grain boundaries for positive (**b**) and negative sample bias (**d**).* ***c)*** *Local doping map displaying a substantially reduced p-doping all over the GB triple junction region.*

Revealing the grain structure of graphene grown by chemical vapor deposition

(JKHLN 2010K000980, OTKA K067793)

P. Nemes-Incze, K.J. Yoo (KRISS, Korea), L. Tapasztó, G. Dobrik, Z. E. Horváth, C. Hwang (KRISS, Korea), and L. P. Biró

The physical processes occurring in the presence of disorder: point defects, grain boundaries, etc. have detrimental effects on the charge transport properties of graphene. This is especially true in the case of CVD grown graphene samples. Improving these properties is a goal best achieved by finding the growth parameters that result in samples with the highest crystallinity and the smallest number of grain boundaries. However, this is usually a prolonged, empiric and iterative process of analyzing the grown graphene sample, tweaking growth parameters and performing the CVD growth. We have developed a method that gives a quick assessment of the grain structure of graphene, which if employed in the CVD optimization procedure, has the potential to substantially speed up this process.

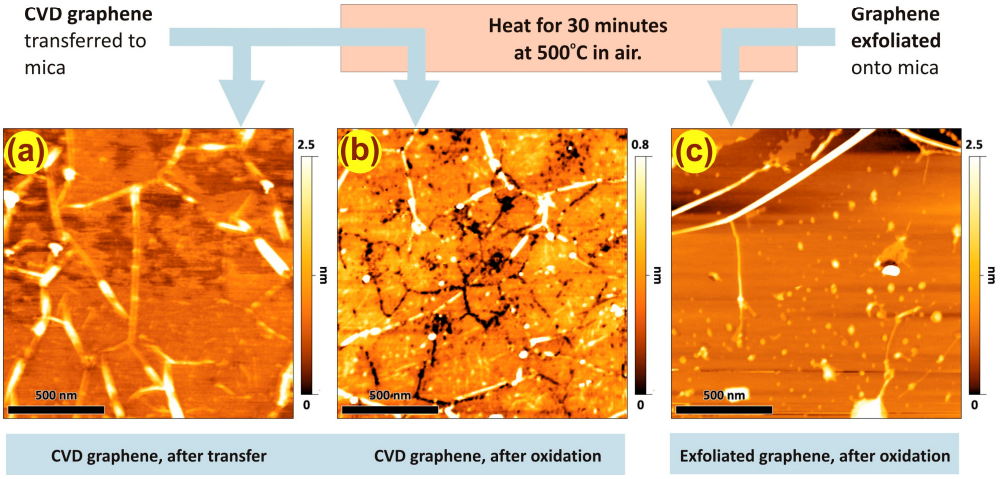

Figure 1. *The process flow of the sample preparation and tapping mode AFM images of the graphene samples: (a) pristine CVD graphene sample transferred to mica, showing wrinkles; (b) CVD graphene on mica after oxidation, black lines correspond to etch trenches; (c) control sample: graphene exfoliated onto mica from high grade graphite, after oxidation.*

The mapping technique relies on the selective oxidation of grain boundaries in air, at 500 °C (Fig. 1). At defect sites, the carbon gasification reaction has lower activation energy and thus the defects can be revealed by etching away the carbon in their close vicinity. We have exploited this effect to reveal the grain structure of graphene. After performing this simple heat treatment and subsequent atomic force microscopy (AFM) measurements we obtain a map of the grain boundaries, which can be further

processed by image analysis software to yield the areas enclosed by the etch trenches. This can be used to construct a histogram of the characteristic size of grains and by using lattice resolution AFM images, the distribution of misorientation angles of the grain boundaries (Fig. 2).

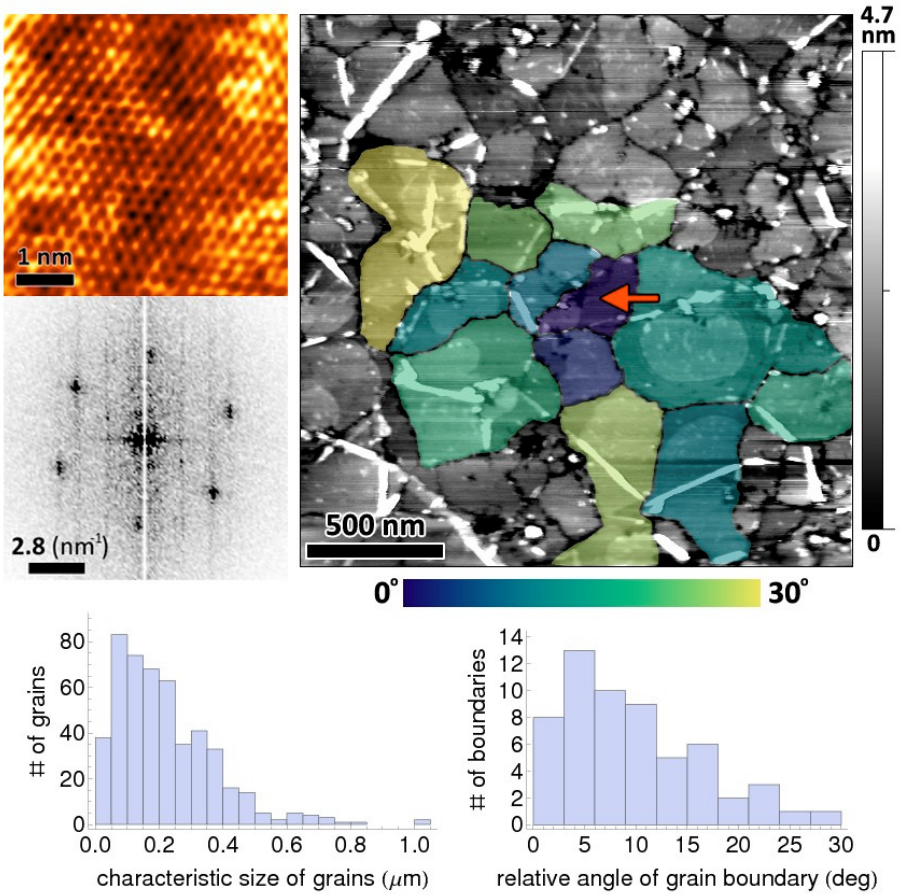

Figure 2. *AFM image of CVD graphene showing the etch trenches. By comparing the Fourier transform of atomic resolution AFM images of individual grains, we coud make a false color map of the crystallographic orientation of the grains relative to a given direction. Two small images to the left show one such atomic resolution image and the Fourier transform thereof. The atomic resolution image was recorded by contact mode AFM on the grain shown by the red arrow. Histograms at the bottom show the distribution of the grain size (left) and the relative angle of the grains forming the boundaries (right). This data is a compilation of multiple AFM mapping measurements.*

Our grain boundary analysis method is easy to implement and can give quick feedback for researchers involved in the CVD growth of graphene, helping to bring closer the goal of growing graphene with high crystallinity and better control over the microstructure.

Polyommatine butterfly wing nanostructures used for selective gas/vapor sensing

(OTKA PD 83483)

K. Kertész, G. Piszter, E. Jakab (HAS, CRC), Z. Vértesy, Zs. Bálint (HNHM, Hungary), and L. P. Biró

In this work we will show the results of recent measurements on nine closely related Polyommatine lycaenid blue butterfly species. Their wing scales contain a characteristic "pepper-pot" type nanoarchitecture, composed of a chitinous nanoarchitecture with air filled hollows (see previous material in the Yearbook). The optical response of a butterfly wing on chemical changes in the environment is determined by the spectral changes in the reflected light. These changes depend on one hand on the composition of the ambient atmosphere and on the other hand on the characteristic wing nanostructure. When the refractive index in the air gaps changes, - for example replacing air by an air / vapour (gas) mixture - the optical properties of the Nanocomposite are altered. Therefore, the natural photonic nanoarchitectures are able to act as selective optical gas / vapour sensors. The general layout of the investigated nine structures is similar, but the colours generated by the specific nanoarchitectures are species specific [Piszter et al. Anal. Methods 3, 78-83]. For the wing scale structure see Fig. 1.

If the blue wing reflectance in dry air is specified as 100%, the deviation for a specific gas (vapour) appears as is shown in Fig. 2 by the modification of the reflectance in time. The process can be presented in a 3D diagram, the end of gas exposure is marked with the arrow. One can observe from Fig. 2 that a fast response is developed.

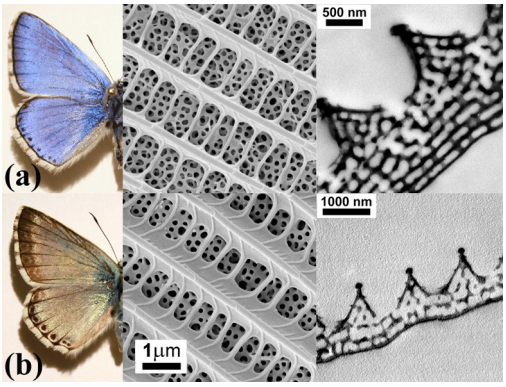

Figure 1. *Dorsal side photgraph, SEM and TEM images of P. bellargus and P. coridon*

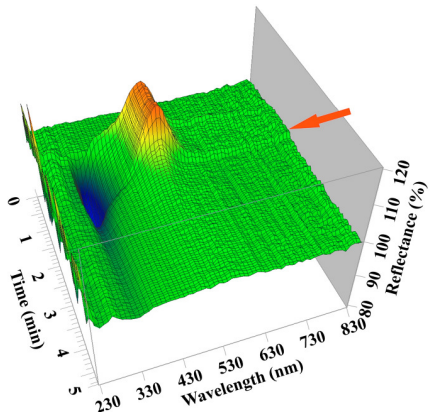

Figure 2. *Temporal variation of the reflectance for ethanol exposure.*

Similar nanoarchitectures generate similar colours and develop similar response upon exposure to the same vapour. We investigated nine closely related blue Lycaenid

species (see the previous article in the Yearbook). For every species we extracted curves corresponding to the same amount of elapsed time from the 3D diagrams. As an example in Fig. 3 similar wings are shown giving similar response.
We tested increasing vapour concentrations of ethanol and water vapour. In figure 4 the time dependence of two integrated wavelength intervals are represented. Both D1 (250 nm – 332 nm) and D4 (700 nm – 750 nm) show a close to linear dependence with the vapour concentration used. The main difference is clearly visible in the D4 behaviour. The appearance of minimum and maximum peaks separates well water vapours from ethanol. This shows that these types of nanoarchitectures are suitable to be used as selective chemical sensors.

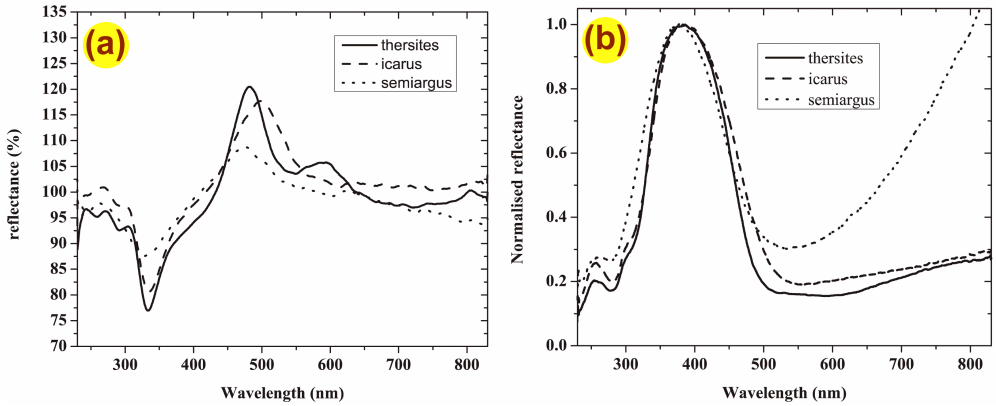

Figure 3. *Optical reflectance of the wings in dry air (a.) and spectral response (b.) in the case of ethanol exposure for the three wings with similar colour.*

Using sets of different nanoarchitectures, the selectivity of detector arrays composed for example from the wings of different butterfly species can be increased further.

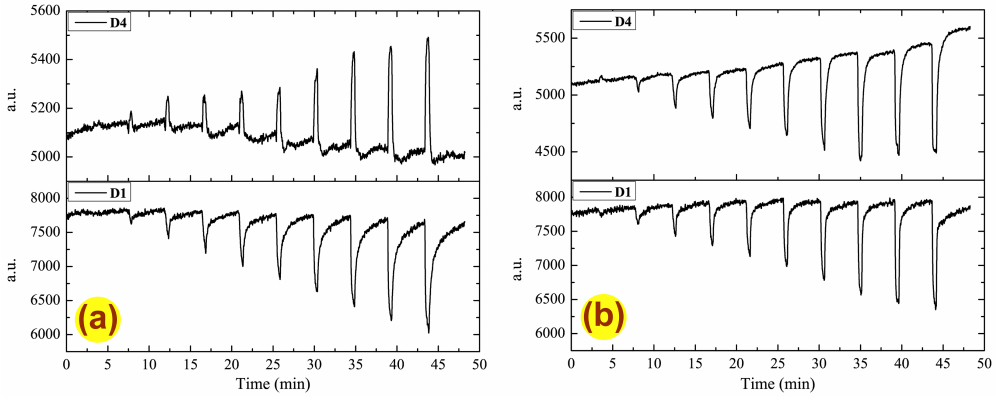

Figure 4. *Effect of repeated, increasing concentration of ethanol (a.) and water (b.) vapours in the case of P. icarus wing. At y axis there is shown the integrated value of the reflectance curves at two wavelength ranges.*

Species specific photonic nanoarchitectures in the scales of male Lycaenid blue butterflies

(OTKA PD 83483)

K. Kertész, Zs. Bálint (HNHM, Hungary), G. Piszter, Z. Vértesy, and L. P. Biró

Photonic nanoarchitectures are a special class of nanocomposites able to generate color by the spectrally selective interaction of light with the nanocomposite. Opposite to dyes and pigments the color originates not from the molecular structure, but from the specific nanostructure of the composite, usually consisting of two transparent media with different optical properties. Such nanoarchitectures were first manufactured 20 years ago, but interestingly enough biologic evolution generated such structures as early as 50 million years ago. The photonic nanoarchitectures responsible for the blue color of the males of nine, closely related, polyommatine butterfly species living in the same site (Normafa, Budapest) were investigated structurally by electron microscopy and spectrally by reflectance spectroscopy.

Entomologists identify individuals of different species mainly on the basis of "traditional" characters provided by the pattern displayed on the ventral wing surfaces (as an example see two species in Fig. 1.). It is questionable that the butterfly brain may have enough processing power to recognize in fast motion, store and analyze such complex patterns as found on the ventral wing surface of the Blues. It may be hypothesized that the spectrally different colors, arising from structurally characteristic nanoarchitectures, may be used by butterflies as a long range, species specific recognition signal.

In order to check this assumption, we measured under reproducible conditions the reflectance spectra of 110 individuals of the nine species and used neural network software to discriminate between the species. Analyzing the wing scales` structural properties, using a dedicated software, we extracted a series of parameters representing the characteristic dimensions (Fig. 3.). It was found that both the

Figure 1. *Dorsal and ventral wing surface of P. amandus and P. bellargus.*

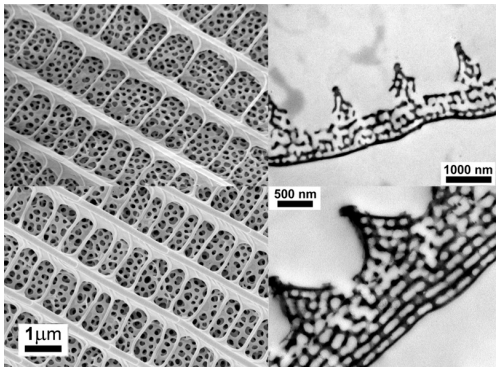

Figure 2. *Wing scale SEM and TEM images of the species from Fig 1.*

structural and the spectral (after proper pre-processing) data allow species identification with an accuracy better than 90% [Bálint et al., to be published].

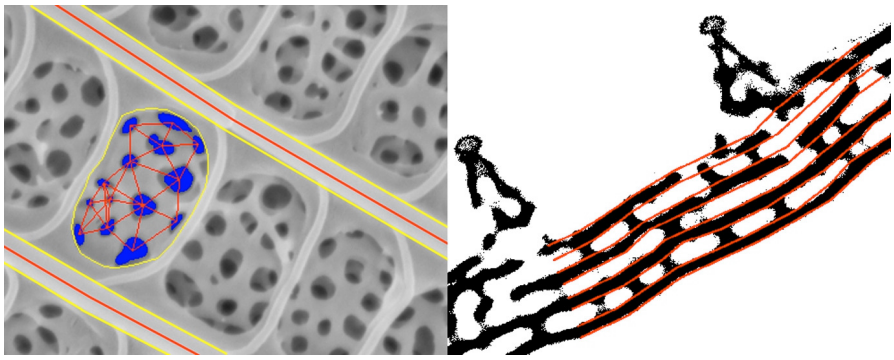

Figure 3. *The extraction of the characteristic dimensions from SEM and TEM images of the scales. The most relevant ones were used as input in the artificial neural network.*

Correlating the temporal distribution of the butterflies (described by the exact time of capture, Fig. 4.) with the structural and reflectance data clearly shows that the species with somewhat similar color have well separated flying periods, this allows safe mate / competitor recognition within the local butterfly fauna. Taking into account the four photoreceptors in the lycaenid butterfly eye, based on the CIE color representation, a similar calculation was carried out for four wavelength-sensitive functions (Fig. 5.). This calculation shows that due to the additional blue-UV visual receptor the butterfly vision allows a safe discrimination of various hues of blue associated with the nine investigated species.

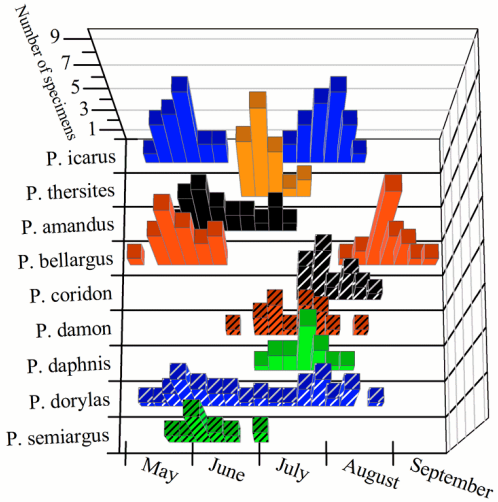

Figure 4. *The distribution of collected specimens represented in function of catching time. (Histogram made of 258 samples from HNHM)*

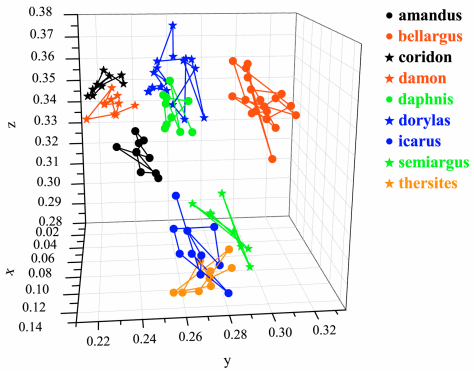

Figure 5. *Representation of blue dorsal wing color of the nine species (total 110 exemplars). Distance is the measure of color difference.*

Wave packet dynamics simulations for the STM tip-graphene system

(OTKA-NKTH K67793)

G. I. Márk, P. Vancsó, Ph. Lambin (FUNDP, Belgium), and L. P. Biró

We investigated in atomic resolution the spreading of electronic wave packets injected from a simulated scanning tunneling microscope (STM) tip on the graphene surface. STM tunneling current is influenced by both the geometry (i.e. the spatial positions of the atoms) and the electronic structure. Geometrical and electronic structure effects of the three dimensional tunneling process were identified by studying three models of increasing complexity: (i) a tip-jellium half space, (ii) a tip-narrow jellium sheet, and (iii) a tip-graphene system, where the graphene sheet was modeled by a local one electron pseudopotential. (Fig. 1. insets.)

It was found that some of the key characteristics of the STM tip – graphene tunneling process are already present at the jellium models. In system (i) we were able to study the influence of the tip geometry and distance. In system (ii) the direction of the momentum is changed from vertical to horizontal during the tunneling event. The second jellium geometry shows similarities with the graphene. In both cases a transient period can be observed when the probability current still flows between the tip and the surface (Fig. 1.d).

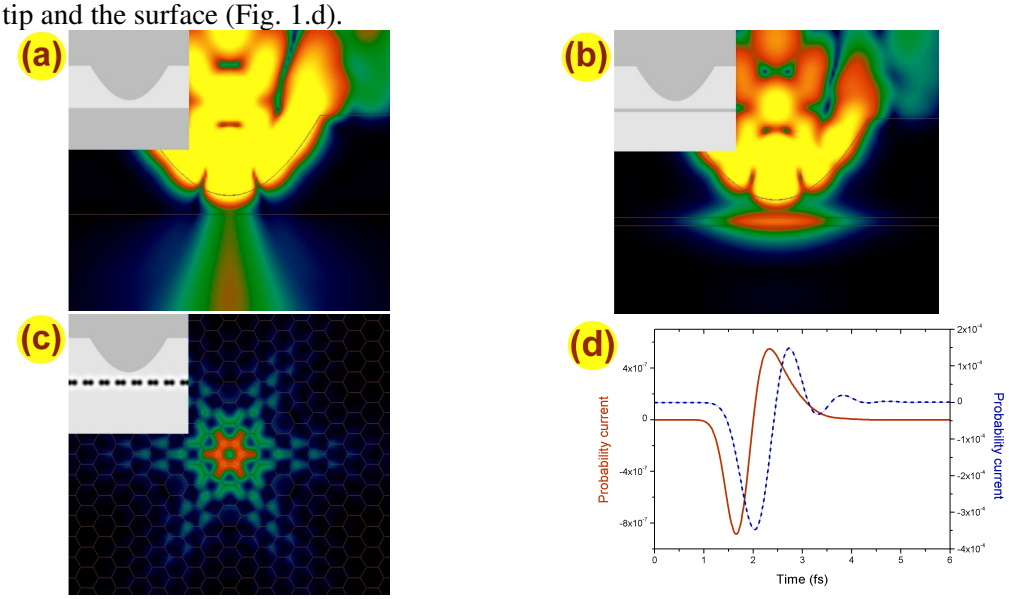

Figure 1. *Time evolution of the wave packet on systems (i),(ii), and (iii) (see the potentials at the inset). (a) and (b): XZ (vertical) cross sections, (c) XY (horizontal) (d) Comparison of the probability current for the jellium and atomistic models of the graphene sheet. Blue dashed curve is for the jellium, red is for the atomistic model.*

If the jellium sheet has a bound state, the wave packet first "fills" the resonant state, and then this state begins to decay. The tunneling event for the atomistic graphene potential proceeds similarly. The density of states (DOS) of graphene has a peak at E_F=+3eV, the wave packet first tunnels into this state then begins to spread along the graphene sheet. (Fig. 2.)

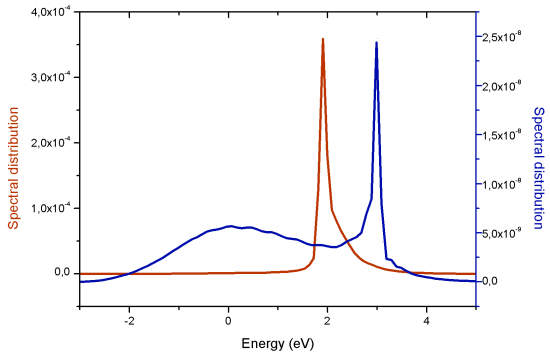

Figure 2. *Spectral distribution of the wave packet calculated for the thin jellium sheet (red) and the graphene (blue). Both functions has a peak matching the DOS peak.*

Understanding the influence of the graphene grain boundaries is important for the realization of graphene based nanoelectronic devices. Hence we performed WPD calculations for an experimentally observed periodical pentagon-heptagon boundary (Fig. 3a). The structure of the grain boundary was relaxed by minimizing a molecular mechanics potential. The STM tip was on the right side of the grain boundaries. In the end of the simulation time, the transmission probability of the WP through the grain boundary is around 10% at the Fermi-energy which is in good agreement with the experimental observations. Wave packet dynamical simulations give a detailed insight into the rich physics of these systems that may lead to devices built on completely new principles.

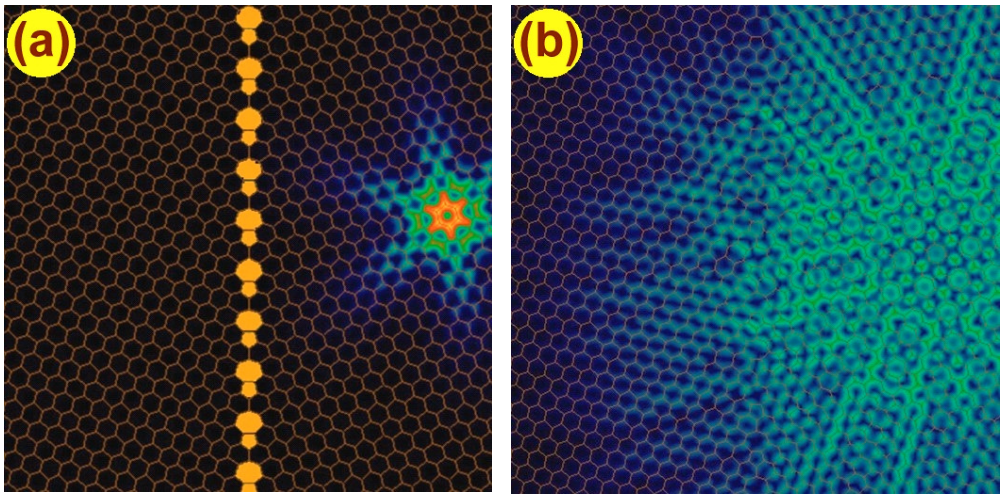

Figure 3. *Snapshots from the time evolution of the probability density of wave packet shown as color coded XZ (horizontal) 2D sections. (a) the tunneled WP before crossing the grain boundary. (b) Wave packet crossing through the grain boundary.*

Carbon nanotube based polymer composites

(EU FP7 CONTACT, OTKA 238363)

B. Pataki, Z. E. Horváth, G. Olowojoba (Fraunhofer ICT, Karlsruhe), C. Hübner (Fraunhofer ICT, Karlsruhe), J. Tiusanen (Promolding BV, Netherland), Daniel Vlasveld (Promolding BV, Netherland)

The effective use of carbon nanotubes (CNT) in polymer composites depends on the ability of their uniform dispersion throughout the polymer matrix. Since the CNTs are smaller than the wavelength of the visible light they can't be investigated by optical microscopy, but their agglomerates. To quantify the state of dispersion is the polymer matrix, transmission electron microscopy (TEM) is regarded as the most accurate method. However TEM is too expensive and time consuming for being used for industrial production control. In the framework of CONTACT Marie Curie ITN FP7 program, we work on the characterization of different CNT/polymer composites by microscopic methods. Using a statistical method combined with image processing, the number of CNT bunches vs. their area can be determined on transmission optical microscopic images. The so prepared graphs can predict the distribution of the CNTs in different polymer composite matrices based on a verification performed by TEM. The key of this method consists in the sample preparation which should be set for each polymer composite type. We intend to adapt this technique for being a quick characterization tool of CNT dispersion.

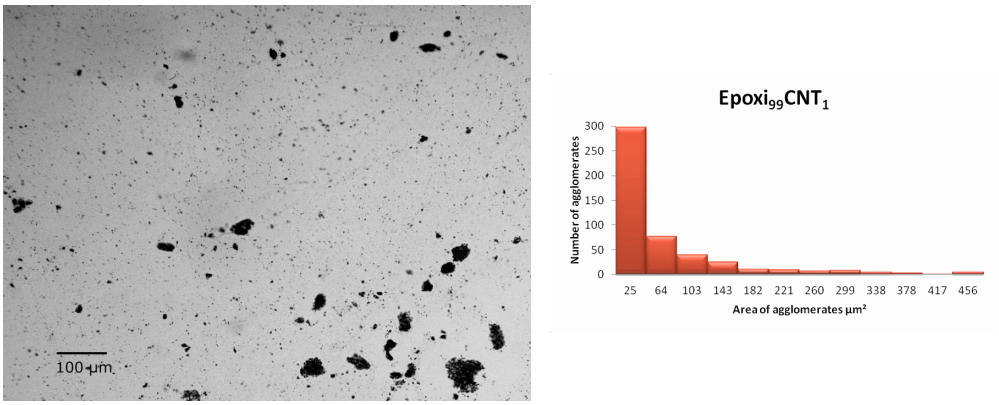

Figure 1. *Transmission optical micrograph (left) of an epoxy nanocomposite containing 1% CNT and CNT agglomerate size distribution (right). The degree of skewness of the distribution gives information regarding the dispersion of CNTs.*

Fig. 1 shows the agglomerate size distribution analysis of an epoxy nanocomposite filled with 1% CNT. On the left, there is an optical microscopy image of a 1 micron thick slice. By counting the agglomerates and measuring their areas, a particle size distribution was obtained and analyzed.

TEM image of a CNT bunch and its surrounding area in the same CNT(1%)/epoxy sample is presented on Fig. 2a. As a comparison, TEM micrograph of a well dispersed CNT filled nanocomposite (CNT 3%/polycarbonate) is shown on Fig. 2b.

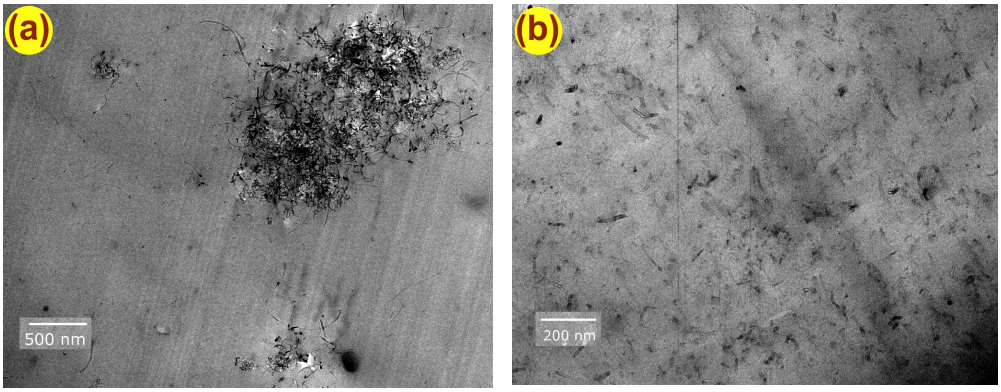

Figure 2. *(a): TEM image of a CNT agglomerate in Epoxy nanocomposite containing 1% CNT; (b): TEM image of a good dispersion Polycarbonate nanocomposite containing 3% CNT.*

CNT/polymer composites are conductive if the CNTs in the matrix form a conductive network. The threshold of conduction depends not only on the CNT content but, again on dispersion, too. The conductive properties of the nanocomposites can be monitored at the microscale by conductive AFM (c-AFM), but the method needs a demanding sample preparation. Combining c-AFM with other microscopic methods, it is possible to get information on the rate and distribution of CNT fractions not involved in the conductive network. Here we present a successful c-AFM investigation of a CNT(3%)/polycarbonate sample. The two images (Figs. 3.a and b.) show parts of the same sample where the differences in CNT distribution were induced by processing.

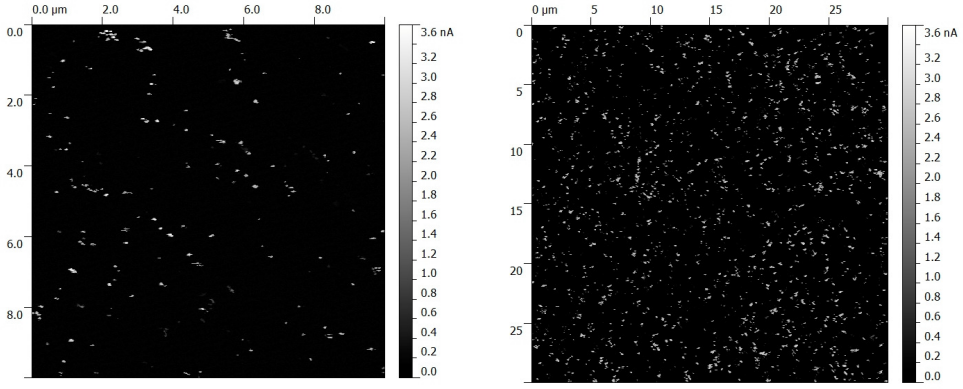

Figure 3. *Conductive atomic force microscopy images (a, b) of the side parts of a Polycarbonate nanocomposite containing 3% CNT.*

Photonics Department

Head: Miklós FRIED, D.Sc., scientific advisor

Research Staff

- Péter PETRIK, Ph.D., Head of Ellipsometry Laboratory
- Miklós SERÉNYI, D.Sc., Head of Semiconductor Photonics Laboratory
- János BALÁZS, Ph.D. (part-time)
- Antal GASPARICS, Ph.D.
- Norbert NAGY, Ph.D.
- András HÁMORI, dr. Univ.
- Róbert HORVÁTH, Ph.D.
- Csaba MAJOR, Ph.D.
- György JUHÁSZ, dr. Univ.
- Zsolt LACZIK, Ph.D. (on leave)
- Tivadar LOHNER, C.Sc.
- János MAKAI, C.Sc. (part-time)

Technical Staff

- Rózsa Mária JANKÓNÉ, technician
- György KÁDÁR, D.Sc.
- Sándor KURUNCZI, Ph.D.
- Olivér POLGÁR, Ph.D.
- Miklós RÁCZ, Ph.D. (part-time)
- Ferenc RIESZ, C.Sc.
- Gábor VÉRTESY, D.Sc.
- Péter TÖRÖK, D.Sc. (on leave)

Ph.D. students / Diploma workers

- Péter KOZMA, Ph.D.
- Dániel PATKÓ, Ph.D. student
- Emil AGÓCS, Ph.D. student
- Bálint FODOR, Ph.D. student
- Andrea NÉMETH, MSc student
- Noémi KOVÁCS, MSc student
- Norbert ORGOVÁN, MSc student
- István MOHÁCSI, MSc student

MFA is involved in the NANOMAGDYE (EU FP7) project with the aim to develop tailored biocompatible magneto-optical nanosystems and to apply them in medical practice. A magneto-optical probe is being fabricated for oncology imaging. In the project, MFA's role was to develop a magnetic sensing system capable of indicating the presence and distribution of the submicron sized magnetic particles. The real challenge of the detection was the very low concentration of the accumulated particles in a typical lymph node. A dual magneto-optical probe was built, which is able to simultaneously detect the dye and the magnetic nanoparticles usable during surgery. For that, magnetic iron oxide nanoparticles and Vital Blue dye were successfully linked in a multifunctional nanoparticle. EURORAD designed and realized the final prototype of the dual opto-magnetic detection system comprising the detection head (probe including magnetic sensor and optical detection in a single surgical housing) and the electronic module. Test measurements have been started with this dual probe. The system proved to be accurate concerning both the localization of the probe within the displayed image as well as the identification of hot and cold areas in the test objects.

A phase shifting optical waveguide interferometer, the so-called Grating Coupled Interferometry (GCI, see in Highlight chapter: "Dual Channel Grating coupled

interferometer configuration for high resolution label-free optical sensing"), was demonstrated for label-free evanescent wave biosensing in aqueous solutions. The sensitivity of the instrument for bulk refractive index was proven being below 10^{-7}. The high phase resolution allows the detection of surface adsorbed molecule densities below 1 pg/mm^2 without using any labeling or on-chip referencing.

In Bioellipsometry we have made a significant progress by developing new optical models and flow cells, as well as investigating the adsorption on different substrates. A multilayer optical model was developed, in that the protein layer was described by effective medium (EMA) sublayers. Applying this method, an in-depth analysis of the protein layer formation was performed. Based on the kinetics in the distribution of the surface mass density, the statistical properties of the filamentous film could be determined computationally as a function of the measurement time. It was also demonstrated that the 3D structure of the protein layer can be reconstructed based on the calculated in-depth mass density profile.

Magnetic Adaptive Testing (MAT) is a recently developed nondestructive magnetic measurement method, which is based on systematic measurement and evaluation of minor magnetic hysteresis loops. Very good correlation was found between the optimally chosen MAT parameters and the independently measured other quantities (Brinell hardness and conductivity). MAT seems to be a good method for replacing the destructive hardness measurements by nondestructive magnetic measurements. Our experiments revealed that MAT is an effective and promising tool for nondestructive detection of local thinning of pipes used in industry, e.g. in chemical and power plants, where wall thinning is one of the most serious defects.

Makyoh topography (MT) is an optical tool for the qualitative flatness testing of specular surfaces, based on the defocused detection of a collimated light beam reflected from the tested surface. Based on our earlier work, a generalized model of the sensitivity of Makyoh topography was developed for a general surface model, including vision physiological effects. The effects of illumination coherence on MT imaging was studied. It was shown that coherence effects are expected even for white-light illumination because of the enhancement of the transverse coherence due to the small source size.

We are involved in a “National technology development” project: “Development of metrology tools based on electrical and optical techniques for in-line and laboratory qualification of thin film solar cells”

MFA is involved in a multidisciplinary research project (including photonics, microfluidics, biochemistry and materials science) called P3SENS (www.p3sens-project.eu) which is funded by EU. This Pan-European cooperation aims to develop high-performance, multichannel optical biosensors for the early detection of brain diseases (for instance, to prevent the occurrence of ischemic damage as a result of stroke) from human blood. Among many other tasks MFA functionalizes the photonic biochips with appropriate surface chemistry and tests the receptor performances by a high resolution label-free optical biosensor called OWLS (Optical Waveguide Lightmode Spectroscopy).

NANOMAGDYE
Magnetic nanoparticles combined with submicronic bubbles and dye for oncologic imaging

(EU FP7 NANOMAGDYE)

G. Vértesy, A. Gasparics

The objective of NANOMAGDYE project is to develop tailored biocompatible magneto-optical nanosystems and to apply them in medical practice. A magneto-optical probe is being fabricated for oncologing imaging. Combining optical and magnetic labelling techniques into a single biocompatible nanosystem will provide increased spatial resolution and will avoid currently used ionising radiation based method in order to improve patient safety and medical effectiveness this way.
In the framework of the project MFA has the role to develop suitable magnetic sensing technology for indicating the presence of the submicron sized magnetic particles. These iron-oxide based particles are close to (or already in) super-paramagnetic state due to their dimension. However, the real challenge of the detection is the very low mass of the accumulated particles in a typical lymph node. Novel Fluxset sensor based method has been used to detect the particles with reasonable signal/noise ratio. Fluxset sensor is a high sensitivity magnetic field sensor, developed formerly in MFA, and in this application the sensor is assembled into a measurung head, which generates AC exciting magnetic field. The response of magnetic particles to this field is detected by magnetic field measurement.
In the first year of the project a magnetic probe was built and tested, with satisfactory results. To improve the sensitivity of the magnetic probe, an improved version of the device was designed and built in the second year. In this version the magnetic excitation is performed by two coils and the magnetic sensor is balanced between the two exciting coils. In such a way a significantly higher sensitivity could be reached. In order to obtain the signal to be evaluated from the magnetic probe response, a signal processing unit was also designed, built and tested with good result. In the third year of the project a dual magneto-optical probe was built, which is able to simultaneously detect the dye and the magnetic nanoparticles usable during surgery. For that purpose, magnetic iron oxide nanoparticles and Vital Blue dye were successfully linked in a multifunctional nanoparticle. EURORAD designed and realized the final prototype of the dual opto-magnetic detection system comprising the detection head (probe including magnetic sensor and optical detection in a single surgical housing) and the electronic module. Test measurements have been started by this dual probe. The system proved to be accurate concerning both the localisation of the probe within the displayed image as well as the identification of hot and cold areas in the test objects. Fig. 1 shows an in-vivo test, while the dual probe set-up for the laboratory test can be seen in Fig. 2.

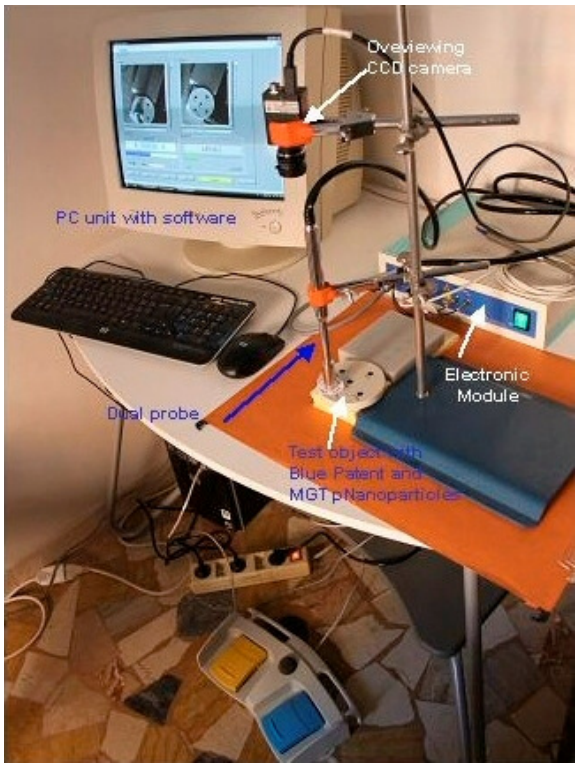

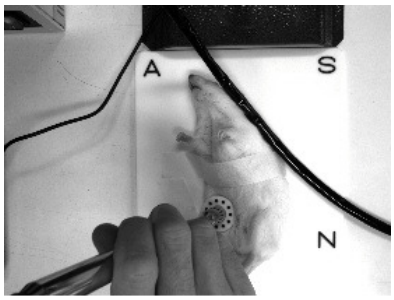

Figure 1. *In-vivo test (above).*

Figure 2. *The dual probe set-up for the laboratory test (left).*

Nondestructive investigation of wall thinning in layered ferromagnetic material by Magnetic Adaptive Testing

(OTKA CK80173)

Gábor Vértesy

For pipes used in industry, e.g. in chemical and power plants, wall thinning is one of the most serious defects. Detection and evaluation of the thickness reduction of pipes are very important issues for prediction of lifetime of the pipes in order to avoid severe accidents. Local wall thinning on the inner surface of a pipe in a nuclear power plant may occur due to the stream of coolant flowing inside the pipe, causing a serious problem of maintenance of piping systems. The inspection should be done from the outer side of the pipe. Additionally, there is a special concern on the local wall thinning at locations under an enforcement shield that covers outside of the pipe, where a branch pipe is connected to the main one. Because the enforcement shield and the pipe wall form two layers of metal, it is difficult to inspect inside of the pipe under the enforcement shield. A novel magnetic method, called Magnetic Adaptive Testing (MAT), which has been recently developed by us, and which is based on

systematic measurement and evaluation on minor magnetic hysteresis loops has been applied for inspection of wall thinning in layered ferromagnetic materials. The measurement is based on the principle that the sample is locally magnetized from outside by an attached magnetizing yoke and the local modification of the sample's thickness modify the density and distribution of magnetic flux inside the sample. The magnetic hysteresis loops reflect this behavior.

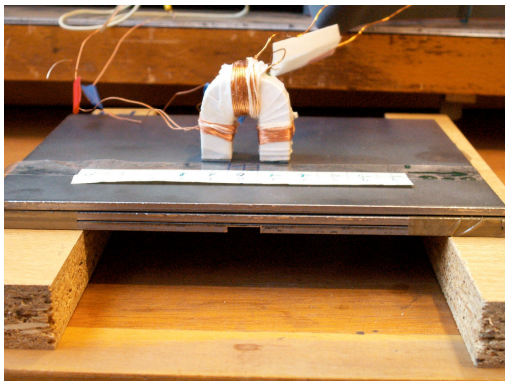

Figure 1. *Measurement of the triple plate system with the magnetizing yoke.*

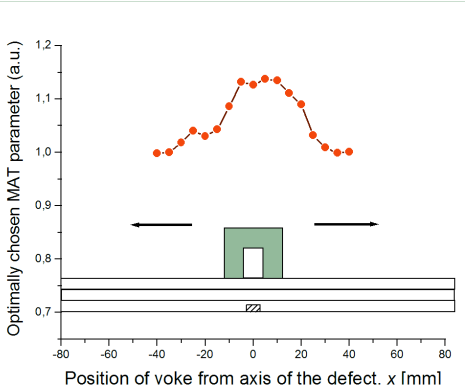

Figure 2. *Optimal MAT parameters as function on the yoke position*

Test measurements, performed on flat samples are presented here. Three plates (180x170x3 mm^3) made of the same low carbon steel were prepared. One of them contained a 9x2 mm^2 slot in the middle. Fig. 1 shows the case in which all the three plates are put together. In this case the slot is placed in the bottom side as can also be seen in the Figure. The measurement with the magnetizing yoke was performed from the top. Hysteresis loops were measured at different positions, by moving the magnetizing yoke step by step along the surface. The result of the measurements, performed on the triple plate system is shown in Fig. 2. The scheme of the magnetizing yoke, which was moved over the surface of the sample, is also given in the graph. The optimally chosen MAT parameters were normalized by the value, measured at the largest distance from the center of the slot (x=–60 mm).

The above described experiments revealed that Magnetic Adaptive Testing is an effective and promising tool for nondestructive detection of local thinning of a plate from the other side of specimen. The method gave good results also in a layered ferromagnetic material. The slot is seen not only in the case when the measuring yoke is positioned exactly above it, but also from about a distance of 10 mm, with acceptable signal to noise ratio.

Makyoh topography

(OTKA K68534, EU FP7 MORGaN)

Ferenc Riesz, and János P. Makai

Makyoh topography (MT) is an optical tool for the qualitative flatness testing of specular surfaces, based on the defocused detection of a collimated light beam reflected from the tested surface. By inserting a square grid into the path of the illuminated beam, the height map can be calculated by integrating the gradients obtained from the distortion of the grid's reflected image (quantitative extension). The effects of illumination coherence on MT imaging was studied. It was shown that coherence effects are expected even for white-light illumination because of the enhancement of the transverse coherence due to the small source size. Under optimum imaging conditions, coherence is manifested as diffraction patterns around isolated defects and at sample edges, as well as speckle due to surface roughness (Fig. 1). These phenomena were analyzed as a function of surface roughness, illumination coherency and wavelength, light source size and instrumental geometrical parameters. The results were corroborated with experiments.

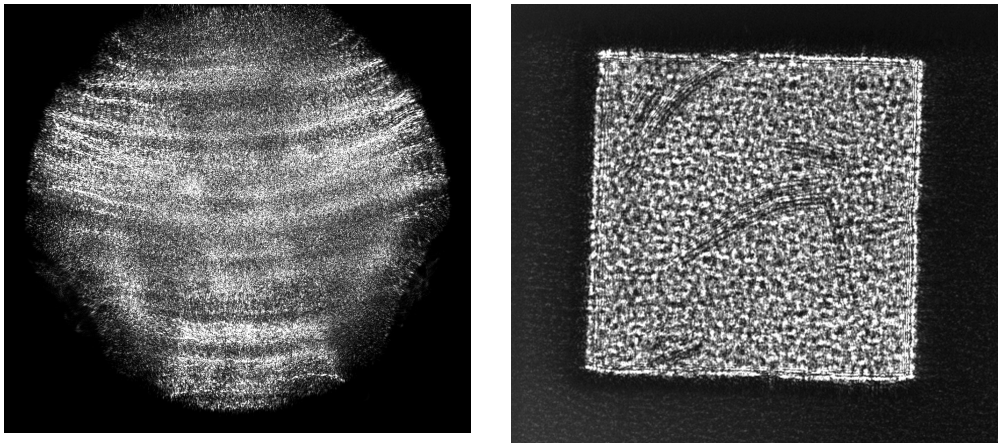

Figure 1. *Examples of speckle in Makyoh topography: the Makyoh images of a semiconductor wafer (left) and a polsihed stainless steel plate (right).*

The nonlinearity of MT was also studied based on a geometrical optical model. It was found that the nonlinearity stems from: (1) the topological mapping caused by the varying surface gradient, (2) an overall reciprocal-like dependence of the image intensity on the local surface curvatures and (3) the local Gaussian curvatures of the surface. The influence of these effects on the evaluation of the Makyoh images were established and criteria were given for the quasi-linear regime of imaging.

Activities were concentrated also on applications. For in-house research, curvature measurements of Si-based thin-film structures were performed for stress evaluation. The flatness of Si substrates have also been assessed for the company Mirrotron Ltd. for neutron optics applications.

Ellipsometric characterization of thin nanocomposite films with tunable refractive index for biochemical sensors

(EU FP7 P3SENS, OTKA K81842, OTKA PD73084, NKTH PVMET08, NKTH TFSOLAR2)

P. Petrik, E. Agócs, M. Fried, B. Pécz, R. Horváth, and H. Egger

Creating optical quality thin films with a high refractive index is increasingly important for waveguide sensor applications. We developed optical models to measure the layer thickness, vertical and lateral homogeneity, the refractive index and the extinction coefficients of the polymer films with nanocrystal inclusions using spectroscopic ellipsometry. The optical properties have been determined in a broad wavelength range from 190 to 1700 nm. The sensitivity of spectroscopic ellipsometry allows a detailed characterization of the nanostructure of the layer, i.e. the surface roughness down to the nm scale, the interface properties, the optical density profile within the layer, and any other optical parameters that can be modeled in a proper and consistent way. In case of particles larger than about 50 nm, even the particle size can be determined from the onset of depolarization due to light scattering. Besides the refractive index, the extinction coefficient, being a critical parameter for waveguiding layers, was also determined in a broad wavelength range. Using the above information from the ellipsometric models the preparation conditions can be identified. A range of samples has been investigated including doctor bladed films using TiO_2 nanoparticles.

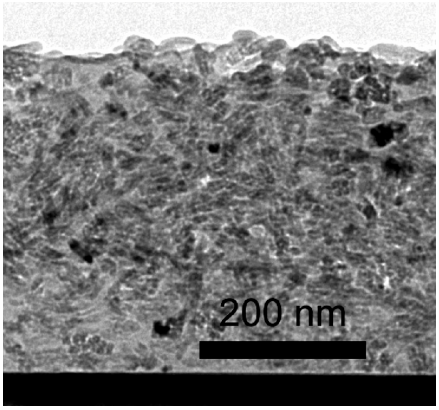

Figure 1. *Transmission electron microscopy image showing the uniform distribution of the nanoparticles in PI prepared by Bayern.*

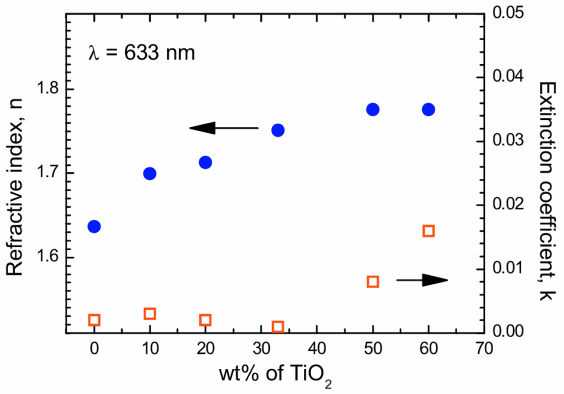

Figure 2. *Refractive index and extinction coefficient as a function of the weight fraction of TiO_2 in the PI solutions for the photon wavelength of 633 nm. The error of the measurements is smaller than the symbol size in all cases.*

Formation of slab waveguides in eulytine and sillenite type BGO crystals by implantation of MeV nitrogen ions

(OTKA K68688)

I. Bányász, S. Berneschi, M. Fried, N.Q. Khanh, Zs. Zolnai, Á. Péter, K. Lengyel, and T. Lohner

Ion implantation proved to be a universal technique for producing waveguides in most optical materials. It has better controllability and reproducibility than other techniques. The first articles reporting fabrication of waveguides by light ions ion implantation appeared between the end of 1960's and early 1980's.
Bismuth germanate (BGO) is a well known scintillator material. Here we present preliminary results in fabricating slab waveguides in both eulytine and sillenite type bismuth germanate crystals using a medium-mass ion, N^+.
We fabricated slab waveguides by implanting 3.5 MeV N^+ ions into eulytine ($Bi_4Ge_3O_{12}$) and sillenite ($Bi_{12}GeO_{20}$) crystals. The ion fluences of slab waveguides implanted into $Bi_4Ge_3O_{12}$ single crystal are shown in Table 1.

Table I. *Results of spectroscopic ellipsometry measurements of eulytine ($Bi_4Ge_3O_{12}$) waveguides.*

Names of the Waveguides	A	B	C	D
Fluences (x10^{16} ions/cm^2)	0,2	0,4	0,8	1,6
Thickness of layer 2 [nm]	2552,7±0,9	2576±1	2632±0,9	2628,1± 0,8
Refractive index of layer 2 at 635 nm	2,115	2,121	2,202	2,35
Thickness of layer 1 [nm]	338±11	288±3	346±4	413±5
Refractive index of layer 1 at 635 nm	2,116	2,131	2,11	2,125
Refractive index of the non-implanted crystal at 635 nm	2,086	2,086	2,086	2,086

Refractive index changes of the waveguides were measured by spectroscopic ellipsometry (SE). The optical model applied in the evaluation of the SE data for different ion-implanted areas consisted of three layers on top of the nonimplanted single-crystalline substrate. The layer adjacent to substrate (layer 1) represents the stopping region for the N^+ ions. The second layer (layer 2) is the region which the implanted ions traverse before they stop in layer 1. The third layer was a surface roughness film. Dielectric functions of layer 1 and layer 2 were described by Cauchy dispersion relation. Parameters of the Cauchy dispersion relation and layer thicknesses were considered as free parameters. Results of SE measurements of

waveguides written in eulytine crystals are presented in Table 1. Thickness of the guiding layer is around 2.6 μm, slightly changing with fluence.
Functionality of the waveguides was tested by m-line (dark-line) spectroscopy and prism coupling technique. The accuracy is around 1 x 10^{-4} and 5 x 10^{-4} for measuring the effective refractive index (n_{eff}) and bulk refractive index, respectively. Six guiding modes were detected at 635 nm in the waveguide implanted in eulytine crystal at fluence of 1.6 x 10^{16} ions/cm^2 (Fig. 1.). Refinement of the ellipsometric model and processing of the m-line measured data are needed to obtain a better assessment of the refractive index profile. Very high modulation, up to 0.15 of the refractive index of the implanted waveguides in the sillenite type BGO crystal was found.

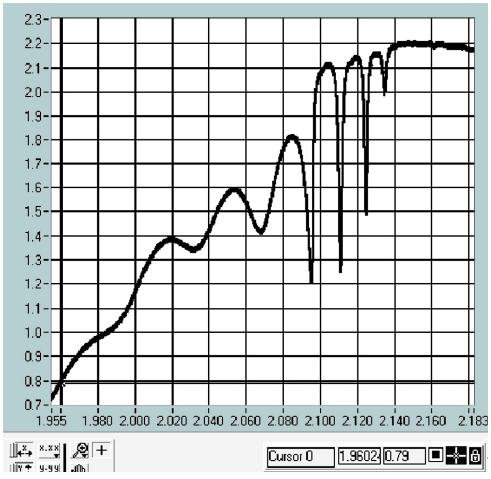

Figure 1. *M-line spectrum of an eulytine BGO waveguide at 633 nm. Fluence = 1.6x10^{16} ions/cm^2 Y-axis: intensity (arbitrary units), X-axis: n_{eff}*

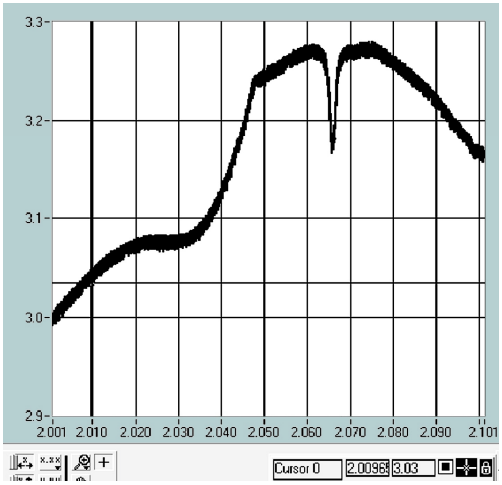

Figure 2. *M-line spectrum of an eulytine BGO waveguide at 1550 nm. Fluence = 1.6x10^{16} ions/cm^2 Y-axis: intensity (arbitrary units), X-axis: n_{eff}.*

In-depth characterization and 3D reconstruction of flagellar filament protein layer structures

(OTKA K81842, OTKA PD73084, MC OPTICELL)

P. Kozma, D. Kozma, A. Nemeth, H. Jankovics, S. Kurunczi, R. Horvath, F. Vonderviszt, M. Fried, and P. Petrik

The statistical 3D structure of hundreds of nanometers thick surface immobilized flagellar filament protein layers were reconstructed in their native environment, in buffer solution. The protein deposition onto the surface activated Ta_2O_5 film was performed in a flow cell, and the immobilization process was followed by in situ spectroscopic ellipsometry. A multilayer optical model was developed, in that the protein layer was described by effective medium (EMA) sublayers. Applying this method, an in-depth analysis of the protein layer formation was performed. Based on the kinetics in the distribution of the surface mass density, the statistical properties of the filamentous film could be determined computationally as a function of the measurement time. It was also demonstrated that the 3D structure of the protein layer can be reconstructed based on the calculated in-depth mass density profile. The computational investigation revealed that the filaments can be classified into two individual groups in approximately equal ratio according to their orientation. In the first group the filaments are close to the laying positions, whereas in the second group they are in a standing position, resulting in a significantly denser sublayer close to the substrate than at a larger distance. Our results were published in Applied Surface Science.

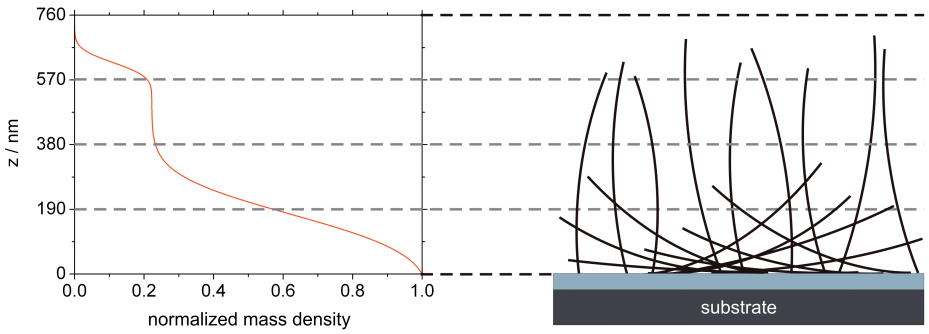

Figure 1. *The calculated continuous in-depth mass density profile (left hand side) and the reconstructed FF structure on substrate surface (right hand side). The interface of the EMA layers of the optical model are marked with dashed lines.*

Kinetics and structure of adsorbed flagellin films monitored by optical biosensors

(OTKA PD 73084, EU FP7 OPTIBIO)

Noémi Kovács, Daniel Patkó, Norbert Orgován, Sándor Kurunczi, Jeremy J. Ramsden (Cranfield University, UK), Ferenc Vonderviszt, and Róbert Horváth

The basic building block of the bacterial filaments is the 51.5 kDa molecular weight flagellin protein (see Fig. 1.). In our research optical waveguide lightmode spectroscopy (OWLS) is applied to in-situ monitoring the adsorption of flagellin on model surfaces.

The flagellin protein domains have rather different characteristics in terms of their surface hydrophobicity making the protein an ideal candidate for studying the roles of the various regions in the adsorption process by systematically removing one or other of the protein domains. This possibility is explored by investigating the adsorption of flagellin and its truncated variants on model surfaces using label-free optical waveguide lightmode spectroscopy. Employing our recently developed methodology to model the adsorbed thin layers as uniaxially anisotropic the internal layer structure of the protein films was revealed, suggesting oriented protein adsorption. In order to investigate the adsorption kinetics a computer program has also been developed that is capable of fitting systems of differential equations directly to the adsorption curve.

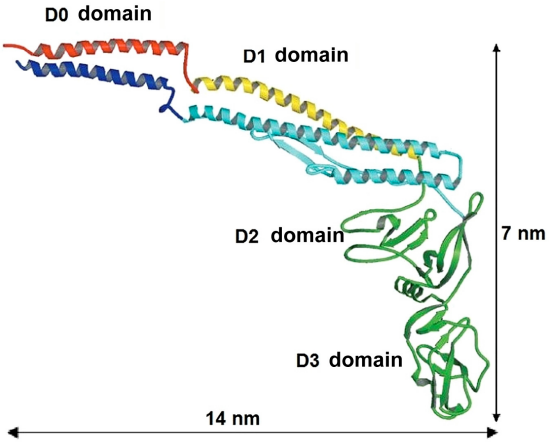

Figure 1. *The polypeptide backbone of flagellin, the building block of flagellar filaments.*

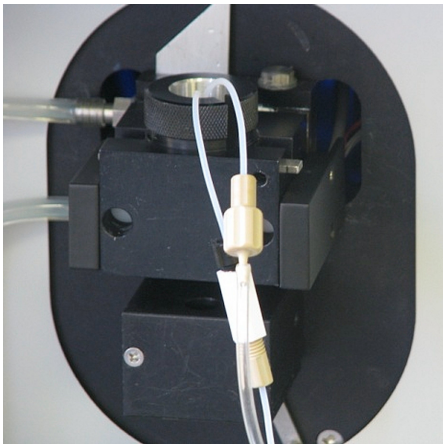

Figure 2. *Measuring head of the OWLS 210 biosensor.*

Immobilization of IgG molecules on sensor surface

(EU FP7 P3SENS)

K. Juhász, D. Patkó, S. Kurunczi, and R. Horváth

P3SENS (**www.p3sens-project.eu**) is a multidisciplinary research project (including photonics, microfluidics, biochemistry and materials science) funded by the European Commission. This Pan-European cooperation aims to develop highperformance, multichannel optical biosensors for the early detection of brain diseases (for instance, to prevent the occurrence of ischemic damage as a result of stroke) from human blood.

The analyte (CRP) was detected through affinity capture on the functionalized sensor surface. The development of the novel immobilization method was controlled step by step using OWLS (Optical Waveguide Lightmode Spectroscopy). The building up of the molecular layers was monitored label free and the CRP was sensitively assayed (DL= 0.1 µg/ml) in phosphate buffered saline. Future work will involve the transfer of this biochemistry onto the real polymer sensor chip.

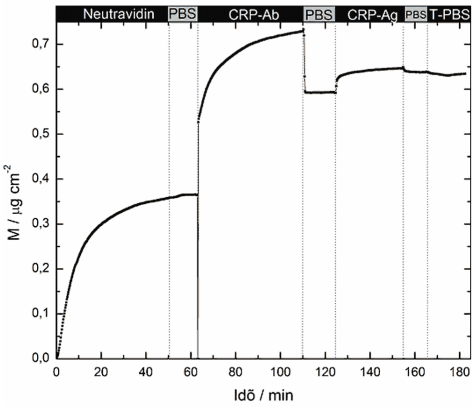

Figure 1. *OWLS sensogram: Immobilization of CRP-IgG molecules on PEI-functionalized surface and subsequent detection of CRP (20 µg/ml).*

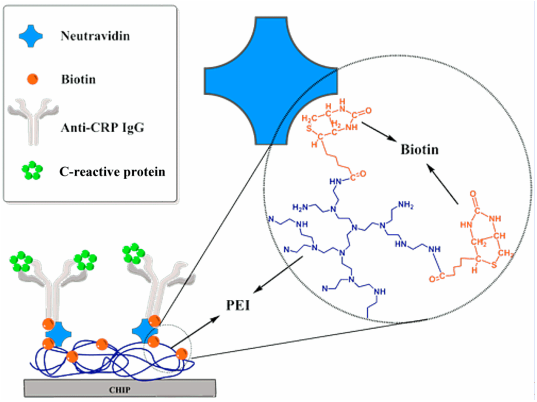

Figure 2. *Design of the immobilization layer of IgG molecules for biosensing.*

Development of metrology tools based on electrical and optical techniques for in-line and laboratory characterization of thin film solar cells

(NKTH TECH_08 PVMET_08)

Fodor B., P. Petrik, C. Major, G. Juhász, Z. Zolnai, N. Nagy, and M. Fried

The aim of this project (led by Semilab, Inc.) is to develop an equipment and measurement technology family, which is capable to perform electrical and optical measurements for in-line and laboratory qualification of thin film solar cells. MFA's task in the project was to make spectroscopic ellipsometry (SE) capable for this task.
We have developed optical models for different (artificially) roughened surfaces. Model surface: monolayers from 100-500 nm silica nanospheres on silicon and modification by 500 keV Xe^{2+} ion bombardment (5×10^{14}-$2{,}4\times10^{16}$ cm^{-2} dose range)
The used optical model (Fig. 1) consisted periodically deformed a-Si layers on c-Si substrate and dose-dependently deformed (ion hammering) silica ellipsoids. In Fig. 2, we can compare the independent results of the same samples measured by SE (cheap) and RBS (expensive).

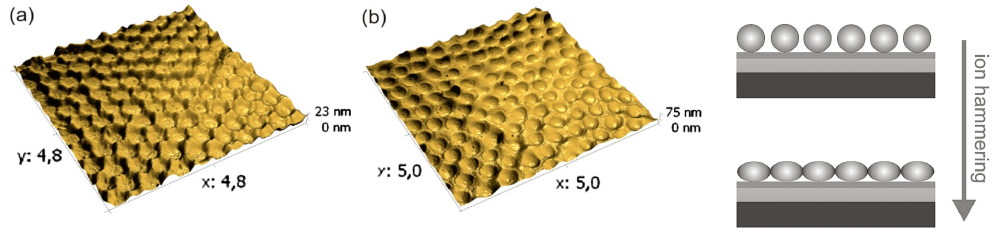

Figure 1. *Surface structure after etching of silica nanospheres (AFM, (a), (b), left); optical model (c), right).*

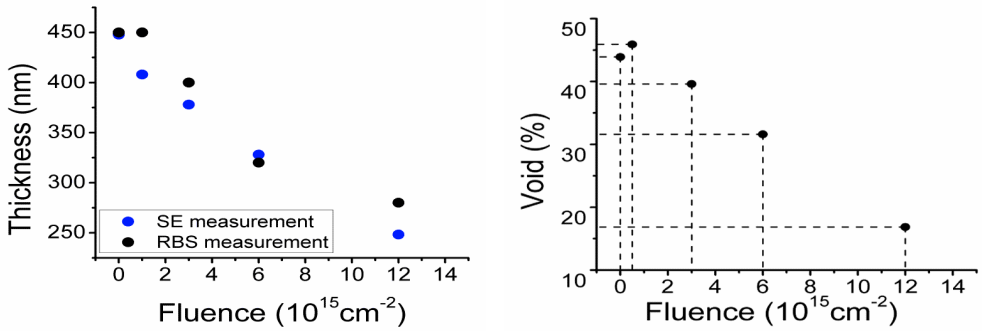

Figure 2. *Thickness reduction from SE and RBS; [air-volume]/[full-volume] ratio depending on the ion bombardement fluence.*

Hydrogen behaviour in amorphous Si/Ge nano-structures after annealing

M. Serényi, and C. Frigeri (CNR)

The H incorporation in a-Si and a-Ge as a function of the H flow rate in the plasma was determined by ERDA measurements on the unannealed mono-layer RF sputtered samples. H is incorporated more than twice more efficiently in a-Si than in a-Ge. The H content exhibits an asymptotic behaviour at the highest H flow rates reaching a value of ~17 at % and ~7 at % for a-Si and a-Ge, respectively.

Fig. 1 a) is the STEM-HAADF image of a superlattice (SL) on the substrate side. A HAADF image is formed by collecting the incoherently scattered electrons at high angles (Rutherford scattering). Single atoms scatter incoherently and the image intensity is the sum of individual atomic scattering contributions. The HAADF intensity turns out to be proportional to Z2, where Z the atomic number. Ge layers appear thus brighter than the Si ones. The layer thickness from Fig. 1 a) is exactly 3 nm for both types of layer.

Structural modifications in the shape of blistering was instead observed in the annealed hydrogenated SLs, with formation of surface bubbles by plastic deformation whose density and size increased with increasing H content, for the same annealing conditions. A typical surface image of an annealed SL is given in Fig. 1 b).

Surface blistering due to bubbles was also observed in the single layers of a-Si and a-Ge. For the highest H content and most severe annealing conditions applied to the single layers (1.5 ml/min, 350 °C, 4 h) it was observed that in the a-Ge layers the bubbles have transformed into craters, i.e. they blew up because of a high internal gas pressure, while they did not significantly undergo such transformation in a-Si. This allows concluding that in a-Ge hydrogen release and formation of H bubbles is more efficient and occurs at an earlier time, with consequent earlier explosion, than in a-Si.

The amount of H in the bubbles in the case of Si can be evaluated with the model of lenticular crack. The height and lateral size of the bubbles suggest that they have a semi-lenticular shape. It is assumed that the bubble is a buckling of the whole deposited layer, i.e. that the layer has delaminated in that position. The pressure P inside the bubble is then given by

$$P = 16Ehd^3 / 3(1-\nu^2)R^4 \qquad (1)$$

where E is Young's modulus, ν Poisson's ratio, h the height of the bubble, R its radius and d the thickness of the layer. The relevant data for the Si monolayer are : E=130 GPa, ν = 0.28, h=250 nm, d=40 nm, R=0.7 μm. With such values the pressure in a bubble is P = 50 MPa = 50 J/cm^3. The number N of gas molecules in a bubble is given by the gas law,

$$PV = NkT \qquad (2)$$

with V the average volume of the semi-lenticular bubble (V= ½ (½πhR^2)), k Boltzmann constant and T the temperature. For T = 350 °C it is N = $5.60 \cdot 10^8$. The density of the bubbles in the sample is ρ = $2.24 \cdot 10^6$ cm^{-2}. The density of the H_2 molecules filling all the bubbles in the layer is then Nρ /d = $3.12 \cdot 10^{20}$ cm^{-3}.

From ERDA measurements the H present in the layer hydrogenated at the flow of 1.5 ml/min after annealing for 4 h at 350 °C is 9.9 at %. By taking the atomic density of amorphous Si as the one of crystalline Si ($5 \cdot 10^{22}$ cm^{-3}) reduced by 1.8 %, it turns out that the H atoms remained in the a-Si mono-layer is $4.86 \cdot 10^{21}$ cm^{-3}. The total amount 2N of H atoms trapped in the bubbles is therefore 12.9 % of the H remained in the layer after annealing. The rest of the unbound H atoms should stay dispersed in the layer as interstitials or inside small bubbles which have not caused blistering and were thus not detected by AFM nor used in the above computation.

A rough estimation of the amount of H in the bubbles for the case of an a-Si/a-Ge superlattice could be obtained by the same model applied above. The data for the superlattice of Fig. 1 a) are: h=80 nm, d=300 nm, R=1.3 µm, $\rho = 6.7 \cdot 10^{6}$ cm^{-2}. For E the average between its value for Si and Ge (E=110 GPa) is used, i.e. E= 120 GPa. $\nu = 0.28$ since ν is almost the same for Si and Ge. The pressure in a bubble turns out to be 526 MPa with the number of H_2 molecules in a bubble $N=6.48 \cdot 10^{9}$. The total concentration of H atoms in all the bubbles is thus $N\rho /d = 2.90 \cdot 10^{20}$ cm^{-3}. The ERDA results show that the H remained in the Si and Ge layers after annealing at 350 °C for 4 h is 9.9 and 0.5 at%, respectively. By using such data as a first approximation to estimate the H remained in the Si and Ge layers of the SL, and assuming that the total concentration of the remained H atoms is the sum of the one of the Si layers and the one of the Ge layers it results that such concentration is $5.08 \cdot 10^{21}$ cm^{-3}. The amount of H atoms in the bubbles is therefore 5.7 % of the H remained in the SL after annealing. This lower value with respect to the mono-layer case may be explained by the lower volume occupied by the bubbles per cubic centimetre of deposited material in the SL ($2.37 \cdot 10^{-3}$ in SL vs $5.38 \cdot 10^{-2}$ in mono-layer), modified (slower) diffusivity of H in the two-phase SL system with respect to the one-phase monolayer or other reasons not understood at present.

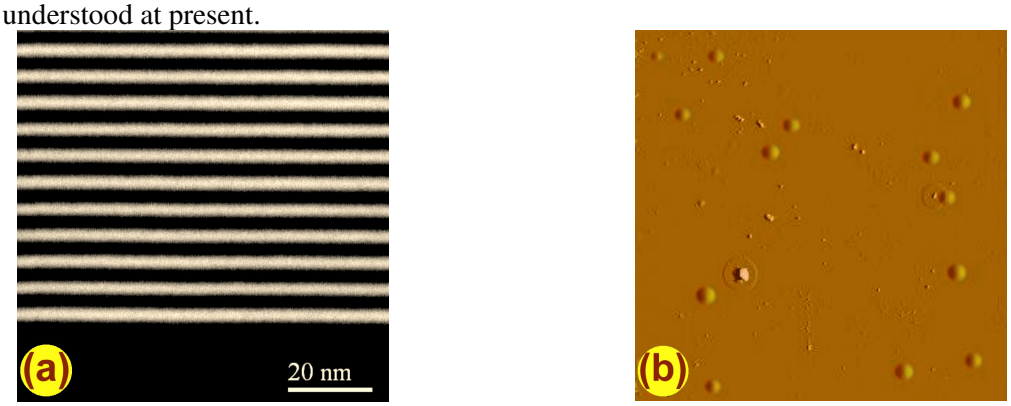

Figure 1. *– (a) Typical TEM-HAADF image of the first grown layers of the a-Si/a-Ge SL nanostructures. The bright stripes are the a-Ge layers, while the dark ones are a-Si. (b) Typical AFM image of blistering in an a-Si/a-Ge SL annealed at 350 °C for 4 h. Area size 50x50 µm. Average bubble height and diameter are 80 nm and 2.5 µm, respectively; bubble density* 6.7×10^{5} cm^{-2}.

Microtechnology Department

Head: Gábor BATTISTIG, Ph.D.

Research Staff

- István BÁRSONY, Member of HAS.,
- László DÓZSA, Ph.D.,
- Péter FÜRJES, Ph.D.,
- Zoltán LÁBADI, Ph.D.,
- György MOLNÁR, Ph.D.,
- Anita PONGRÁCZ, Ph.D.,
- Vilmos RAKOVICS, Ph.D.,
- Zsolt ZOLNAI, Ph.D.
- Ágoston NÉMETH, Ph.D.,
- Andrea Edit PAP, Ph.D.,
- Antalné ÁDÁM, M.Sc., (part time)
- Albert KARACS, M.Sc., (part time)
- Tibor MOHÁCSY, M.Sc., (part time)
- Ákos NEMCSICS, Ph.D. (part time)
- Gábor PETŐ, D.Sc., Prof. Emeritus
- Bálint PŐDÖR, Ph.D. (part time)
- Zsolt József HORVÁTH, D.Sc., (part time)
- Béla SZENTPÁLI, Ph.D., (part time)
- Éva VÁZSONYI, M.Sc., (part time)

Ph.D. students / Diploma workers

- Zsófia BAJI, Ph.D. student
- Ferenc BIRÓ, Ph.D.student
- Réka CSUTAK, Ph.D.student
- Zoltán FEKETE, Ph.D. student
- Tamás KÁRPÁTI, Ph.D. student
- Gergely MÁRTON, , Ph.D.student
- Balázs BENEDEK, M.Sc. diploma w.
- Péter BERINKEI, M.Sc. diploma w.
- Péter NAGY, M.Sc. diploma w.
- Ferenc TOLNER, M.Sc. diploma w.

Technical Staff

- György ALTMANN, technician
- Edvard BADALJÁN, engineer
- Gabriella BIRÓ, technician
- Sándor CSARNAI, technician
- Tibor CSARNAI, technician
- Ábel DEBRECZENY, engineer (part time)
- Magdolna ERŐS, technician
- Csilla ARIAS-SOTONÉ FARAGÓ, technician
- János FERENCZ, engineer
- Róbert HODOVÁN, engineer
- Csaba LÁZÁR, engineer
- András LŐRINCZ, engineer
- Ákos MAJOROS, engineer
- Attila NAGY, technician
- Károlyné PÁYER, technician
- István RÉTI, engineer
- Ádám SZENDREY, engineer
- Magda VARGA, technician
- Katalin Veresné-VÖRÖS, engineer
- Sándor PÜSPÖKI, engineer (part time)
- Zsuzsa PÜSPÖKI, engineer (part time)
- Imre SZABÓ, engineer, dr. Univ. (part time)
- Tamás SZABÓ, engineer (part time)

The mission of the Microtechnology Department is the research, development and system integration of physical, chemical/biochemical sensors and systems:

- MEMS and MEMS related technologies, with special emphasis on development 3D microstructures;
- Development and functional testing of different MEMS based gas, chemical, 3D force, thermal, biology related sensors and sensor systems;
- Development of micro- and nanofluidic components and systems;
- Development and applications of near IR light emitting diodes and detectors;
- Development of solar cells and their competitive technology.

Fundamental research on:

- sensing principles;
- novel materials and nanostructures;
- novel 3D fabrication techniques;
- ion-solid interaction for supporting MEMS development.

Device and material characterizations widely used in our projects:

- Ion beam analysis methods;
- IR and Raman scattering;
- Scanning Microprobes;
- Optical and Electron Microscopy, SEM, TEM, EDX;
- Spectroscopic Ellipsometry;
- Electrical characterisations
- Microfluidic and biofunctional characterisation.

The Microtechnology Department of MFA runs the 300 sqm clean lab (Class 100-10000) with the complete Si-CMOS technology together with a mask shop, unique in Hungary. The CIGS solar cell technology laboratory equipped with a pilot line of sputtering, evaporation and laser scribing modules for 30×30 cm^2 glass substrates is also connected to the clean lab facility.
The technology base of the clean lab has been further improved in the recent years. In 2011 a new Heidelberg DLW66 type laser pattern generator was purchased and installed in our mask shop. The new facility allows us to produce 4”-8” masks with 1 micrometer linewidth. Direct writing of the pattern to the surface of a photoresist coated wafer is also possible by the DWL66 laser writer.
Main technologies available in the Microtechnology lab for our partners and customers:

- High temperature annealing, diffusion and oxidation
- Rapid Thermal Treatment
- Low Pressure Chemical Vapor Deposition of poly-Si, SiO_2 and Si_3N_4 layers
- Low Temperature Chemical Vapor Deposition
- Ion implantation
- Thin film depositions – Electron beam evaporation, DC and RF Sputtering

- Atomic Layer Deposition
- Deep Reactive Ion Etching
- Photolithography with back-side alignment and Nanoimprinting
- Wafer Bonding
- Wet chemical treatments
- Electro-chemical porous Silicon formation
- Molecular Beam Epitaxy of III-V compound semiconductors
- Mask design, laser pattern generator and laser writer
- Polymer structuring by photolithography and micromoulding techniques
- Electrical and functional characterizations

Overview of the MFA Microtechnology clean lab

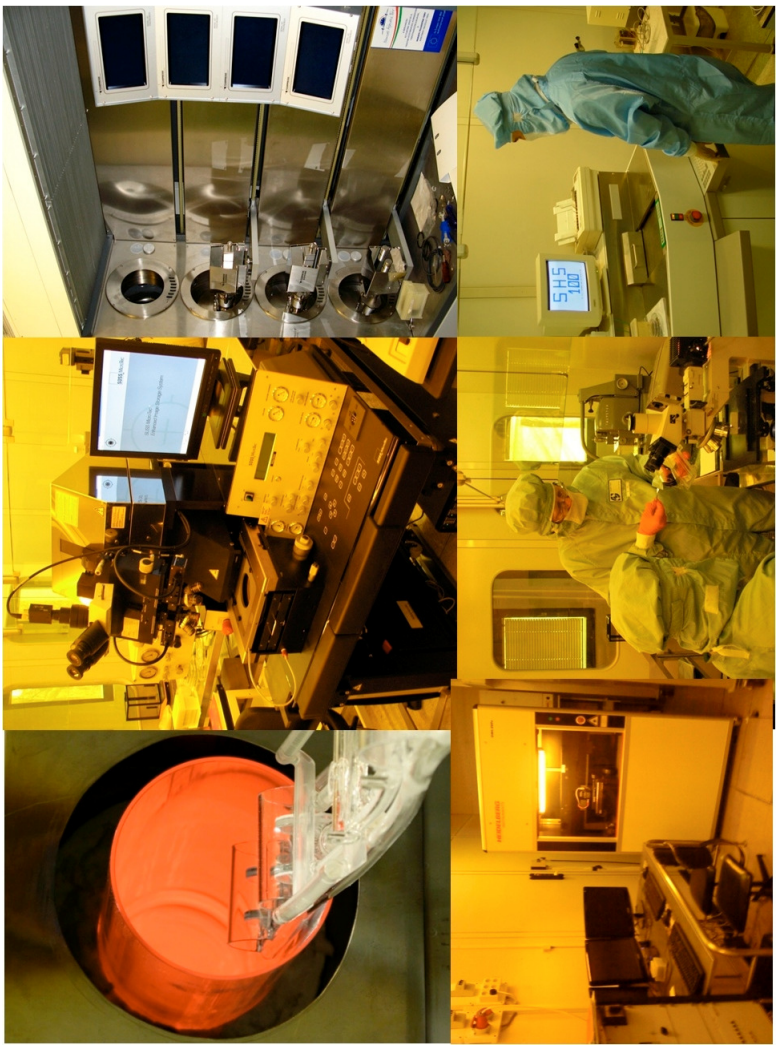

MEMS devices developed in the MFA MEMS lab.

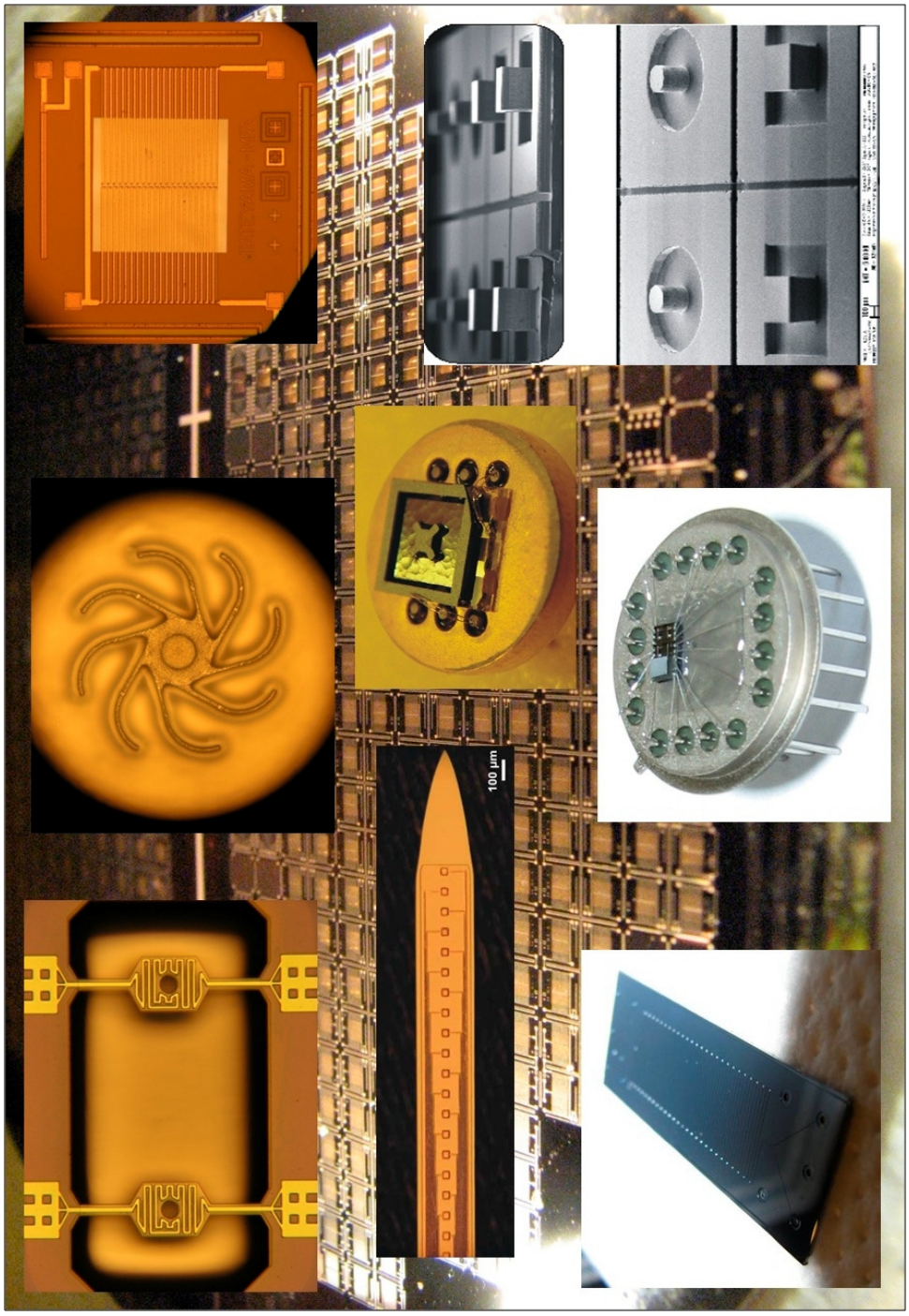

Micro- and nanofluidic elements and devices developed in MFA Microfluidics lab.

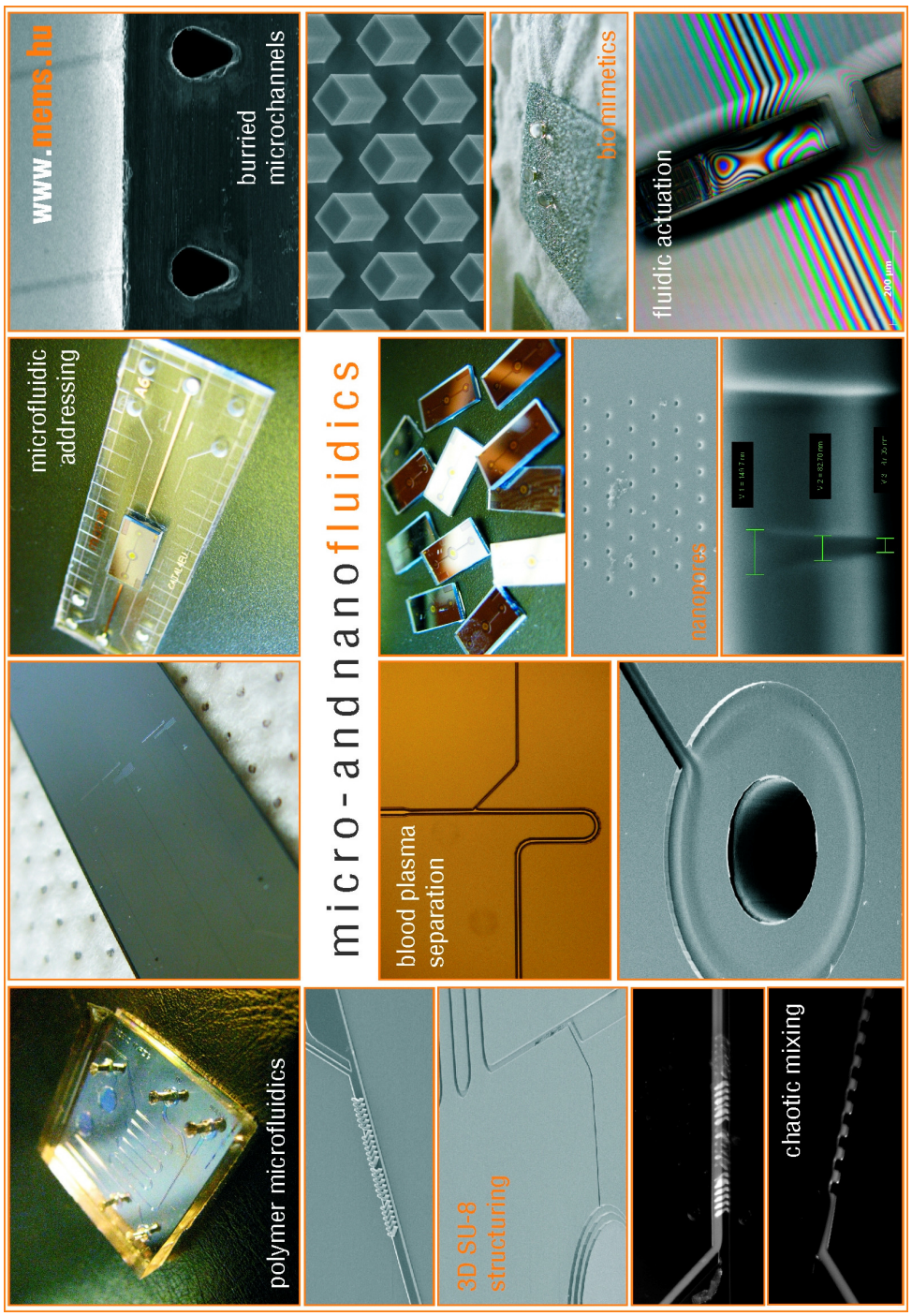

Tyre integrated shear force sensor

(ENIAC JU SE2A)

I. Bársony, A. Pongrácz, M. Ádám, Z. Hajnal, A. Nagy, and G. Battistig

In the frame of the SE2A ENIAC project the MFA MEMS Lab in close cooperation with WESZTA-T Ltd developed a tyre integrated shear force sensor using the Si 3D force sensor in a special package integrated on the sidewall of the tyre.
The Si force sensor is integrated into a rubber patch and this patch is placed on the sidewall of the tyre. Tyre repair patch is a widely used and reliable solution, does not interfere with the tyre deformation, therefore it is suitable for the encapsulation of the sensing element.
A real tyre was analyzed and a complex FEM simulation model was created in order to define the appropriate placment of the patch-encapsulated sensor. The geometric model used in simulations is a simplified version of the real composite structure used in radial tyres. Nonlinear Mooney-Rivlin 2 constant material model was used in early simulations, which was later replaced by a linearized model. Comparing the results of the measurements and the simulations the maximum amount of difference in deformation is less than 15%. In the next stage the FEM simulation model was used to determine the best position of the sensor system.
A measurement construction was built by WESZTA-T Ltd, which is able to cause different stresses in 3 directions in a fixed car-wheel. The measurement board, which contacts with the wheel, can be moved in 3 direction (vertical, lateral and longitudinal force) the forces can be increased up to 2200 kg. Exact value of the forces can be measured using load cells in each direction with 0.1% accuracy. The surface of the measurement board is asphalt, to provide real circumstances.
A 2×2 mm^2 sensor was integrated in the tyre using the rubber patch assembly and was tested under different loads using the measurement setup described above. Inductive supply and communication was tested on a rotating tyre. Reliable communication is working up to 8cm distance with 5mW transmitted power at 60km/h speed.

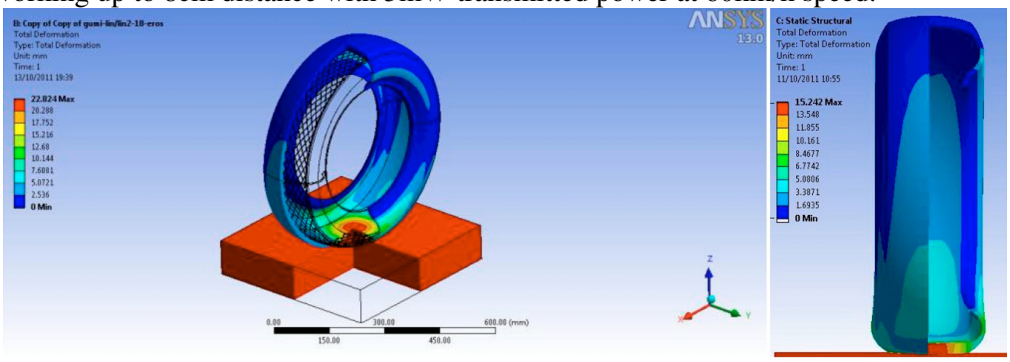

Figure 1. *Tyre deformation simulated in ANSYS using 0.22 MPa internal pressure and 2 kN load.*

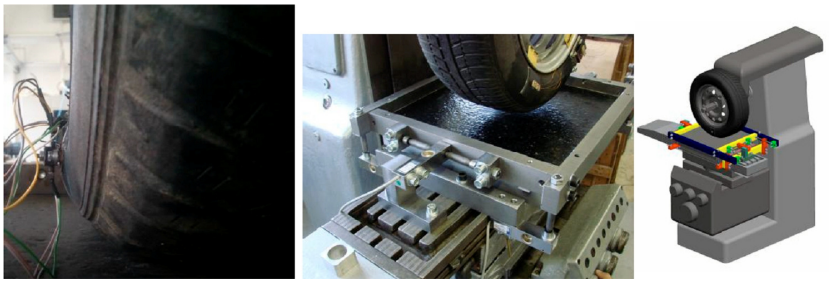

Figure 2. *Sensor is mounted on the sidewall of a tyre using a rubber patch (left). The applied load is 2 kN. Measurement pad with 8 load cells is shown on the right with a schematic illustration.*

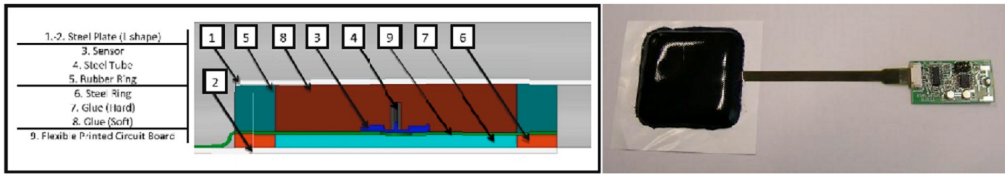

Figure 3. Schematic of the sensor packaging (left) and the realized unit (right).

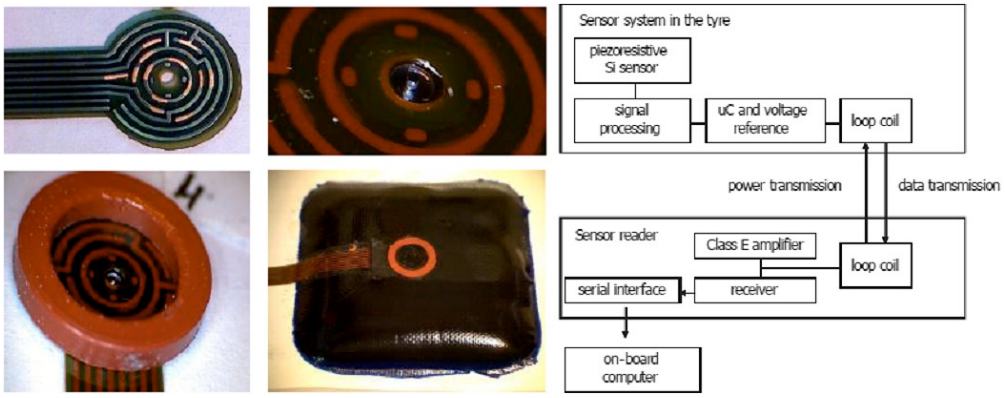

Figure 4. *Sensor packaging step-by-step. a) flexible PCB b) Si chip mounted in the center of the PCB c) rubber spacers d) sensor in the rubber patch e) sensor in the rubber patch assemby ready for installation. Diagram of the system built-in the tyre (right).*

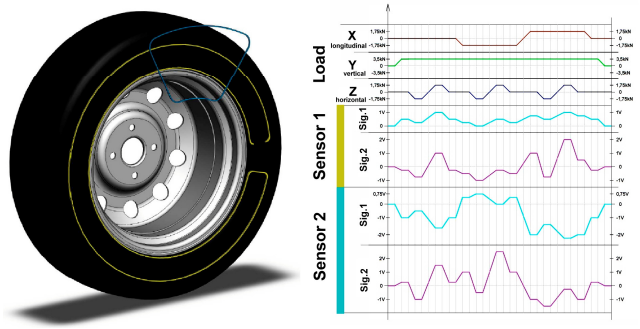

Figure 5. *Sensor signals versus different x-y-z loads (left). Shape and positioning of the standing (blue) and rotating (yellow) loop coil on tyre for the wireless communication and suppl.*

Glue free packaging development of the full membrane 3D force sensor using wafer bonding

(ENIAC JU SE2A)

I. Bársony, A. Pongrácz, M. Ádám, Z. Hajnal, A. Nagy, and G. Battistig

Micromachined 3D force sensors gain importance not only in the field of tactile sensing, robotics and biomedical sciences, but also in automotive applications. Development of a sensor-specific packaging technology for the piezorezistive force sensors is a crucial object in order to eliminate or minimize the functional instabilities generated by the system level thermal and thermomechanical effects.

The developed design and process flow [É. Vázsonyi, M. Ádám, Cs. Dücső, Z. Vízváry, A. L. Tóth and I. Bársony: Sensors and Actuators, A 123-124 (2005), pp.620-626.] was improved by an additional hybrid wafer bonding step consisting of a simultaneous anodic and metal fusion bonding process. Using the glass substrate improves thermal isolation and thermo-mechanical stability of the system. Because of the thermal expansion coefficients of the chosen glass and the Si-only slightly differ, the residual thermomechanical stress during the operation is minimized.

The technology involves the formation of piezoresistors on the backside of a thin Si membrane, while on the front side a circular silicon rod is emerging out of the center of the membrane produced by subtractive dry etching (Deep Reactive Ion Etching) technology. A hybrid wafer bonding (Si to glass and Al to Al) facilitates the reliable signal read-out from the ion-implanted piezoresistors and ensures the thermal isolation of the sensing elements and the packaging. Through-wafer Si etching opens up windows over the contact pads of the glass carrier wafer making the pads accessible for wire bonding.

In Figure 3 the optical image of a successfully bonded structure is shown. Our recently presented procedure enables parallel cavity formation, metal outlet fabrication from backside, electrical and mechanical bonding of the sensor chip to a glass carrier wafer, while keeping the chip thermally isolated and minimizing the sensitivity of the functional parameters to the thermomechanical effects which has crucial importance in the planned biomedical and automotive applications.

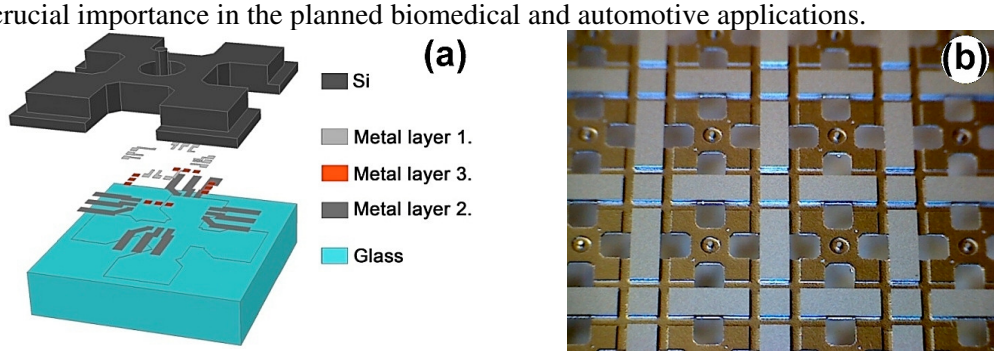

Figure 1. *(a) Schematic cross section of the structure, (b) Wafer level realization of the Si 3D force sensor*

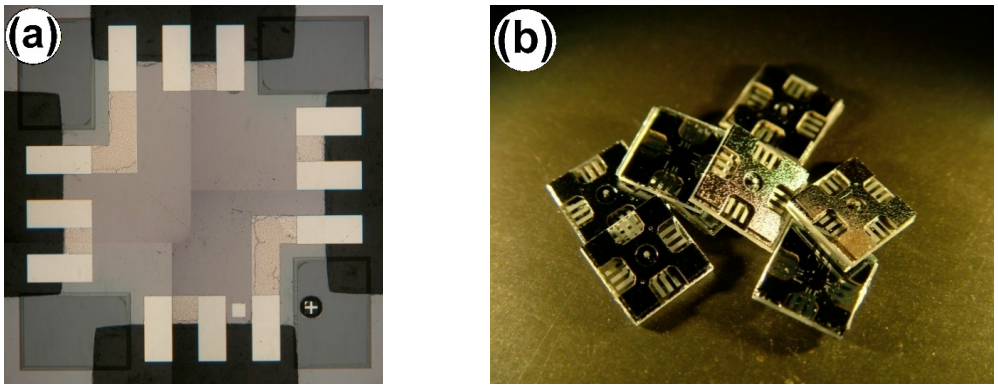

Figure 2. *(a) An optical image of the hybrid bonded test structure from glass side. (b) A bunch of 3D force sensors with the realized Si/glass heterostructure.*

THz detectors

B. Szentpáli, G. Battistig, P. Fürjes, A. Pongrácz, P. Földesy

The development of the THz detector was continued under the OTKA project TERASTART. The principal structure of the device and the photo of a chip are shown in Fig. 1.

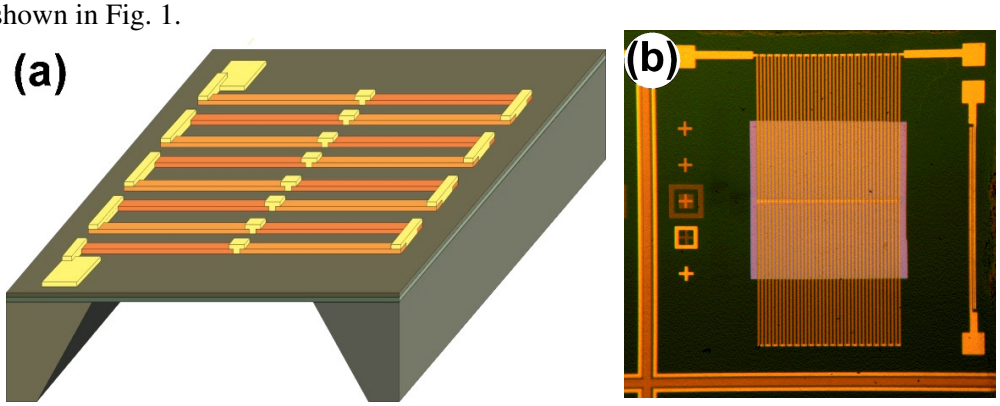

Figure 1. *(a) the schematic of the device. (b) the photo of the chip. The chip size is 2x2 mm^2, it holds 40 linearly arranged thermocouples.*

The thermocouple lines act as short circuited dipole antennas, in which the distribution of the induced current is sinusoidal, having the maximum value at the center. Therefore the associated Joule heat formation reaches its maximum also around the middle of the lines, exactly where it generates the highest thermoelectric effect. The thermocouple lines are composed from p- and n-type poly-silicon, deposited by LPCVD process at 630 ^{o}C with SiH_4 as the precursor. The p- and n-type parts are ion-implanted by B and P respectively. The doping concentrations were determined in such a way that they result in the same electrical conductivity as far as

possible in order to ensuring the electric symmetry of the antennas. The membrane is a double layer of non-stoichiometric silicon-nitride (SiN_x) and silicon-oxide (SiO_2) with the appropriate thickness ratio resulting enhanced mechanical stability and minimizing the residual stress in the suspended membrane area. The antenna-like operation was demonstrated by the strong dependence on the polarization of the high-frequency radiation, as it is shown in Fig. 2.

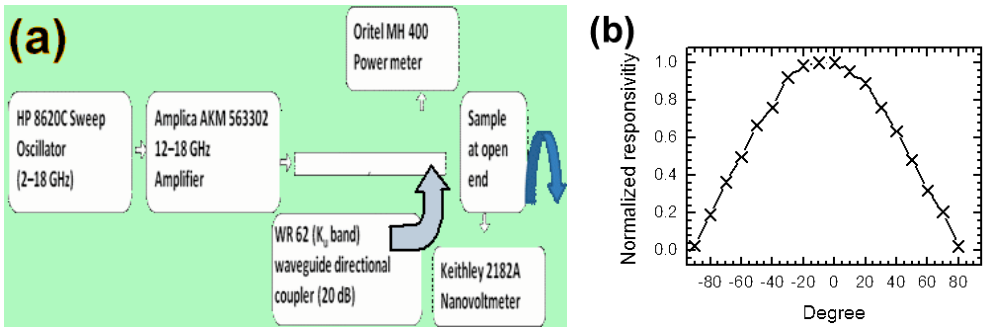

***Figure 2**. (a) The set-up for measuring the responsivity at 13 GHz, (b) The output in the function of the polarization angle. The maximum is obtained when the electric field is parallel to the thermocouple lines.*

In the THz band two measurements were performed: at 100 GHz and in a broad-band THz radiation. The 100 GHz signal was generated by successive multiplication of the microwave power and radiated to the chip by a W-band horn antenna. The broad-band THz signal was produced by the excitation of a non-linear crystal ($LiNb_bO_3$) by ps laser pulses. Beyond these investigations the responsivity to infrared radiation was also measured. The source was a heated black body formed from a 5×5 cm^2 aluminum plate covered by "black velvet" paint. Its temperature was regulated by a controlled Peltier element between 0...100 ^oC. The results are summarized in the Table I.

***Table I.** The responsivities of the same chip to different excitations.*

excitation	13 GHz	100 GHz	Broad-band THz	Black-body radiation
responsivity [V/W]	0.2	5.6	21	20
coupling factor	0.22%	6.2%	23.3 %	22.2 %

The coupling factors are the ratios of the estimated responsivities and the 90 V/W, the responsivity to the direct electric heating, which can be considered as an absolute reference value. This value was obtained on a kindred structure having an integrated electric heater on the chip. The recorded data clearly indicate that the efficiency increases with the increase of the frequency, further the responsivities to IR and to the broad-band THz are very close. The coupling factor of the THz radiation is rather high, competitive with other published values of THz detectors with different working principles.

MEMS Capacitive pressure sensor

T. Kárpáti, A. E. Pap, A. Adam, and A. Pongrácz

Pressure sensing systems are used in many applications such as automation in manufacturing industries, medical applications, monitoring in vehicle industry and so on. The pressure sensors and transducers transform the induced force in a sensing area to displacement or mechanical stress. In many case the industrial applications showed that measuring is required at low pressure range. Our silicon based capacitance pressure sensor with the range under 1000 mbar was developed in co-operation of the MFA and Weszta-T Ltd.

The sensor is built up from two parts; single crystalline Si membrane electrode and the carrier Borofloat 33® glass with aluminum capacitor plate (fix electrode) and bonding pads (See Fig. 1.).

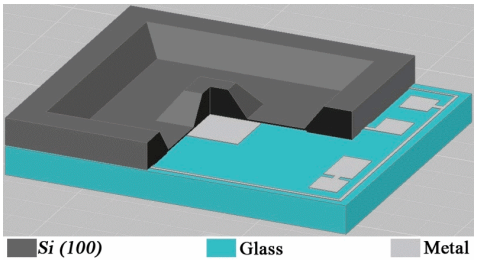

Figure 1. *Diagram of silicon-based capacitance pressure sensors.*

The thin diaphragm was formed by using an anisotropic alkaline etching combined with Electro-Chemical Etch Stop. The initial thickness of Si wafer was stet at the center and round the side of the chip. The total thickness frame on the chip side serves the electrode mechanical strength, the good tractability during technology methods Due to the center reinforcement the capacitor structure behaves like a parallel capacitor once the membrane deforms. In order to promote free moving of the membrane during the bonding method and for the outlet of the fix electrode a cavity on the bottom side of the Si chip was etched. The static bottom electrode on glass substrate was realized by aluminum evaporation and it was patterned by etching technique. The fabricated structures are presented in Figs. 2-3.

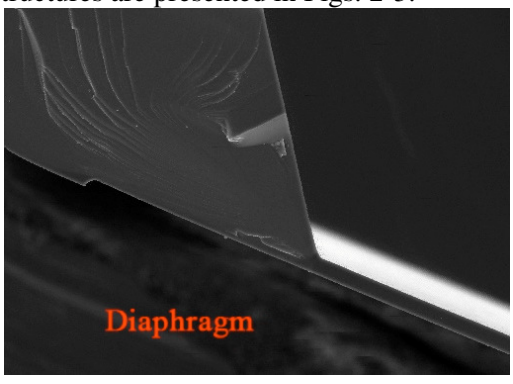

Figure 2. *The free standing silicon membrane forming the moving electrode of the capacitor fabricated by bulk micromachining.*

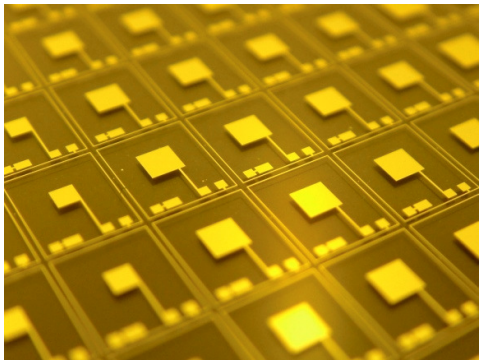

Figure 3. *Metal electrodes of the capacitive sensors realized on glass wafer.*

Finally, the 500 μm thick metalized Borofloat 33® glass with the Al pattern and the structured silicon wafers were anodically bonded at low temperature (T=200 °C) which guaranteed a very high mechanical strength. For anodic bonding the wafers was aligned by a SÜSS MicroTech MA6/BA6 type Mask Aligners. The equipment is adapted for two side mask alignment, which facilitates to form the diaphragm structure. After the alignment, the clamped wafer pair was bonded by the SÜSS MicroTech SB6L wafer bonder device. The applied parameters of anodic bonding were 200°C temperature, -1000 V voltage, 1000 mbar tool pressure, 40 min process time, and the procedure made under 10^{-3} mbar chamber pressure. The bonded area in a single chip was approximately 9,503 mm^2 and the bond strength between the two electrode was allocated at 33,95 MPa by tensile strength measurement method.
The bonded wafer pair was slicing up for chips and than packaged in a socket (TO8 Schott). Following the packaging, the trench for the outlet of the fix electrode was being filled up. The relative pressure sensor was formed through a hermetical separation of the cavity from the outer atmosphere.

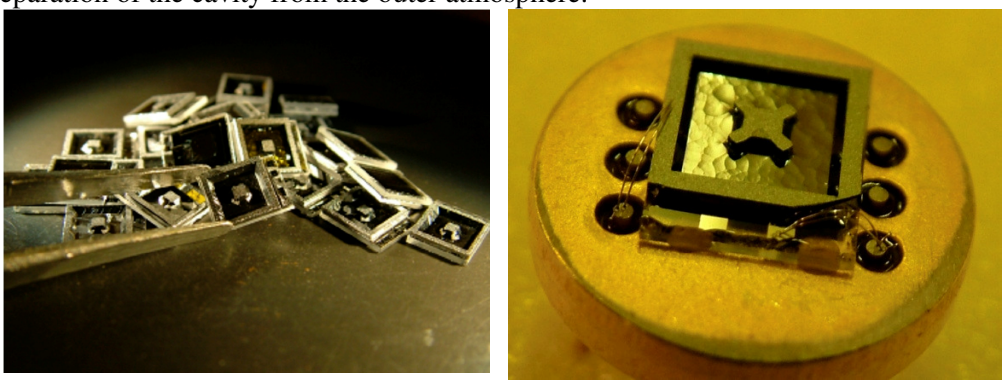

Figure 4. *Assembled and packaged capacitive pressure sensors.*

The fabricated and packaged capacitance pressure sensors (see Fig. 4.) were functionally tested in the working pressure range. The output capacity was measured under pressure range of 80 to 1000 mbar. As required the device had near linear response in the measured pressure range as presented in Fig. 5. The general properties of the capacitive pressure sensor are showed in Table 1.

Table I. *Datasheet of the MEMS capacitive pressure sensor*

Pressure Range [mbar]	Pressure Measurement	Sensing Structure	Thermal Sensitivity	Signal Output	Size [mm]
1-10; 10-50; 50-250; 250-1000;	Absolute Ref.: 1 atm	10 μm thick Si membrane	No	Capacitive	5 × 6 × 1

Response Capacity [pF]	Sensitivity [fF/mbar]
1-10	2-4

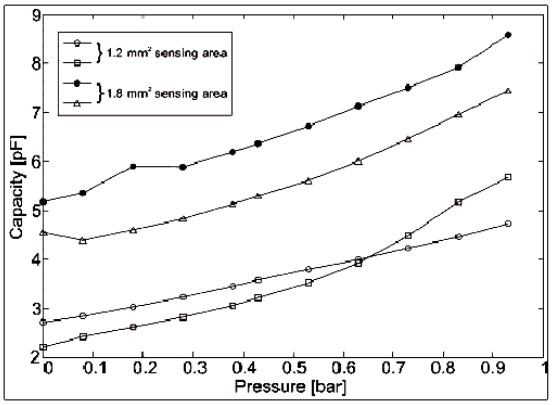

Figure 5. *Test characteristics of the pressure sensor.*

Application of nanosize hexagonal WO_3 sensing layer in MEMS based gas sensor

A. E. Pap, R. Csutak, A. Adam, and J. Pfeifer

Metal -oxide semiconductor gas sensors are of significant interest to detect toxic and hazardous gases. Nowadays the energy efficiency, small dimensions, low cost and high reliability may be the most significant requirements for electronic gas sensing devices, to be adequate in industrial and commercial applications. The use of small and cheap devices is preferable since a large number of sensors can be placed easily to different sites to monitor the concentration of different species without involving huge investments.

Heatable suspended membrane systems have been developed at MTA MEMS laboratory which temperatures reach few hundred degrees of Celsius by several mW of electric power. These devices with a suitable sensing layer may be adequate to achieve the expectations mentioned above.

Among of other semiconducting metal oxides, tungsten trioxide is the most promising material for gas sensing applications as an active layer.

Crystalline hexagonal-WO_3 (h-WO_3) powder was prepared by J. Pfeifer and co-workers at Ceramics and Nanocomposites Department of Research Institute for Technical Physics and Material Science. They investigated the response of the sensing material under exposure of organic vapors and NO_x gases. Results show that the sensitivity of the wet processed h-WO_3 to NO_x gases at temperature of as low as 150 °C is outstanding. In our development we used this type of h-WO_3, as active layer which had been provided by Dr. J. Pfeifer.

The base structure of the solid state sensors were manufactured by single side bulk micromachining silicon technology. A single microhotplate element and its layer structure are illustrated in Fig 1. The most obvious features are the suspended hotplate, four support beams, and the etch pit. The device shown also has two comb-

shaped top electrodes that are used for measuring the electrical resistivity of the deposited sensing film at the top of the plate. A serpentine platinum element embedded in SiO_2, Si_3N_4 multilayer serves as a resistive heater. Above the heater, separated by an insulating layer of SiO_2, is a metal electrode pair made of gold to conduct electric current through the h-WO_3 sensing layer. The suspended microhotplates are typically ~100 µm across. This 3D microstructure is able to fulfill the strict requirements of decreased power dissipation due to the enhanced thermal insulation achieved by porous silicon sacrificial technology. The h-WO_3 powder was dispersed in destillated water and the hotplates were coated with this dispersion by dip&drop method and dried for 12 hours at room temperature. Fig. 2. shows the cross-sectional area of the porous sensing layer.
During the test measurements sensor were exposed to continuous gas stream of 100 ppm NH_3-N_2 or clear N_2 gas by turns, in 30 minutes. The resistance of the semiconducting film at different temperatures was obtained by measuring the potential drop between the pins of the interdigitated electrodes whilst 1 µA direct current was driven through the active layer. The resulted curves (Fig. 3.) plotted the variation of the resistivity of the sensing layer as a function of the time for different hotplate temperature.

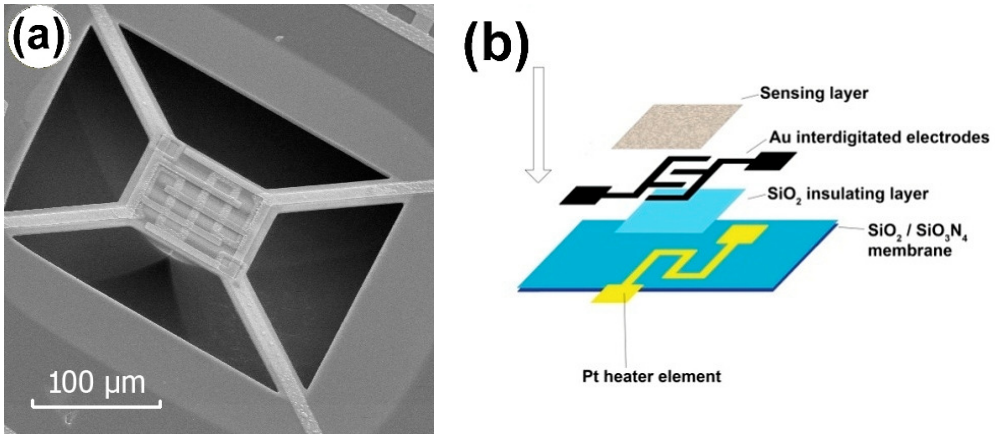

***Figure 1**. (a) Micrograph of single microhotplate with two interdigitated electrodes, (b) schematics of functional layers in a surface micromachined microhotplate.*

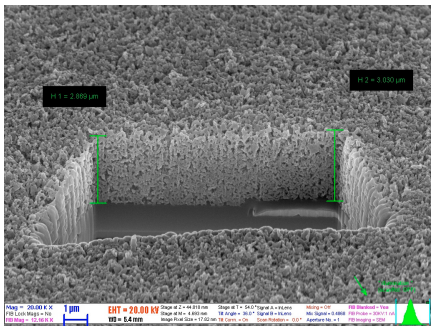

***Figure 2.** SEM picture of the Cross sectional area of the h-WO_3 sensing layer.*

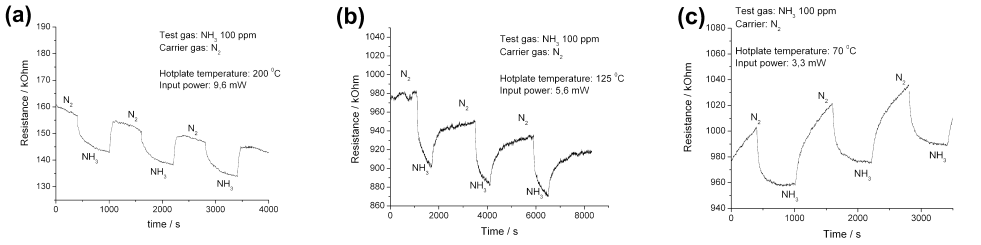

Figure 3. *Time dependence of the resistance of the h-WO_3 active layer during exposure to 100 ppm NH_3, in presence of nitrogen.*

Shaping of micropatterned structures by anisotropic deformation under ion irradiation

Z. Zolnai, A. L. Tóth, and G. Battistig

Recent modern topics of micro- and nanotechnology relate to the fabrication of 2D or 3D arrays of hetero-structures built up from different elementary objects with regular shape and well-controlled size. There is an increasing demand for appropriate tools which can couple micro- and nanoscale dimensions as top-down or bottom-up

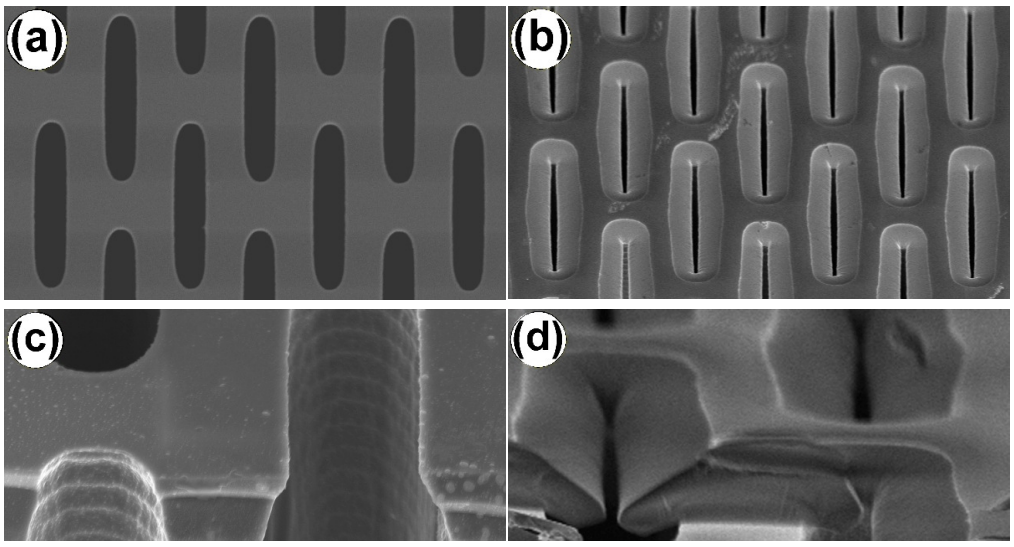

Figure 1. *(a) SEM view of regular arrays of Si micropores formed by deep reactive ion etching (DRIE) through a silicon dioxide masking cap layer. The width and length of the pores is 3 μm and 15 μm, respectively, with a spacing of 3 μm in both directions (b) Similar view of the structure after irradiation carried out perpendicular to the sample surface with 2.8 MeV N+ ions to a fluence of 1016/cm2. Here the slit between two facing edges is reduced to about 220 nm. (c) and (d) shows SEM side views recorded with higher magnification on the cross sectional edges of the samples shown in (a) and (b).*

techniques, especially when particular applications call for specific solutions. As Fig. 1 shows, one example can be the formation of a horizontally continuous or nearly continuous planar-like cap layer on the top of micro-patterned surfaces of porous 3D Si structures. The aim should be to protect the pores as reservoirs from the ambient or to tailor the distance between two facing edges in order to control transport properties or optical coupling at the surface layer on sub-micron scale. The closing of surface slits can be realized by the so-called ion irradiation-induced plastic deformation (often called ion-hammering) process of silicon dioxide or amorphous silicon. In this case the irradiated layer contract parallel to the ion beam and expand perpendicular to the ion beam without significant volumetric change.

As the deformation rate can be finely tuned with the applied ion fluence, the ion hammering process should be considered as a successful one-step micro/nanofabrication tool. Note, high deformation rates can be achieved and no heat treatment of the sample is needed. The thickness of the transformed layer is determined by the penetration depth of the energetic ions, e.g. when a silicon dioxide layer is bombarded with N^+ projectiles of 2.8 MeV energy, a surface layer with thickness of about 3 μm is exposed to the ion hammering process.

The parameters of shape transformation also depend on the type and energy of the ions as well as on the density and initial shape of the target, the temperature, and the direction of the ion beam with respect to the sample surface. Nevertheless, the phenomenological model of the anisotropic deformation process is well described and the mean features can be estimated as a function of the applied ion fluence [*T. Van Dillen et al., Phys. Rev. B **71**, 024103 (2005)*].

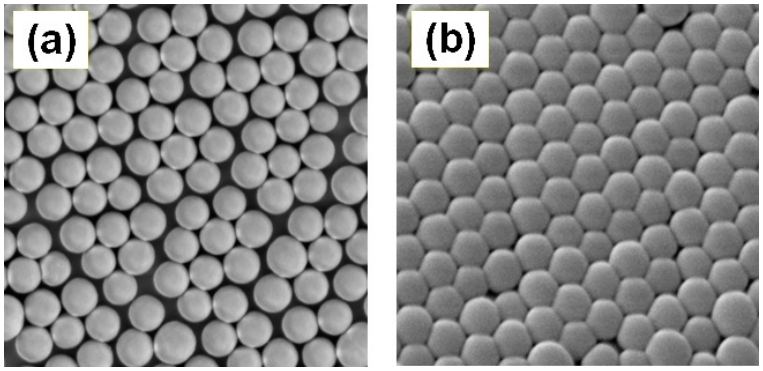

***Figure 2**. One monolayer of colloidal silica particles with diameter of D = 450 nm deposited on Si substrate with Langmuir-Blodgett technique (a) before and (b) after irradiation carried out perpendicular to the film plane with 500 keV Xe^{2+} ions to a fluence of $10^{16}/cm^2$. Due to irradiation induced plastic deformation, the particle shape changes from sphere to oblate ellipsoid with its minor axis parallel to the direction of the bombarding ion beam. For details see: Z. Zolnai et al., Phys. Rev. B 83, 233302 (2011) and Z. Zolnai et. al, Nucl. Instrum. Methods in Phys. Res. B 268, 79-86 (2010)*

Fig. 2 shows the result of the hammering effect when a monolayer of colloidal silica particles is irradiated with energetic Xe^{2+} ions. Here the particles undergo anisotropic deformation upon changing their shape from spherical to oblate ellipsoidal. Such

anisotropic particles can be applied as tunable photonic crystals [*K. P. Velikov et al, Appl. Phys. Lett.* ***81*** *838-840 (2002)*] or as shadow nano-masks for the deposition of single dots on the underlying substrate through the holes of neighboring particles [*D. L. J. Vossen et al., Nano Letters* ***5*** *1175-1179 (2005)*]. Note, for 500 keV Xe^{2+} ions the penetration depth is about 350 nm into silica and almost the full fraction of the particle volume is exposed to the ion hammering process. Note, below a particle diameter of 200 nm the hammering effect is strongly reduced due to surface capillary forces [*T. Van Dillen et al., Phys. Rev. B* ***74****, 132103 (2006)*].

Integration of buried channels in cerebral silicon microprobes

Z. Fekete, A. Pongrácz, and P. Fürjes

Microfluidic channels for local fluid injection or sampling integrated on silicon (Si) based neural multi-electrodes (see Fig. 1) are required for better understanding of different brain mechanisms during in-vivo experiments. Drug delivery systems buried underneath the Si surface is recommended to minimize the diameter of the probe and to keep the surgery minimally invasive. Simplified fabrication technology of completely buried passive microfluidic channels using dry etching methods is presented to meet the demands of today's complex microsystems. The applied process flow with selective edge-protection (patent pending) resulted in sealed microchannels while preserving the surface planarity above the buried structures as presented in Fig. 2.

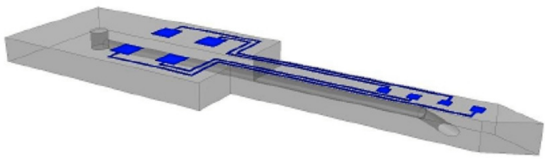

Figure 1*. Artistic representation of the silicon microprobe with integrated buried microchannel for simultaneous drug delivery and electric measurements.*

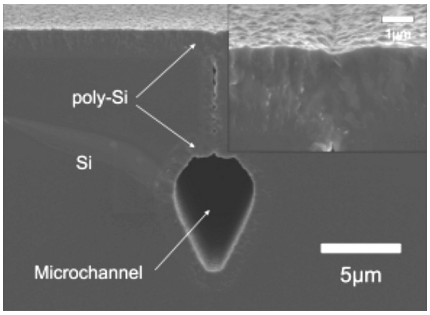

Figure 2. *Cross-section of a buried microchannel realized by our group after the sealing by LPCVD poly-Si deposition is completed.*

The formation mechanism of the predefined trench and the buried channel is characterized in details. The etching reaction forming the final geometric profile of the channel slows down generally with increasing aspect ratio of the predefining trench. The vertical component is influenced mainly by the depletion of the radicals. The horizontal etch rate is decreasing faster than the vertical, causing a more anisotropic cross section profile of the channel with increasing depth. We suppose that the horizontal etch rate is influenced not only by the depletion of the radicals, but

a highly decreasing horizontal ion flux is superposed, originating from the shadowing/collimating effect of the trench walls.

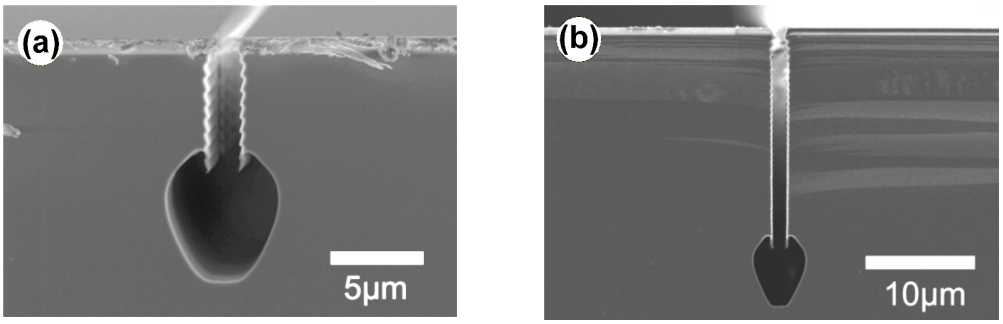

Figure 3. *Profile of DRIE etched buried channels before trench-filling in case of aspect ratios 4:1 (a.) and 14:1 (b.).*

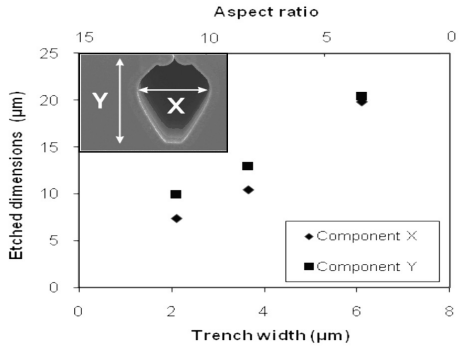

Figure 4. *Change of etch components vs. final geometry of the trenches. Trench width is 2μm.*

The functional parameters of the proposed micro-needles as hydrodynamic resistance and mechanical stability were also characterized as the function of the geometrical parameters of the realized structures considering the technological limitations also. Experiments proved that aspect ratio of the predefined trench on the silicon wafer is a key parameter and should be carefully tuned in order to fabricate microchannels in microprobes in a reasonable way, fulfilling both mechanical and fluidic specifications.

Growth and properties of Al doped ALD ZnO

(OTKA NK73424)

Zs. Baji, Z. Lábadi, Z. E. Horváth, M. Fried, K. Vad, J. Tóth, and I. Bársony

ZnO has attracted great attention recently because of its versatility in a number of applications, such as sensors and photovoltaic devicess. It can be doped with aluminium to increase its conductivity, and be used as transparent conductive oxide layer.

We developed an ALD process for the in situ Al doping of ZnO. The procedure consists of periodic alternate injection of Al-precursor pulses intermixed with the sequences of Zn-precursor pulses. The specific resistances of the ALD Al:ZnO layers were evaluated as a function of the introduced atomic fraction of Al (i.e. number of Al precursor pulses) and temperature. We examined in details the effects of Al doping on the layers in a wider doping and temperature range. We found that in the case of Si and glass substrates the ALD grown ZnO films are polycrystalline, and the deposition temperature determines the dominant crystalline orientation of the layers: At lower temperatures the (100) orientation is dominant, that is, the crystallites stand perpendicular to the surface. At higher temperatures the (002) peak becomes the dominant orientation, that is, the crystallites are parallel to the surface.

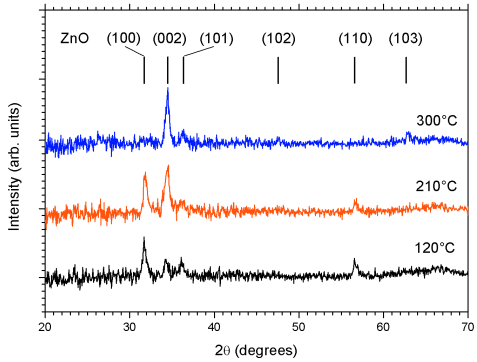

***Figure 1**. The orientation of the ZnO layers at different temperatures.*

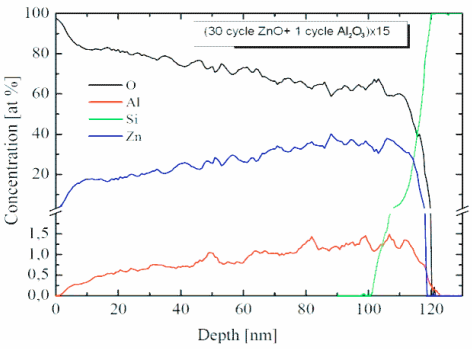

***Figure 2**. The SNMS depth profile of a doped layer.*

Since the source of Al doping are the AlO_x sublayers, the Al content is not homogenously distributed throughout the layer. Instead it rather forms a multilayered structure (as seen from the SNMS results).

XPS analysis of the layers show that the majority of the introduced Al is present in the form of AlO_x, and only a fraction of the Al (about 10%), is incorporated as electrically active dopant. However it is sufficient to reduce the resistivity of the intrinsic layers by two orders of magnitude. Sheet resistance of the best doped doped layers was as low as 9E-04 Ohmcm. Van der Pauw analysis of the samples showed that the carrier concentration monotonously increases with the increasing amount of electrically active aluminium, while the mobility monotonously decreases. This phenomenon results in an optimum of the resistivity as a function of introduced Al. As a function of the deposition temperature the carrier concentration develops a maximum, while the mobility decreases monotonously.

This optimum has also been established by the analysis of bandgap values from spectroscopic ellipsometry, and optical absorption results The AlO_x doping linearly increases the band gap of the layers. As a function of the deposition temperature the band gap has a minimum. The most perfect crystal structure and largest grain size was found at 2 at% Al content at every growth temperature, while the accumulation of compressive strain developed a monotonous increase with the growth temperature.

The resistivity of the samples in lateral and normal directions develops similar qualitative tendencies. Despite this change in the orientation the conductivity shows no anisotropy, therefore we concluded that the conduction mechanism is not grain boundary related.

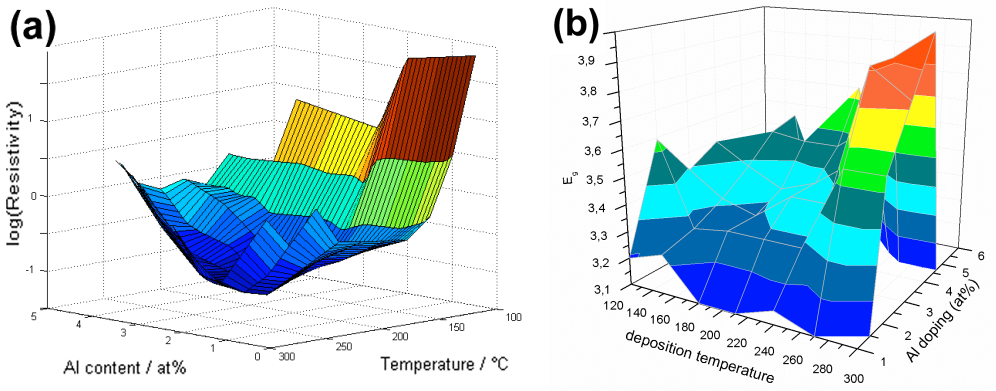

Figure 3. *The resistivity (a) and the band gap (b) of the layers as a function of deposition temperature, and doping.*

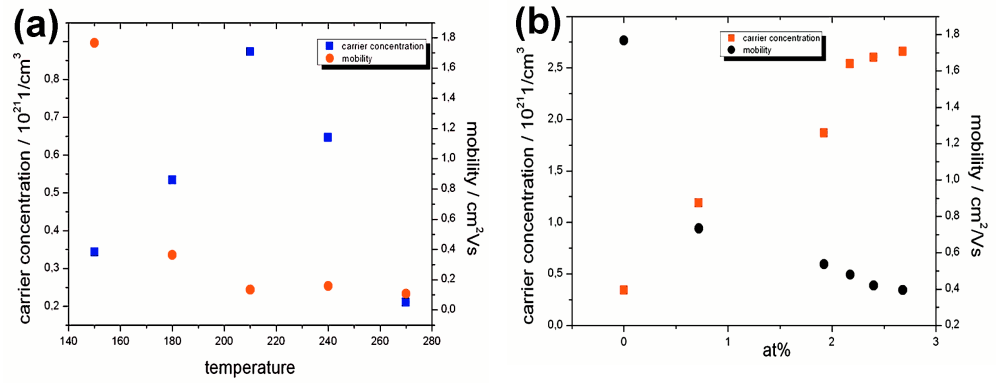

Figure 4. *Carrier concentration and mobility of the layers as a function of temperature (a) and doping (b).*

We have deposited ZnO layers on Si, GaN and sapphire substrates, and found completely different morphologies. Epitaxial growth is possible both on GaN and sapphire with a proper tuning of the deposition. The TEM micrograph below shows a cross section of the epitaxial ZnO layer on a sapphire substrate.

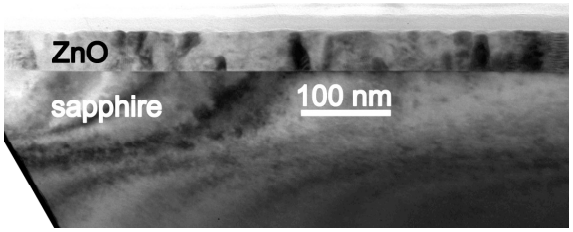

Figure 5. *Epitaxial ZnO layer on sapphire (TEM micrograph).*

Properties of CIGS films deposited by flash evaporation and post selenization

(OTKA NK73424)

Zs. Baji, Z. Lábadi, Gy. Molnár, A. L. Tóth, K. Vad, and I. Bársony

Chalcopyrite CuInGaSe materials are very promising candidates for photovoltaic applications due to their high absorption coefficients (10^5 cm^{-1}), long term electrical and thermal stability, and outstanding resistance against photo-degradation.
Post selenization of the precursors is a promising method for low cost large scale production of solar cells. Selenization is usually achieved by using Se vapour, or H_2Se. (The latter is highly toxic, therefore rises environmental and health concerns.)
The aim of our work is to present a new way of fabricating CIGS material by flash evaporation of Cu, In and Ga metal precursors from a single source followed by post-selenization. We studied the effect of CIG precursor morphology and selenization parameters on the CIGS material.
A new method was developed for evaporating the 3 metallic components from the same evaporating source, similar to using an alloy-like source, except that in our case the alloy forms only whilst heating the source. The best efficiency solar cells can be obtained with the following ratio of the components: In:Ga:Cu/0,,8:0,,2:1. For the post selenization of the layers CIG samples with Se pellets were sealed in 10^{-2} Torr vacuum, and annealed at 500 ºC in order to form the $Cu(In,Ga)Se_2$ phase.
The morphology and element distribution of the as deposited CIG precursor was studied by SEM microscopy using Electron Dispersive Spectra (EDS). Fig. 1. shows that the indium –which evaporated first- formed droplets on the surface, which were then covered with a uniform thin layer of gallium and copper..

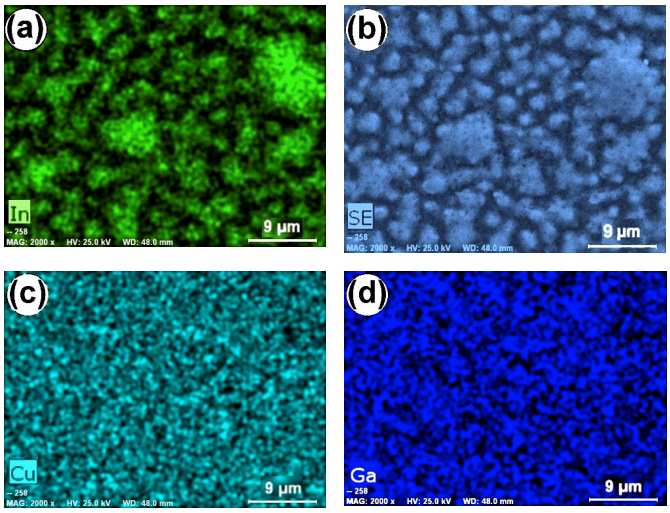

Figure 1. *The morphology and element distribution of the as-deposited CIG layers. (Seconder electron micrographs: In (a), Se (b), Cu (c), and Ga (d) EDS maps.)*

According to the literature, rough morphology of a co-evaporated CIG layer may deteriorate the resulting CIGS morphology, and thus the overall quality of the selenized CIGS film. Our layers, on the other hand, became homogenous after selenization (see Fig. 2), and their elemental composition is in agreement with the required CIGS composition, according to the literature.

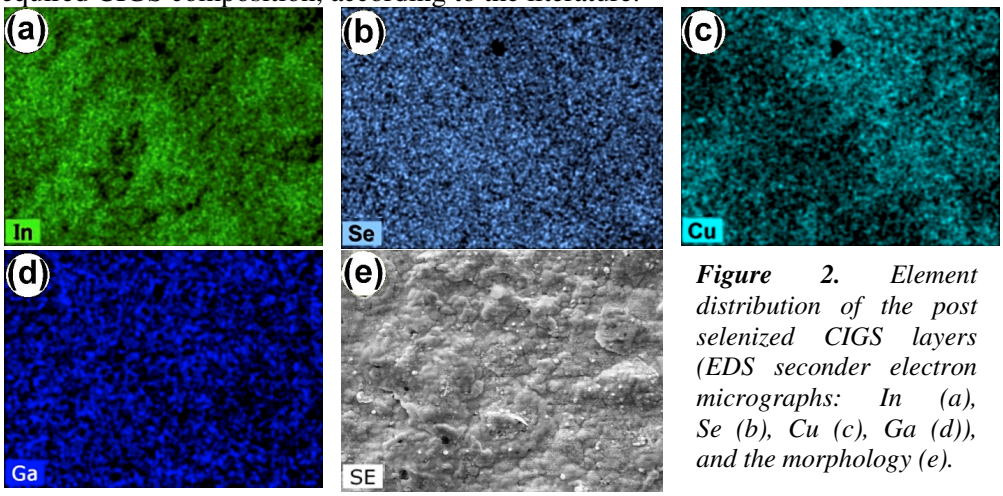

Figure 2. *Element distribution of the post selenized CIGS layers (EDS seconder electron micrographs: In (a), Se (b), Cu (c), Ga (d)), and the morphology (e).*

Another major drawback of the post-selenization method is that CIGS layers deposited by this technology tend to have excess Ga near the back contact of the layers, which decreases the overall device efficiency. Our samples, on the other hand, showed no sign of this effect, their composition is uniform throughout the film. On Fig. 3. It is shown the Secondary Neutral Mass Spectroscopy (SNMS) depth profile of our CIGS film.

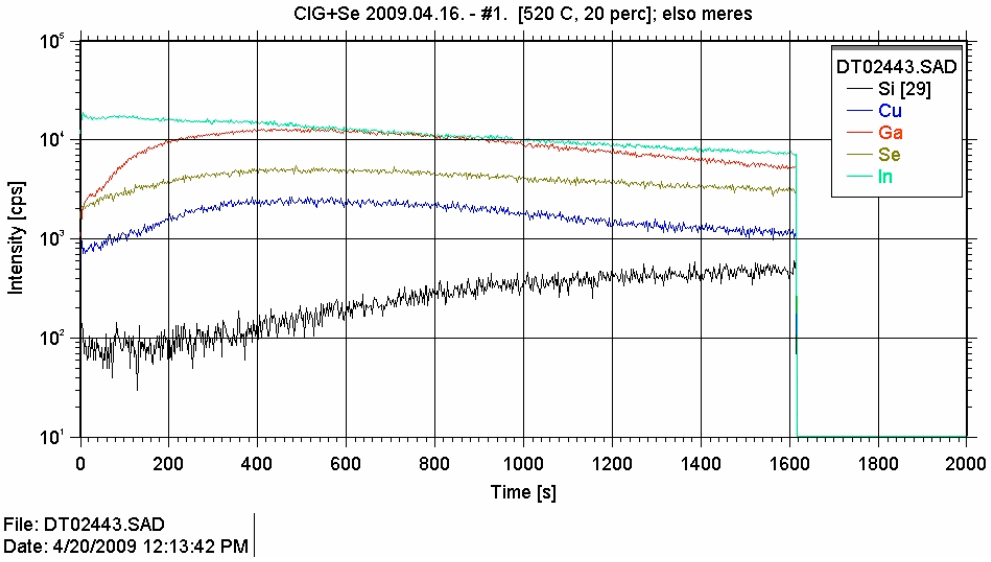

Figure 3*. SNMS depth profile of the post-selenized CIGS layers.*

LPE growth and characterization of InP/InGaAsP infrared emitting diodes

V. Rakovics, S. Püspöki, and I. Réti

Infrared LEDs have been rapidly achieving new applications in near infrared (NIR) spectroscopy. LED module based on a linear array of LED chips and a fixed monochromator provides a solid-state electrically scanned source for pre-dispersive spectrometers. NIR absorptions are most often associated with –OH, –NH, and –CH functional groups. Also, absorptions due to electronic transitions of organometallic molecules in blood appear in the NIR. The emission spectra of different composition InP:InGaAs(P) LEDs can cover the 900–1700 nm wavelength range. In this work double heterostructure InP/InGaAs(P) LEDs were prepared to cover completely the 900–1700 nm wavelength range. Small area planar structures were fabricated for diode array application. The spacing of peak wavelengths was planned according to the spectral bandwidth of InP/InGaAsP LEDs. Unfortunately, the literature data for spectral bandwidths varied from 52 to 75 meV. At first, we used our previous data for planning the peak wavelengths of the LEDs chips. In the present work, we have deduced that the spectral bandwidth is strongly affected by the growth conditions. Narrow bandwidths can be obtained by choosing the appropriate growth temperature for each wavelength. InP/InGaAsP heterostructure diodes with uniform thick active layers, abrupt interfaces, and where the p–n junction was located inside the active region, showed narrow spectral bandwidths.

Double heterostructure InP/InGaAs(P) LED structures were grown by liquid phase epitaxy using (100) oriented InP substrate. The LEDs were grown in a computer controlled LPE apparatus equipped with multibin slider boat

Infrared transmission (Figs. 1-2) and photoluminescence measurements were used for the characterization of LPE-grown InGaAsP/InP LED wafers.

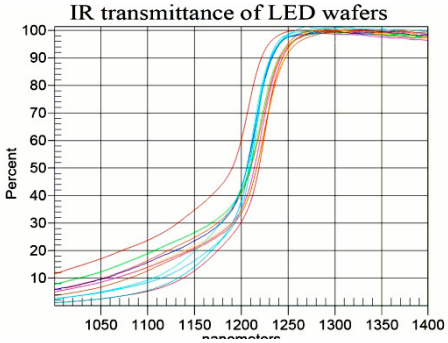

Figure 1. *Infrared transmittance spectra of 1220-1230 nm LED wafers.*

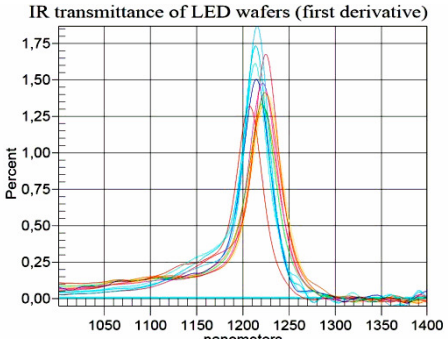

Figure 2. *First devivative of the infrared transmittance spectra of 1220-1230 nm LED wafers wafers.*

The emission spectra of the mounted devices were measured at different driving currents (Fig. 3) and temperatures (Fig. 4). The current heating effect was taken into

account by extrapolation to zero current. The optical band gap was found to be strongly correlated with the extrapolated peak energy of the emission spectrum. Infrared transmittance measurements therefore offer a fast, reliable, and non-destructive way for the determination of the device emission wavelength using a wafer characterization method.

LED devices emitting below 1000nm were investigated carefully because their efficiency were lower than the efficiencies of long wavelength LEDs. The emission spectra of different LED's were compared with each other (Fig 5). The full width at half maximum (FWHM) for a 979 nm LED is considerably smaller than the same parameter for the 1008 nm device. Optical absorption of the substrate is responsible for the loss of efficiency. Optical transmittance spectrum of the InP wafer can be seen in Fig. 6.

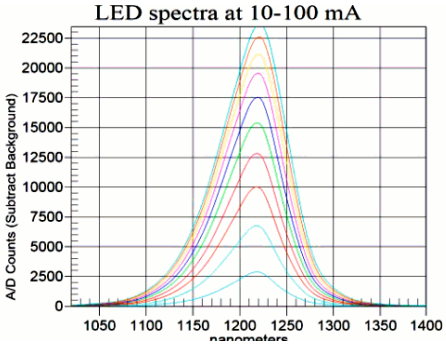

Figure 3. *Emission spectra of 1220 nm LED at 10-100 mA driving.*

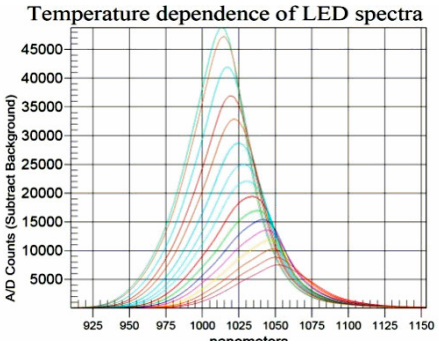

Figure 4. *Emission spectra of 1020 nm LED at 23-180 °C.*

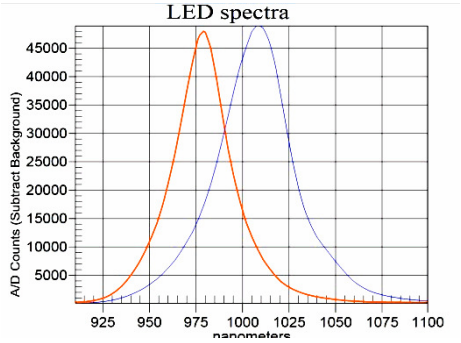

Figure 5. *Emission spectra of short wavelenght LED's.*

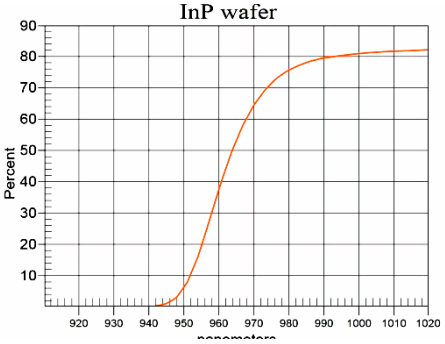

Figure 6. *Optical transmittance spectrum of the InP wafer.*

Activity in the joint MBE laboratory: investigations of the droplet-epitaxially grown nano-structures and equipment developments

Á. Nemcsics, I. Réti, P. Harmat, L. Tóth, M. Csutorás, G. Bátori, B. Plósz, L. Dobos, A. Ürmös, B. Pődör, S. Gruber, F. Pruzsina, P. Kucsera, G. Tényi, T. Sándor, J. Balázs, J. Makai, B. Kupás-Deák, and L. Nagy

Droplet-epilaxial nano-structures: In our project, nano-structures (such as quantum dot, quantum ring and nano hole) grown on AlGaAs (001) surface, were investigated (in-situ by RHEED and ex-situ by AFM, TEM and PL). In this year, inverted droplet-epitaxially grown quantum dot was investigated by TEM and PL methods (Fig. 1.). Here, the faceting and the growth kinetics were determined. The inverted quantum dot was prepared with the filling of the nano hole. We investigated the evolution kinetics of the nano holes and the quantum rings, too. The RHEED has also many open questions. Hysteretic phenomena of the RHEED intensity was modelled and explained for GaAs (001) and InAs (001) surfaces (Fig. 2.).

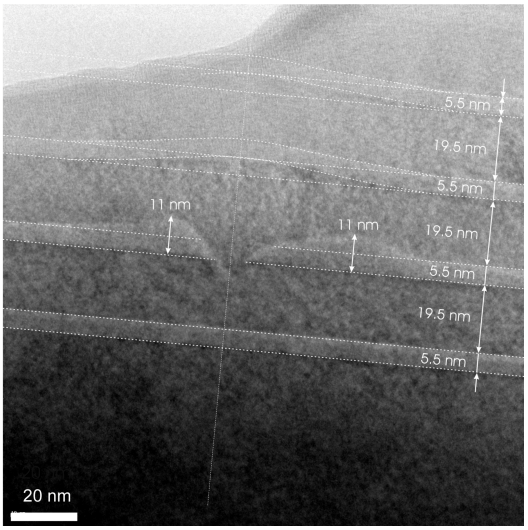

Figure 1. *TEM picture o fan inverted quantum dot.*

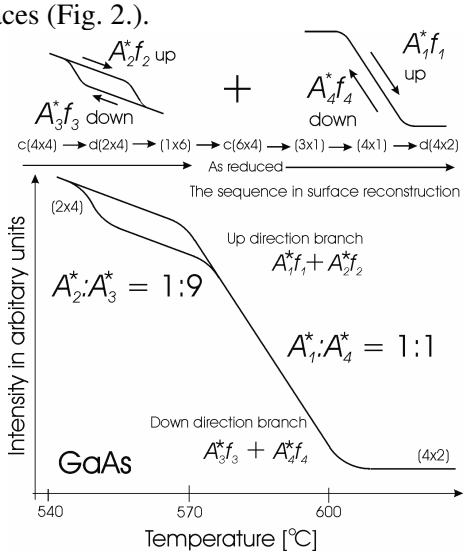

Figure 2. *Hysteretic behaviour of the GaAs (001) surface*

Developments on the MBE machine: In this year, we got and installed a QMS (QMG 220F3) for the residual gas analysis, and a gate valve (VAT 10844-E01) for the separation of the turbo molecular pump of the main chamber (Fig. 4). Furthermore, we developed a mechanical and electronic control (PLC) of the shutter movement (Knudsen cells). Computer visualization was developed for the MBE processes (Fig. 3.). The outheating of the UHV chambers was improved with a boxing. Boxes were developed for the covering of the very complicated UHV chambers (Fig. 5). A movable CCD camera holder was developed for the RHEED evaluation. A computer program for the in-situ RHEED evaluation was developed (Fig. 6.).

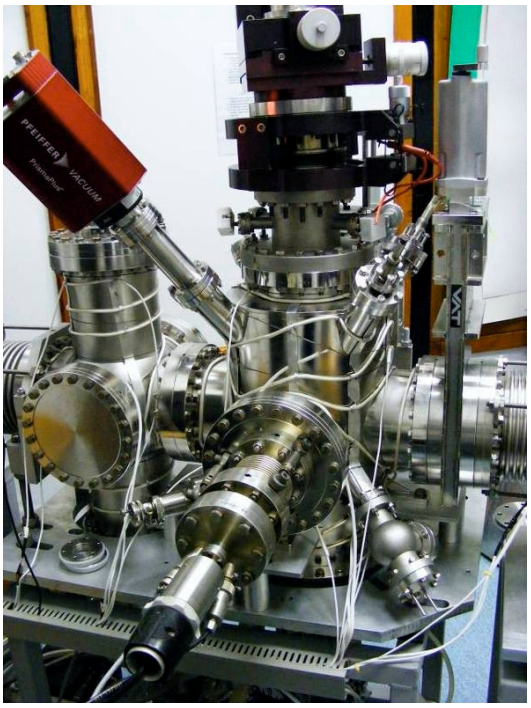

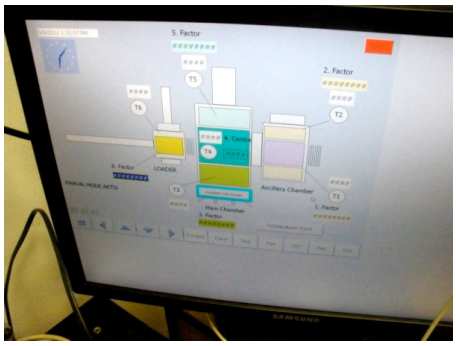

Figure 3. *Visualization of the control (above).*

Figure 4. *The main chamber with the QMS (left).*

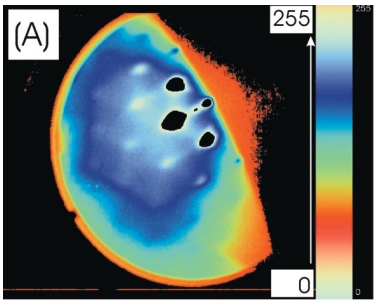

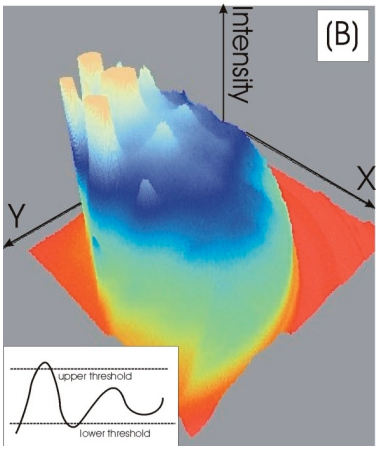

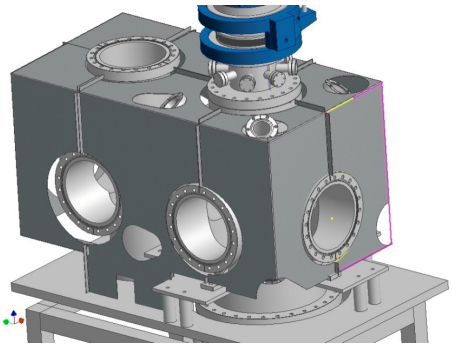

Figure 5. *Chamber cover for the outheating (above).*

Figure 6. *The RHEED evaluation (left).*

High sensitivity scanning probe capacitance sensing

L. Dózsa, G. Molnár, and Š. Lányi,

Introduction: DLTS using a special preamplifier measured with a scanned sharp tip and over a semiconductor surface was proved to be sensitive enough to detect point defects. C-V and I-V measurements of the scanning tip over a clean silicon surface were carried out under different conditions to better understand the effects of the different parameters on the local C-V and I-V measurements.

Experimental setup: The employed Deep-Level Transient Spectrometer contains a sensitive capacitance meter working at 1 MHz using a 0.1V measuring signal. A preamplifier with a gain 50 at 1 MHz increases the capacitance resolution to 1 aF (10^{-18}F) and its dc gain (1000) increases the dc current resolution to 1 pA. An 80 μm thick tungsten wire was sharpened in KOH solution to 50 nm radius and is fixed in a 110 μm internal diameter by friction. Coarse approach of the tip is made manually using a microscope. The fine positioning of the tip was tuned by observing and setting the tunnelling current measured at +2 V bias.

Results: C-V and I-V measurements carried out on Si wafers with 10^{16} cm^{-3} n-type dopant level are shown in Fig. 1. The scans are made starting at -5 V. The curves resemble a quasi-static C-V MOS with high density of interface states. Similar C-V curves were observed when dc current was below 10 pA at +2V bias. In this region the I-V characteristics are symmetric. These type measurements can be used for testing the surface potential and density of interface states, for example distinguishing different phases (insulator, metallic, semiconductor), but not for characterization of semiconductor electric transport properties or defects in the semiconductor below the tip . Fig. 2 shows typical C-V curves measured with smaller tip/surface distance. Such curves are typical when the forward current at +2 V is above 10 pA but below 500 pA. The C-V and I-V curves are Schottky barrier-like, with rectification character. The capacitance at positive bias tends to be in accumulation, the capacitance is limited by the air gap. This region is appropriate for the regular I-V and C-V characterization, since the current flowing through the semiconductor locally changes the charge distribution in the semiconductor near the tip. When the tip current exceeds about 500 pA the tip-silicon junctions degrades in a short time, the current becomes noisy, and I-V and C-V curves are not repeatable. This region is not useful for characterization. Measurements following prolonged biasing strongly changed the interface states at the surface of the silicon or the tip as it is shown in Fig. 3, after applying different bias' for 1 minute. The accumulation capacitance is strongly affected, surface charge changes.

Fig. 4 shows that the structure is sensitive to atmosphere. The interface states of the sample were strongly changed when the chamber is filled with air.

At negative bias inversion develops at the surface, which reduces the width of the depletion layer. This is demonstrated by the observed effect of light shown in Fig. 5. White light enhances the generation of electron-hole pairs thus developing inversion layer. In planar MOS capacitors in inversion the capacitance approaches at low

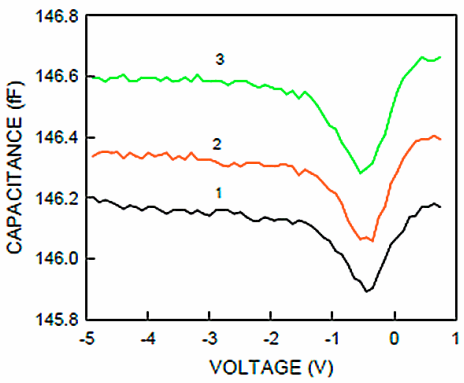

Figure 1. *MOS-type C-V curves measured when tunneling current at +2V is below 10 pA. The tip/surface distance decreases from 1 to 3.*

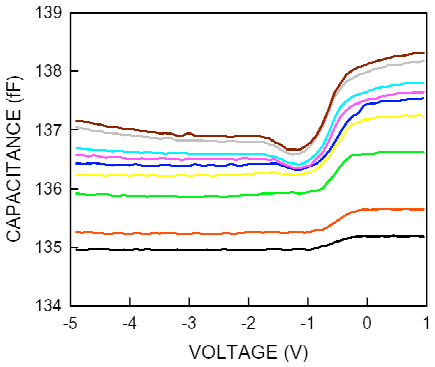

Figure 2. *C-V curves with decreasing tip/surface distance when at +2V the tunneling current is below 500 pA, and rectifying I-V characteristics are measured.*

frequencies a constant value, essentially equal to the accumulation capacitance. A high quality oxide would passivate most interface states. In a measurement on free surface the defect states at the semiconductor/insulator, their density may be very high. Some of them are related to the humidity, explaining the differences found in air and vacuum (Fig. 4). The disappearing of accumulation capacitance after biasing the sample by negative voltage can be explained by flat band shift, caused by charge trapped in surface states. This type of measurements offers a unique possibility to analyse the local density of surface states and defects in the semiconductor.

In most cases the capacitance modulation was rather small, indicating the magnitude of the stray capacitance. With the present probe, depending on actual protrusion of the tungsten wire from its holder, it was 136 to 146 fF. The changes indicate that capacitance measurement is not a secure way to position of the probe. Monitoring the tunnelling current was found to be more reliable, however, insulating island or particles on the surface may also lead to damage of the tip.

Conclusions: The capacitance and current measurement sensitivity of DLTS instrument has been increased using a preamplifier. Fine positioning the tip with a piezo scanner local C-V and dc I-V measurements could be carried out using a sharp tungsten tip at room temperature. The sensitivity is high enough to measured effects of a single elementary charge trapped on the surface, so the measured 'large signal' may be related to a few atomic interactions. Depending on the tip/surface separation 3 type of measurements may be worth to developed on the base of the setup, depending on possible budget and other strategic goals:

- At low tunnelling current (in our setup below 10 pA) the C-V shows a MOS characteristics. The current in forward and reverse bias is nearly symmetric, i.e. the current flowing through the tip does not significantly change the density of states in the semiconductor. This type of measurement can distinguish different surface phases (insulators, semiconductors with possibility to measure their gap, metals).

- At tunnelling currents exceeding 10 pA but below 500 nA the characteristics are similar to a Schottky junctions. The measured capacitance depends on the history of applied voltage, induced by atoms trapped on the surface. Scanning tip electrical characterisation of the semiconductor is viable in this case, however, it is very sensitive to the surface cleanness. Presently the change of temperature is not possible since it makes the control of the tip-surface distance very difficult, due to thermal expansion and to mechanical stress.
- The I-V and C-V characteristics are not stable when the current at + 2V bias is above 500 pA, the tip-semiconductor interface it is visible degraded. This type of measurements may be interesting for understanding the interaction of the tip-surface, since the industrial standard scanning tip measurements often use this bias region without control in order to reach high sensitivity.

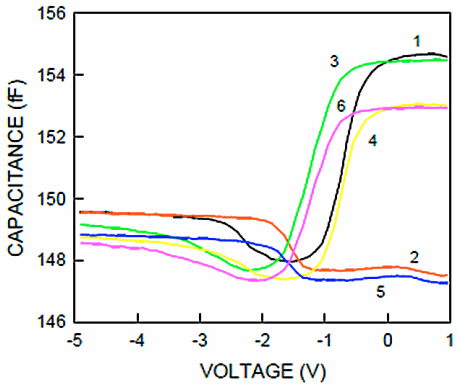

Figure 3. *C-V curves measured after holding the tip bias for 1 min at: (1) 0 V, (2) –2 V, (3) +1 V, (4) 0 V, (5) -2 V, (6) +1 V.*

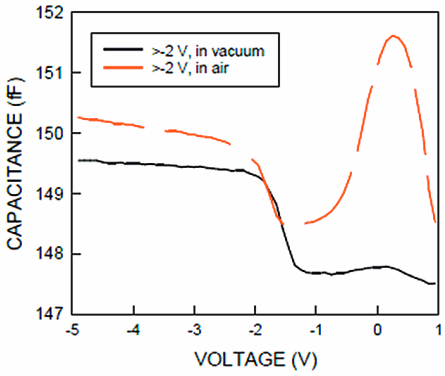

Figure 4. *C-V measurement after -2 V bias of tip for 1 minute in vacuum (black) and in air (red/dashed).*

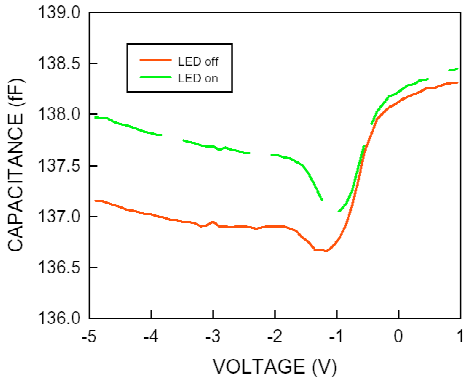

Figure 5. *The effect of illumination by white LED. The light increases the inversion (generation of minority carriers) near the tip.*

Integrated solid-state nanopores for biochemical sensing applications

(ENIAC JU CAJAL4EU, OTKA NF69262)

R. E. Gyurcsányi, Z. Fekete, A. L. Tóth, L. Illés, and P. Fürjes

The micro and nanotechnology based biosensing principles enable the development and realisation robust, user-friendly and cost-effective in-vitro diagnostic platforms. Furthermore, label-free and multi-analyte detection is envisioned to allow more accuracy and mass parallelism in clinical diagnostic. The final goal of this work is to develop nanopore based multi-parametric biosensing platform, applicable for label-free detection of blood marker proteins of cardiovascular symptoms, taking advantage of the built-in transport-modulation-based amplification mechanism.

Here we are presenting a line of nanopore based sensor development, including methodologies for fabrication and functional characterization of single channel solid state nanopores with diameters ranging from 5 to 100nm, their chemical modification and application for bio(chemical) sensing. Solid state single nanopores were fabricated by the combination of silicon micromachining and subsequent Focused Ion Beam nanofabrication processes considering the chemical, electrical and mechanical requirements.

The mechanical layer structures were realized by wet alkaline or double step Deep Reaction Ion Etching process respectively demonstrated in Figs. 1(a) and 1(b). Considering the nanopore based electrochemical metrology described high electrical and chemical resistance of the mechanical layers are crucial requirements. To ensure enhanced both chemical and electrical resistance and low residual stress a SiO_2 / SiN_x stacked supporting membrane with adequate layer thickness ratio was realized.

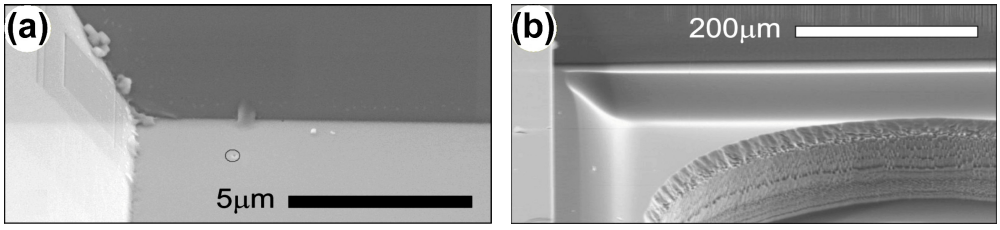

Figure 1. *Layer structures realized by wet alkaline etching (a) and double-step DRIE process (b).*

According to the biochemical application the structure of the realized nanopore transducers is absolutely critical regarding the possible receptor immobilization techniques. To discover and verify the adequate deposition chemistries different material structures were designed and fabricated. The supporting membrane material composition was already chosen to ensure low stress mechanical structures, but the functional layer of the nanopore was altered as Fig. 2 represents.

- Gold nanopores for thiol chemistry: in this case the nanopores were drilled in the vacuum evaporated Gold layer, which enable to apply thiol chemistry for the receptor immobilisation. (a)
- Silicon-Nitride nanopores for fluoro-alkil passivation tests: surfaces were passivated by fluoro-alkil chemistry (CEA-LETI) and the nanopores were drilled subsequently in the Silicon-Nitride (b)
- Poly-Silicon nanopores for electrografting tests: the nanopores were drilled in Poly-Silicon layer and the immobilisation were proceed by electrografting (c)
- Silicon-Dioxide nanopores for silanisation chemistry: the nanopores were drilled in Silicon-Nitride layer passivated by Gold, and shrinked by EBAD (electron-beam assisted deposition) grown TEOS Silicon-Dioxide. (d)

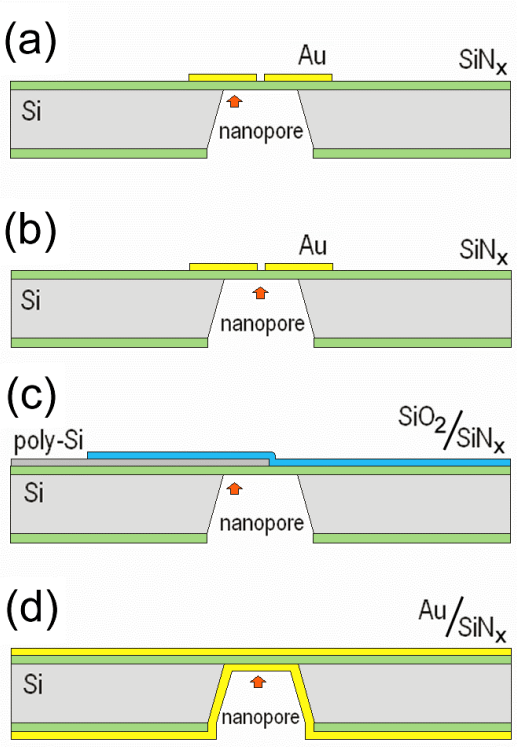

Figure 2. *Designed and fabricated nanopore structures for different immobilisation chemistries.*

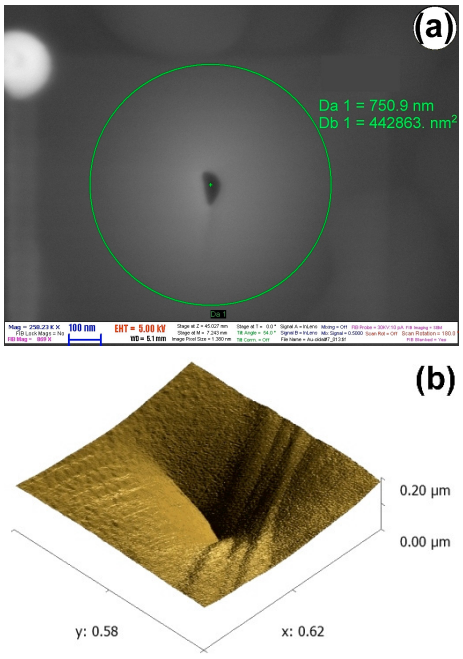

Figure 3. *Solid-state single nanopore fabricated by Focused Ion Beam drilling and subsequent selective electron-beam induced oxide deposition from TEOS gas: SEM image (a), AFM profile (b).*

The wafer level fabrication of the sensor unit is also described, considering the integrability of the silicon based solid state device consisting 3D fluidic connections, microfluidic system and nanoscale sensing transducers too. The schematic representation of the 3D microfluidic system and its assembling on the microfluidic flow-cell is shown in Fig. 4. The vertical fluidic connects ensure the addressing of the two sides of the nanopore membrane electrically through electrolyte solution and the injection of the sample analyte too.

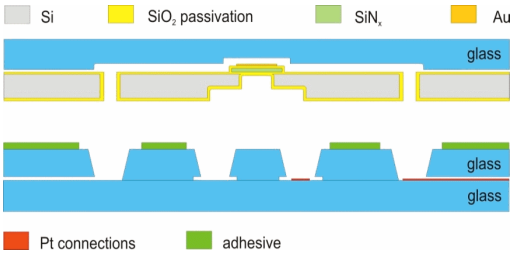

Figure 4. *Schematic cross-sectional and back side view of the proposed nanopore membrane structure integrable into the transport microfluidic system.*

The realized silicon structure was anodically bonded to the glass microfluidics in wafer level applying adequate working parameters (temperature, chamber pressure) limited by the integrated materials (gold) and thin layer structure. The solid state nanopores were fabricated by Focused Ion Beam milling subsequently in chip level and the final stacked structure was bonded onto fluidic connection platform designed and realized by the Micronit Microfluidics BV. This flow-cell is equipped with platinum electrodes, so the glass flow-cell and the silicon/glass sensor system are forming the sample loading and read-out system cooperatively, containing the fluidic and electrical addressing lines. The achieved structures are presented in Fig. 5.

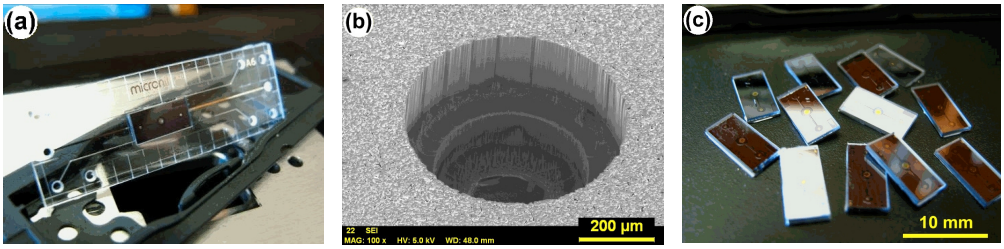

Figure 5*. The back side fluidic connections (a) of the bonded silicon-glass chips (b), and the glass microfluidic flow-cell (c) with the mounted nanopore platform.*

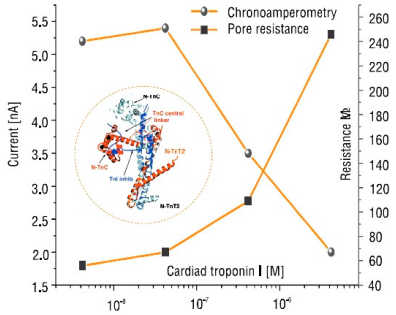

Figure 6*. Sensor response for Cardiac Troponin-I applying artificial aptamer receptors.*

To apply nanopores as selective detectors their inner surfaces must be chemically modified by specific receptors. Aspects of thiol (dithiolan disulfide) chemistries for building up self-assembled molecular architectures with molecular recognition capabilities are discussed in case of the gold nanopores. The applicability of the solid state nanopores for biochemical sensing was modeled and verified by coupling Gold-Streptavidin nanoparticle conjugates on the biotinated nanopores and by detection of the cardiac Troponin-I as the biomarker of the Cardio-Vascular Diseases applying artificial aptamer receptors (Fig. 6).

Separation of biological samples in microscale

(ENIAC JU CAJAL4EU, OTKA NF69262)

Z. Fekete, G. Huszka, F. Tolner, and P. Fürjes

Significant number of the clinical test is aimed to quantitatively or qualitatively analyse the presence of proteins, ions, crystalloids or diluted gases in human blood. In this case, the presence of blood cells in the sample could be a serious drawback, so the first stage of the tests must be the separation of plasma or serum from the whole blood in order to provide adequate sensitivity of measurements.
When aiming a complete microfluidic analysis system for human blood tests the blood plasma separation should be preferably also integrated in the device, so in this work the performance of microfluidic test structures utilizing the Zweifach-Fung effect in terms of two performance metrics: separation (SE) and purity efficiency (PE). These terms are defined as follows.

$SE = \frac{V_{plasma}}{V_{plasma} + V_{cell}}$ where V_{plasma} is the volume of sample liquid flowing through the plasma branch of a bifurcation, and V_{cell} represents the collected sample from the main channel.

$PE = 1 - \frac{C_{plasma}}{C_{in}}$ where C_{in} and C_{plasma} are the concentration of particle in the inlet and plasma branch respectively.
A series of silicon-glass based microfluidic chip was designed and fabricated by conventional MEMS technology. The influence of geometric parameters of several bifurcation arrangements was quantitatively analyzed under different flow conditions. Finite element modelling of the fluid flow in the vicinity of the bifurcations is also implemented to help the understanding of the experimental results. Our work contributes to optimal geometric design of separation components of microfluidic based diagnostic chips.

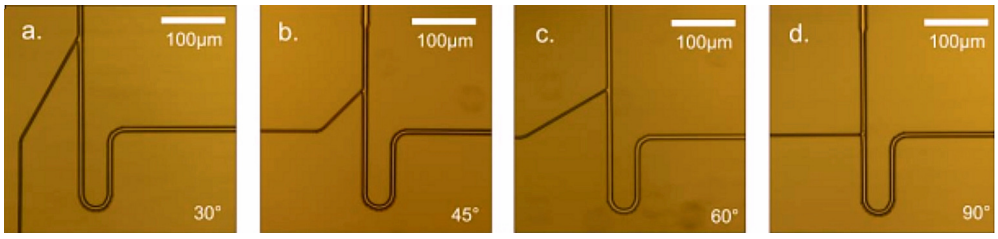

Figure 1. *Filtering test structures with different bifurcation angles: 30° (a), 45° (b), 60° (c), and 90°(d), fabricated in silicon. The input stream is to be considered from the top in each microscopic view of the bifurcations.*

The microfluidic channel system and the backside fluidic vias (inlets & outlets) of the separation chip is etched by the Bosch-process of deep reactive ion etching (DRIE). The silicon wafer is anodically bonded to a borosilicate glass substrate, which serves

as a sealing layer on top of the microfluidics. A representative SEM micrograph of a DRIE etched bifurcation and vertical via are illustrated in Fig. 2.

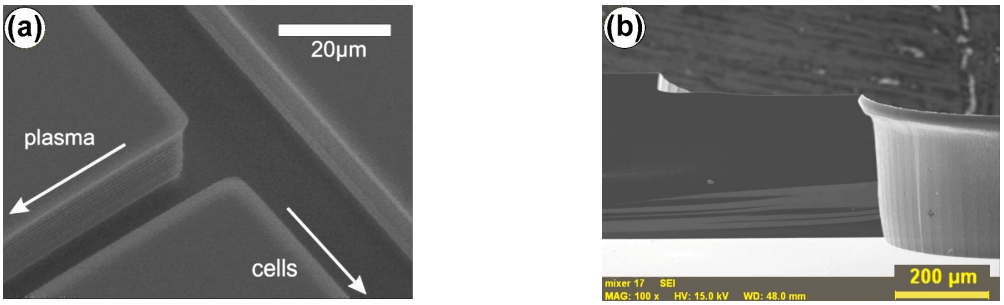

***Figure 2**. SEM view of a bifurcation (a) and the cross-section of the vertical via (b) in silicon fabricated by deep reactive ion etching.*

We found that increasing flow rate ratio between bifurcation branches increase purity, but degrade efficiency of the system, therefore a compromise should be made, when both purity and high throughput are required in clinical applications. The effect is more remarkable, if plasma channels are getting thinner. The angle of bifurcation should be also considered, since at higher inclination angle the purity deteriorates. The proposed results of the characterization support the future design of cascade type separation systems.

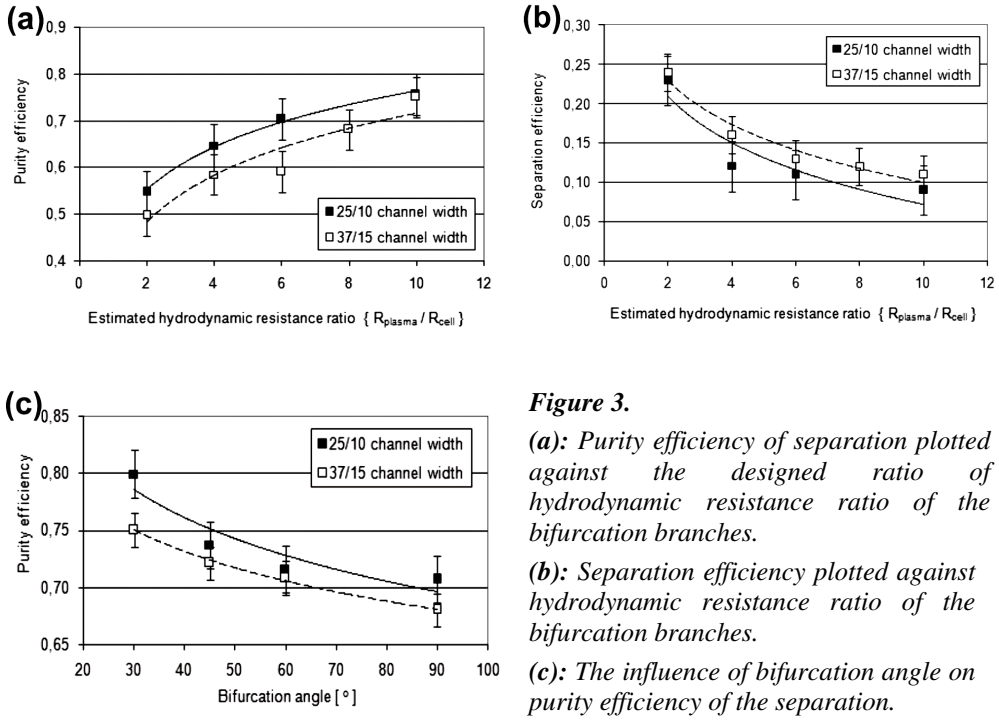

Figure 3.

***(a):** Purity efficiency of separation plotted against the designed ratio of hydrodynamic resistance ratio of the bifurcation branches.*

***(b):** Separation efficiency plotted against hydrodynamic resistance ratio of the bifurcation branches.*

***(c):** The influence of bifurcation angle on purity efficiency of the separation.*

Design and process development of polymer based microfluidics for photonic biosensors

(EU FP7 P3SENS)

Z. Fekete, E. Holczer, and P. Fürjes

In this work, we report advances in the fabrication technology and testing of polymer microfluidics as a part of a polymer biosensor photonic device developed in the European Union project P3SENS (FP7-ICT4-248304). The main target of the development is to design and realize robust microfluidic systems which are applicable for cost-effective sample transport and still can contain some simple sample preparation functions, such as washing, mixing or dilution.

The polymer based microfluidic structure was realised by fast prototyping applying SU-8 epoxy based negative photoresist as moulding replica for polydimethilsiloxane (PDMS) moulding. The PDMS is a silicon based organic polymer: $(H_3C)_3[Si(CH_3)_2O]_nSi(CH_3)_3$ which is absolutely feasible to form microfluidic structures in bioanalytical applications due to its reliable geometric transfer, flexibility, transparency, biocompatibility and price, moreover it is beneficial for both the large scale production and fast prototyping. Disadvantages are the hydrophobic character (adsorption of hydrophobic ligands) and the possible long term degradation.

An improved 3D multilayer formation process was developed in order to achieve reliable SU-8 structuring for the formation of high aspect ratio sidewalls and advanced functional elements of the microfluidic system. Moulding forms developed by multilayered SU-8 photoresist for chaotic mixer structures are presented in Fig. 1.

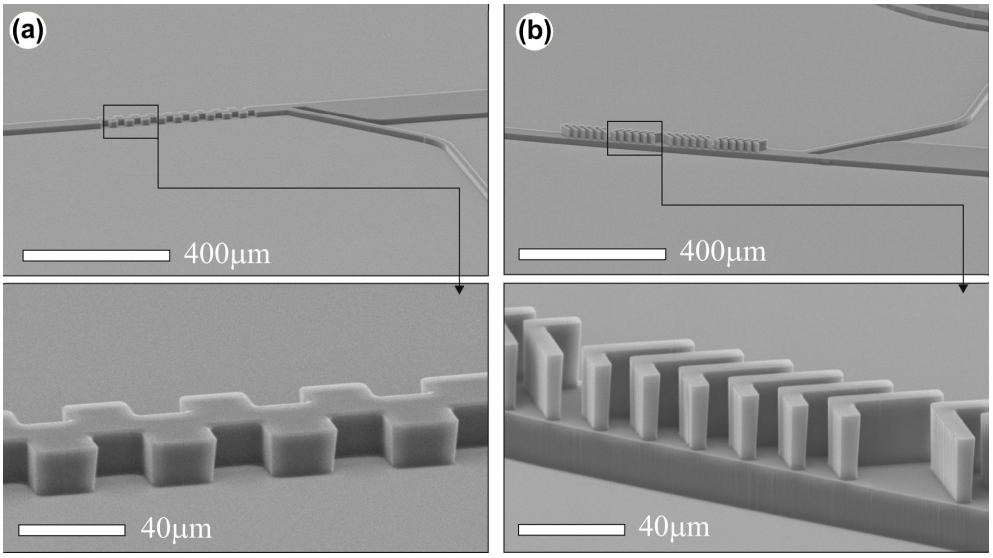

Figure 1. *SU-8 moulding replica for the Staggered blocks (a.) and the Herring-Bone type (a) mixer structure fabricated by 3D multilayer technology.*

Due to the low cost requirements of point-of-care applications, the photonic chip is fabricated from nano-composite polymeric materials, using highly scalable nano-imprint-lithography (NIL). The key issues investigated during the research from the point of the integrability and final applicability of the developed structures are an appropriate polymer material selection, which has a natural impact on the leakage-free bonding between the optical (sensing) and the fluidic (sample transport) part of the device. To obtain a stable and high adhesion between the fluidic and the optical units, several different materials (polyimide, poly(methyl-metacrylate), SU-8) and bonding strategies were qualified. Adequate adhesion were achieved by subsequent silanisation (applying organofunctional alkoxysilanes as (3-aminopropyl)-triethoxysilane – APTES) processes and oxygen plasma treatments applied for the polymer surfaces as illustrated in Fig. 2.

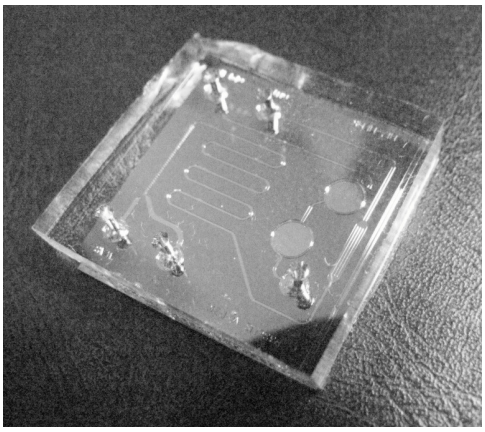

Figure 2. *PDMS microfluidics bonded reliably onto the polymer surface of the photonic chip.*

Surface modification in PDMS based microfluidic devices

(EU FP7 P3SENS)

E. Holczer, Z. Fekete, and P. Fürjes

Notable drawback of the application of PDMS in biosensors is the hydrophobic surface characteristics, significantly affecting the maximal flow rate in the channel system. Moreover, the non-specific binding of proteins or ligands on the channel surfaces is also a critical issue due to the possible depletion of the target molecules during the transport to the active sensing area of the device. Our work is also intended to define a modified material composition, which is appropriate to significantly improve both the wettability and the non-specific binding characteristics of PDMS. TX-100 surfactant was added to the raw PDMS before polymerization and the influence of the tenside was studied considering the polymerization reaction, the surface characteristics and the device functionality also.

A significant change in the contact angle was observed, which is attributable to the embedded TX-100 molecules. The decreasing in contact angles refers to the improvement of the wettability of PDMS surface, facilitating the design of microfluidics featured by enhanced capillarity. The change of the characteristic capillary pressure in these systems indicates a beneficial use in passive microfluidic pumps as well. Figure 1 represents the change of the PDMS surface from hydrophobic to hydrophilic (from positive to negative capillary pressure) in the case of different characteristic channel widths. The height of the microchannel was 20µm, defined by the thickness of SU-8 2015 layer as molding replica.

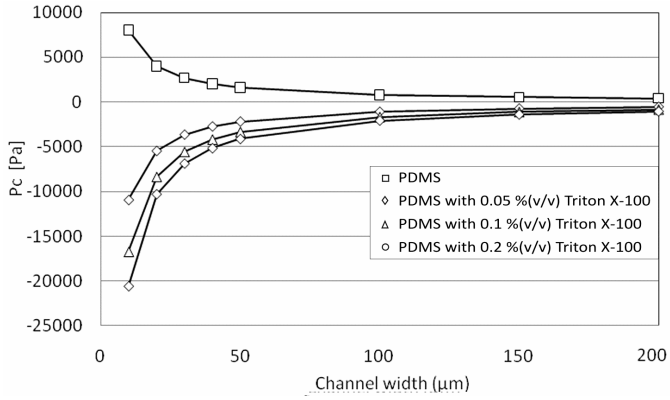

Figure 1. *Representative capillary pressures in the modified PDMS micro-channels calculated from the measured contact angles.*

The non-specific adsorption of proteins on the PDMS surface is crucial regarding the applicability of the microfluidic structure in bioanalytical systems. Accordingly, the binding of proteins to the channel sidewalls was characterized in case of different material compositions. To qualify PDMS from this aspect, surface adsorption of fluorescein-isothiocyanate (FITC) labeled HSA was recorded by measuring the time dependent change of fluorescent intensity detected in the microchannel by using a fluorescent microscope. Various compositions of PDMS and alternative surface blocking method were also tested. In Figure 2, the irreversible protein adsorption on different PDMS surfaces was characterized by recording the relative fluorescent intensity of the applied HSA. The recorded relative values were determined as intensity increments compared to the natural intensity of the HSA solution. Fluorescent intensity of 100% was detected, when PDMS surface was blocked by bovine serum albumin (BSA). The resident intensity after washing proves that irreversible HSA adsorption on the PDMS surface can be decreased by embedding TX-100 in the material.

We can conclude that non-specific protein adsorption can be decreased by almost 100% by this surface modification method parallel with the improvement of the capillary characteristics of the microfluidic system, although the application of additional surface blocking protocols is advantageous in sensitive bioanalytical measurements alike.

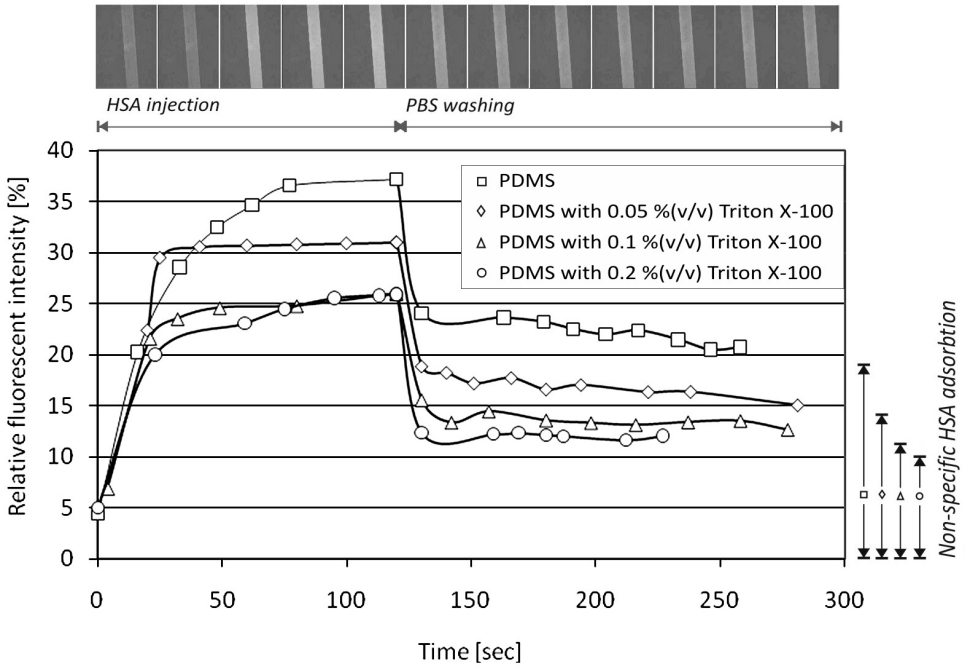

***Figure 2**. Adsorption of the fluorescent labelled HSA protein on different PDMS surfaces characterised by time dependent fluorescent intensity.*

Chaotic mixing in polymer based microfluidics for bioanalytical system

(EU FP7 P3SENS)

Z. Fekete, E. Holczer, E. Tóth, K. Iván, and P. Fürjes

Integrated microfluidic elements are essential components of all lab-on-a-chip devices. One of the important functions of the microfluidic system integrable into bioanalytical devices is the dilution and complete mixing of the analyte with an adequate buffer solution to ensure homogeneous concentration distribution of the species reaching the sensing area. The chaotic advection can be considered an ideal mixing method in the case of microfluidics where flows are stable and laminar.

Advection is the transport phenomenon generated by the fluid flow, where simple flows can cause a nonlinear or even chaotic distribution of molecules. The term chaotic advection refers to a transport phenomenon where advection, i.e. species transport is generated by the fluid flow in such a way that simple laminar flow velocity distribution leads to a chaotic behaviour of particle distribution without the need for turbulence.

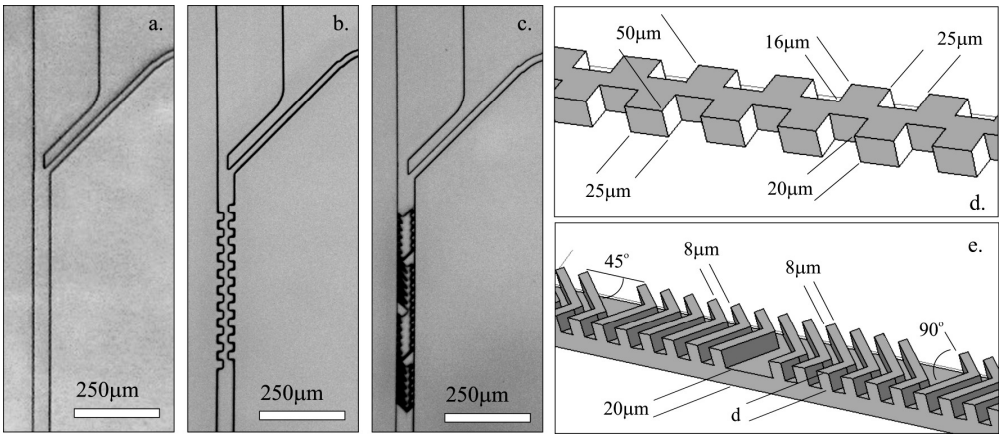

***Figure 1**. Realized mixer structures: T-mixer (a), T-mixer staggered blocks (b), Herring-Bone type (c) chaotic mixers. Applied geometric parameters for the modeling/design (d-e).*

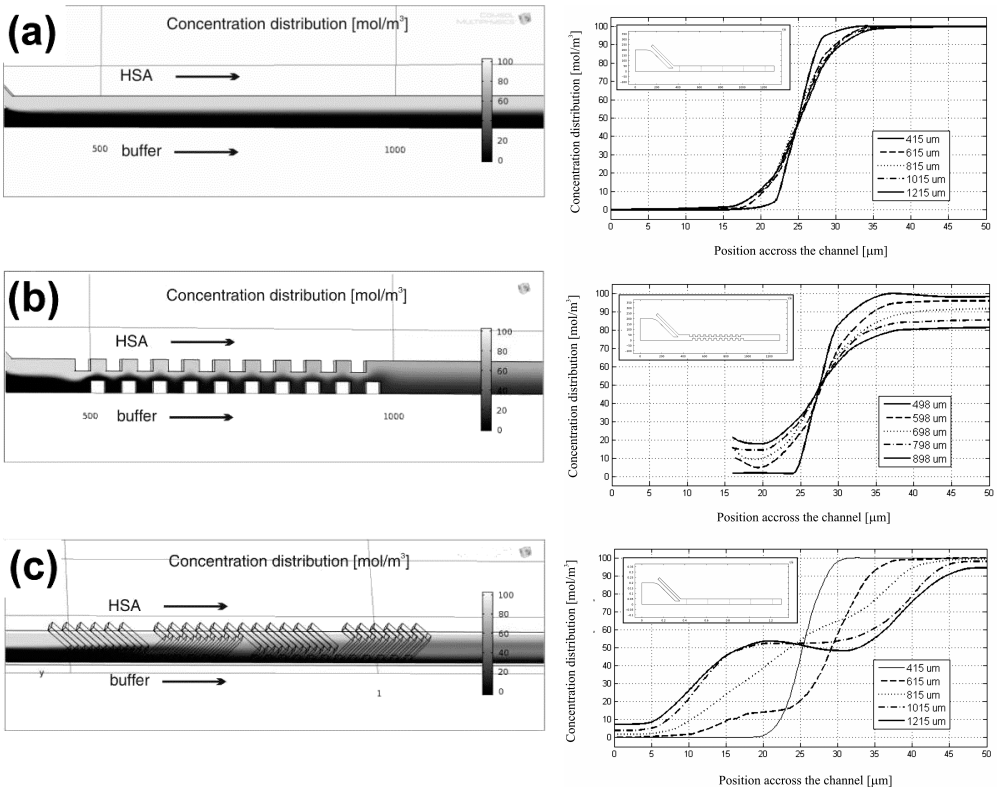

***Figure 2.** Concentration distributions of the analyte in the centreline of different surface slides (distances from the inlet indicated) of the mixer structures. (a): T-mixer, (b): T-mixer staggered blocks, (c): Herring-bone mixer. (On the left a qualitative view of simulated mixing is presented, while on the right the quantitative results are shown.)*

The behavior of different chaotic mixer structures was analyzed by numerical modeling and experimentally to determine their practical efficiency. T-mixer staggered blocks (Fig. 1.b.) and Herring-Bone type (Fig. 1.c.) chaotic mixer structures realized by polymer fabrication technology were characterized by comparing them to a simple T-mixer as reference (Fig. 1.a.).
The fluidic behavior of these three different mixer structures was analyzed by Finite Element Modeling using COMSOL Multiphysics solving the Navier-Stokes and the diffusion equations. Initial boundary conditions were set to 0,1mM/mL concentration of human serum albumin solution and 2 µL/min flow rate in each model. The calculated concentration distributions are presented in Fig. 2.

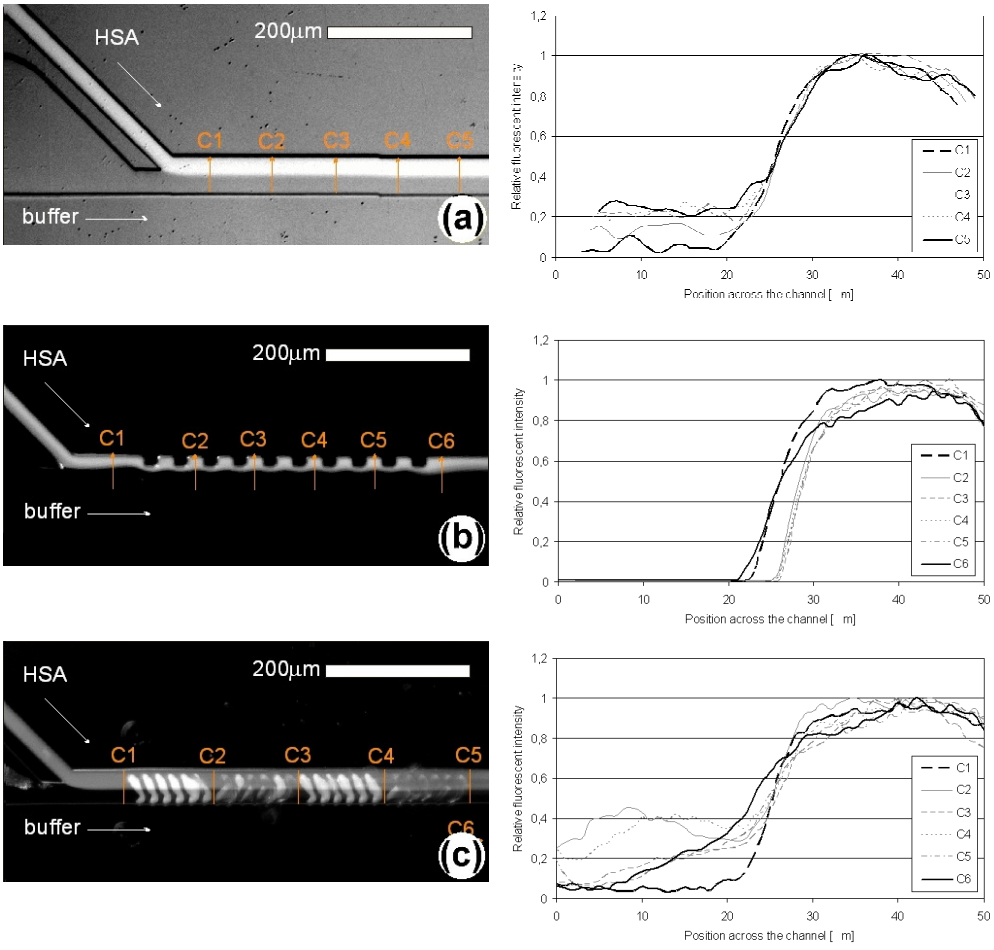

Figure 3. *Concentration distributions of the analyte characterised by the fluorescent intensity in the centreline of different surface slides (distances from the inlet indicated) of the mixer structures. (a): T-mixer, (b): T-mixer staggered blocks, (c): Herring-Bone type mixer.*

To create microfluidic structures in polydimethilsiloxane (PDMS), SU-8 epoxy based negative photoresist was used as a replica mould developed by a special multilayer technology (presented before) characterized by a channel width of 50µm and a depth of 20µm. The fluidic channels with the reservoirs and the Herring-Bone mixer structure were formed by different SU-8 layers. The simulation results were verified by diluting fluorescent labeled human serum albumin (HSA) in phosphate buffered salt solution as presented in Figure 3. The channel surfaces were blocked by bovine serum albumin against the non-specific binding of the test proteins.
In the applied intermediate Reynolds number regime the characterized Herring-Bone type mixer shows the highest mixing efficiency in contrast with the staggered blocks mixer and the T-mixer applied as references. According to the results, the most promising mixer structures are the Herring-Bone type structures, although their mixing efficiencies are significantly influenced by the number of the V-groove blocks, due to the asymmetry of the proposed structure.

Design and characterisation of digital microfluidic chips

T. Pardy, Z. Fekete, and P. Fürjes

Compared to analogous microfluidics, digital microfluidics can operate with smaller – droplet-based - sample volume, while the functionality is programmable, since each elementary cell of the device is independently addressable. This flexibility offers large integrity in a bioanalytical chip involving sample preparation, transport and evaluation.

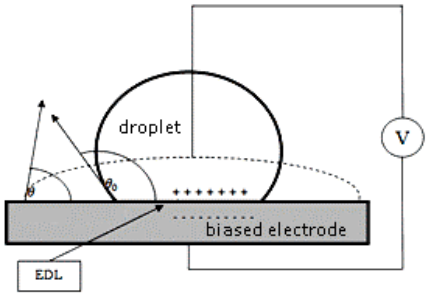

Figure 1. *Principle of electrowetting. Changing the electric field on the boundary surface modifies the energy equilibrium, and the droplet turns from hydrophobic to hydrophilic state.*

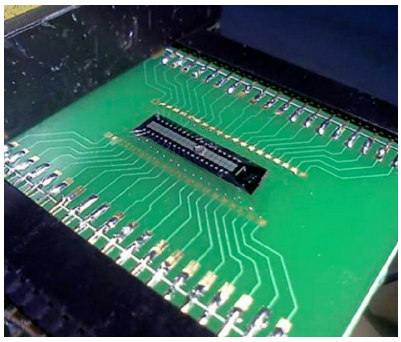

Figure 2. *Experimental setup containing Si-based EWOD chip with linear layout mounted on a Printed Circuit Board providing the excitation to the cells.*

Our group focuses on the optimization of electrode design using several test devices fabricated by standard MEMS technology. In cooperation with the Pázmány Péter Catholic University, motion frequency at several excitations is being analyzed both in linear and some complicated EWOD (Electro-wetting-on-dielectrics) chip layout, providing the separation and the mixing of functions, as necessary.

Thin Film Physics Department

Head: János L. LÁBÁR, D.Sc., scientific advisor

Research Staff

- György SÁFRÁN, C.Sc., Deputy Head of Department
- Árpád BARNA, D.Sc., Emeritus
- Péter B. BARNA, D.Sc., Emeritus
- György GERGELY, D.Sc., Emeritus
- Miklós MENYHÁRD, D.Sc
- Béla PÉCZ, D.Sc, Deputy Director
- Görgy RADNÓCZI, D.Sc
- Katalin BALÁZSI, Ph.D. (partly on leave)
- Zsolt CIGÁNY, Ph.D.
- László DOBOS, Ph.D.
- Olga GESZTI, M.Sc. (part time)
- Sándor GURBÁN, M.Sc.
- Viktória KOVÁCSNÉ KIS, Ph.D.
- Fanni MISJÁK, Ph.D.
- György Zoltán RADNÓCZI, Ph.D.
- Attila SULYOK, Ph.D.
- Péter SÜLE, Ph.D.
- Lajos TÓTH, C.Sc.

Ph.D. students / Diploma workers

- Zsolt FOGARASSY, Ph.D. student
- Ákos Koppány KISS, Ph.D. student
- László KÓTIS, Ph.D. student
- Marianna SZERENCSI, Ph.D. student (part time)
- Lajos SZÉKELY, Ph.D. student
- János SZÍVÓS, Ph.D. stud. (part t.)
- Mohamed FATHY, Ph.D. student
- Eszter BOKÁNYI, diploma worker
- Tamás KOLONITS, diploma worker
- Klára NAGY, diploma worker
- Ákos VALENTINI, diploma worker

Technical Staff

- Sándor CSEPREGHY, part ime engineer
- Ferenc GLÁZERNÉ, part time lab . assistant
- Andrea FENYVESI-JAKAB, engineer
- Valéria OSVÁTH, engineer
- Andor KOVÁCS, engineer
- István KOVÁCS, engineer
- László PUSKÁS, part time technician

The Thin Film Physics Department has continued research on thin film phenomena for half a century. That research has included construction of models for phenomena of structure formation and their experimental verification, together with developing both methods and instrumentation for those experiments and it is continued in the activity of 2011.

Basic research was continued on a few model systems in 2011. Influence of Oxygen on the development of texture was studied in TiN thin films. Alternative ways of phase separation (kinetic segregation vs. spinodal decomposition) were investigated in Cu-Mn and Cu-Ag thin films. A method was developed for geometrical characterization of grain boundaries and applied to Si thin films.

Practical application of scientific results was targeted in 3 European projects, 4 National projects, several scientific cooperations and 2 industrial contracts. Members of the Department won 4 new Bolyai scholarships, 2 new OTKA projects and obtained 1 new patent.
The Department produced 39 referenced publications (cumulative impact factor 75.957) and received 545+ independent citations for their previous publications in 2011. Twelve additional scientific papers are already accepted for publication in 2012 (6 of them is already available on-line).
Béla Pécz received the very prestigious Prize of the Hungarian Academy of Sciences. Zsolt Czigány obtained the Outstanding Paper Award of European Microscopy Society, the Schmid Rezső Prize (ELFT) and the Pócza Jenő Prize of the Hungarian Microscopy Foundation. Four members are founding members of PhD Schools and the Department gave the President of the Hungarian Microscopy Society, the Vice President of the European Microbeam Analysis Society and two (out of 200) D.Sc. Representatives at the General Assembly of the Hungarian Academy of Sciences, furthermore a member of the Board of Trustees of the Mathematics and Natural Science Section of the Academy, four members of the Solid State Physics Committee of the Academy and the secretaries of two working groups of the Academy. One member of the Board of Trustees of the Hungarian Science Foundation (OTKA) is also from the Department.
Scientists from the Department edited an IOP volume, acted as members of the Editorial Board for 4 scientific journals and organized 5 international and 4 Hungarian conferences. Six invited talks, 28 oral presentations and 18 poster presentations were given at scientific conferences.

Nucleation and competitive growth of fcc-TiN and hcp-AlN phases in the first growth stages of $Ti_{1-x}Al_xN$ thin films prepared by magnetron sputtering

(Cooperative research with Department of Physical Metallurgy and Materials Testing, Montanuversität Leoben, Leoben, Austria*)

L. Székely, G. Sáfrán, M. Moser*, P.H. Mayrhofer* and P.B. Barna

The $Ti_{1-x}Al_xN$ coatings are widely used in industrial applications due to their superior mechanical and chemical properties. The effect of Al content on the structure have been investigated and published in our earlier paper [M. Moser, P. H. Mayrhofer, L. Székely, G. Sáfrán, and P. B. Barna: Surface and Coatings Technology, 2034 (2008) 148-155]. It has been shown that the film of $Ti_{0,41}Al_{0,57}Y_{0,02}N$ composition exhibit one axis <111> texture and a new, unusual columnar structure. The V-shaped columns are composed of TiN and AlN nanocrystals with biaxial orientation. The evolution of this peculiar structure has been interpreted by spinodal decomposition taking place in a mother phase of supersaturated solid solution of the two nitrides and the one axis texture of the film is related to the competitive growth of crystals of this

supersaturated phase. The kind of the mother phase (the fcc-TiN or the hcp-AlN) remained however an open question. This has been clarified in the present study by the detailed analysis of the film structure in the thickness range of the first growth stages at the substrate. The film was deposited by DC magnetron sputtering at 550^0C on Si(001) single crystal surface covered by natural oxide. Fig. 1 shows the cross sectional bright field and dark field TEM image of the film and Fig. 2 summarizes the selected area diffraction patterns taken on the plane view specimen containing the thickness domain at the substrate surface (Figs. 2 a, b and c), while Fig. 2 d is the diffraction pattern taken on the upper part of the film. In case of Figs. 2 a and b the film surface normal was tilted by 20^0 to the electron beam, while in case of Figs. 2 c and d it was parallel to the electron beam. Fig. 2 a is the diffraction pattern of the substrate Si crystal and the very first part of the film. That clearly prove that crystals of both phases nucleated with random orientation. SAED pattern of the thicker domain at the substrate (Fig. 2. b) shows that both phases coexist and already textured. In thickness domain farther from the substrate (Fig. 2. c) the dominant phase is the hcp-AlN with 002 texture. In the upper part of the film both phase coexist again and are textured.

This structural information makes possible to propose a model for the development of this peculiar structure. At the very first stage of film growth both phases nucleate on the substrate developing randomly oriented TiN and AlN crystals. Textures start to develop in both phases by competitive growth. However a competition develops also between the two phases and the hcp-AlN phase is overgrowing the fcc-TiN developing narrow columns of AlN crystals. These AlN crystals of the supersaturated hcp-Al(Ti)N phases are growing with orientation competition during the thickness growth of the film. This competition results in the development of the 002 hcp-Al(Ti)N texture with V-shaped columns. This will determine the grain morphology of the film. And, at least, the nanocrystalline structure of coherently oriented hcp-AlN and fcc-TiN crystal domains develops within the columns by spinodal decomposition.

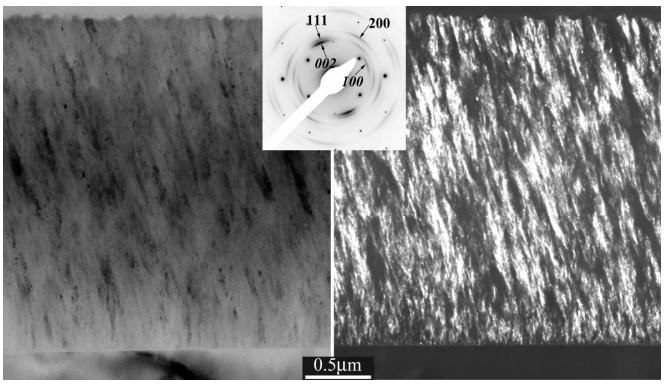

Figure 1. *Cross sectional bright field and dark field images of the $Ti_{0,41}Al_{0,57}Y_{0,02}N$ film illustrating the columnar nanocomposite structure.*

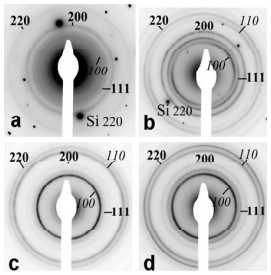

Figure 2. *Selected area diffraction patterns of plane view specimens illustrating the development of textures and competition of phases at the substrate (bold:fcc-TiN; italics:hcp_AlN).*

Cu-Mn and Cu-Ag sputtered alloy films: structure and phase separation

(OTKA K81808)

G. Radnóczi, F. Misják, E. Bokányi, Zs. Czigány, and M. Menyhárd

The scope of this work is to substantially contribute to the basic knowledge of atomic mechanisms and kinetics of self organized nanostructures in order to facilitate their use in technological processes like for advanced semiconductor devices. In this aspect, a detailed investigation of the Cu-Mn and Cu-Ag systems is aimed at the background knowledge for technological developments.

Cu-Mn films were prepared by DC magnetron sputtering onto thin C film as substrates. The basic intention was the detailed understanding of the Cu-Mn phase diagram and the establishment of the relation between composition, structure and morphology of Cu-Mn layers. The thickness of the films was ~50 nm in the composition range of 0-100 at% of Mn. The growth was carried out in the temperature range of 20-600°C. TEM+EDS as well as HREM+EELS were used to determine the morphology and chemical composition.

At room temperature and low Mn contents (below 30 at%) films grow in fcc solid solution phase and the lattice parameter shows a slight deviation from Vegard's low. At higher Mn contents (above 40 at%, Fig. 1) the fcc component is not detectable and the α-Mn structure becomes dominant. The grain size of the films is very small at all compositions and it has a minimum of 1-2 nm around 65 at% Mn content.

By the help of matching of simulated and measured electron diffraction patterns a new, triclinic phase in the Cu-Mn system has been supposed at higher temperatures (above 300°C) in the concentration range of 10-100 at% of Mn. A phase diagram has been proposed for the Cu-Mn thin film system on the basis of measurements (Fig.1).

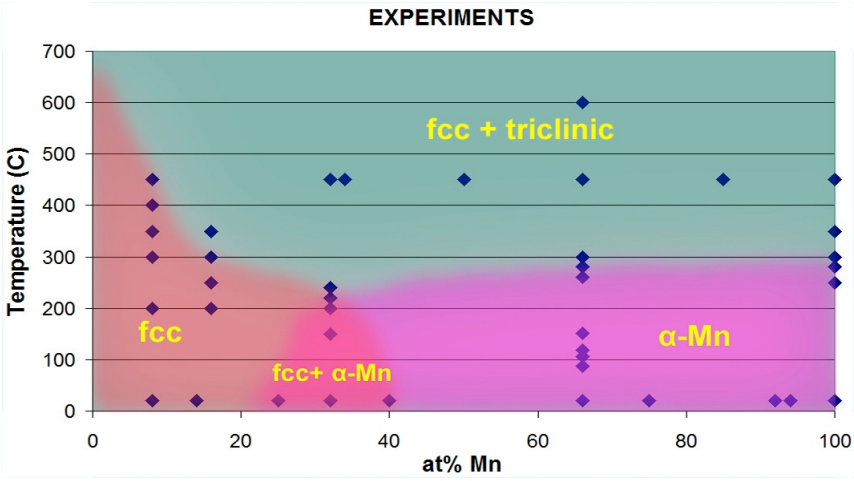

Figure 1. *The measured phase diagram of sputtered Cu-Mn alloy thin films.*

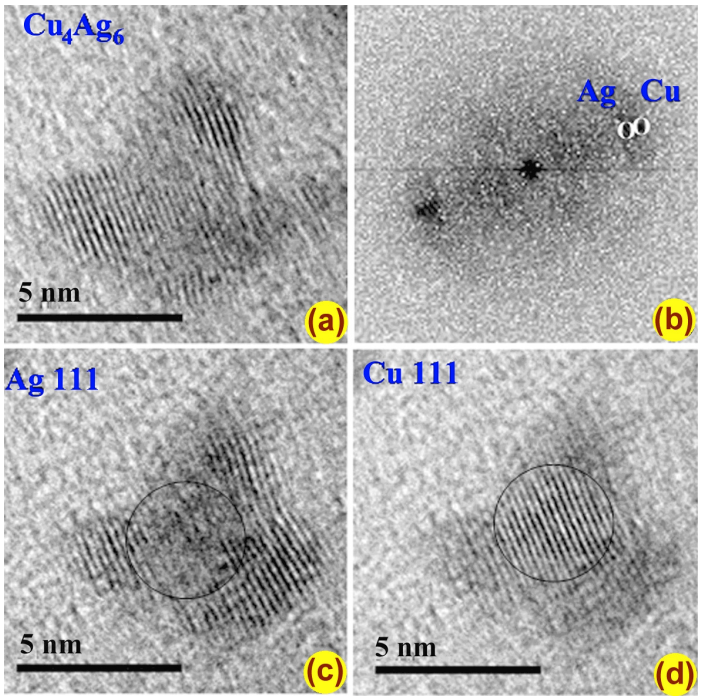

Figure 2. *HREM image (JEOL 3010) of a single crystal, two phase Cu_4Ag_6 alloy particle (a), the Fourier transform of (a) showing two periods in the particle (b), filtered image of Ag domain (c), and filtered image of the Cu domain, (d).*

The phase separation processes in the Cu-Mn system have been modelled by the Cu-Ag system which is much less the subject of oxidation processes. The Cu-Ag films were prepared by DC magnetron sputtering onto thin carbon films. The effective film thickness of 1-2 nm resulted in island film structure of island size between 2-20 nm. HREM measurements revealed that the alloy particles can be single or polycrystalline, in many cases contain twin crystals. Revelation of single crystalline (even defective) alloy particles proves that these crystallites grow in the form of non-equilibrium homogeneous fcc solid solution. This is considered to be the dominating nucleation and growth mode. The as formed particles can undergo spinodal decomposition. The result of this process is shown in Fig. 2. The centre of the selected particle shows the spacing corresponding to Cu(111) while the spacing at the periphery of the crystallite corresponds to Ag(111). The two parts (Ag and Cu) are epitaxial to each other, having a coherent interface. A complete phase separation took place i.e. the measured spacing corresponds to pure components. Monte Carlo simulation of spinodal decomposition in one dimensional system [D. L. Beke, C. Cserháti, Z. Erdélyi, I. A. Szabó: "Segregation in nanostructures", Nanoclusters and Nanocrystals, American Scientific Publishers (2003) Ed. H. S. Nalwa, Vol.1., Ch.7, pp.211-253], corresponding to Cu-Ag has shown that decomposition can be partial or full, and the spinodal wavelength is around 2 nm. This corresponds to our observations, where the size of the Ag and Cu regions could be estimated to be between 1-3 nm (Fig. 2).

Effect of oxygen doping on the evolution of 002 texture and the crossover between 002 and 111 textures in TiN films

(Cooperative research with Sapientia University, Tg-Mures, Romania[1], Bay Zoltán Ltd., Miskolc, Hungary[2], and Eötvös Loránd University, Department of Mineralogy, Budapest[3])

D. Biró[1], M. F. Hassanen, L. Székely, M. Menyhárd, S. Gurbán, P. Pekker[2], I. Dódony[3], and P. B. Barna

The pure and doped TiN coatings are widely used in industrial applications due to their superior physical and chemical properties. Oxygen is used as doping element to improve the properties by developing oxinitride structures. However, oxygen could be also co-deposited as non controlled and non expected contamination during the preparation of the films resulting in the development of peculiar structures unusual in pure TiN films. The most surprising and not yet understood structural peculiarity is the crossover between the first developing 002 and the later appearing 111 textures. At the preparation of oxinitride films it has been found that at oxygen concentrations beyond 15at% the formation of 002 texture is promoted [Chan, M. H. and Lu F. H., Surf. Coat. Technol., 203 (2008) 614], however, the formation mechanisms of this structure were not studied in details. In the present study the effect of the oxygen doping on the structure evolution of TiN films deposited by unbalanced magnetron sputtering on oxidized Si wafers was investigated. The sputter parameters used at the deposition promoted the formation of 111 texture and V-shaped columnar morphology in undoped TiN films [Barna, P. B. and Adamik, M.: Thin Solid Films, 317 (1998) 27]. The films were prepared at 450^0C substrate temperature and $3x10^{-1}$Pa argon-nitrogen atmosphere. The microstructure was investigated by θ-2θ XRD, transmission electron microscopy (TEM) and selected area electron diffraction (SAED), the chemical composition by EDS and XPS applying also depth profiling. The development of the V-shaped columnar morphology and textures by competitive crystal growth was demonstrated at first by PED-ASTAR technique in the TEM.

Results:

The colored PED-ASTAR image in Fig. 1. demonstrates the V-shaped columnar morphology of TiN films doped by 18 at% oxygen. The <002> axis of crystals shown in red is situated in the plane of the image and parallel to the substrate surface normal of the substrate. It is to be seen that the structure evolution starts by nucleation and growth of randomly oriented TiN crystals (marked by different colors) and the crystals with 002 orientation (red) are overgrown the others developing V-shaped columns. The pole figure shown in Fig. 2 taken at the thickness marked by arrows in Fig. 1 demonstrates that beside the <002> crystals still random oriented crystals are also present.

Figs. 3 a and b show the crossover developed between the 002 (red in Fig. 3 b) and 111 (blue in Fig. 3 b) orientations, related to the changes in the level of oxygen doping. Both, the 002 and 111 textures developed by competitive growth. The crossover corresponds to the thickness marked by arrows in Fig. 1, at which one part

of the crystals was still randomly oriented, as shown in Fig. 2. Consequently, crystals with <111> were also present and their growth was promoted at the lower oxygen level, initiating the competitive growth of <002> and <111> oriented crystals, developing the V-shaped columns of the <111> crystals.

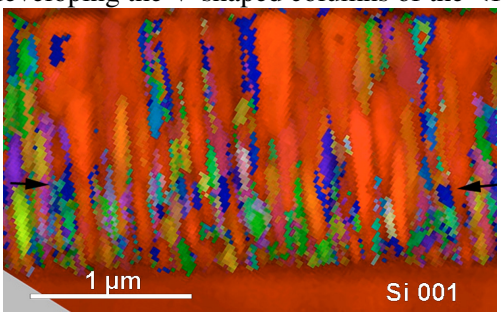

Figure 1. *PED-ASTAR X_TEM image of an oxygen doped TiN film. The oxygen content is 18 at%.*

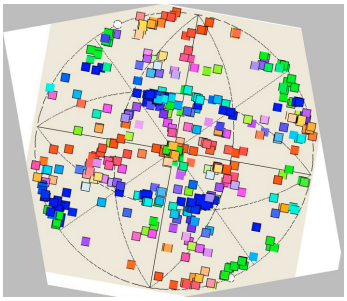

Figure 2. *Pole figure taken from the PED-ASTAR image at the thickness marked by arrows shown in Fig. 1.*

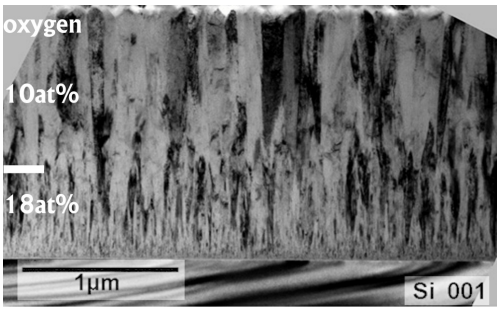

Figure 3 (a). *X-TEM image of TiN film prepared at changing oxygen pressure.*

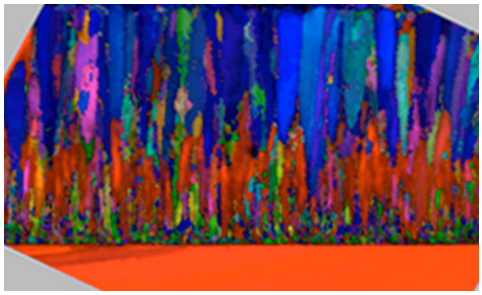

Figure 3 (b). *PED-ASTAR image of the film shown in Fig. 3 a demostrating the crossover of 002 (red) and 111 (blue) textures developed by competitive growth.*

Microscopy of AlN/AlGaN superlattice for the reduction of dislocation density in nitride layers

(OTKA K75735)

B. Pécz (MFA), L. Dobos (MFA), A. V. Tikhonov (Novosibirsk),
T. V.Malin (Novosibirsk), and K. S. Zhuravlev (Novosibirsk)

AlGaN layers have an important application area in the high electron mobility transistors (HEMT). It is essential to control the polarity of the grown layers for any device application. Another critical issue in the dislocation density, what influences the lifetime and efficiency of the electronic device.

We report here on experiments in which the nitride layers were grown by ammonia molecular beam epitaxy (MBE) in Novosibirsk and the grown structures were investigated in details by transmission electron microscopy (TEM) at MFA. An overview of a typical structure grown is shown in Fig. 1.

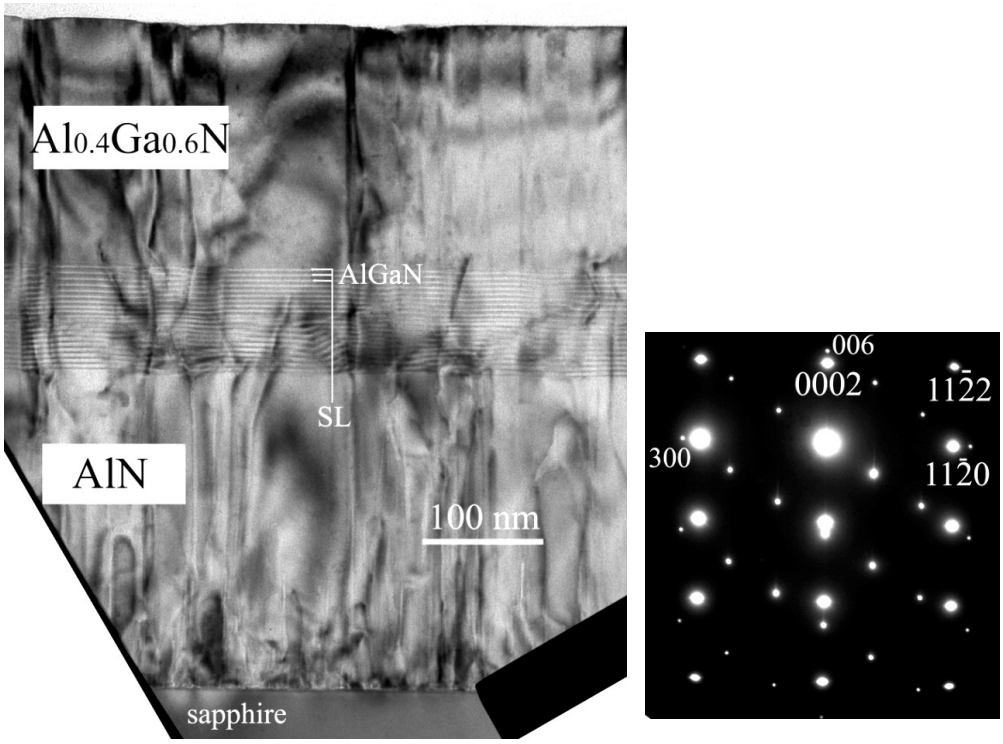

Figure 1. *Cross sectional bright field image (left) and selected area diffraction pattern taken on a layered structure with superlattice of AlGaN/GaN (right).*

The first about 30-40 nm thick region of AlN was grown at 870°C (low temperature, LT), while the thicker region was grown at 950°C (high temperature, HT). The polarity of the grown layers can be intentionally controlled during the LT growth of AlN for example metal polar AlGaN can be received at Al rich growth conditions. Our results [A. V. Tikhonov, T. V. Malin, K. S. Zhuravlev, L. Dobos, B. Pecz: Journal of Crystal Growth, 338 (2012) 30–34] show, that the strain relaxation in the grown layers depends on the polarity as well. There are some dislocation loops observed in the AlN region. There are also some inversion domains, which extend to the surface and reaches that in a small and shallow pit. The annihilation of some of the dislocations by the superlattice is also observed in this sample, which shows metal polarity. This effect is even stronger in samples grown with nitrogen polarity, therefore the dislocation density could be reduced to the middle of the 10^9 dislocation/cm^2 range.

Acknowledgements:
Support of OTKA K75735 and the Hungarian-Russian bilateral project of the Academy of Sciences is aknowledged.

Types of grain boundary planes in thin Si films laser-crystallized from a-Si

Á. K. Kiss (MFA / PE), J. L. Lábár, S. Christiansen (IPHT), and F. Falk (IPHT)

Last year we reported the development of a method that determines the five macroscopic parameter of a grain boundary (GB) by using a transmission electron microscope. In the present paper we present some results obtained by using this method on laser crystallized Si thin films.

Our method determines the misorientation from two convergent beam electron diffraction (CBED) patterns taken on the neighboring grains, and the plane-normal is calculated from bright field (BF) images of the GB. The thickness of the sample is also needed and it is measured from a CBED pattern taken in two-beam condition. The rotation of the electromagnetic lenses is also calibrated including the treatment of the 180° ambiguity, facilitating the transformation of orientations from the CBED pattern to the coordinate system of the BF picture or vice versa.

In the studied Si thin film samples produced by melt mediated crystallization, the majority of the boundaries were $\sum 3$ with low energy density {111} planes. They are generally identified prior to the exact measurements by their appearance as straight lines. We intentionally selected for evaluation other special high-angle boundaries and general boundaries, too, in excess of their statistical occurrence, to see if the two groups of boundary types behave identically or differently in our case of Si thin film crystallization.

We measured 90 GBs, out of which 37 were $\sum 3$ boundaries, 14 GBs were other special high angle boundaries with (near or exactly) $\sum n$ misorientation (n=5,9,19,25,27) and the remaining 39 GBs contained 24 general high angle GBs and 15 low angle boundaries. Although this amount of studied GBs is not so much as it should be to receive any statistically significant result, it seems to be enough to corroborate the assumption that there are two alternative ways of energy minimization in our thin films. In bulk samples the special GBs are generally formed by twin-planes with low energy-density (for $\sum 3$ misorientation coherent twins are formed with {111} planes or incoherent twins with {211} planes, for $\sum 9$ misorientation with {221} or {411} planes, etc.). In samples crystallized as thin films, the alternative way to minimize the energy of the boundary is minimizing the whole area of the GB planes by turning it almost perpendicular to the free surfaces of the sample. We have found that both types of GB-planes are present in our samples and they form disjunct sets.

We found that there is a significant difference between the $\sum 3$ boundaries and all the rest in the way of energy minimization. This can be shown by plotting the number of the GBs against the angle they extend to the sample surface. (*Fig. 1.*)

In the case of $\sum 3$ boundaries (boundaries with exact $\sum 3$ misorientation) the distribution of angles (between the GB-plane and the surface) has a broad rage. 35 out of the thirty seven $\sum 3$ boundaries had {111} coherent twin planes and we only found one $\sum 3$GB with incoherent {211} plane, and one $\sum 3$ boundary with general plane. Figure 1 shows that the twin-planes are oriented randomly from the sample surface.

In the case of all the other boundaries we only found GB-planes with general indices. The special high-angle GBs with other ∑-value did not form twin-planes either. Their angle distribution (from the surface) is definitely narrower than that of the ∑3 boundaries, and this distribution peaks at 90°. The difference in the orientation distributions of the two groups of GB-planes suggests that GBs with misorientation other than the exact ∑3 misorientation, the plane-energy is minimized by minimizing the area, forming a boundary almost perpendicular to the surface of the thin film, while for low energy-density type planes the area of the GB-plane (closely related to the angle extended to the free surface) is not so important. The reader is also reminded that GB-planes with too low angle from the surface can not be measured conveniently in a lateral TEM sample, so they are under represented in Fig.1. The angle distribution for ∑3 twin planes is very broad even without those at low angles.
In conclusion we found that two alternative ways are present to minimize the energy of a GB-plane in thin films. The grains with exact ∑3 misorientation mainly form low energy-density {111}-type planes, similarly to the situation in bulk samples, but the other GBs do not follow the same pattern. Instead, they minimize the area of the GB-plane.

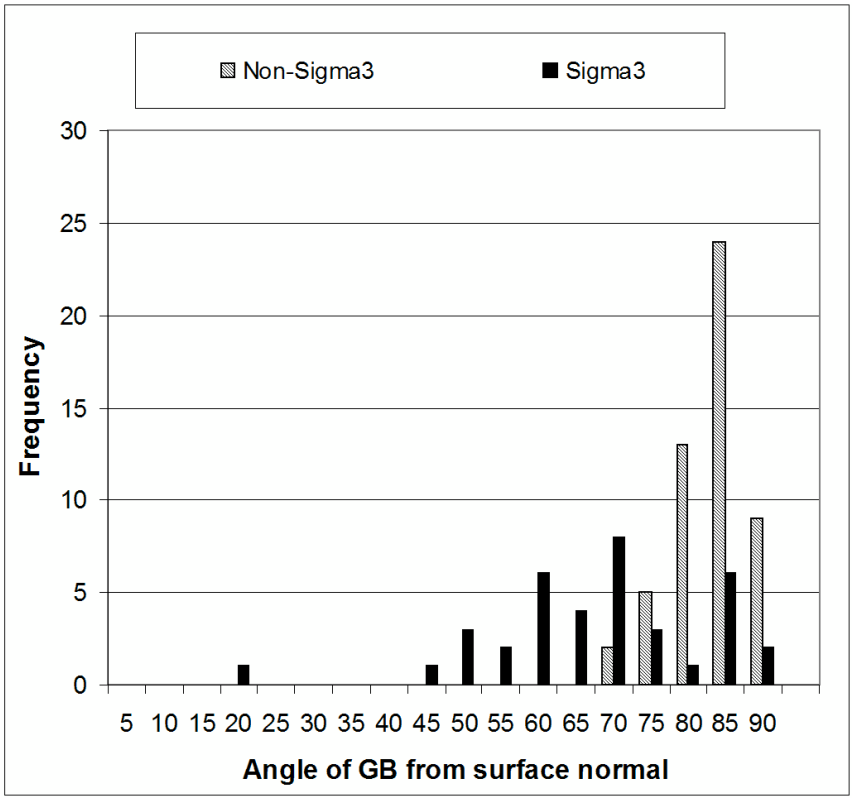

Figure 1. *Distribution of the angles between the GB-planes and the surface of the sample. Area of the GB-plane increases by increasing deviation from 90°.*

Microstructure Formation of Magnetically Annealed Co/Pt $L1_0$ multilayers

G. Sáfrán, A. Markou[1], I. Panagiotopoulos[1], T. Bakas, D. Niarchos[2], Wanfeng Li[3], and G. C. Hadjipanayis[3]

Hard magnetic film applications range from information storage media with the conflicting requirements of high density, thermal stability, and writability, to magnetic microelectro-mechanical systems that need high power at reduced dimensions. These applications favour the $L1_0$ ordered phase of Co/Pt oriented with the magnetic easy axis typically perpendicular to the substrate (001).
The effect of magnetic annealing on the texture was investigated by XRD and TEM in a series of CoPt films of different thickness. This study was carried out in a co-operation with the University of Ioannina, Greece[1], the Institute of Materials Science[2], NCSR "Demokritos", Greece and the University of Delaware, Newark, USA[3]: CoPt films with thickness of 17 nm, 34 nm, and 68 nm were prepared by heat treating Co-Pt multilayer films deposited by magnetron sputtering on oxidized silicon wafers at RT. The samples have been annealed in a magnetic field of 1 kOe in two stages, at 450 ºC for 120 min followed by 750 ºC for 30 min.

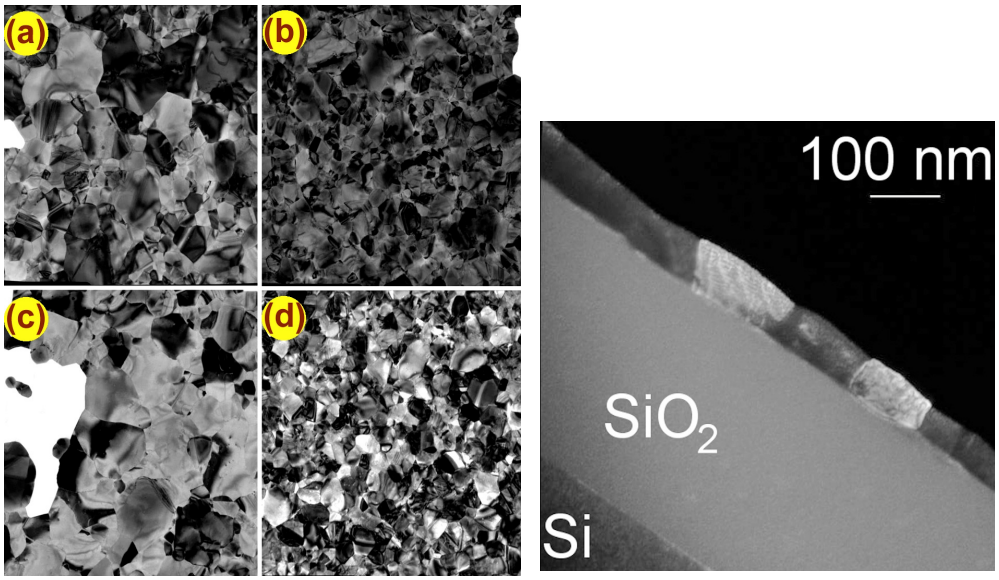

Figure 1. *Plan view TEM image of 17 nm (a), 34 nm (b), and 68 nm (d) Co-Pt films annealed in magnetic field and zero field annealed (c) (left). Cross sectional TEM of the 68 nm thick film (right).*

The field was applied both in-plane (//) and perpendicular to the film plane (⊥). The samples have been also heat-treated in zero field (ZF) for reference. The volume fraction of the various textures was investigated by the analysis of SAED patterns with the Process Diffraction Software developed at our laboratory.

Magnetic field is found to promote the (001) texture by selective (001) grain growth driven by the magnetic field and biaxial strain. A correlation between in plane biaxial strain and the degree of (001) texture is found only for the magnetically annealed samples. The fact that (111) texture appears in thicker films is inconsistent with a surface anisotropy mechanism, which would favour (111) for the thinner ones. Thus, it seems the transformation strain may be the main factor determining texture.

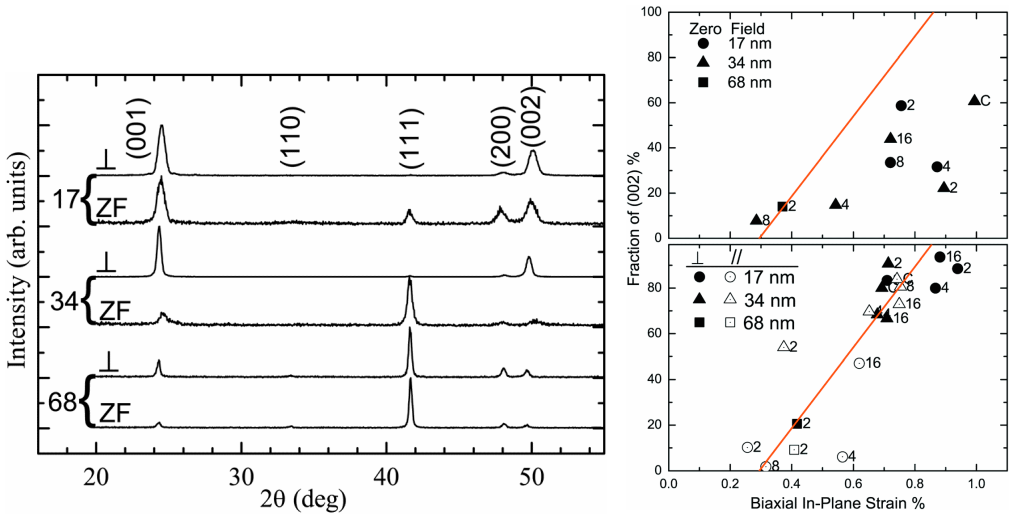

Figure 2. *XRD patterns for the 17 nm, 34 nm, and 68 nm bilayer films annealed under a perpendicular field compared to the those under zero field (left). Fraction of (001) texture as a function of biaxial in-plane strain. Top panel: zero field heat-treated samples. Bottom: films heat-treated under perpendicular and in-plane fields (right).*

A plausible reason is that the $L1_0$ ordering transformation from the fcc A1 structure to a tetragonal one with c< a is consistent with a tensile in-plane strain in crystals with the c-axis perpendicular to the film plane. The occurrence of anisotropic strain due to ordering transformation favours (001) texture. In accordance, (001) texture cannot be obtained for the 68 nm samples, since these films are not sufficiently thin for a plane-stress condition to hold. The (100), (010), and (001) variants of the A1 structure are easily amenable to (001) of $L1_0$. Thus, even an in-plane field can lead finally to an (001) texture. On the other hand, surface energy anisotropy favours (111) growth in the fcc as-deposited state, and the initial (111) seeds cannot recrystallize to (001). In short, the (001) texture proceeds by transformation driven selective grain growth of (001) at the expense of other textures. (Literature: [J. L. Lábár: "Electron Diffraction Based Analysis of Phase Fractions and Texture", Nanocrystalline Thin Films, Part II: Implementation, Microsc. Microanal. 15 (1) (2008), 20-29], [A. Markou, I. Panagiotopoulos, T. Bakas, D. Niarchos, G. Sáfrán Wanfeng Li, and G. C. Hadjipanayis: "Formation of L10 with (001) texture in magnetically annealed Co/Pt multilayers", Journal of Applied Physics, 110, 083903 (2011)])

Thin TaC adlayers produced by ion mixing

A. Barna, L. Kotis, J. L. Lábár, A. Sulyok, M. Menyhárd, G. Sáfrán, A. L. Tóth, L. Illés, A. Kovács, and A. Savenko (UD)

Tantalum carbide (TaC) has favorable properties like high melting point and hardness, good chemical and corrosion resistance, etc. Thus the TaC is a promising material from the point of view of coating of e.g. semiconductor based sensors. To create a thin layer of TaC usually high temperature process is necessary. Previously we have shown that medium energy ion bombardment of C/metal interfaces results in formation of carbide layer with sharp intefaces. Thus, the undesired high temperature step can be circumvented by applying ion bombardment induced layer growth. C/Ta layer systems of various thicknesses were irradiated applying FIB using Ga^+ ions in the energy range of 5- 30 keV. Fig. 1 below shows the structure of the sample (layer structure is C 22 nm/Ta 26 nm/ C22 nm) after a Ga^+ irradiation of 30 keV applying $4*10^{15}$ ions/cm^2 fluence. The black vertical line shows the depth value, where the $TaC_{0.5}$ (stable compound) concentration is reached. It is clear that a well-developed TaC_x layer formed with some Ga contamination. Varying the thickness of the layers and the Ga^+ ion energy various carbide thicknesses could be obtained. Using focused ion beam for irradiation thin carbide layer can be produced according to any desired template.

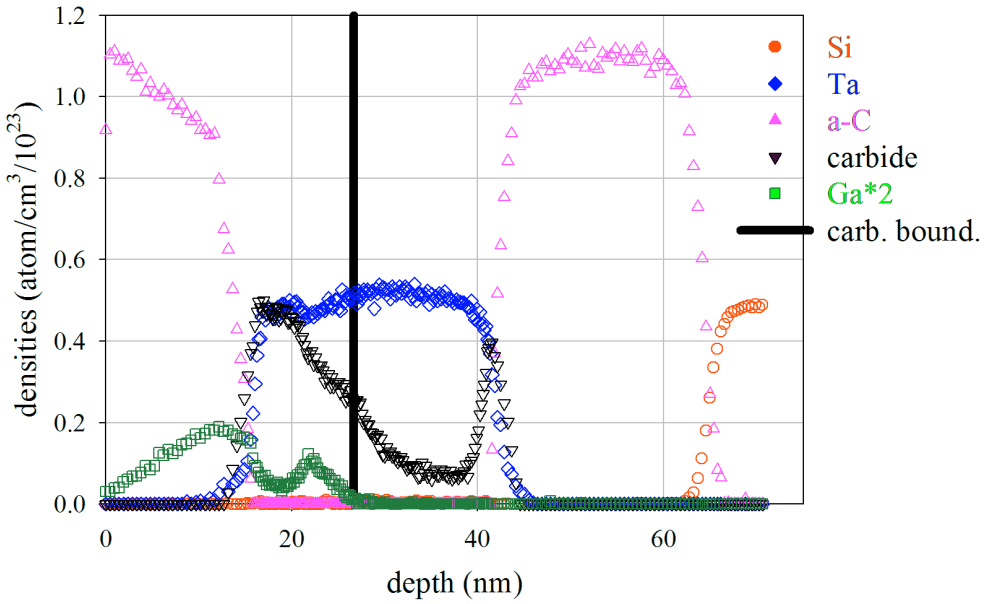

Figure 1. *Layer structure of the sample (C 22 nm/Ta 26 nm/ C22 nm) after Ga^+ irradiation at 30 keV, applying $4*10^{15}$ ions/cm^2 fluence.*

Deceptive Lattice Fringes; HRTEM Simulation of Au and Au-Pd Core-Shell nanoparticles

(OTKA PF63973)

V. K. Kis, O. Geszti, P. Süle, Zs. Kovács, and G. Sáfrán

Catalytic properties of Au-Pd bimetallic nanoparticles are strongly influenced by the composition, the distribution of Au and Pd atoms and the related lattice distortions within the individual particles. These characteristics depend on the method of synthesis, the applied precursors and additives, resulting in a wide variety of nanostructures. HRTEM imaging is a frequently applied method in the structural analysis of nanoparticles providing direct information on particle size, morphology and structure. We use HRTEM image simulation to investigate the role of lattice distortions of Au and Au-Pd nanoparticles in conventional and Cs corrected transmission electron microscopy (cTEM and Cs corrected TEM, respectively). The experimental and simulated HRTEM images of Au-Pd bimetallic nanoparticles are compared and the limits of identification of the lattice periods and the core-shell structures are discussed. Our conclusions can be summarized as follows:

- HRTEM imaging effects can change periodicity in case of small particle size
- Fringes may be visible even at extreme tilts (Figure 1.)
- At certain tilts new periods appear as a different zone axis approaches
- Measured deviation can be as high as ±10% in cTEM, while it is limited to 2-3% in Cs corrected TEM.
- Thickness alteration in cTEM may cause core-shell-like contrast features, while this imaging artefact can be avoided using Cs corrected TEM.
- Accurate measurement gets difficult due to contrast reversal in cTEM.

Averaging periodicity from a set of lattice spacings decreases the scattering of the data, however in case of core-shell nanostructures it is only possible with limitations. Information can be compiled for particles with more structural details (e.g. core-shell structures) if a set of images of the same particle are taken from different orientations.

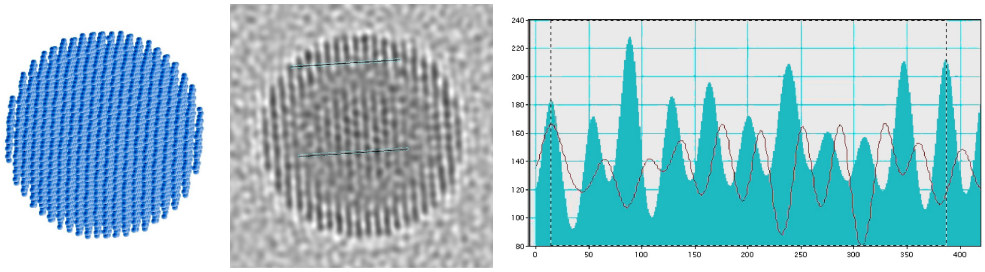

Figure 1. *Example for imaging artefact in cTEM. The lattice periodicity appears at extreme tilt (z=60° , x=40°). Model (left), simulated image (middle) and intensity profile (right) along the marked lines showing changing periodicity and contrast reversal.*

Chemically etched nanostructures for solar cells

(EU FP7 RODSOL)

B. Pécz, J. L. Lábár, Gy. Z. Radnóczi, J.-P. Ahl, H. Behmenburg, C. Giesen (AIXTRON), V. A. Sivakov, T. Stelzner, B. Hoffmann, G. Bronstrup, A. Berger, M. Krause, and S. H. Christiansen (IPHT)

The ROD_SOL project (All-inorganic nano-rod based thin-film solar cells on glass) coordinated by IPHT Jena ended 31st December 2011 after 3 years of successful work. By the end of the 3 year project participants demonstrated a nano rod based solar cell reaching 9.1% efficiency. During the past three years several ways of producing nano rods and making contact layers to them were tested. The role of MFA was to characterize these structures and to give feedback to other partners and to characterize the optimized structures.

Nano rods were produced using two different approaches: by catalysed growth of NRs following the Vapour-Liquid-Solid (VLS) scheme and by catalysed chemical etching of bulk material. For the latter approach Si was used to form NRs while catalyzed growth was attempted with Si and GaN (InGaN) with gold [J-P. Ahl, H. Behmenburg, C. Giesen, I. Regolin, W. Prost, F. J. Tegude, Gy. Z. Radnóczi, B. Pécz, H. Kalisch, R. H. Jansen, and M. Heuken: "Gold catalyst initiated growth of GaN nanowires by MOCVD", physica status solidi 8, 7-8, pp.2315–2317 (2011)] and Ni catalyst material. See Fig. 1 for examples.

ITO and AZO layers were tested, Si NRs obtained from the two approaches were coated with AZO layers to test coating uniformity and quality while GaN NRs were grown onto various substrates with a wide range of parameters to obtain NRs suitable for solar cell applications.

The best NRs for solar cells were obtained by a newly developed simple and cheap chemical etching process [V. A. Sivakov, G. Bronstrup, B. Pécz, A. Berger, Gy. Z. Radnóczi, M. Krause, and S. H. Christiansen: "Realization of Vertical and Zigzag Single Crystalline Silicon Nanowire Architectures", J. Phys. Chem. C, 114, pp.3798–3803 (2010)]. In this process Ag nano particles sink into the etched substrate by catalyzing the etching process locally. As the surface is densely covered by the catalyst particles a dense array of etched channels forms during the process. The remaining material between the channels are NRs of inherently very good crystalline quality and uniform alignment but random cross section. Patterning the Ag particle layout is also possible to tailor the NR array (shape, cross section, density).

To overcome the problems of the CVD Si quality a SIS (Semiconductor-Insulator-Semiconductor) solar cell concept without the CVD Si layer was tested. (Figure 2.) Using Atomic Layer deposition (ALD) process to deposit Al_2O_3 insulating layer and AZO transparent conductive layer a working solar cell was produced. Earlier attempts to produce SIS solar cells suffered from difficulties in producing a uniform thin insulating layer, but the ALD deposition technique has successfully overcome this obstacle.

The forest of NRs also exhibits advantageous optical properties due to its 3D geometry. The nano rod forests have high active surface area which enables efficient light absorption – much more efficient than in convenient 2D thin film solar cells. In addition, the contact configuration in such a nano structure radically improves the minority carrier charge transport and thus the amount of electricity that can be extracted from the cell.

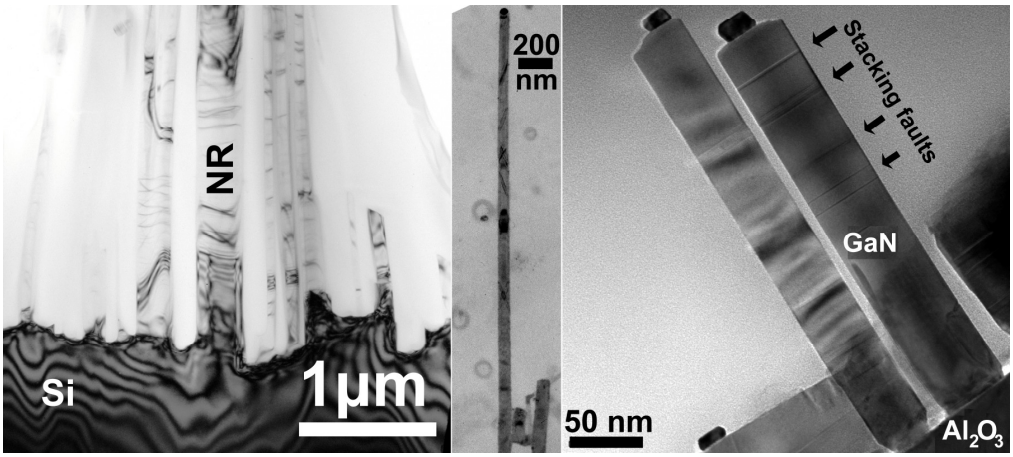

Figure 1. *TEM micrographs of chemically etched Si nano rods (left) , VLS grown Si nano rods (middle) and VLS grown GaN nano rods with gold catalyst (right).*

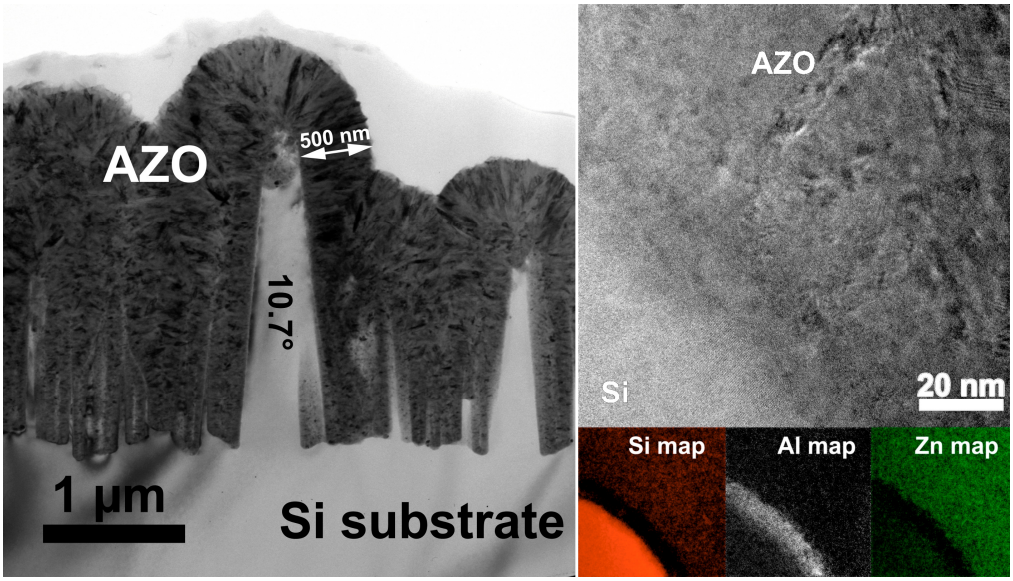

Figure 2. *Chemically etched Si nano rods covered with AZO (Al doped ZnO) (left) and a closer look at the Si/AZO interface (right). Elemental maps show a few nm thick Al_2O_3 layer at the interface.*

Composite silicon-polycrystalline diamond substrates for high power nitride HEMT devices

(EU FP7 MORGaN)

Á. Barna, L. Tóth, B. Pécz, D. Allsop (Bath), Q. Jiang (Bath), T. Mollart (E6), S. Delage (3-5 Lab)

In the frame of the MORGaN project finished in 2011 several approaches were exploited to realize an enhanced heat extraction from the GaN-based HEMT devices working at extreme environmental and power conditions. A common point among them was the use of diamond, the highest heat conductivity material known, either as substrate material or as top coating of the devices. Results on the latter solution were reported in [2]. Single crystal diamond chips of various orientations were used directly as substrates of the MBE deposited AlGaN/GaN heterostructures. As reported in [112] epitaxial GaN films were succesfully grown onto single crystal diamond substrates of (001), (011) and (111) orientation with their [0001] axis parallel to the surface normal in all cases. With the optimization of the AlN nucleation layer parameters smooth GaN films were grown with relatively low defect density. Based on this, growth experiments were also made on polycrystalline diamond wafers (available in sizes up to 4") but they have resulted in much poorer quality GaN films.
The third approach to be presented here was the use of composite substrates consisting of a thin Si plate on thick polycrystalline diamond wafer. (Fig. 1) They represent a compromise between the excellent heat conductivity of diamond and surface quality of single crystal silicon necessary for the epitaxial growth of HEMT devices. The AlN/GaN growth took place by MOCVD technique.

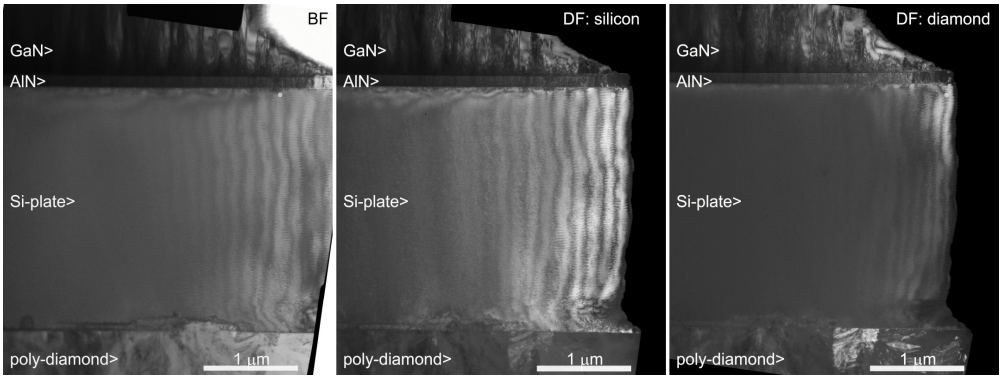

Figure 1. *Cross sectional bright field (a) and dark field (b,c taken with Si and diamond reflection respectively) electron micrographs of the GaN film epitaxially grown by MOCVD on the Si side of a composite substrate. The Si wafer was defect free with uniform thickness of 2.5 μm.*

High resolution and energy filtered TEM (EFTEM) observation (Fig. 2) also revealed a thin region between the diamond and the silicon wafers identified as a mixture of cubic SiC nanocrystals and amorphous carbon phase(s). This is most probably a residue of the early stage of CVD diamond growth which usually starts with the formation of SiC phase on silicon substrate. Above this thin nucleation zone the thick diamond film was found to be grown as single phase with polycrystalline, columnar microstructure.

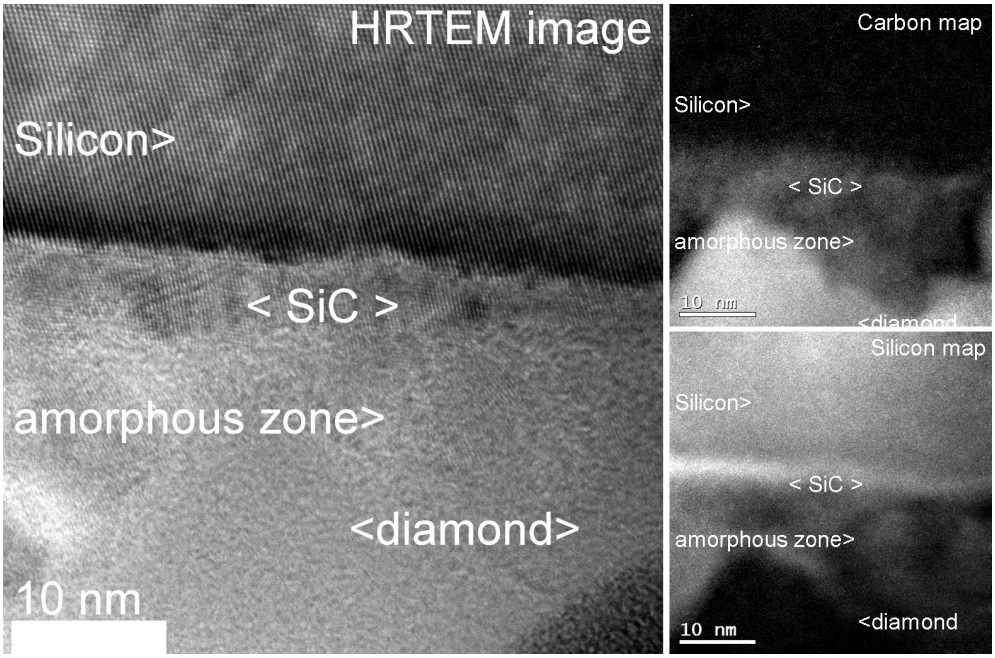

Figure 2. *High resolution TEM image shows the transition zone between the 2.5 μm thick Si plate and the CVD grown polycrystalline diamond wafer. This interface reveals that the CVD growth of diamond phase has started on the silicon substrate with the formation of nanosized cubic SiC phase and that was later followed by the nucleation and growth of columnar grains of diamond. The two inserts on the right showing the carbon and silicon elemental maps of the same area confirm the above explanation.*

Acknowledgements:
The research leading to the above results has received funding from the European Community's 7th Framework Program under grant agreement EU-FP7-NMP-214610.

Hydrogen-Argon Plasma Pre-treatment for Improving the Anti-Corrosion Properties of Thin Al_2O_3 Films on Carbon Steel Deposited Using Atomic Layer Deposition

(EU FP7 CORRAL)

S. E. Potts (LIC), L. Schmalz (DAP), M. Fenker (LIC), B. Diaz (CPT), J. Światowska (CPT), V. Maurice (CPT), P. Marcus (CPT), G. Radnóczi, L. Tóth, F. Misják, M. C. M. van de Sanden (LIC), and W. M. M. Kessels (LIC)

Corrosion is a persistent problem for many modern high-precision applications, such as automotive and aerospace components or specialty gas equipment These require many high-purity precision parts and instruments of rather complicated form which are commonly manufactured from steel or aluminum alloys. As such, dense and defect-free protective coatings are necessary to prevent corrosion of these parts. Atomic layer deposition (ALD) is an ideal candidate for this application, as it gives high-quality films with excellent conformity, and provides precise thickness control.

The effect of *in* and *ex* situ H_2-Ar plasma pre-treatment prior to thermal or plasma-enhanced atomic layer deposition (ALD) of Al_2O_3 on 100Cr6 steel was considered. Time-of-flight secondary ion mass spectrometry (ToF-SIMS) and transmission electron microscopy (TEM) were used to observe the changes in the interface. Electrochemical properties of the samples were studied with polarization measurements, and coating porosities were calculated from the polarization results for easier comparison of the coatings.

Cross sectional TEM images of 50 nm thermal ALD Al_2O_3 coatings on untreated and 60 min *in situ* plasma pre-treated 100Cr6 steel are presented in Fig 1. The ALD coatings appear to be amorphous and defect free, as expected. Some voids could be observed in between the coating and the untreated steel substrate indicating problems with adhesion (Fig. 1a). This observation is in line with the adhesion problems observed previously with thermal ALD coatings on steel and aluminium [122]. The coating on the 60 min in-*situ* plasma pre-treated substrate was well adhered (Fig. 1b). Such an improvement of adhesion was observed on all the plasma pre-treated samples studied with TEM. The improved adhesion was probably due to the decreased amount of organic impurities on the steel surface. ALD films grow by chemical reactions of precursors with a surface. Therefore, an organic contamination layer, which does not have suitable surface groups for the film growth, could result in poor quality films at least in the early state of the film growth. This theory is supported by the decrease of carbon and hydroxyl impurities in the ALD films after the plasma pre-treatments as observed with ToF-SIMS.

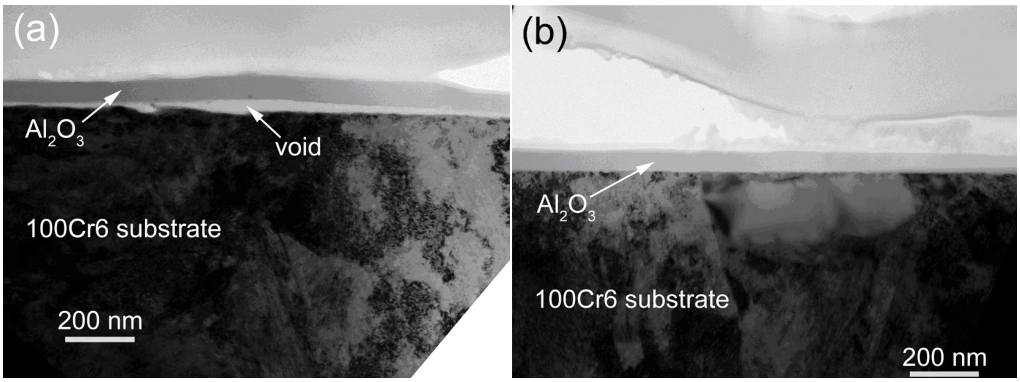

Figure 1. *TEM images of 50 nm Al_2O_3 on 100Cr6 steel substrate deposited using thermal ALD with no pre-treatment (a), and with a 60 min* in situ *H_2-Ar plasma pre-treatment (b).*

Influence of *in* and *ex situ* H_2-Ar plasma pre-treatment on the corrosion protection properties of 50 nm Al_2O_3 coatings deposited with thermal ALD and PEALD on carbon steel was studied. All plasma pre-treatments improved the corrosion protection properties of thermal ALD on steel. Adhesion to the substrate was increased and coating porosity decreased. The improvement was increased with pre-treatment time. PEALD coatings could be improved with 30 minutes *in* and *ex situ* pre-treatments provided that reformation of a protective native oxide layer was enabled. Deposition of the coating immediately after the pre-treatment allowed the growth of an enhanced interfacial oxide layer, which decreased the protective qualities of the coating. *Ex situ* pre-treatment was the most effective in improving PEALD coating performance.

The project successfully ended in 2011, resulting in new, very thin coatings of enhanced corrosion properties, applicable also to parts of complicated form and precision sizing. CORRAL coatings of 50 nm thickness match the corrosion resistance of state of the art coatings of several μm thickness. This has been demonstrated for stainless steel, carbon steels like 100Cr6 and cold and hot working steels. CORRAL ALD coatings are perfect sealants for the defects in state of the art (PVD, electroplate and electroless) coatings: increasing their lifetime by 3-10 times.

Acknowledgements:

The European Community´s Seventh Framework Program under grant agreement n◦ CP-FP 213996-1" is acknowledged for financial support. The authors would also like to thank Daniel Morel from Haute Ecole Spécialisée de Suisse occidentale (HES-SO) for the substrate surface preparation and Dr. Jaakko Niinistö from the University of Helsinki for help with the plasma pre-treatments done with the Beneq TFS-200 ALD reactor.

The role of inert gas in CN_x and a-C thin film deposition in HiPIMS and DC-MS techniques

Zs. Czigány, S. Schmidt and L Hultman

Neon, argon and krypton were used to map the role of inert gases in sputtering of pure carbon and reactive sputtered carbon-nitride (CN_x) compounds in high power pulsed magnetron sputtering (HiPIMS) and DC-MS modes. Thin solid films were synthesized in an industrial deposition chamber from a pure graphite target. In the case of a-C films the deposition took place in a pure Ne, Ar and Kr atmosphere, whereas CN_x thin films were grown in an Ne, Ar or Kr/N_2 atmosphere with a constant N_2/inert gas flow ratio of 0.16. Throughout the deposition the pressure was kept constant at 400 mPa and the average target power was similar for both deposition techniques.. The resulting thin films were characterized regarding their bonding and microstructure as well as film properties by X-ray photoelectron spectroscopy (XPS), Raman spectroscopy, transmission electron microscopy (TEM), contact angle measurements, and nanoindentation.

The peak target current was found to decrease with increased inert gas mass. This was mirrored in the microstructure of the thin films in a more pronounced ordering towards fullerene-like films in inert gases with higher atomic mass. Carbon and carbon nitride films deposited in Ne atmosphere were found to be fully amorphous. However, the effect of the inert gas on the microstructure was not as distinct whenever N_2, as reactive gas, was introduced into the deposition chamber. XPS data showed a dependency on the sputter mode as the sp^3/sp^2 seem to increase comparing films produced by DC-MS either in Kr or in Ne atmosphere. An opposite trend was found for pure carbon thin films deposited via HiPIMS which can be attributed to different ion energy distribution and higher ionisation rate in HiPIMS.

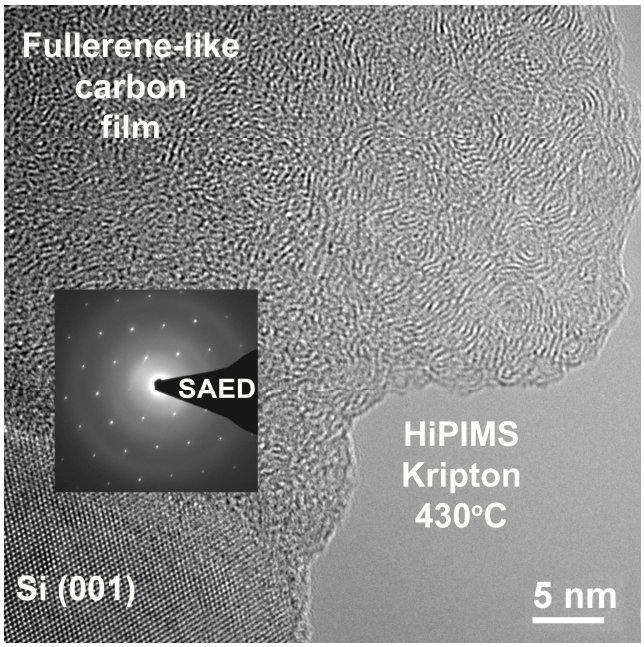

Figure 1. *Fullerene-like carbon film deposited by HiPIMS in kripton.*

HRTEM and EELS study of Silica-Supported Au Catalyst Nanoparticles Decorated by CeO_2

(OTKA F62481)

G. Sáfrán, O. Geszti, A. Horváth*, A. Beck*, G. Stefler*, T. Benko*, Z. Varga*, J. Gubicza**, and L. Guczi*

High Resolution Transmission Electron Microscopy (HRTEM) combined with Electron Energy Loss Spectrometry (EELS) is a very efficient tool for the analysis of catalyst nanoparticles providing direct information on particle size, morphology, structure and the local distribution of the chemical components. In a co-operation with the Institute of Isotopes of H.A.S.* and the Eötvös Loránd University Budapest** we studied the correlations of synthesis, morphology, nanostructure and elemental distribution with the activity of Au-CeO_2 catalyst nanoparticles. SiO_2-supported Au nanoparticles derived from sol were promoted with 0.04-7.4 wt % CeO_2 using two methods. The Ce precursor was added directly to the Au sols before sol immobilization (method A) or to the suspension of parent Au/SiO_2 (method B). Both preparation routes resulted in CeO_2 decoration of 1-3 nm over Au nanoparticles, which induced high CO oxidation activity. However, above 0.6 wt % CeO_2 content, the activity did not change significantly, but it greatly exceeded that of pure Au/CeO_2 used for reference. HRTEM and EELS revealed that up to this concentration ceria patches are attached to gold surface, and further increase in Ce-content caused CeO_2 spread over the support surface as well. As a consequence, (1) ceria addition can be optimized at about 0.6 wt % and (2) CeO_2 localization on gold can be explained by the strong interaction of Ce species with stabilizer ligands located around Au [49].

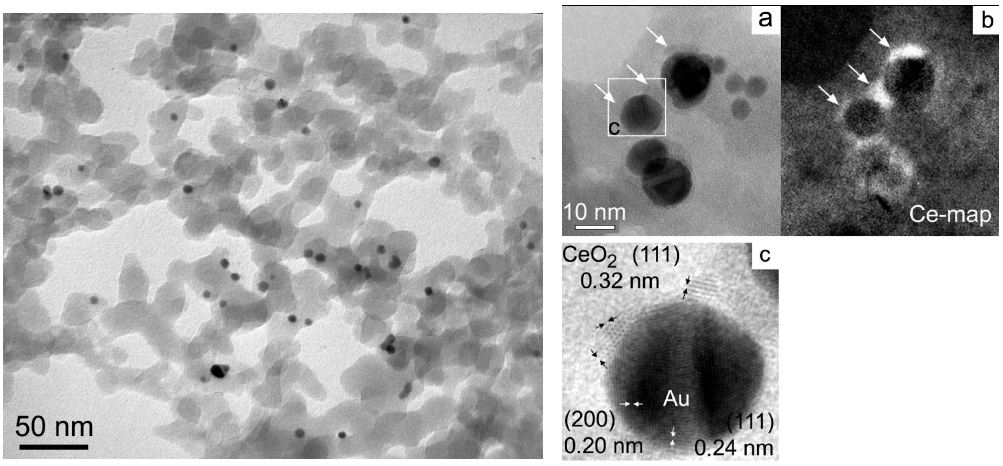

Figure 1. *Au particles in Au/SiO_2 after calcination at 450ºC + catalytic run (left). TEM (a), EELS Ce map (b), and HRTEM (c) images revealing Au-CeO_2 decoration (right).*

Bilayer Cr/Au and Ti/Au contacts on n-GaN

(OTKA K77331)

L. Dobos, L. Tóth, B. Pécz, Zs. J. Horváth, Z. E. Horváth, and A. L. Tóth

In recent years, the structurally related layered ternary compounds $M_{N+1}AX_N$, where N=1, 2 or 3, M is an early transition metal, A is an A-group (mostly IIIA and IVA) element, and X is either C and/or N, attract increasing interest owing to their unique properties. MAX-phases represent a new class of nitrides and carbides and can be best described as polycrystalline nanolaminates.

Forming a low resistance thermally stable and uniform ohmic contacts to wide band gap semiconductors such as GaN and related materials is still a challenge. Hence understanding of the metallurgy of contacts to GaN is needed. For contact formation, samples were submitted to thermal annealing in vacuum [(40 nm)Cr/Au(65 nm) metal layers], and N_2 [(40 nm)Ti/Au(120 nm) contact metallization] for 10 min at temperatures 400-900 °C. The interaction between the contact metallization and the GaN epitaxial layer was investigated by electron microscopy, XRD and I-V measurements.

In the vacuum heated n-GaN/Cr/Au and nitrogen heated n-GaN/Ti/Au samples Au diffused to GaN at 400 °C. The TEM investigations of the (65 nm)Au/Cr(40 nm)/n-GaN contacts show that, after annealing at 700 °C larger ingrowths developed at the interface of metal/GaN (Fig. 1a). EDS analysis confirms the presence of a Cr-rich phase containing also a little amount of Au in the ingrowth (Fig. 1b). The TEM investigation of CrAu contact did not exhibit remarkable change after heat treatment at 900 °C. But EDS analysis of the ingrowth showed bigger Cr and Au content. The HRTEM investigations of Cr/Au contacts show that, after annealing in vacuum at

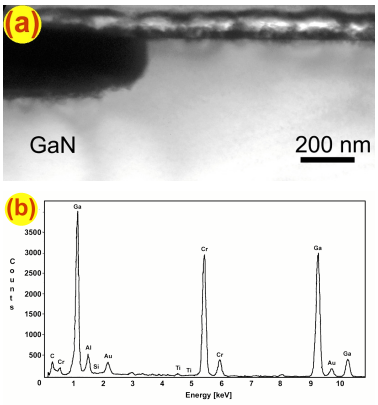

Figure 1. ***(a)*** *XTEM micrograph of the ingrowth of n-GaN/Cr(40 nm)/Au(65 nm) contact annealed in vacuum at 700 °C for 10 min.* ***(b)*** *EDS spectrum of the ingrowth of n-GaN/Cr(40nm)/Au(65nm) contact heated in vacuum at 700 °C.*

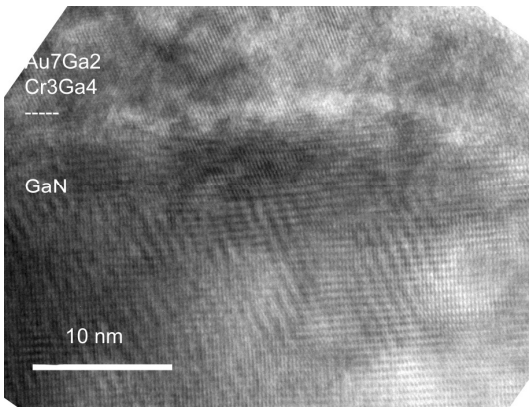

Figure 2. *HRTEM micrograph of the n-GaN/Cr(40 nm)/Au(65 nm) contact with the formed phases annealed in vacuum at 900 °C for 10 min.*

900 °C Au_7Ga_2 and Cr_3Ga_4 phases developed at the interface of metal/GaN (Fig. 2).
X-ray diffraction examinations showed, that there are new interfacial phases – Au_7Ga_2 and Cr_3Ga_4 – and maybe Cr_2GaN MAX phase in the n-GaN/Cr/Au samples annealed in vacuum at 700 and 900 °C. The current-voltage characterizations showed that the as-deposited and annealed Cr/Au contacts are rectifying up to 600 °C. After heat treatment in vacuum at 700 °C and 900 °C the Cr/Au contacts were linear. The diffusion of Cr and Au into the epi GaN layer led to ohmic behavior and increased series resistance above 600 °C. Microstructural and nanostructural characterization revealed the thermal stability of CrAu contact layers prepared on GaN.
In the n-GaN/Ti/Au samples grains have grown on the GaN, under the metallization at 700 and 900 °C (Fig. 3). It is evident from EDS analysis that Ti is distributed not only at the metal/GaN interface. EDS spectrum of the lower grain of n-GaN/Ti(40 nm)/Au(120 nm) contact heated in nitrogen at 700 and 900 °C revealed the presence of a Au-rich phase. The layer above the grains is contained mainly Ti revealed by EDS. Between the Au-rich grain and the n-type GaN layer a Ti-rich thin layer located by EDS analysis. The large Ti content of EDS spectrum suggests the presence of a Ti-based phase , which agrees with XRD indications of $TiN_{0.26}$ and TiO_2 phases.
The HRTEM investigations of Ti/Au samples revealed that the formation of an about 25 nm layer of $TiN_{0.26}$ phases arose at the vicinity of Ti/n-GaN interface after annealing at 900 °C in nitrogen. The distance between the adjacent lattice fringes is 0.48 nm. The TiN layers are parallel to the interface at 900 °C (Fig. 4). Rutile (TiO_2)

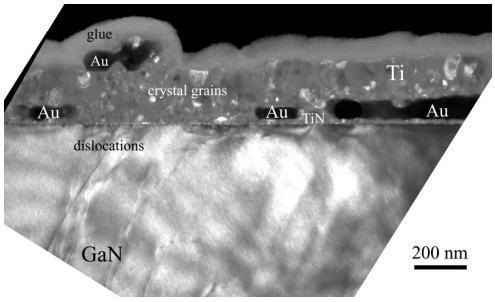

Figure 3. *DF XTEM micrograph of n-GaN/Ti(40 nm)/Au(120 nm) contact annealed in nitrogen at 700 °C for 10 min in N_2.*

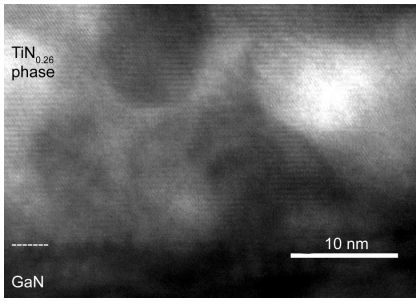

Figure 4. *HRTEM micrograph of the n-GaN/Ti(40 nm)/Au(120 nm) contact with the formed phases annealed in nitrogen at 900 °C for 10 min in N_2.*

and $TiN_{0.26}$ phases and Au peaks were detected by XRD analysis in the N_2 heated n-GaN/Ti/Au contacts at 700 and 900 °C as well. However, the appearance of rutile (TiO_2) peaks in samples annealed above 700 °C is unexpected.
FESEM investigations revealed, that in the case of in the vacuum heated n-GaN/Cr/Au contacts the metal surface became rough after the thermal annealing. In the N_2 heated n-GaN/Ti/Au contact surfaces stayed smooth. The solid phase alloying properties of the same Ti/Au contacts annealed in vacuum were completely different, as Ti_2GaN MAX and GaAu phases were formed in those samples. However, in the present study, thanks to the annealing ambient (N_2), gold did not react with GaN.

Secondary electron emission of samples with layered structure

A. Sulyok, M. Menyhard, L.Zommer (IPC), A.Jablonski (IPC)

Monte Carlo (MC) simulation of electron transport is a useful tool to explain the fine details of a spectrum in electron spectroscopy. The inclusion of the secondary electron generation makes possible to interpret physical events that are dominated by the low energy part of backscattered electron spectrum. Backscattered electrons (BSE) separated by an energy analyzer have been recorded during the depth profiling of a layered sample Ni/C/Ni/C/Ni/C/Si, using primary energies 5, 2.5 and 1.25 keV. Scanning electron microscopy (SE) images were also taken on the layered specimen. Similarity in shapes of SE depth dependence to BSE depth dependence were found, thus the contrast relations on the SE pictures can be interpreted on the ground of the MC simulated intensity curves..

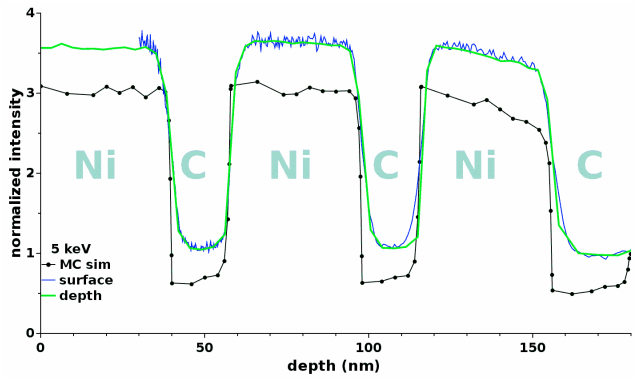

Figure 1. *Depth dependence of backscattered electron yield (at 100 eV) on Ni-C multilayers, induced by 5 keV primary electrons. Thin solid lines – experimental curves determined by surface profiling and by depth profiling; line with symbols - Monte Carlo simulation.*

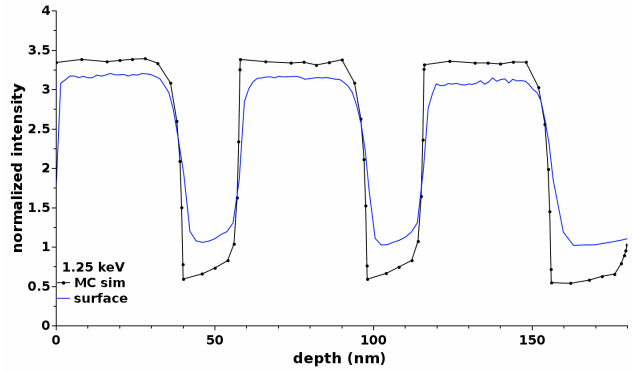

Figure 2. *Depth dependence of backscattered electron yield (at 100 eV) on layered Ni-C specimen, induced by 1.25 keV primary electrons. Thin solid line - experimental curve determined by surface profiling, line with symbols - Monte Carlo simulation.*

The MC simulation method was applied to calculate the depth profile of the BSE current emitted in the 90-110 eV range. Good agreement between the measurement and simulation was found for all studied cases. Simple phenomenological rules cannot be obtained, however. Thus, to describe the contrast formation of SEM imaging in real life cases, MC simulation of the electron transport is to be used.
It was demonstrated by two examples that a contrast can appear on a chemically homogeneous surface if the underlying material structure is changing.

1. The Ni-C multilayer specimen was prepared by removing 4 nm from the first Ni layer in a 200x200µm square before the depth profile measurement. Several SEM images were taken during depth profiling (one is shown in Fig. 3) while the surface morphology remained constant. The SEM images were taken when the whole actual surface was chemically identical, according to Auger electron spectroscopy. The square showed varying contrast during the profiling: dark, light or none. These contrast changes can be interpreted by the simulation.
2. SEM image was taken on a shallow crater produced by depth profiling (Fig. 4). The dark and light regions are pure carbon and pure Ni layers checked by Auger electron spectroscopy. The pattern is determined by the crater shape in the layer structure. The most noticeable, however, not obvious intensity change is visible on the central plate. It is less bright in the centre than in its edge. It is explained by the changing thickness of the Ni layer as shown in the cross section part of Fig.4. The Ni thickness is about 20 nm at the center of the plate while 40 nm at the edge of the plate.

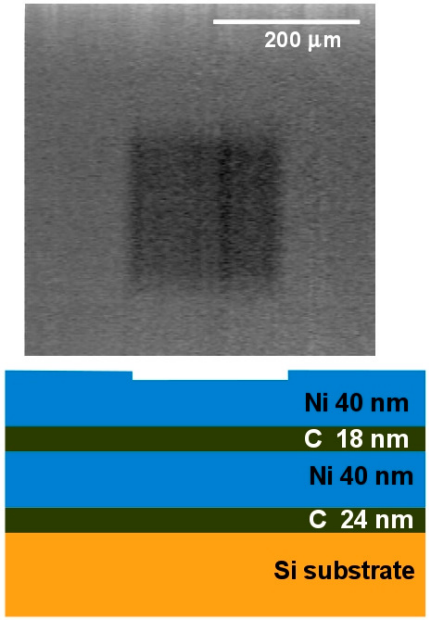

Figure 3. *Upper panel: SEM image taken at 5keV electron beam on Ni-C multilayer showing lower thickness of the upper Ni layer in the dark square. Lower panel: schematic cross section of specimen.*

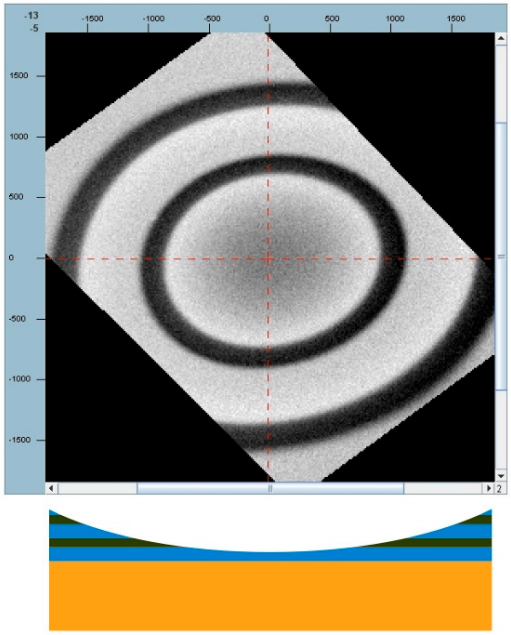

Figure 4. *Upper panel: SEM image taken by 5keV electron beam on a shallow crater in Ni/C multilayer. Dark rings: carbon layers. Light rings and center plate: Ni layers. The center of Ni plate is visible darker then its edge. Lower panel: schematic cross section of specimen.*

NTPCRASH

(NKTH TECH-08-A2/2-2008-0104)

M. Menyhárd, S. Gurbán, A. Sulyok, Z. Kabács (Panac), G. Kőfalvi (IbB), Cs. Balázsi, V. Varga, and F. Wéber

In the framework of the project, a bio-composite based underrun protection for trucks has been developed. The main purpose of the project was to decrease the weight while maintaining the safety. Two different types were studied: bio-fiber and carbon fiber reinforced polyester composites. Bending measurements to characterize the materials was carried out obtaining stress-strain diagrams in standard way using five samples. The maximum strain reached was about the same for all bio-fiber-composites. It was found that the plate with 12 fiber layers has the most uniform mechanical behavior out of the 4 different fiber layer structure measured. The diagrams of plates with 8 and 12 fiber layers are shown in Fig. 1. and Fig. 2., respectively. The carbon fiber reinforced plates showed 4 times larger stress tolerance, however, its maximum was reached already at 2 % strain. Thus, based on the larger stress tolerance and better uniformity and the large energy absorption capability, the bio-composite with 12 fiber layers and the carbon fiber composite was proposed to be used in a proper combination.

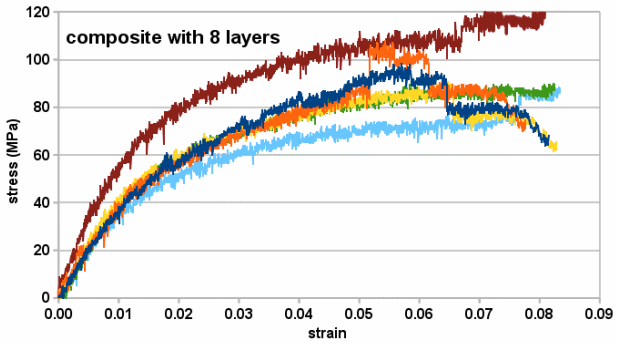

Figure 1. *Stress-strain diagram of cellulose/ polyester bio-composite with 8 fibre layers. Visible feature: large variance of strain.*

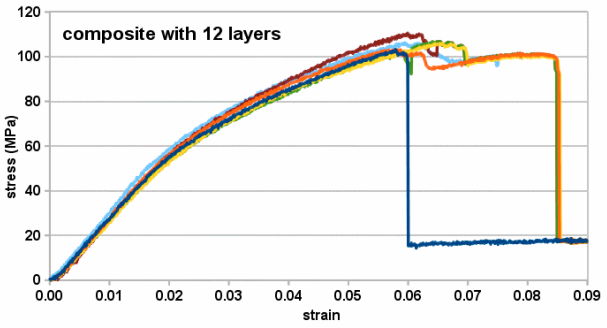

Figure 2. *Stress-strain diagram of cellulose/ polyester bio-composite with 12 fibre layers. Visible feature: small variance of strain.*

Ceramics and Nanocomposites Department

Head: Csaba BALÁZSI, Ph.D., senior scientist

Research Staff

- János VOLK, Ph.D., Deputy Head of Department
- Péter ARATÓ, D.Sc.*
- László BARTHA, D.Sc. Professor Emeritus **
- Csaba Sándor DARÓCZI, dr. Univ.
- András DEÁK, Ph.D.***
- István GAÁL, C.Sc.**
- Gréta GERGELY, Ph.D.***
- Ngyuyen Quoc KHANH, Ph.D.
- István Endre LUKÁCS, Ph.D.
- Judit PFEIFER, C.Sc.**
- Attila Lajos TÓTH, Ph.D.
- László URAY, Ph.D.**

Technical Staff

- Levente ILLÉS, engineer
- Attila PETRIK, engineer
- Viktor VARGA, technician
- Ferenc Viktor WÉBER, engineer

Ph.D. students / Diploma workers

- Róbert ERDÉLYI, Ph.D. student
- Eszter FÜLÖP, Ph.D. student
- Tamás GOMBOR, diploma worker
- Péter KONCZ, diploma worker
- Kristóf KUBINA, diploma worker
- Imre KULCSÁR, diploma worker
- Péter KUN, diploma worker
- Áron NAGY, diploma worker
- Etelka ROVÁCS, diploma worker
- Zoltán SZABÓ, Ph.D. student
- Orsolya TAPASZTÓ, Ph.D. student
- Mihály TÓTH, diploma worker

*** MFA board** *****on leave**

**** part time**

The main task of the laboratory is to study the relationships between processing parameters, micro- and nanostructures and properties of ceramics and their nanocomposites. Some recent activities:

- investigation of structural, mechanical, electrical, biological properties,
- development of CNT/nano-graphite silicon nitride nanocomposites,
- 1D, 2D and 3D semiconductor (ZnO, WO_3) oxides for sensor devices,
- nano-hydroxyapatite biocomposites for medical and enviromental uses,
- development of nanostructured stainless steels by powder metallurgy,
- production of silicon nitride tools and parts.

The Department has intensive co-operation with universities and industry. Joint laboratories with Budapest University of Technology and Economics (Chemical nanostructures and Electron-beam Lithography) have been established. Experienced research staff is actively participating in training and supervising of undergraduate and graduate students (Summer School, M.Sc., Ph.D.); is giving chairs, scientific committee members to international conferences.

Nano hydroxyapatite and polymer based bio-compatible nanocomposites

(OTKA BIOCER, TéT HU-Korea)

Cs. Balázsi, G. Gergely, M. Tóth, I. Kulcsár, K. Balázsi, A. L. Tóth, and I. E. Lukács

Nanomaterials used in biomedical applications include nanoparticles for molecules delivery, nanofibres for tissue scaffolds, surface modifications of implantable materials or nanodevices. The combination of these elements within tissue engineering is an excellent example of the great potential of nanotechnology applied to regenerative medicine. Artificial bone tissue scaffolds based on natural hybrids of cellulose acetate (CA) and nano-hydroxyapatite (nHA) in a bio-mimicking 3D matrix architecture using a single step nanomanufacturing technique have been developed in co-operation with Department of Materials Science and Engineering, State University of New York at Stony Brook (USA), Molecular Foundry at LBNL and West Virginia University. The scaffold preparation scheme is presented in Fig. 1. These scaffolds have been used for in-vitro bone regeneration studies by using human osteoblast-like SaOS-2 cells for up to 14 days. Osteoblasts grown on these scaffolds were found to interact strongly with the nHA nanoclusters that were uniformly distributed on the CA fibers, promoting cell elongation, growth and phenotype retention.

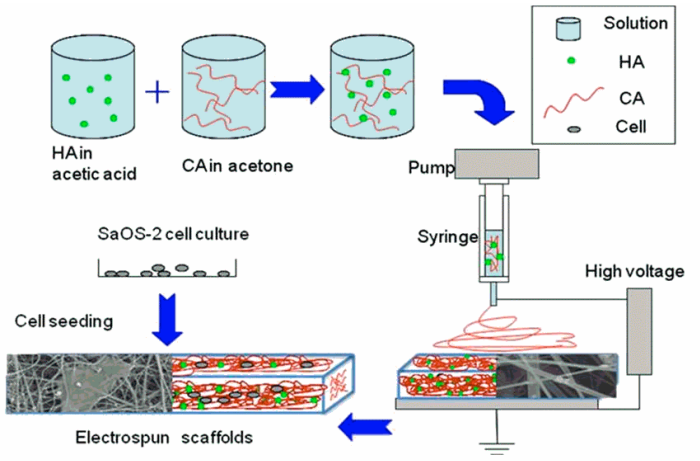

Figure 1. *Scheme of the electrospinning and cell culture process used to obtain 3D cell seeded scaffolds. Insets are SEM micrographs revealing cross sectional views of the scaffolds before and after the cell seeding process.*

Cell differentiation and functional activity of osteoblasts were evaluated by means of the Alkaline-phosphatase (ALP) expression. The nano scaffolds have positive human osteoblastic cell responses. Starting from day 7, the ALP activity of the cells on CA-HA scaffolds was dramatically increased. Fig. 2 shows a comparison of cells growth on CA fibers only and nHA containing CA fibers. Cells grown on CA are showing a rounded morphology with an average diameter 8.5±1.4 µm (Fig. 2a). The osteoblasts seeded on CA scaffold are seen attached to the thinner section of the ribbon-like CA fibers and the cells were typically attached on a single fiber. Most of the cells exhibited a flat morphology with pronounced spreading on nHA containing

CA fibers (Fig. 2b and Fig. 2c). It was observed that the HA nanoclusters provided anchoring sites for cell attachment.

Hexagonal apatite crystals were shown to crystallize on the nHA seeds. The natural, open, hybrid, 3D nanoscaffolds thus appear to be the most promising bone repair agents. Bone regeneration with scaffolds made of nHA derived from eggshell has been studied in animal and human clinical models in co-operation with the Hallym University and the Gangneung-Wonju National University, Korea. Animal and clinical testing results are presented in Fig. 3.

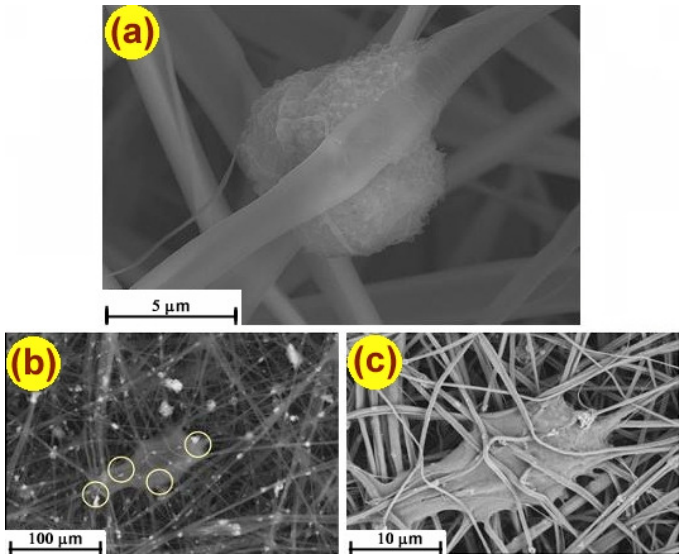

Figure 2. *Osteoblast cells grown on CA fibers only (a), nHA containing CA fibers at low magnification (b) and at high magnification (c) in SEM.*

The nHA graft showed much more bone regeneration than unfilled control in both µCT analysis and histomorphometric analysis. All measured variables of the µCT analysis showed that grafted (nHA) groups were significantly higher than the unfilled control groups in 8 weeks after operation ($p<0.05$). Considering that the eggshell is easily available and cheap, nHA from the eggshell can be a good calcium source in tissue engineering.

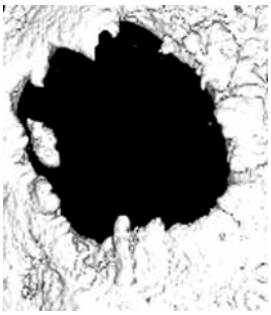

Figure 3a. *µCT images of unfilled control group at 8 weeks.*

Figure 3b. *µCT images of nano-HAp grafted group at 8 weeks.*

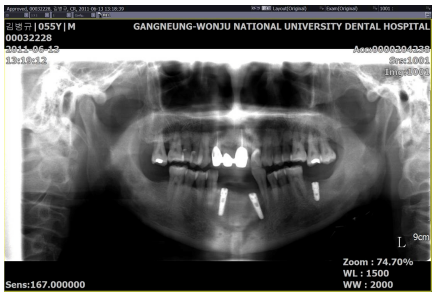

Figure 3c. *Implants installation. The gap between implant and bone was restored by bone graft (nHA from Hungary). There was no infection in the graft site.*

In co-operation with the Department of Human Physiology and Clinical Experimental Research, Semmelweis University (Hungary) we tested the biological properties of nano-hydroxyapatite (nHA)-zirconia (ZrO_2) and carbon nanotube (CNT) composites produced by spark plasma sintering (SPS). Biological compatibility of the constructs was tested by seeding human bone marrow derived mesenchmyal stem cells onto autoclave-sterilized composites and kept under standard cell culture conditions. Cell survival and proliferation was monitored for 18 days with confocal microscopy. All of the observed constructs provided suitable surface for cell culture.
In co-operation with BUTE, we studied the bone (femur) resistance to applied mechanical loads. As resulted, the bone regeneration process should allow applying loads to the bones to assure building up a strong bone tissue. In the beginning of the regeneration process the implant should take a larger load from the missing bone tissue, but by time it would be better if the new bone is getting more and more load to prevent osteoporosis. The ideal material of the implant is similar to the bone tissue, it helps the bone tissue to regenerate and after regeneration it disintegrates.

Silicon nitride-based ceramics and nanocomposites

(OTKA K63609)

O. Tapasztó, P. Kun (BUTE), F. Wéber, A. Petrik, P. Arató, and Cs. Balázsi

Graphene multilayers have been prepared by mechanical method based on milling of graphite in high efficient attritor mill. We demonstrated that the high efficient milling is a succesful tool for producing graphene multilayers. The results showed that intensive milling in ethanol is the improved way to separate the graphite layers, rather than in water or in air. The 10h milling showed the largest distance between separated adhering multilayers (can exceed 1 μm) proving the highest degree of exfoliation. The average thickness of graphene multilayers was LC = 13.76 nm. This result implicates that the graphene multilayers were composed of approximately 40 graphene layers on average.
Silicon nitride based nanocomposites have been prepared with different amount (1 and 3 wt%) of multilayer graphene (MLG) as well as exfoliated graphite nanoplatelets (xGnP) and nano graphene platelets (Angstron). Scanning electron images of the starting graphene materials are presented in Fig. 1. Homogeneous distribution of the MLG additives have been observed on the fracture surface of the sintered material. The SEM examinations showed that graphene platelets are inducing porosity in matrix. The superior mechanical properties of the MLG/silicon nitride composites were observed. MLG added composites were found to possess strength enhanced by 10 to 50% as compared to carbon nanotube (CNT) added composites prepared under the very same experimental conditions and filler content. In order to understand the resulting mechanical properties, it is of fundamental importance to obtain information on the distribution of the different carbon nanostructures in the ceramic matrix.

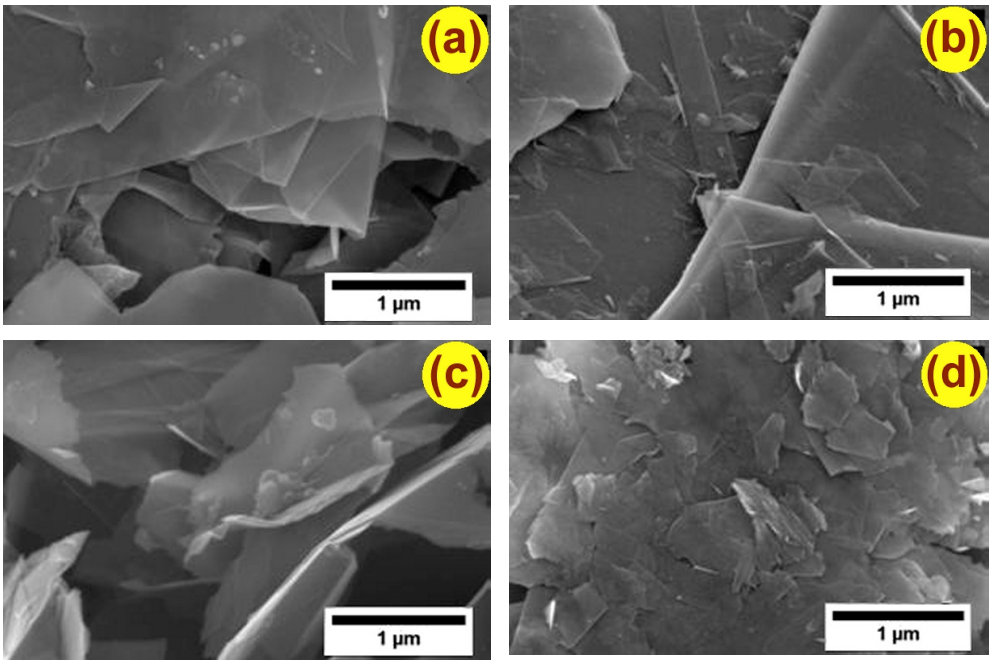

Figure 1. *Scanning electron images of the starting graphene materials: a) xGnP-M-5, b) xGnP-M-25, c) Angstron N006-010-P, d) multilayer graphene (MLG)*

We have performed small angle neutron scattering (SANS) measurements on both our graphene and nanotubes reinforced samples to gain information on the distribution of carbon nanostructures of the entire volume of the ceramic matrix (Fig. 2). As can be seen from the plots, the scattering intensities are following a power law behavior for both MLG and CNTs, although, characterized by significantly different exponents (slopes), providing information about the morphology of the scattering centers.

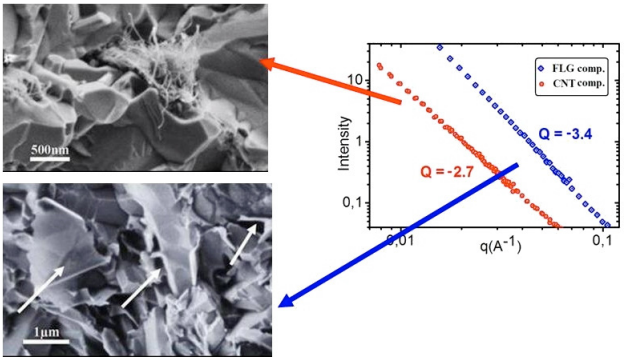

Figure 2. *Small angle neutron scattering spectra of Si_3N_4 composites reinforced with graphene (blue squares) and carbon nanotubes (red circles) both following a power law behavior, though characterized by significantly different decay rates (exponents) of Q = -2.7 for nanotubes, and Q = -3.4 for graphene.*

The exponent measured for nanotube composites is around -2.7. Based on the experience of SANS measurements on CNT dispersions in solutions and polymers, it is known that slope values between -2 and -3 are characteristic to disordered 3D nanotube networks. The most important consequence of the above finding is that

unlike nanotubes, MLG flakes are not present in the form of disordered 3D agglomerates in the ceramic matrix. They are dispersed as individual 2D platelets throughout the entire volume of the composite. In order to support the conclusions of our SANS measurements on MLG composites, SEM imaging of fracture surfaces has been performed.
We have shown that graphene can be much more efficiently dispersed in ceramic matrix composites than carbon nanotubes under the same experimental processing conditions, as demonstrated by small angle neutron scattering measurements and scanning electron microscopy investigations.

Nanostructured oxide dispersed strengthened steels

(Collaboration with AEKI KFKI and Istanbul Technical University)

Cs. Balázsi, P. Koncz (Pannon U.), K. Balázsi, F. Wéber, V. Varga, and A. Petrik

Oxide-dispersion-strengthened (ODS) steels have attracted attention for advanced nuclear power plants applications such as fast and fusion reactors, because of their superior high temperature mechanical properties.

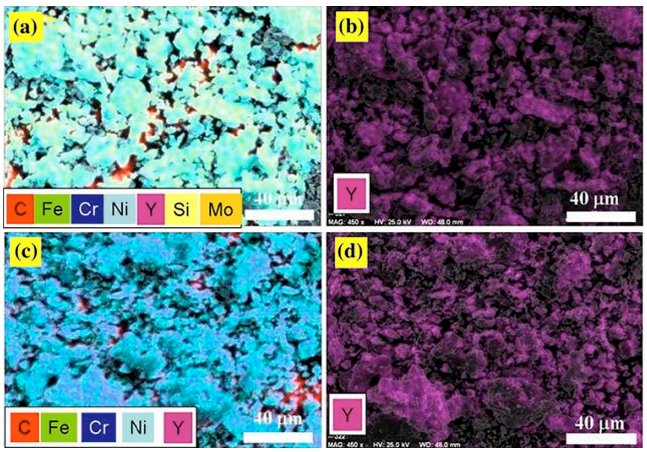

Figure 1. *Elemental analysis of ODS powder prepared by combined milling.a) EDS map of different phases of austenitic powder , b) EDS map of yttrium of austenitic powder, c) EDS map of different phases of martensitic powder, d) EDS map of yttrium of martensitic powder.*

The ODS steel has been conducted in the field of fast reactor fuel cladding application and fusion reactor materials application. As for irradiation effects on the mechanical properties, recent irradiation experiments clearly showed that the ODS steels are highly resistant to irradiation embrittlement at temperatures between 575 and 775 K. We developed ODS steels produced by intensive milling together with spark plasma sintering. The structure of powders is considerably changed after intensive combined (wet and dry) milling. The grain size of steel powders has been reduced from 100 µm to 1-2 microns in average after milling. The elemental mapping of austenitic and martensitic ODS powders containing 1 wt% yttrium oxide as dispersed oxides made with the help of energy dispersive spectroscopy is presented in Fig. 1. It is easy to observe that besides the iron, nickel and chrome are the main

components of the steel powders. The most interesting, however, is that with intensive milling an efficient distribution of yttrium (introduced in form of yttrium oxide) may be achieved (Fig. 1b and d). Addition of 1 wt% yttrium oxide to the starting powder has the aim to achieve improvements in mechanical properties. At the same time the combined milling assures a more efficient grain size reduction. Dense samples showing nanostructural characteristics have been achieved after sintering at only 1210-1220 K, 50 MPa, 5 minutes dwelling time by spark plasma sintering. Grains of steel with 100 nm mean size have been observed by SEM in austenitic ODS steel (Fig. 2). In comparison the martensitic ODS microstructure consisted of grain size with 100-300 nm (Fig. 3).

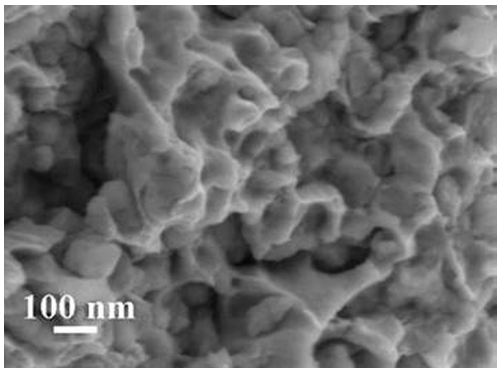

Figure 2. *SEM images of fracture surface of sintered austenitic ODS with 1 wt% Y_2O_3 addition.*

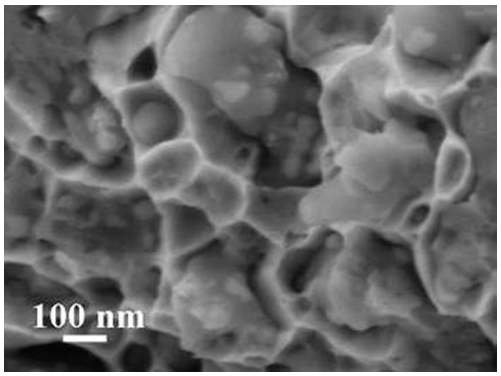

Figure 3. *SEM images of fracture surface of sintered martensitic ODS with 1 wt% Y_2O_3 addition.*

Tungsten oxide functional ceramics

Cs. Balázsi, A. K. Nagy, A. L. Tóth, K. Balázsi, and I. E. Lukács

The excellent gas sensing properties of the tungsten oxides have been manifested first in nanostructure and 1D, and 2D open structured forms. We used the electrospinning – a candidate for fabrication of large specific surface tungsten oxide nanofibers.

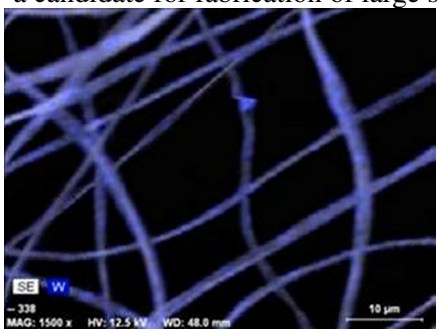

Figure 1a. *EDS map of CA tissue doped by $WO_3.1/3H_2O$*

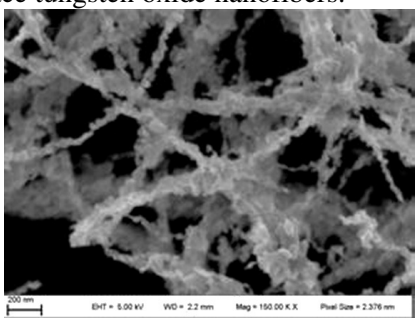

Figure 1b. *SEM image of heat treated WO_3 nanowires.*

Nanofibrous tissues containing reasonable amounts of tungsten oxide have been prepared by electrospinning method. Tungstic acid hydrate (H_2WO_4 H_2O) and the tungsten oxide hydrate ($WO_3.1/3H_2O$) have been added to the polymeric precursor. We analyzed the structure of the samples with scanning electron microscope. The tungsten content of fibers was monitored by energy dispersive spectroscopy (EDS, Fig. 1a). The preparation conditions for the maximal WO_3 content of the cellulose acetate (CA) tissue were found. Due to the WO_3 content the fibers became thinner and rougher. Singular WO_3 particles (of mostly sub micrometer size) are visible in the SEM images. The phase of the WO_3–containing compound is preserved after electrospinning. The EDS maps show the distribution of W in the fibers (Fig. 1a). The typical particle size of the dopant was in the nanorange in the produced cellulose acetate tissue after dispersion process, electrospinning and heat treatment (Fig. 1b).

Fabrication and characterization of regular nanopillar arrays using nanosphere photolithography and Kelvin probe force microscopy

Z. Szabó, E. Fülöp, R. Erdélyi, A. Deák, and J. Volk

Vertically aligned nanopillar arrays are currently attracting a great interest due to several potential applications as self formed laser cavities and novel photovoltaic cells with enhanced broad-band light absorption. In our previous works, it was demonstrated that regular ZnO nanorods (NRs) could be grown onto different ZnO template using a seed window pattern, which is generated by e-beam lithography. However, for most applications an alternative patterning method is needed to reduce the cost and to up-scale the fabrication procedure.

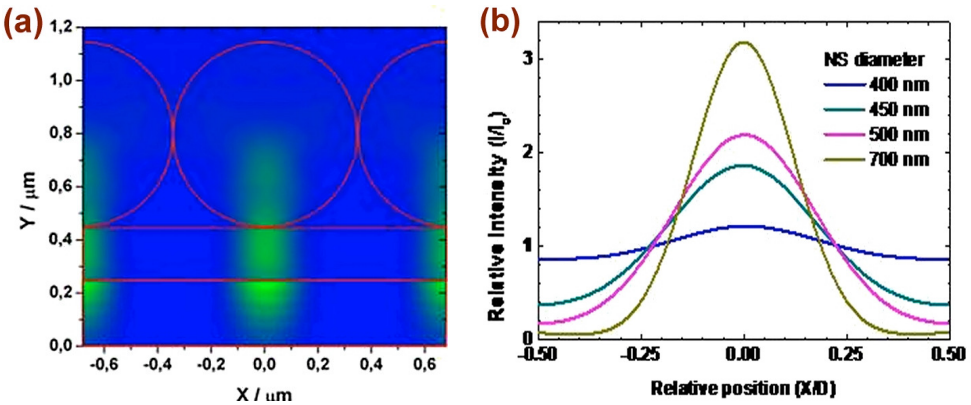

Figure 1. *Cross sectional energy distribution during the nanosphere photolithography process simulated by FDTD method at sphere diameter of 700 nm (scaled from deep blue minimum to light green maximum) (a). In-plane intensity distribution in the photoresist at different NS diameters (b).*

Nanosphere photolithography (NSPL) is a promising inexpensive and up-scalable patterning technique where the contact mask is a self-assembled nanosphere (NS) monolayer on top of a photoresist layer. The polystyrene particles, like spherical lens, focus the UV light into the photoresist and intensify it to exceed exposure dose limit just in the focused region. According to the finite-difference time-domain (FDTD) simulations the NSs with diameter below the exposure wavelength of 405 nm does not generate a definite and distinguishable focal spot in the thin photoresist. Above this diameter limit, however, focal spots appear directly underneath the NSs as shown on the example of 700 nm NS diameter in Fig. 1a. By increasing the diameter of the nanospheres from 400 to 700 nm this focusing behavior becomes gradually stronger with increasing in-plane exposure modulation as illustrated in Fig. 1b.
The theoretically and experimentally optimized NSPL with 700 nm NS diameter was utilized on single crystal ZnO substrate to grow regular nanopillar array. SEM observation in Fig. 2 revealed that the hexagonal pattern was transferred with high fidelity from the Langmuir Blodgett deposited NS layer via the photoresist to the nanopillar array. According to the analysis of the high resolution SEM images, nanospheres with an averaged diameter of 692±12 nm resulted in an average hole diameter of 379± 4 nm in the photoresist after development and an average nanopillar diameter of 466±18 nm after wet chemical growth.

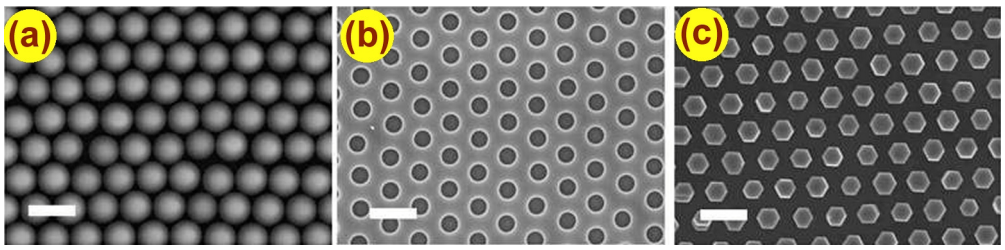

Figure 2. *Top-view SEM images of polystyrene nanospheres (a), patterned photoresist after nanosphere lithography (b), and grown nanopillars (c).*

The Kelvin Probe Force Microscopy (KPFM) map, recorded by a Pt coated tip in air showed slightly different relative value for the polar top-surface of ZnO nanopillars (W_{NR}-$W_{Pt\text{-}tip}$=0.56 eV) and for the surface of substrate (W_{NR}-$W_{Pt\text{-}tip}$=0.59 eV) (Fig. 3). By calibrating the Pt tip with an air-stable Highly Ordered Pyrolytic Graphite (HOPG) surface, the absolute work function of the n-type ZnO can also be estimated (4.2-4.3 eV).

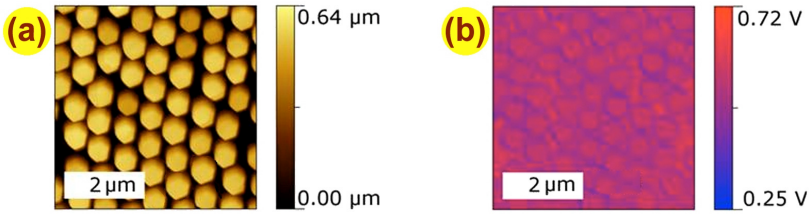

Figure 3. *AFM height image (a), and the corresponding work-function map (b) taken on the regular ZnO nanopillars.*

Hydrothermal synthesis of horizontal ZnO nanowires for biosensor application

(OTKA K76287)

N. Q. Khanh, I. Lukács, R. Erdélyi, Z. Szabó, E. Fülöp, and J. Volk

ZnO as a biocompatible, wide band gap semiconductor is a very promising candidate material for chemical and biosensor applications. Selectively grown lateral 1D nanostructures will be an important development since these laterally orientated nanostructures constitute the very basic building blocks for the realization of integrated nanoscale devices on a planar substrate. In our approach, the chrome electrodes have been deposited on the top of the RF sputtered ZnO seed layer to prevent the growth of nanowire in vertical direction. After patterning by lift-off the nanowires have been synthesized in zinc nitrate and hexamethylenetetramine equimolar (0.2 mM) aqueous solution at 95^{o}C for 14 hours.
The horizontal nanowires (NWs), as revealed by TEM, are single crystalline grown in *c*-direction and have a hollow structure (Fig. 1).

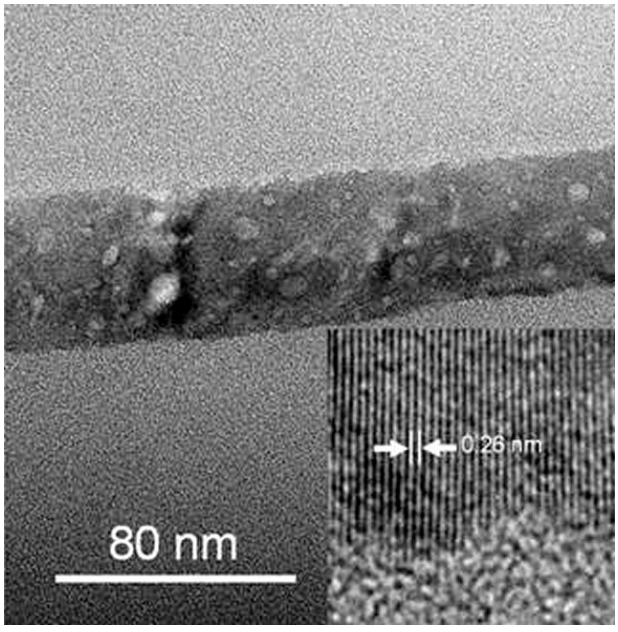

Figure 1. *TEM image of ZnO nanowires laterally grown in 0.2 mM aqueous zinc nitrate/(HMT) solution at 95 °C for 14 h. Shown in the inset is HRTEM micrograph.*

The voids inside the NWs decrease the cross-section of the wires, therefore further increase the sensitivity of the sensor *via* increasing surface to volume ratio may be expected. In our device, the electrical conduction between two electrodes is ensured by the interlacing of the NWs grown from them, which has obscured nonlinearity mani-festing an Ohmic-like contact. Sensing capability of the lateral NW based device has been demonstrated for *Z* domain/immunoglobulin (IgG) pairs. To prevent the Faraday current, the electrodes have been isolated using polymethyl methacrylate (PMMA) polimer and electron lithography.

The modulation effect was observed at very low concentration of IgG (25 nM).

ZnO nanowire based organic-inorganic bulk heterojunction solar cell

(AUT-HUN TéT)

R. Erdélyi, Z. Szabó, and J. Volk

Although the performance of the bulk heterojunction (BHJ) solar cells has been continuously improved in the last decade, the low electron mobility of the n-type fullerene derivatives remains a limiting factor. ZnO nanowire (NW) covered anodes may overcome this obstacle by ensuring high electron mobility direct pathway for the generated electrons. In this study multilayer structure on glass substrate build up of consecutive layers of indium tin oxide, ZnO, ZnO (NW), organic blend and silver based inverted photovoltaic cells with different active layer thicknesses were fabricated and characterized. The organic blend consisted of the same amount of fullerene derivative electron conductor (PCBM, n-type) and of a newly optimized hole conductor (PBDTTT-C, p-type) material. The thickness of the infiltrated ZnO NW/organic blend composite layer was changed by the concentration of the organic component in the solution before spin coating (10-25 mg/ml). Current-voltage curves taken under a light illumination of ~50 mW/cm^2 revealed that the optimal blend concentration is around 15-20 mg/ml. External quantum efficiency measurements show similar trends, max. EQE values occur at 15-20 mg/ml concentrations (Fig. 1).

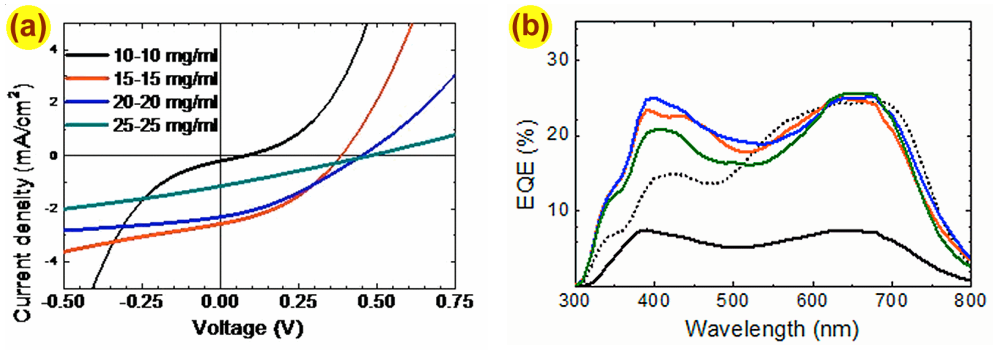

Figure 1. *Measured current density-voltage curve under illumination (50 mW/cm^2) (a), and the corresponding external quantum effeciency spectra (b).*

These results show that the thickness of polymer blend has to be tuned to the nanostructured electrode. Too thin layer can be pierced by the ZnO, which leads to a short-circuit of the photovoltaic (PV) cell. On the other hand, too thick blend is also deteriorative, since it increases the serial resistance and enhances the electron-hole recombination probability by increasing their path length. This explanation is in line with SEM observation of the cleaved devices at moderate layer thickness the ZnO NW are fully covered by the organic blend but this over-layer is still thin compared to the 25 mg/ml case (Fig. 2).

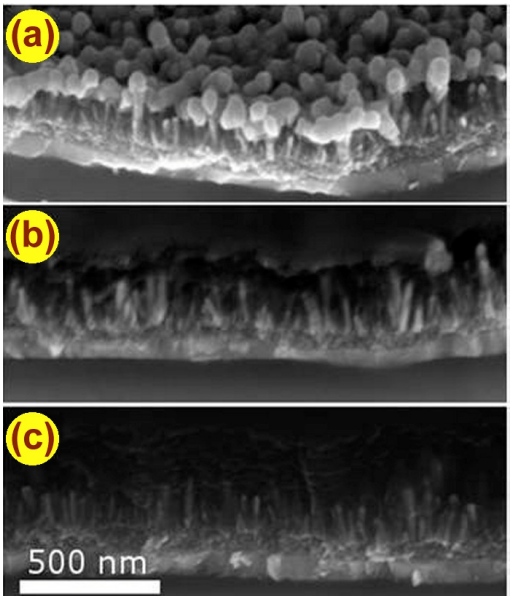

Figure 2. *Cross-sectional SEM image of hybrid photovoltaic cells with three different active layer thicknesses. The corresponding blend concentration are 10 (a), 17.5 (b), and 25 mg/ml (c).*

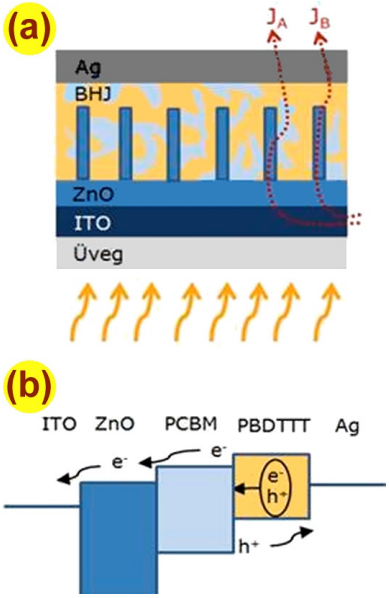

Figure 3. *Scheme of the hybrid photovoltaic cell (a) and band diagram illustrating the dominant A-type photocurrent generation route (b).*

The complex n-type ZnO/n-type PCBM/ p type polymer composite active layer allow several exciton generation/dissociation scenarios (Fig. 3a). One of them is illustrated in Fig. 3. The incident photon generate a strongly bound exciton in the PBDTTT-C layer which is dissociated at the PCBM/ PBDTTT-C interface. The free electron is collected to the anode via the high specific surface ZnO nanostructure.

Improvements in FIB TEM lamella preparation

A. L. Tóth , L. Illés, Gy. Sáfrán , and Gy. Z. Radnóczi

The transmission electron microscopy (TEM) is one of the most versatile methods of the visualization and investigation of micro- and nanosized structures. The ideal TEM sample has to be free of artifacts. The amorphization is one of the most detrimental artifact of ion beam preparation, and unfortunately the Si samples are sensitive to amorphization. We optimized the milling sequence, the angle of incident beam, the intensity and energy of the Ga^+ ion beam current, in order to decrease the amorphization. Combining the capabilities of the updated SmartSEM software instead of a fixed 30 keV a wider (10-30 keV) energy range became accessible. The sample with optimized FIB parameters exhibit ~90 nm broad amorphized region, if we estimate identical wedge shape of the thinned edge of the sample. This means a much higher quality TEM sample with less artifact.

Complex Systems Department

Head: György SZABÓ, D.Sc., scientific advisor

Research Staff

- István BORSOS
- Imre EÖRDÖGH, dr. Univ.
- Zoltán JUHÁSZ, Ph.D.
- Géza ÓDOR, D.Sc., scientific advisor
- Károly SZÁSZ, engineer
- Attila SZOLNOKI, D.Sc., scientific advisor

Ph.D. students / Diploma workers

- Lilla CZAKÓ, B.Sc./M.Sc. student

The main scientific activity of this group is focused on the application of tools and concepts of statistical physics for the quantitative investigation of various non-equilibrium models describing solid state systems and evolutionary or co-evolutionary games on graphs. As a large portion of our efforts is based on numerical simulations therefore some of us studied the ways to enhance our computational capacities. After installing a computer facility (of 4 TFlop capacity) with the application of graphical processors Géza Ódor and István Borsos in collaboration with Heinig and Liedke (FZD, Dresden-Rossendorf) developed several algorithms and their speed/efficiency are compared for the analysis of different large lattice systems. This system allowed them to investigate numerically the surface patterns occurring on crystalline surfaces under different technological conditions. In addition, Ódor together with Juhász (SzFKI, Budapest), Munoz (University of Granada) and Castellano (University of Roma "La Sapienza") were capable to study extremely slow dynamical processes for several types of large networks.

Two engineers, Eördögh and Szász, improved the efficiency of image processing algorithms developed by them previously for the quantification of morphological features used in the control of several technological processes. These investigations/developments are made in collaboration with their industrial partners (e.g., General Electric Hungary).

Results achieved in research of evolutionary games and folk songs are surveyed below. The main results are published in scientific journals. The international echo to the previous results of this group is characterized by 850 citations in this year. Behind this figure there are several papers available on the list of Top-10 for ranked scientific journals.

Evolutionary games

(OTKA K73449)

G. Szabó and A. Szolnoki

The evolutionary game theory provides a general mathematical background for the quantitative analysis of large living systems composed of small objects. In the corresponding models the players can represent microbes, plants, animals, human individuals or even their groups (firms, countries, etc). The concept of payoff matrix is used to describe the interactions between the players who can modify their own strategy (decision, types, etc.) by following an evolutionary rule determined by payoff differences dependent on the neighboring strategies.

Within the framework of evolutionary game theory we studied the efficiency of punishments in the maintenance of cooperative behavior among selfish players in the case of social dilemmas. More precisely, we have studied a system of players located on the sites of a square lattice. The player's income comes from five five-person public goods games (PGG) played with their neighbors. For the simplest two-strategy case the players decide simultaneously whether they contribute a unit sum into a common pool or not. The corresponding strategies represent cooperation (C) and defection (D). For each group the total investment is multiplied by a factor r and divided equally among the group members irrespectively of their cooperative or defective behavior. In this situation the rational (selfish) players should decline investment if the cost of investment exceeds the part of profit related to their own investment. As a result the selfish players cannot exploit the advantage of mutual cooperation, instead of it, their society evolves into the "tragedy of the commons" where all the players choose defection.

According to many experimental and theoretical investigations the introduction of punishment supports the maintenance of cooperative behavior. In these models the defector's income is reduced by a fine if a neighboring punisher pays the cost of punishment. First we studied the effects a pool-punishment as an additional strategy O in spatial evolutionary PGGs and the results were contrasted with the case of peer-punishment (strategy E) when the punishers pay the cost of punishment only if it is necessary, that is, when the defection is sanctioned. In the case of pool-punishers the punisher's contributions cover the cost of institutions (police, judge, etc.) independently of their efficiency. As a result, in the absence of defection the pure income of peer-punishers is equivalent to those of cooperators considered as "second order free-riders" while a pool-punisher's income is always exceeded by the cooperators. A preceding study on pool-punishment in well-mixed populations concluded that pool-punishers can prevail over peer-punishers only if the second-order free-riders are punished as well. For the present spatial systems a randomly chosen player x can adopt the strategy from one of the neighbors (y) with a probability $W=1/(1+\exp(P_x-P_y)/K)$ dependent on the payoff difference (P_x-P_y) and a noise parameter K characterizing the stochasticity in the imitation process. The resultant stationary states are summarized on phase diagrams exhibiting a surprisingly

rich set of behaviors when tuning the multiplicative factor as well as the cost and fine parameters at a fixed noise level.

The snapshot in Fig. 1 illustrates how cooperators spread along the interfaces separating the territory of D and E strategies. Within a certain range of parameters the presence of C along these interfaces reverses the direction of invasion and yields a selforganizing pattern with three strategies or a trend towards the homogeneous defection in a way resembling the real-life situation referred as "The Moor has done his duty, the Moor may go".

Figure 1. *Spreading of cooperators along the boundaries separating the regions of peer-punishers and defectors..*

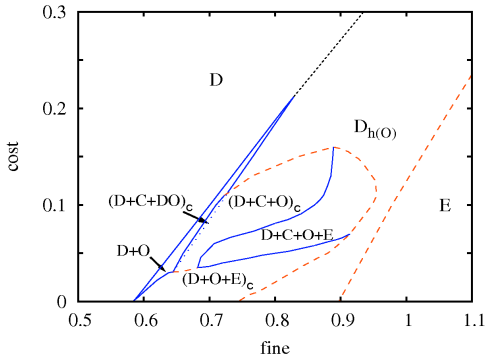

Figure 2. *Fine-cost phase diagram for r=3.5 in the four-strategy system at the low noise limit.*

In most of the cases the peer-punishers are found to be more efficient in the elimination of the "tragedy of the commons" when all players choose defection. Notice that only peer-punishers (E) remain alive if the fine exceeds a threshold value dependent on cost as indicated in the phase diagram in Fig. 2. For the given value of r defectors prevail the whole system, if the fine is lower than another threshold value increasing linearly with the cost. Sometimes, however, both types of punishments coexist with cooperators and defectors (see the D+C+O+E region in the phase diagram of Fig. 2.

Beside the above models we have studied other evolutionary games, too. For example, the competition between the fraternal and egoist players exhibit a more complex behavior where two of the four strategies (egoist defector, egoist cooperator, fraternal defector, fraternal cooperator) form a sublattice ordered structure on the analogy of the antiferromagnetic arrangements of spin "up" and "down" states in the two-dimensional antiferromagnetic materials. The exploration of the above-mentioned phenomena and phase diagrams required the extension of the stability analysis both numerically and theoretically. In many cases we faced phenomena where the concepts of competing associations proved to be useful in the explanation of the self-organizing spatio-temporal patterns.

A new AI technique for analyzing vector data applied for computational ethnomusicology

(OTKA K81954)

Z. Juhász

A widely used kind of artificial neural networks, the self organising map (SOM) proved to be a very versatile tool of computing musicology. The operation of a SOM can be summarised for such a purpose as follows: Our input data to be classified are contour vectors, containing subsequent pitch values of melodies of a folksong database. The main goal of self organising mapping is to characterise the local condensations of the multidimensional point system constructed by the set of these melody contour vectors by a significantly smaller set of locally averaged "contour type vectors". Beyond that, the SOM assigns the resulting contour type vectors to the lattice points of a grid topographically. However, stretching a more complicated structure into a plain lattice results in a significant loss of the accuracy of the classification on one hand, and a non-perspicuous map on the other hand. Therefore, we elaborated a system combining the SOM technique with a special version of the multidimensional scaling (MDS) algorithm. In MDS technique, the input data to be visualised are presented in a quadratic matrix containing some distance-like or similarity-like values between some objects. The aim of the algorithm is to represent the objects (in our case: melody contour vectors) in a low dimensional space with the requirement that the distances of the low dimensional points must optimally correspond to the input values.

The first stage of our new system is a simplified, non-topographic version of SOM learning. In the second stage, the topographic low-dimensional mapping of the resulting contour type vectors is accomplished by a variant of the MDS algorithm. This allows us to project the spatial regularities of the multidimensional input vector system to a continuous low-dimensional space without the restrictions of the planar grid structure of the SOM. In order to express the contact to the original SOM principle and to emphasize the increased degree of freedom of the low dimensional mapping, we call this technique "self organising cloud" (SOC).

We applied the SOC to analyse the characteristic melody forms and their connections in 31 representative Eurasian and North-American folksong collections. The studied cultures are as follows: Chinese, Mongolian, Kyrgyz, Mari-Chuvash-Tatar-Votiac (Volga Region), Sicilian, Bulgarian, Azeri, Anatolian, Karachay, Hungarian, Slovak, Moravian, Romanian, Cassubian (North-Poland), Warmian (East-Poland), Great-Polish (Southern-Central Poland), Finnish, Norwegian, German, Luxembourgish, French, Dutch, Irish-Scottish-English (mainly Appalachian), Spanish, Dakota, Komi, Chanty, Serbian-Croatian (Balkan), Kurd, Russian (Pskov). Our database contains digital notations of nearly 32000 folk songs arising from different written sources. We trained the SOC by a unified set of these 32000 melodies, in order to determine all of the characteristic forms existing anywhere in the given cultures. The resulting 2D

point system shows a very geographic and musically well interpretable structure, as it is shown by some characteristic contour type vectors in Fig. 1.
The individual cultures activate different areas of the above mentioned unified musical map. The analysis of the overlaps of these areas resulted in a very visual graph of the connections of the cultures, with well identifiable "musical language groups" (Fig. 2). The graph was also automatically constructed using a special variant of the MDS technique.

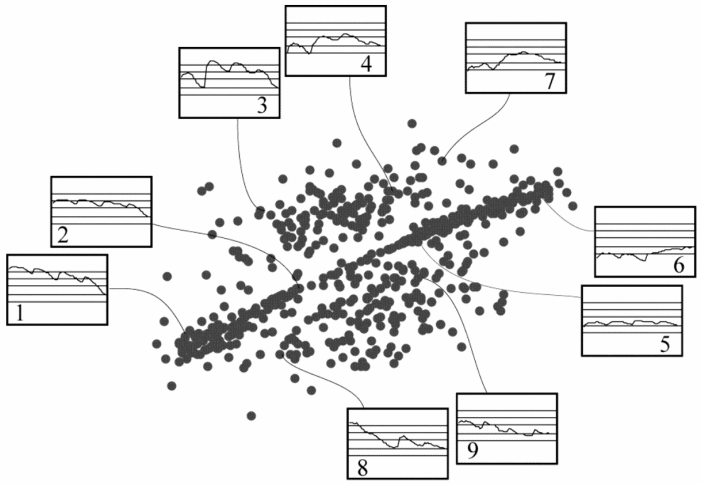

Figure 1. *MDS point system and characteristic contour type forms in the clusters of the unified melody collection.*

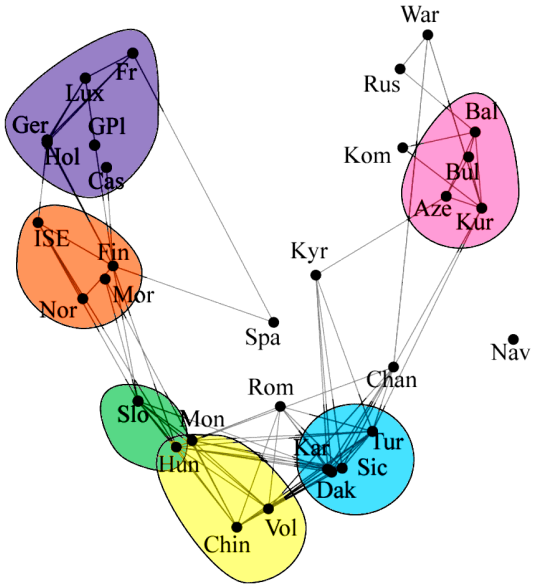

Figure 2. *MDS plot of the connections of 31 folk music cultures.*

ACTIVITIES

MFA Seminar Talks

2011.01.12 **Tamás UNGÁR**
(ELTE, Budapest, Hungary): "*Spallation neutron source in Oak Ridge*"

2011.01.19 **István LAGZI**
(ELTE, Budapest, Hungary): "*Nanostructures – link between nanoscience and non-linear chemical dynamics*"

2011.01.26 **András PÁLYI**
(ELTE, Budapest, Hungary): "*Electron Valley Resonance – coherent control of the valley-izospin in carbon nanotubes*"

2011.03.09 **József CSERTI**
(ELTE, Budapest, Hungary): "*The Klein-paradox or Fresnel-forms and negative refractive index in graphene*"

2011.03.23 **Alexander JABLONSKI**
(PAS, Poland): "*The back-scattering correction factor in AES: current status*"

2011.04.13 **Michael GOLUB**
(Tel Aviv): "*Scalar and resonance domain diffractive optical elements and their applications*"

2011.05.16 **Z. Q. QIU**
(Berkeley): "*Quantum well states in magnetic nanostructures*"

2011.05.25 **Miklós FRIED**
(MTA MFA, Budapest, Hungary): "*Adventures of the wide-angle ellipsometer in the USA*"

2011.06.16 **A. SUBRAHMANYAN**
(Madras): "*Thin films in bio-medical engineering: emerging concepts*"

2011.09.21 **Zsolt SZABÓ**
(BME, Budapest, Hungary): "*Composite thin films for subwavelength imaging*"

2011.10.05 **Nikolay GALKIN**
(Vladivostok, Russia): "*Structure and properties of Si, silicide nano-hetero-structures with buried nanocrystals*"

2011.10.05 **Konstantin GALKIN**
(Vladivostok, Russia): "*Thermoelectrical properties of Si double heterostructures with buried Mg-Si 2D crystals*"

2011.10.19 **Gábor JUHÁSZ**
(ELTE, Budapest, Hungary): "*Molecular complexity approach: the systems biology in neuroscience*"

2011.10.26 **Gábor JUHÁSZ**
(ELTE, Budapest, Hungary): "*What to measure in the nervous system next?*"

2011.11.02 **István DÓDONY**
(ELTE, Budapest, Hungary): "*Transmission electron microscopy for materials science*"

2011.11.23 **Péter NEMES-INCZE**
(MTA MFA, Budapest, Hungary): "*Fabrication and characterization of graphene and carbon nanotube based nanostructures*"

2011.11.30 **Fréderic CAYREL**
(Tours): "*Recent progresses in GaN power rectifier*"

Research and Development Partners, Foreign Visitors

AUFHAMMER, Alexander *(SUSS)*
BACAKOVA, Lucie *(Institute of Physiology, CAS, Prague, Czech Republic)*
BAKKER, Fritz *(JRC Petten, Netherlands)*
BENOIT, Nicole *(CNRS, Strasbourg)*
BERNHARDT, Ingolf *(Saarland University, Saarbrücken)*
BIRÓ Domokos *(Sapientia Erdélyi Magyar Tudományegyetem, Tg-Mures, Romania)*
BYONG-TAEK, Lee *(School of Medicine, Soonchunhyang Univ., Korea)*
CAYREL, Frederic *(LMP, Tours, France)*
CHANG-HOON, Chae *(Clinical Dentistry, Hallym University, Korea)*
CHIRCO, Piero *(SOFTEC Technology and Research, Bologna, Italy)*
CHRISTOF, Hübner *(Fraunhofer Inst. for Chem. Techn. ICT, Pfinztal, Germany)*
CHUNG-YU, Wu *(Program Director)*
CSEHOVÁ, Erika *(Institute of Materials Research, Kosice, Slovak Republic)*
DELAGE, Sylvain *(III-V Lab of Alcatel-Thales)*
DIMTRUK, Mikola *(Institute of Semiconductor Physics, Kiev, Ukraine)*
DONG, Yizhi *(Deputy DirectorShenyang Development and Reform Commission)*
DUMITRICA, Traian *(University of Minnesota, USA)*
DUSZA, Ján *(Institute of Materials Research, Kosice, Slovak Republic)*
DUSZOVÁ, Annamária *(Institute of Materials Research, Kosice, Slovak Republic)*
EHIASARIAN, A.P. *(Nanotechnology Centre for PVD Research, Materials and Engineering Research Institute, Sheffield Hallam University, UK)*
FABIAN, Dortu *(Multitel Ltd.)*
FELDER-FLESCH, Delphine *(CNRS, Strasbourg)*
FRIGERI, Cesare *(Instituto CNR-JMEN, Italy)*
GALKIN, Konstantin *(Institute of Automation and Control Processes, Far Eastern Branch of Russian Academy of Sciences)*
GALKIN, Nikolay *(Institute of Automation and Control Processes, Far Eastern Branch of Russian Academy of Sciences)*
GÖLLER, Gultekin *(Istanbul Technical University, Turkey)*
GOLUP, Michael *(Tel Aviv University)*
GOUMA, Pelagia-Irene *(State University of New York, Stony Brook)*
GROBERT, Nicole *(University of Oxford)*
GRUBER, Stefan Gruber *(Hochschule, München)*
GUMPRECHT, Thomas *(FhG IISB, Erlangen, Germany)*
HALGAS, Radoslav *(IMR SAS)*
HAMPSHIRE, Stuart *(Materials Ireland Research Institute, Limerick University)*
HEGEDŰSOVÁ, Lucia *(Institute of Materials Research, Kosice, Slovak Republic)*

HEINIG, Karl-Heinz *(Helmholtz-Zentrum Dresden-Rossendorf)*
HORNÁK, Peter *(Institute of Materials Research, Kosice, Slovak Republic)*
HOVSEPIAN, P.Eh. *(Nanotechnology Centre for PVD Research, Materials and Engineering Research Institute, Sheffield Hallam University, UK)*
HUBER, Carmen *(National Science Foundation, USA)*
HÜBNER, Christof *(Fraunhofer Inst. for Chem. Techn. ICT, Pfinztal, Germany)*
HULTMAN, Lars *(Thin Film Physics Dept., IFM, Linköping University, Sweden)*
HVIZDOS, Pavol *(Institute of Materials Research, Kosice, Slovak Republic)*
HWANG Chan, Young *(Korean Research Institute of Standards and Science, Daejon, South Korea)*
ICHIKAWA, Mr. *(Tateyama Kagaku, Toyama, Japan)*
JABLONSKI, Alexander *(Inst. Physical Chemistry, Polish TA, Warsawa, Poland)*
JEDRYKA, Ewa *(Institute of Physics, Warszawa, Poland)*
JOU-LAY, Huang *(Program Co-Director)*
JUN, Ariake *(Akita R&D Center, Akita, Japan)*
KASIAROVÁ, Monika *(Institute of Materials Research, Kosice, Slovak Republic)*
KELLING, Jeffrey *(Helmholtz-Zentrum Dresden-Rossendorf)*
KHALFAOUI, Wahid *(LMP, Tours, France)*
KIM, Wondong *(Korea Research Inst. of Standards and Science, Daejon, Korea)*
KIM, Yong Suk *(Korean Trade Agency, Korea)*
KIM, Yong Sung *(Korea Research Inst. of Standards and Science, Daejon, Korea)*
KIRIY, Anton *(IPF, Dresden, Germany)*
KOVALCÍKOVÁ, Alexandra *(Institute of Materials Res., Kosice, Slovak Republic)*
KRAFT, Marie Pierre *(CNRS, Strasbourg)*
KRAMSKA, Pavlina *(Assistant STD TECO Prague, Czech Republic)*
KUENY-STOTZ, Marie *(CNRS, Strasbourg)*
LA, Truong *(CNRS, Strasbourg)*
LAMBIN, Philippe *(Facultés Univ. Notre-Dame de la Paix, Namur, Belgium)*
LI ,Wei *(Deputy Director, Shenyang Science and Technology Bureau, China)*
LIANFANG, Wang *(Director, Shenyang Liaozhong Science and Technology Bureau)*
LIEDKE, Bartosz *(Helmholtz-Zentrum Dresden-Rossendorf)*
LOBOTKA, Peter *(Electrotechnical Inst. of SAV, Bratislava, Slovakia)*
LOFAJ, Frantisek *(Institute of Materials Research, Kosice, Slovak Republic)*
MAMYKIN, Sergey *(Institute of Semiconductor Physics, Kiev, Ukraine)*
MAYRHOFER, P. *(Department of Physical Metallurgy and Materials Testing, Montanuversität Leoben, Leoben, Austria)*
MING-DOU, Ker *(ITRI, Shinchu, Taiwan)*
MIZUGUCHI, Mr. *(Tateyama Kagaku, Toyama, Japan)*
MOERSDORF, Daniel *(Saarland University, Saarbrücken)*

MORGIEL, Jerzy *(Inst. of Metallurgy, Polish Academy of Sci., Krakow, Poland)*
NAGATA, Takahiro *(NIMS, Tsukuba, Japan)*
NAJIMA, Mr. *(Tateyama Kagaku, Toyama, Japan)*
NGUYEN PHUC, Nghia *(CNRS, Strasbourg)*
NUTSCH, Andreas *(Fraunhofer IISB, Germany)*
OSSI, Paolo *(Milano University, Italy Sebastiano Trusso, CNR, Messina, Italy)*
PANAGIOTOPOULOS, Ioannis *(Dept. of Materials Science and Engineering, University of Ioannina, Greece)*
PERC, Matjaz *(University of Maribor, Slovenia)*
PETER CHUNG-YU, Wu *(ITRI, Shinchu, Taiwan)*
PILVI, Tero *(Picosun Oy, Finland)*
PISCHOW, Kaj *(Savo-Solar Oy, Mikkeli, Finland)*
POLAVARAPU, Prasad *(CNRS, Strasbourg)*
POURROY, Genevieve *(CNRS Strasbourg)*
PRAMATOROVA, Lyliana *(Institute of Solid State Physics (ISSP), Sofia, Bulgaria)*
PUCHY, Viktor *(Institute of Materials Research, Kosice, Slovak Republic)*
QIU, Z.Q. *(Department of Physics, University of California at Berkeley, USA)*
RODRÍGUEZ, Pedro *(Institute for Materials Science of Madrid, Spain)*
ROEDRE, Georg *(Fraunhofer IISB, Germany)*
ROLAND, Bogdan *(Ukraine)*
RÖSCH, Matthias *(Heidelberg Instruments, Heidelberg, Germany)*
ROSOVA, Alica *(ELU SAV, Electrotechnical Institute of the SAS, Bratislava)*
ROTH, Alain *(CNRS, Strasbourg, France)*
RUIFENG, Guo *(General Manager, Shenyang High Precision CNC Techn. Co.)*
SAHIN, Filiz Cinar *(Adnan Tekin High Tech. Cer. and Comp. Res. Center, Istanbul)*
SANG DUK, Park *(Vice Mayor for Administrative Affairs of Daejeon)*
SARICIFTCI, Niyazi Serdar *(Linz Inst. for Organic Solar Cells, JKU, Linz, Austria)*
SEVC, Peter *(IMR SAS)*
SHIEH, Jonathan *(Director STD TECO Prague, Czech Republic)*
SHIMIZU, Mr. *(Tateyama Kagaku, Toyama, Japan)*
SIMON, Hervé *(Eurorad, Strasbourg)*
SLUCKIN, Timothy *(Southampton University, UK)*
STAN, Katarzyna *(Institute of Meatallurgy, Poland)*
STOEMEONES, J. *(University of Thessaloniki, Greece)*
SUBRAHMANYAM, A. *(Indian Instiotute of Technology, Madras, Chennai, India)*
SUZUKI, Takashi *(Akita R&D Center, Akita, Japan)*
SZLEZYNGER, Maciej *(Institute of Meatallurgy, Poland)*
TAKAMI, Seiichi *(Tohoku University, Sendai, Japan)*
TATARKO, Peter *(Institute of Materials Research, Kosice, Slovak Republic)*

TOBISCH, Alexander *(FhG IISB, Erlangen, Germany)*
TOMAS, Ivan *(Czech Academy of Sciences, Prague)*
TOU TECK, Yong *(Multimedia University, Selangor, Malaysia)*
TSUNG-TSAN, Su *(ITRI, Shinchu, Program Co-Director, Taiwan)*
VAVRA, Ivo *(Electrotechnical Inst. of SAV, Bratislava, Slovakia)*
VÁZQUEZ, Manuel *(Institute for Materials Science of Madrid, Spain)*
VIGNERON, Jean Paul *(Facultés Univ. Notre-Dame de la Paix, Namur, Belgium)*
VILA, Roger *(Institut de Biologia Evolutiva, Barcelona, Spain)*
VRAUX, Jean-Pierre *(CNRS, Strasbourg)*
WAKAYAMA, Yutaka *(National Institute for Materials Science (NIMS), Japan)*
WANG, Zhen *(Hong Kong Babtist University, Kowloon Tong, Hong Kong)*
WATON, Gilles *(CNRS, Strasbourg, France)*
WHITE, Matthew *(LIOS, Linz, Austria)*
WOO, Seung Je *(Manager of International Exchange Team)*
YAKOVLEV, Yuri *(Ioffe Institute, Sankt-Peterburg, Russia)*
YANG-TUNG, Huang *(ITRI, Shinchu, Taiwan)*
YUCEL, Onuralp *(Adnan Tekin High Tech. Cer. and Comp. Res. Center, Istanbul)*
YU-TING, Cheng *(ITRI, Shinchu, Taiwan)*
ZAYIM, Esra Ozkan *(Physics Institute, Istanbul Technical University)*
ZHANG, Ge *(Director, Shenyang Association for International Exchange of Personnel)*
ZHANG, Hengxi *(Deputy Director, Shenyang, Financial Management Bureau)*
ZHANG, Qingfeng *(Department Director, Shenyang Science and Technology Bureau)*

MŰSZAKI FIZIKAI ÉS ANYAGTUDOMÁNYI INTÉZET

INSTITUTE FOR TECHNICAL PHYSICS AND MATERIALS SCIENCE

PHOTOVOLTAIC SERVICES - FOTOVILLAMOS MÉRÉSI SZOLGÁLTATÁS

Az MTA TTK Műszaki Fizikai és Anyagtudományi Intézet (MFA) több évtizedes tapasztalattal rendelkezik szervetlen, funkcionális anyagok mérése és minősítése terén. Egyik kiemelt kutatási területe a fotovillamos szerkezetek és anyagok előállítása és vizsgálata ipari együttműködésben.
Az MFA 2008-tól üzemelteti a fotovillamos napelemek bemérésére és minősítésére alkalmas korszerű vizsgáló-laboratóriumát.

A mérőberendezés műszaki adatai:

Energy Equipment Testing Service Limited (E.E.T.S)
PVMT 11250 Module Tester

- A mérhető maximális napelem modul felület: 1.5m x 0.75m.
- A megvilágításhoz Philips 1462I Halo Nr. 55060 típusú halogénizzó mátrixot használ 2% laterális homogenitás mellett.
- A megvilágítás egyenletességének pontossági osztálya: IEC 904-9 szabvány szerint “A”.
- A megvilágítás folyamatos üzemmódú, intenzitása 750-1250 W/m^2 között állítható.
- A megvilágítás erősségét kalibrált referencia cella méri.
- Méréshatárok:
  - Feszültség: 0-120 V DC (1% FSO)
  - Áramerősség: 0 - 20 A DC (1% FSO)

A műnaphoz kapcsolt számítógépes mérő-adatgyűjtő rendszer rögzíti:
- a napelem ill. modul áram-feszültség jelleggörbéjét;
- a teljesítmény-feszültség jelleggörbéjét;
- a minta pillanatnyi hőmérsékletét.

A berendezés külön igény és egyeztetés alapján lehetővé tesz:
- hőmérsékletfüggő paraméter-vizsgálatot;
- megvilágításfüggő paraméter-vizsgálatot;
- vékonyréteg modulok bemérését.

Visitors: Konkoly-Thege M. út 29-33, BUDAPEST, 1121 HUNGARY, **Mail:** P.O. Box 49., H-1525, **Fax:** +36-1-3922226
Phone, Director: +36-1-3922224, **Phone, Administration:** +36-1-3922227, **Web:** http://www.ttk.mta.hu/

MŰSZAKI FIZIKAI ÉS ANYAGTUDOMÁNYI INTÉZET

INSTITUTE FOR TECHNICAL PHYSICS AND MATERIALS SCIENCE

Az intézet mérési szolgáltaltást ajánl mono- illetve polikristályos napelemeken és napelem-paneleken az alábbi feltételekkel:

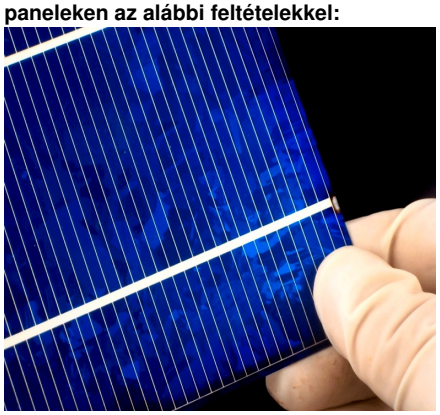

Mérési beállítások:

- 800 W/ m^2 , 1000 W/ m^2 és 12000 W/m^2 besugárzás, műnappal;
- 25 °C normált hőmérséklet értéken történő mérés.

Mért paraméterek:

- üresjárási feszültség /open circuit voltage (U_{OC});
- rövidzárási áram / short circuit current (I_{SC});
- maximális teljesítmény, feszültség és áram (U_{MPP}, I_{MPP}, P_{MPP});
- modulhatásfok /solar module efficiency (η);
- kitöltési tényező /fill factor (FF).

A mérési értékeket az IEC 60891 szabvány szerint standard hőmérsékletre korrigálva adjuk meg.

Jegyzőkönyv

A mérésről az MTA TTK MFA jegyzőkönyvet állít ki, amely tartalmazza:

- a modul azonosítóját;
  - gyártó,
  - típus,
  - serial number,
- táblázatot a névleges paraméterekkel;
- táblázatot a mért értékekkel;
- mért karakterisztikákat;
- a mérést végző nevét;
- a mérések idejét.

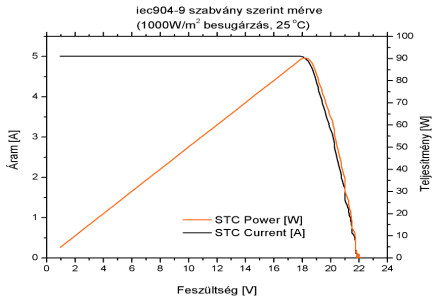

A szolgáltatás ára

A szolgáltatás ára magában foglalja a vizsgálat elvégzésének költségeit (kalibrálás, mérések) és a jegyzőkönyv készítését. Az ár nem tartalmazza:

- a mintadarab laboratóriumba történő oda- és visszaszállítását;
- az egyedi igények alapján kért mérések költségeit.

A standard program szerinti szolgáltatás ára mintadarabonként: 60.000 Ft+ ÁFA.

Nagyobb mennyiség bemérésének megrendelése esetén kedvezményt adunk, speciális igények esetében az ár egyedi megállapodás alapján kerül meghatározásra.

További információ, előzetes műszaki egyeztetés:

Dr. Lábadi Zoltán, laborvezető
Labadi.zoltan@ttk.mta.hu
+36-1-392 2222/3528

Visitors: Konkoly-Thege M. út 29-33, BUDAPEST, 1121 HUNGARY, **Mail:** P.O. Box 49., H-1525, **Fax:** +36-1-3922226
Phone, Director: +36-1-3922224, **Phone, Administration:** +36-1-3922227, **Web:** http://www.ttk.mta.hu/

MŰSZAKI FIZIKAI ÉS ANYAGTUDOMÁNYI INTÉZET

INSTITUTE FOR TECHNICAL PHYSICS AND MATERIALS SCIENCE

AKKREDITÁLT VIZSGÁLÓLABORATÓRIUM MÉRÉSI SZOLGÁLTATÁSA

http://www.ellipszometria.hu/

Az MTA TTK Műszaki Fizikai és Anyagtudományi Intézet (MFA) több évtizedes tapasztalattal rendelkezik anyagok vizsgálata és minősítése terén. Az ellipszometria olyan polarizációs optikai módszer, amely alkalmas mikrométernél vékonyabb rétegek vastagságának nanométeres pontosságú roncsolásmentes mérésére, valamint a réteg törésmutatójának, és számos, a törésmutatótól függő tulajdonságának (pl. kristályosság, homogenitás) meghatározására.


AKKREDITÁLÁSI OKIRAT
ACCREDITATION CERTIFICATE

Az MFA Ellipszometria Laboratórium a Nemzeti Akkreditáló Testület által akkreditált, az ISO 17025 szabvány szerint működő mérőlabor. A laboratórium tagja az ANNA konzorciumnak (http://www.i3-anna.org/) amely széles körben kínál nanotechnológiákhoz hozzáférhető vizsgálati módszereket.

Alkalmazási területek:

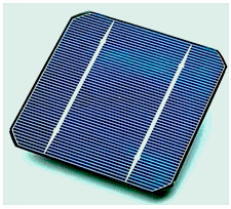
Napelemtechnológia

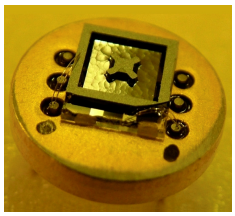
Szenzorikai rétegek

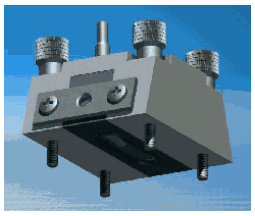
Bioszenzorika

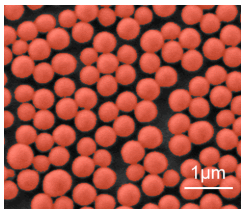

Felületi nanostruktúrák

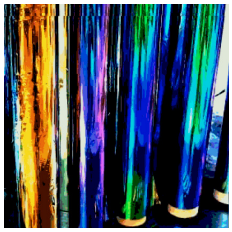
Bevonatok


Felületminőség

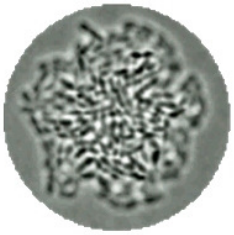
Biológiai vékonyrétegek

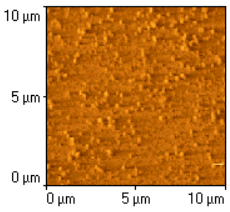

Nanoérdesség

A legfontosabb minősíthető mintatulajdonságok:

- rétegvastagság (0.5-1000 nm);
- optikai törésmutató (pontosság: ~0.001);
- homogenitás,
- határfelületek minősége;
- porozitás (pl. pórusos rétegben az üregtartalom);
- felületi nanoérdesség;
- réteg-összetétel bizonyos esetekben (pl. Si nanoszemcse tartalom szilíciumdioxidban);
- kristályosság (egykristályos anyagok rácsrendezetlensége, roncsoltsága).

Visitors: Konkoly-Thege M. út 29-33, BUDAPEST, 1121 HUNGARY, **Mail:** P.O. Box 49., H-1525, **Fax:** +36-1-3922226
Phone, Director: +36-1-3922224, **Phone, Administration:** +36-1-3922227, **Web:** http://www.ttk.mta.hu/

MŰSZAKI FIZIKAI ÉS ANYAGTUDOMÁNYI INTÉZET

INSTITUTE FOR TECHNICAL PHYSICS AND MATERIALS SCIENCE

A mérőberendezés (számítógépvezérelt spektroszkópiai ellipszométer) műszaki adatai:

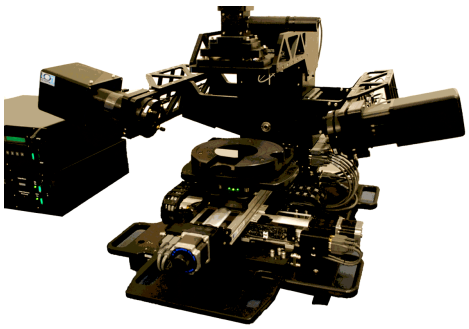

- Gyártó és típus: Woollam M-2000DI
- Hullámhossztartomány: 192-1690 nm
- Érzékenység: 0.1-5.0 nm (nagyon függ a mintától)
- Maximális mintaméret: 200 mm x 200 mm
- Minimális mintaméret: 5 mm x 3 mm
- Térképezhető felület: 150 mm x 150 mm
- Mérhető minta: **1 mikronnál vékonyabb optikai minőségű vékonyrétegek** (a határfelületek érdessége/hullámossága néhányszor 10 nm-nél kisebb legyen; általában a ránézésre nem fényes, matt felület nem mérhető)

Jegyzőkönyv

A mintaminősítésről a Labor ISO 17025 szabvány szerinti jegyzőkönyvet állít ki.
A jegyzőkönyv tartalmazza:

(1) a minta leírását;
(2) a mérési körülmények részletes leírását;
(3) a mért spektrumokat;
(4) a kiértékelés során alkalmazott optikai modellek kidolgozásának lépéseit;
(5) a paraméterillesztések részleteit;
(6) a meghatározott rétegtulajdonságokat.

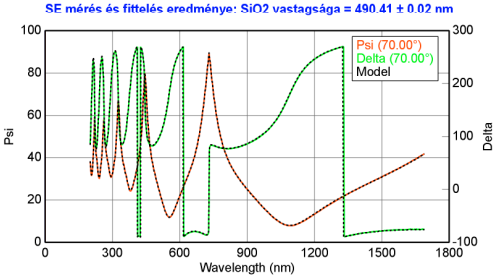

A mérési szolgáltatás ára

Az ellipszometriában a kiértékelés munkaigénye nagyságrendekkel nagyobb, mint a mérésé. A kiértékelés komplexitása nagyban függ a mintától. A mérés tartalmazza a berendezés kalibrációjának ellenőrzését, referenciamérést etalonmintán, a spektrumok felvételét, az optikai modell kidolgozását, a mérések kiértékelését és dokumentálását, a hivatalos jegyzőkönyv elkészítését. Az ár nem tartalmazza a minta szállítási költségeit. A minimálisan elszámolandó egység egy munkanap.

A mérés+kiértékelés díja munkanaponként: 73000 Ft+ÁFA.

Az alábbi speciális (mikroelektronikai minőségű) minták esetében az egy munkanap alatt megmérhető minták száma:

- termikusan oxidált Si: 10 minta
- leválasztott dielektrikum rétegek (a törésmutató meghatározásával): 5 minta

Nagyobb mennyiség és speciális igények esetén az munkadíj egyedi megállapodás tárgya. A laboratórium egy *díjmentes próbamérés* alapján fenntartja magának a jogot annak eldöntésére, hogy a minta vizsgálható-e.

További információ, előzetes műszaki egyeztetés:

Dr. Petrik Péter, laborvezető
Petrik.peter@ttk.mta.hu
+36-1-392-2222/1693

Visitors: Konkoly-Thege M. út 29-33, BUDAPEST, 1121 HUNGARY, **Mail:** P.O. Box 49., H-1525, **Fax:** +36-1-3922226
Phone, Director: +36-1-3922224, **Phone, Administration:** +36-1-3922227, **Web:** http://www.ttk.mta.hu/

MFA Publications in 2011

1. **Ahl JP**, Behmenburg H, Giesen C, Regolin I, Prost W, Tegude FJ, Radnóczi GyZ, Pécz B, Kalisch H, Jansen RH, Heuken M: „*Gold catalyst initiated growth of GaN nanowires by MOCVD", Phys Status Solidi C Curr T Solid State Phys 8: (7-8)2315-2317 (2011)*
2. **Alomari M**, Dipalo M, Rossi S, Diforte-Poisson MA, Delage S, Carlin JF, Grandjean N, Gaquiere C, Tóth L, Pécz B, Kohn E: „Diamond Overgrown InAlN/GaN HEMT", *Diam Relat Mater 20: (4)604-608 (2011)*
3. **Ansari F**, Kavosh M, Horváth R, Ramsden JJ: „Particle speciation during PEG-Fe_3O_4 hybrid nanoparticle self-assembly on Si(Ti)O_2", *J Nanopart Res 13: (1)193-198 (2011)*
4. **Arató P**: „Contacts in Ceramic-Carbon Nanocomposites", *World Journal of Engineering 8: (Suplement 1) 63-64 ISSN:1708-5284 (2011)*
5. **Baji Zs**, Lábadi Z, Horváth ZE, Fried M, Szentpáli B, Bársony I: „Temperature dependent in situ doping of ALD ZnO", *J Therm Anal Calorim 105: (1)93-99 (2011)*
6. **Balázsi Cs**, Gillemot F, Horváth M, Wéber F, Balázsi K, Sahin FC, Onüralp Y, Horváth Á: „Preparation and structural investigation of nanostructured oxide dispersed strengthened steels", *J Mater Sci 46: (13)4598-4605 (2011)*
7. **Balázsi Cs**, Gouma PI, Chae CH, Kim SG: „Nanostructured hydroxyapatite composite for medical applications", *In: Á Jobbágy (szerk.) 5th European IFMBE Conference: IFMBE Proceedings 37 Akadémiai Kiadó, 2011. pp.996-999*
8. **Balázsi Cs**, Koncz P, Wéber F, Horváth Á: „Oxidkerámia-szemcsékkel erősített nanoszerkezetű acélok előállítása porkohászati módszerekkel*", BKL Kohászat 144: (2)41-45 (2011)*
9. **Barna Á**, Kotis L, Lábár J, Sulyok A, Tóth AL, Menyhárd M, Panjan P: „Growing imbedded Ni_3C-rich layer with sharp interfaces by means of ion beam mixing of C/Ni layers", *J Phys D Appl Phys 44: (12) (2011)*
10. **Bauernfeind T**, Préda I, Szakolczai K, Szűcs E, Kiss RG, Simonyi G, Kerecsen G, Duray G, Medvegy M: „Diagnostic value of the left atrial electrical potentials detected by body surface potential mapping in the prediction of coronary artery disease", *Int J Cardiol 150: (3)315-318 (2011)*
11. **Beck A**, Magesh G, Kuppan B, Schay Z, Geszti O, Benkó T, Viswanath RP, Selvam P, Viswanathan B, Guczi L: „Specific role of polymorphs of supporting titania in catalytic CO oxidation on gold", *Catal Today 164: 325-331 (2011)*
12. **Beke D**, Szekrényes Z, Balogh I, Veres M, Fazakas E, Varga LK, Kamarás K, Czigány Zs, Gali A: „Characterization of luminescent silicon carbide nanocrystals prepared by reactive bonding and subsequent wet chemical etching", *Appl Phys Lett 99: (21) (2011)*
13. **Berneschi S**, Brenci M, Nunzi-Conti G, Pelli S, Bettinelli M, Speghini A, Bányász I, Fried M, Khanh NQ, Lohner T, Petrik P, Watterich A, Zolnai Z: „Slab optical waveguides in Er^{3+}-doped tellurite glass by N^+ ion implantation at 1.5 MeV", *Opt Eng 50:* 071110 *(2011)*
14. **Bin-Anooz S**, Schwarzkopf J, Dirsyte R, Agócs E, Petrik P, Kwasniewski A, Wagner G, Fornari R: „Spectroscopic ellipsometry studies on the optical constants of Bi $4Ti_3O_{12}$:xNa

thin films grown by metal-organic chemical vapor deposition", *Thin Solid Films 519: (11)3782-3788 (2011)*

15. **Bin-Anooz S**, Schwarzkopf J, Petrik P, Schmidbauer M, Duk A, Agócs E, Fornari R: „Optical constants of MOCVD-grown Aurivillius phases in the $Bi_4Ti_3O_{12}$-Na0.5Bi 0.5TiO_3 system measured by spectroscopic ellipsometry", *Appl Phys A-Mater 105: (1)81-88 (2011)*
16. **Biró LP**, Nemes-Incze P, Dobrik G, Hwang C, Tapasztó L: „Graphene nanopatterns with crystallographic orientation control for nanoelectronic applications", *Diam Relat Mater 20: (8)1212-1217 (2011)*
17. **Biró LP**, Vigneron JP: „Photonic nanoarchitectures in butterflies and beetles: valuable sources for bioinspiration RID A-3057-2010", *Laser Photonics Rev 5: (1)27-51 (2011)*
18. **Bosi M**, Attolini G, Ferrari C, Frigeri C, Calicchio M, Rossi F, Vad K, Csík A, Zolnai Z: „Effect of temperature on the mutual diffusion of Ge/GaAs and GaAs/Ge*", J Cryst Growth 318: (1)367-371 (2011)*
19. **Bosi M**, Attolini G, Watts BE, Rossi F, Ferrari C, Riesz F, Jiang L: „Wafer curvature analysis in 3C-SiC layers grown on (001) and (111) Si substrates", *J Cryst Growth 318: (1)401-405 (2011)*
20. **Czigány Zs**: „Plan-View Preparation of TEM Specimens from Thin Films Using Adhesive Tape", *Microsc Microanal 17: (6)886-888 (2011)*
21. **Czyzniewski A**, Gulbinski W, Radnóczi Gy, Szerencsi M, Pancielejko M: „Microstructure and mechanical properties of W-C:H coatings deposited by pulsed reactive magnetron sputtering", *Surf Coat Tech 205: (19)4471-4479 (2011)*
22. **Daróczi CsS**: „Akiket az elektromosság szikrája megcsapott…", *Fizikai Szemle LXI (61): (5)169-172 (2011)*
23. **Daróczi CsS**: „High School Relations", In: Menyhárd M, Daróczi CsS, Zolnai Zs, Radnóczi GyZ (szerk.), *MTA MFA Yearbook 2010, pp.27-29, Budapest, MTA MFA (2011)*
24. **Daróczi CsS**: „Kutató diákok a KFKI-ban: MFA nyári iskola középiskolásoknak", *Természet Világa 142. évf.: (1.különszám) p.89 (2011)*
25. **Deák R**, Néda Z, Barna PB: „A Kinetic Monte Carlo Approach for Self-Diffusion of Pt Atom Clusters on a Pt(111) Surface", *Commun Comput Phys 10: (4)920-939 (2011)*
26. **Dobos L**, Tóth L, Pécz B, Horváth ZsJ, Horváth ZE, Tóth AL, Poisson MA: „Annealing of Ti/Cr/Al metallizations on n-GaN", *8th International Conference on Nanosciences & Nanotechnologies – NN11 – 12-15 July 2011, I. Vellidis Congress Center Thessaloniki, Greece, Abstract Book p.283 (2011)*
27. **Dortu F**, Egger H, Kolari K, Haatainen T, Fürjes P, Fekete Z, Bernier D, Sharp G, Lahiri B, Kurunczi S, Sanchez JC, Turck N, Petrik P, Patkó D, Horváth R, Eiden S, Aalto T, Watts S, Johnson NP, De La Rue RM, Giannone D: „Design and process development of a photonic crystal polymer biosensor for point of care diagnostics", *In: Ramanujam N, Popp J: Clinical and Biomedical Spectroscopy and Imaging II., Bécs; Berlin: SPIE - The International Society for Optical Engineering, pp.1-11. (2011)*
28. **Dózsa L**, Lányi S, Raineri V, Giannazzo F, Galkin NG: „Microscopic study of electrical properties of $CrSi_2$ nanocrystals in silicon", *Nanoscale Res Lett 6: (2011)*

29. **Dózsa L**, Molnár Gy, Raineri V, Giannazzo F, Ferencz J, Lányi S: „Scanning tip measurement for identification of point defects", *Nanoscale Res Lett 6: (2011) 140*
30. **Ehiasarian AP**, Vetushka A, Aranda-Gonzalvo A, Sáfrán G, Székely L, Barna PB: „Influence of high power impulse magnetron sputtering plasma ionization on the microstructure of TiN thin films", *J Appl Phys 109: (10)104314-1-104314-15 (2011)*
31. **Erdélyi R**, Nagata T, Rogers DJ, Teherani FH, Horváth ZE, Lábadi Z, Baji Zs, Wakayama Y, Volk J: „Investigations into the Impact of the Template Layer on ZnO Nanowire Arrays Made Using Low Temperature Wet Chemical Growth", *Cryst Growth Des 11: (6)2515-2519 (2011)*
32. **Erinc M**, HJ van de Wiel, Werkhoven RJ, Pongrácz A, Battistig G, Fischer HR: „Vibration characterization of a MEMS 3D force sensor", *In: Thermal, Mechanical and Multi-Physics Simulation and Experiments in Microelectronics and Microsystems (EuroSimE): 12th International Conference on 1011. pp.1-6 (2011)*
33. **Fekeshgazi IV**, Sidenko TS, Mitsa OV, Barna P, Kikineshi OE: „Effects of layer nanodefects on the light transmission by optical elements with multilayer interference coatings", *Ukr J Phys 56: (11)1165-1170 (2011)*
34. **Fekete Z**, Holczer E, Vázsonyi É, Pongrácz A, Battistig G, Fürjes P: „Surface modification of silicon by 3D etching processes and subsequent layer deposition", *EuroNanoForum, Budapest, Hungary 30 May – June 1 2011 (2011)*
35. **Fekete Z**, Pongrácz A, Marton G, Fürjes P: „Mechanical characterization of hollow silicon microprobes fabricated by Deep Reactive Ion Etching", *Eur Biophys J 40: 226 (2011)*
36. **Fekete Z**, Pongrácz A, Szendrey Á, Fürjes P: „Buried microchannels in silicon with planar surface", *22nd Micromechanics and Micro systems Europe Workshop, Toensberg, Norway, June 19-22, 2011 (2011)*
37. **Fiáth R**, Grand L, Kerekes B, Pongrácz A, Vázsonyi É, Márton G, Battistig G, Ulbert I: „A novel multisite silicon probe for laminar neural recordings", *Proc Comp Sci 7: 310 (2011)*
38. **Fried M**, Juhász Gy, Major Cs, Petrik P, Polgár O, Horváth Z, Nutsch A: „Expanded beam (macro-imaging) ellipsometry", *Thin Solid Films 519: (9)2730-2736 (2011)*
39. **Frigeri C**, Serényi M, Khanh NQ, Csík A, Erdélyi Z, Nasi L, Beke DL, Boyen HG: „Hydrogen release in annealed hydrogenated a-Si/a-Ge multilayers", *Cryst Res Technol 46: (8)877-880 (2011)*
40. **Frigeri C**, Serényi M, Khanh NQ, Csík A, Riesz F, Erdélyi Z, Nasi L, Beke DL, Boyen HG: „Relationship between structural changes, hydrogen content and annealing in stacks of ultrathin Si/Ge amorphous layers", *Nanoscale Res Lett 6: p.189 (2011)*
41. **Gaál I**, Tóth AL, Uray L: „Effect of Process Parameters on the Low Temperature Electrical Resistivity of PM Materials", *Powder Metall Progr - J Sci Tech Part Mater 11: (3-4)210-221 (2011)*
42. **Galkin NG**, Dózsa L, Chusovitin EA, Dotsenko SA, Pécz B, Dobos L: „Influence of $CrSi_2$ nanocrystals on the electrical properties of Au/Si-p/$CrSi_2$ NCs/Si(111)-n mesa-diodes", *Phys Proc 11: 35-38 (2011)*
43. **Gergely G**, Gurban S, Menyhárd M, Jablonski A, Zemek J, Goto K: „Experimental determination of the electron elastic backscattering probability and the surface excitation parameter for Si, Ni, Cu and Ag at 0.5 and 1 keV energies", *Surf Interface Anal 43: (11)1365-1370 (2011)*

44. **Grand L**, Pongrácz A, Vázsonyi É, Márton G, Gubán D, Fiáth R, Kerekes BP, Karmos G, Ulbert I, Battistig G: „A novel multisite silicon probe for high quality laminar neural recordings", *Sensor Actuat A Phys 166: (1)14-21 (2011)*

45. **Gubicza J**, Dobatkin SV, Khosravi E, Kuznetsov AA, Lábár JL: „Microstructural stability of Cu processed by different routes of severe plastic deformation", *Mat Sci Eng A Struct 528: 1828-1832 (2011)*

46. **Gueorguiev GK**, Czigány Zs, Furlan A, Stafstrom S, Hultman L: „Intercalation of P atoms in Fullerene-like CP_x", *Chem Phys Lett 501: (4-6)400-403 (2011)*

47. **Gyulai G**, Pénzes CsB, Mohai M, Lohner T, Petrik P, Kurunczi S, Kiss É: „Interfacial properties of hydrophilized poly(lactic-co-glycolic acid) layers with various thicknesses*", J Colloid Interf Sci 362: (2)600-606 (2011)*

48. **Hegedűs Z**, Gubicza J, Kawasaki M, Chinh NQ, Fogarassy Zs, Langdon TG: „The effect of impurity level on ultrafine-grained microstructures and their stability in low stacking fault energy silver", *Mat Sci Eng A Struct 528: 8694-8699 (2011)*

49. **Horvath Á**, Beck A, Stefler G, Benko T, Sáfrán Gy, Varga Z, Gubicza J, Guczi L: „Silica-Supported Au Nanoparticles Decorated by CeO_2: Formation, Morphology, and CO Oxidation Activity", *J Phys Chem C 115: (42)20388-20398 (2011)*

50. **Horváth A**, Stefler G, Geszti O, Kienneman A, Pietraszek A, Guczi L: „Methane dry reforming with CO_2 on CeZr-oxide supported Ni, NiRh and NiCo catalysts prepared by sol-gel technique: Relationship between activity and coke formation", *Catal Today 169: (1)102-111 (2011)*

51. **Horváth R**: „Evanescent optical waves for label-free monitoring of live cell status and behavior", *2011 IEEE Photonics Society Summer Topical Meeting Series, art. no. 6000051, pp.73-74 (2011)*

52. **Horváth R**: „Optikai bioszenzorok és alkalmazásaik", *A mi világunk kémiája, Budapest 2011 (2011)*

53. **Horváth ZsJ**, Basa P, Jászi T, Molnár KZ, Pap AE, Molnár Gy, Dobos L, Tóth L, Pécz B, Pődör B, Turmezei P: „Charging properties of Si_3N_4 based structures with embedded Si or Ge nanocrystals: Experiment and Simulation", *In: 19th Int. Symp. "Nanostructures: Physics and Technology"Ekaterinburg: 2011. pp.207-208*

54. **Horváth ZsJ**, Basa P, Molnár Gy, Jászi T, Pap AE, Dobos L, Tóth L, Pécz B, Molnár KZ: „Silicon nitride based memory elements with embedded Si or Ge nanocrystals", *EuroNanoForum, 2011 Budapest, May 31 - June 2, 2011 (2011)*

55. **Horváth ZsJ**, Basa P, Molnár KZ, Jászi T, Pap AE, Molnár Gy, Dobos L, Tóth L, Pécz B: „Charging behaviour of MNOS memory structures with embedded Si or Ge nanocrystals", *8th International Conference on Nanosciences & Nanotechnologies – NN11 – 12-15 July 2011, I. Vellidis Congress Center Thessaloniki, Greece, Abstract Book p.284 (2011)*

56. **Horváth ZsJ**, Molnár KZ, Kovalev AI, Wainstein DL, Molnár Gy, Basa P, Jászi T, Pap AE, Turmezei P, Lovassy R, Dobos L, Pécz B, Tóth L: „Search for Si and Ge nanocrystals by computer simulation", *Int. Symp. Applied Informatics and Related Areas AIS 2011, Nov. 16, 2011, Székesfehérvár, Hungary (2011)*

57. **Hourdakis E**, Nassiopoulou AG, Parisini A, Reading MA, Van Den Berg JA, Sygellou L, Ladas S, Petrik P, Nutsch A, Wolf M, Roeder G: „Electrical and structural properties of ultrathin SiON films on Si prepared by plasma nitridation*", J Vac Sci Tech B 29:(2) (2011)*

58. **Hwang C**, Yoo K, Kim SJ, Seo EK, Yu H, Biró LP: „Initial Stage of Graphene Growth on a Cu Substrate", *J Phys Chem C 115 (45) (2011) pp.22369-22374*

59. **Hvizdoš P**, Duszová A, Puchý V, Tapasztó O, Kun P, Dusza J, Balázsi Cs: „Wear behavior of ZrO_2-CNF and Si_3N_4-CNT nanocomposites", *Key Eng Mater 465: 495-498 (2011)*

60. **Jenei P**, Yoon EY, Gubicza J, Kim HS, Lábár JL, Ungár T: „Microstructure and hardness of copper - carbon nanotube composites consolidated by High Pressure Torsion", *Mat Sci Eng A Struct 528: 4690-4695 (2011)*

61. **Juhász R**, Ódor G, Castellano C, Munoz MA: „Rare region effects in the contact process on networks", *arXiv:1112.5022 (2011)*

62. **Juhász Z**: „Gépi adatbányászat a Czuczor-Fogarasi szótárban", *Életünk 49: (3-4)99-110 (2011)*

63. **Kárpáti T**, Pongrácz A, Ádám M, Mohácsy T, Battistig G: „Design and Development of a 3-Axial Pioresistive Force Sensor", *EuroNanoForum, Budapest, Hungary May 30 - Jun 1. 2011 (2011)*

64. **Kelling J**, Ódor G: „Extremely large-scale simulation of a Kardar-Parisi-Zhang model using graphics cards", *Phys Rev E Stat 84: (6)* 061150 *(2011)*

65. **Koncz P**, Horvath Á, Wéber F, Petrik A, Balázsi Cs: „Diszpergált oxidkerámia szemcsékkel erősített nanoszerkezetű acélok: előállítás és szerkezeti tulajdonságok", *Anyagvizsgálók Lapja 3-4: 112-118 (2011)*

66. **Konrád C**, Kiss G, Törőcsik B, Lábár JL, Gerencsér AA, Mandi M, Ádám-Vizi V, Chinopoulos C: „A distinct sequence in the adenine nucleotide translocase from Artemia franciscana embryos is associated with insensitivity to bongkrekate and atypical effects of adenine nucleotides on Ca^{2+} uptake and sequestration", *FEBS J 278: (5)822-836 (2011)*

67. **Kovács N**, Patkó D, Orgován N, Kurunczi S, Vardai A, Muskotál A, Vonderviszt F, Horváth R: „Adsorption of flagellin based protein layers", *EuroNanoForum, Budapest 2011 (2011)*

68. **Kovács N**, Patkó D, Orgován N, Kurunczi S, Várdai A, Muskotál A, Vonderviszt F, Horváth R: „Flagellin alapú fehérje rétegek felületi adszorpciója", *A mi világunk kémiája, Budapest 2011 (2011)*

69. **Kovácsné-Kis V**, Németh T, Keresztes M: „Iron Induced Crystallization in Silicate Glass", In: P Gorria, J.A. Blanco (szerk.) *ISMANAM – International Symposium of on Metastable, Amorphous and Nanostructured Materials, 2011. pp.230*

70. **Kovalcíková A**, Tapasztó O, Balázsi Cs, Dusza J: „Indentation thermal shock resistance of Si_3N_4/CNT composites", *Chem Listy 105: (7)s824-s825 (2011)*

71. **Kozma P**, Hámori A, Kurunczi S, Cottier K, Horváth R: „Grating coupled optical waveguide interferometer for label-free biosensing", *Sensor Actuat B Chem 155: (2)446-450 (2011)*

72. **Kozma P**, Kozma D, Németh A, Jankovics H, Kurunczi S, Horváth R, Vonderviszt F, Fried M, Petrik P: „In-depth characterization and computational 3D reconstruction of flagellar filament protein layer structure based on in situ spectroscopic ellipsometry measurements", *Appl Surf Sci 257: (16)7160-7166 (2011)*

73. **Kun M**, Szegedi-Elek E, Moór A, Kóspál Á, Ábrahám P, Apai D, Kiss ZT, Klagyivik P, Magakian TYu, Mezo Gy, Movsessian TA, Pál A, Rácz M, Rogers J: „Inner disc rearrangement revealed by dramatic brightness variations in the young star PV Cep", *Mon Not R Astron Soc 413: (4)2689-2695 (2011)*

74. **Kun P**, Wéber F, Balázsi Cs: „Preparation and examination of multilayer graphene nanosheets by exfoliation of graphite in high efficient attritor mill", *Cent Eur J Chem 9: (1)47-51 (2011)*

75. **Kweon HY**, Lee KG, Chae CH, Balázsi Cs, Min SK, Kim JY, Choi JY, Kim SG: „Development of Nano-Hydroxyapatite Graft With Silk Fibroin Scaffold as a New Bone Substitute", *J Oral Maxil Surg 69: (6)1578-1586 (2011)*

76. **Lábadi Z**, Németh Á, Molnár Gy, Fried M, Bársony I: „Atomic Layer Deposition and characterisation of ZnO thin films for CIGS solar cell buffer layer", *In: EMRS 2010 Spring meeting, 2011. pp.*

77. **Lamperti A**, Radnóczi Gy, Geszti O, Birjega R, Caricato AP, Trautmann C, Ossi PM: „Structural changes in thin films of yttria-stabilized zirconia irradiated with uranium ions in the electronic stopping regime", *J Nucl Mater 416: 173-178 (2011)*

78. **Lohner T**, Csíkvári P, Khanh NQ, Dávid S, Horváth ZE, Petrik P, Hárs G: „Spectroellipsometric and ion beam analytical investigation of nanocrystalline diamond layers", *Thin Solid Films 519: (9)2806-2810 (2011)*

79. **Lugomer S**, Zolnai Z, Tóth AL, Bársony I: „Self-organization of silica nano-particles induced by the ion beam", *Phys Status Solidi C Curr T Solid State Phys 8: (9)2858-2861 (2011)*

80. **Markou A**, Panagiotopoulos I, Bakas T, Niarchos D, Sáfrán Gy, Li WF, Hadjipanayis GC: „Formation of L1(0) with (001) texture in magnetically annealed Co/Pt multilayers", *J Appl Phys 110: (8) (2011)*

81. **Márton G**, Pongrácz A, Grand L, Vázsonyi É, Fekete Z, Ulbert I, Karmos G, Battistig G: „Formation of a Si based multisite neural probe with improved electrode impedance", *International Conference on Electrochemical Sensors, Dobogókö, Hungary, June 19–24, 2011 (2011)*

82. **Márton G**, Pongracz A, Grand L, Vazsonyi E, Ulbert I, Karmos G, Fekete Z, Battistig G: „Neural signal recording with a novel multisite silicon probe", *Eur Biophys J 40: 229 (2011)*

83. **Menyhárd M**, Daróczi CsS, Zolnai Zs, Radnóczi GyZ (szerk.): „MTA MFA Yearbook 2010", *Budapest, MTA MFA (2011)*

84. **Merkel DG**, Bottyán L, Tanczikó F, Zolnai Z, Nagy N, Vértesy G, Waizinger J, Bommer L: „Magnetic patterning perpendicular anisotropy FePd alloy films by masked ion irradiation", *J Appl Phys 109:* 124302 *(2011)*

85. **Merkel DG**, Horváth ZE, Szőcs DE, Kovács-Mezei R, Kertész GGy, Bottyán L: „Stress relaxation in Fe/Si neutron supermirrors by He+ irradiation", *Physica B 406: (17)3238-3242 (2011)*

86. **Mohácsi I**, Petrik P, Fried M, Lohner T, van den Berg JA, Reading MA, Giubertoni D, Barozzi M, Parisini A: „Characterisation of ultra-shallow disorder profiles and dielectric functions in ion implanted Si", *Thin Solid Films 519: (9)2847-2851 (2011)*

87. **Molnár Gy**, Dózsa L, Vértesy Z, Koós AA, Vouroutzis N, Dimitriadis CA, Paraskevopoulos KM: „Reactive deposition epitaxy growth of iron silicide nanoparticles on Si(001): EMRS-C 'Materials devices and economics issues for tomorrow's photovoltaics'", *Energy Procedia 3: 35-41 (2011)*

88. **Muskotál A**, Klein A, Tóth B, Jankovics H, Vonderviszt F: „A polymerizable GFP variant", *Eur Biophys J 40: 238-239 (2011)*

89. **Nemcsics Á**, Balázs J, Pődör B, Makai J, Stemmann A: „Photoluminescence studies of GaAs quantum dots and quantum rings", *Phys Status Solidi C Curr T Solid State Phys 8: (9)2826-2829 (2011)*

90. **Nemcsics Á**, Heyn Ch, Tóth L, Dobos L, Stemmann A, Hansen W: „Cross-sectional transmission electron microscopy of GaAs quantum dots fabricated by filling of droplet-etched nanoholes", *J Cryst Growth 335: 58-61 (2011)*

91. **Nemcsics Á**, Nagy Sz: „Plausible quantum-mechanical interpretaions of RHEED oscillation", *Vacuum 86: in press (2011)*

92. **Nemcsics Á**, Stemmann A, Takács J: „To the understanding of the formation of the III-V based droplet epitaxial nanorings", *Microelectron Reliab 51: in press (2011)*

93. **Nemcsics Á**, Takács J: „Modeling of the Hysteretic Phenomena in RHEED Intensity Variation Versus Temperature for GaAs and InAs Surfaces", *Semiconductors+ 45: (1)91-95 (2011)*

94. **Nemcsics Á**, Tóth L, Dobos L, Stemmann A: „Facetting of the self-assembled droplet epitaxial GaAs quantum dot", *Microelectron Reliab 51: (5)927-930 (2011)*

95. **Nemcsics Á**: „Contribution to a round church reconstructed from its foundation wall", *Pollack Periodica 6: (1)87-98 (2011)*

96. **Nemcsics Á**: „Formation kinetics of the self-assembled droplet epitaxially grown III-V based nanostructures", *Acta Politech Hung 8: 120-137 (2011)*

97. **Nemcsics Á**: „Hűtés napenergiával, különös tekintettel ennek napelemes vonatkozásaira", *Magyar Épületgépészet 59: (3)7-11 (2011)*

98. **Nemes-Incze P**, Kónya Z, Kiricsi I, Pekker A, Horváth ZE, Kamarás K, Biró LP: „Mapping of Functionalized Regions on Carbon Nanotubes by Scanning Tunneling Microscopy*", J Phys Chem C 115: (8)3229-3235 (2011)*

99. **Nemes-Incze P**, Yoo KJ, Tapasztó L, Dobrik G, Lábár J, Horváth ZE, Hwang C, Biró LP: „Revealing the grain structure of graphene grown by chemical vapor deposition", *Appl Phys Lett 99: (2)023104 (2011)*

100. **Neumann PL**, Tóvári E, Csonka S, Kamarás K, Horváth ZE, Biró LP: „Large scale nanopatterning of graphene", *European Materials Research Society (E-MRS) 2011 Spring Meeting, IUMRS ICAM 2011 & E-MRS / MRS Bilateral Conference on Energy, Symposium B, May 9-13 2011, Nice, France (2011)*

101. **Neumann PL**, Tóvári E, Csonka S, Nemes-Incze P, Horváth ZE, Biró LP: „Periodic, large scale nanolithography of graphene", *International Workshop Advanced Materials & Technologies, 2011, 23-25th of March, Budapest (2011)*

102. **Neumann PL**: „Grafén, a nanoelektronika új ígérete", *Technika BP 1: 14-15 (2011)*

103. **Neuróhr K**, Csík A, Vad K, Bartók A, Molnár Gy, Péter L: „Composition depth profile analysis of electrodeposited alloys and metal multilayers: the reverse approach", *J Solid State Electr 15: (11-12)2523-2544 (2011)*
104. **Ódor G**, Juhász R, Castellano C, Munoz MA: „Griffiths phases in the contact process on complex networks", *In: Pedro L Garrido (szerk.) Griffiths phases in the contact process on complex networks, New York: American Institute of Physics, 2011. pp.172-178*
105. **Orgován N**, Horváth R: „Élő sejtek jelölésmentes vizsgálata optikai bioszenzorral*", A mi világunk kémiája, Budapest 2011 (2011)*
106. **Orgován N**, Patkó D, Kovács N, Kurunczi S, Horváth R: „Fluid handling in biosensor experiments: OWLS fluidics", *EuroNanoForum, Budapest 2011 (2011)*
107. **Orgován N**, Patkó D, Kovács N, Kurunczi S, Horváth R: „Folyadékkezelés OWLS kísérletekben", *A mi világunk kémiája, Budapest 2011 (2011)*
108. **P Süle**: „Ion-erosion induced surface nanoporosity and nanotopography on Si", *J Chem Phys 134: 244706 (2011)*
109. **Patkó D**, Cottier K, Hámori A, Horváth R: „Jelölésmentes interferometrikus optikai bioszenzor referencia csatornával", *A mi világunk kémiája, Budapest 2011 (2011)*
110. **Patkó D**, Cottier K, Hámori A, Horváth R: „Label-free optical biosensor with improved stability and sample handling", *EuroNanoForum, Budapest 2011 (2011)*
111. **Patkó D**, Hámori A, Cottier K, Kurunczi S, Horváth R: „Label free biosensing using Grating Coupled Interferometry", *In: 8th EBSA European Biophysics CongressBudapest, 2011, pp.230-231 (40) (2011)*
112. **Patkó D**, Kolari K, Kurunczi S, Aalto T, Horváth R: „Compact Atomic Layer Deposited Overlayers to Increase Biosensor Stability", *EuroNanoForum, Budapest 2011, p.1. (2011)*
113. **Pécz B**, Tóth L, Barna Á, Tsiakatouras G, Ajagunna AO, Georgakilas A, Kovács A: „Microscopy of nitride layers grown on diamond", *In: Microscopy of Semiconducting Materials, 2011 Springer, J. Phys: Conf. Series 326 (2011) 012010*
114. **Pelli S**, Berneschi S, Nunzi-Conti G, Soria S, Righini GC, Bányász I, Lengyel K, Péter Á, Watterich A, Lohner T, Fried M, Zolnai Z: „Characterisation of Optical Waveguides in BGO Crystals Fabricated by N^+ Ion Implantation", *In: CLEO/Europe, EQEC 2011 Conf. Digest, Conference on Lasers and Electro-Optics Europe (ISBN:978-1-4577-0533-5)*
115. **Penttila S**, Horváth Á, Toivonen A, Zolnai Z: „Effect of surface modification on the corrosion resistivity in supercritical water", *In: The 5th International Symposium SCWR2011. pp.*
116. **Pető G**, Daróczi CsS, Pécz B, Kiss LF, Kemény T: "Photoelectric Properties of ion Implantation Induced Ge-Mn Layer Regrown at 400 and 600 °C on Ge(100)", *MAX-lab Activity Report 2010, National Laboratory, Lund, Sweden, (2011), pp.84-85, Edited by: U. Johansson, K. Lilja, A. Nyberg, R. Nyholm*
117. **Petrik P**, Zolnai Z, Polgar O, Fried M, Betyak Z, Agócs E, Lohner T, Werner C, Röppischer M, Cobet C: „Characterization of damage structure in ion implanted SiC using high photon energy synchrotron ellipsometry", *Thin Solid Films 519: (9)2791-2794 (2011)*
118. **Pietralunga SM**, Feré M, Lanata M, Radnóczi Gy, Misják F, Lamperti A, Martinelli M, Ossi PM: „Sputtered Ge-on-Si heteroepitaxial pn junctions: nanostructure, interface morphology and photoelectrical properties", *Microelectron Eng 88: 518-521 (2011)*

119. **Piszter G**, Kertész K, Vértesy Z, Bálint Z, Biró LP: „Color based discrimination of chitin-air nanocomposites in butterfly scales and their role in conspecific recognition", *Anal Method 3: (1)78-83 (2011)*
120. **Piszter G**, Kertész K, Vértesy Z, Bálint Zs, Biró LP: „Photonic Nanoarchitectures in Butterfly Scales Allowing Species Identification*", Proc. of the 2nd European Future Technologies Conf. and Exhibition 2011 (FET 11), Proc Computer Sci 7: 200-201 (2011)*
121. **Polcar T**, Mohan DB, Sandu CS, Radnóczi Gy, Cavaleiro A: „Properties of nanocomposite film combining hard TiN matrix with embedded fullerene-like WS2 nanoclusters", *Thin Solid Films 519: 3191-3195 (2011)*
122. **Portavoce A**, Blum I, Mangelinck D, Hoummada K, Chow L, Carron V, Lábár JL: „Boron clustering in implanted NiSi", *Scripta Mater 64: (9)828-831 (2011)*
123. **Potts SE**, Schmalz L, Fenker M, Diaz B, Swiatowska J, Maurice J, Seyeux A, Marcus P, Radnóczi Gy, Tóth L, Kessels WMM: „Ultra-thin aluminium oxide films deposited by plasma-enhanced atomic layer deposition for corrosion protection", *J Electrochem Soc 158: (5)C132-C138 (2011)*
124. **Pődör B**, Nemcsics Á, Balázs J, Makai J, Stemmann A: „Photoluminescence investigation of GaAs quantum nanostructures", *In: 34th International Spring Seminar on Electronics Technology (ISSE) 2011. pp.542-545*
125. **Radnóczi GyZ**, Sivakov V, Schreivogel M, Christiansen SH, Pécz B: „Chemically Etched Silicon Nanostructures for Solar Cell Applications", *In: Proceedings 10th Multinational Congress on Microscopy 2011, pp.549-550 (2011)*
126. **Rakovics V**: „LED-ek stabilitása", *Elektrotechnika 104: (7-8)9-11 (2011)*
127. **Ratkovic S**, Vujicic D, Kiss E, Boskovic G, Geszti O: „Different degrees of weak metal-support interaction in Fe-(Ni)/Al_2O_3 catalyst governing activity and selectivity in carbon nanotubes' production using ethylene*", Mater Chem Phys 129: (1-2)398-405 (2011)*
128. **Riesz F**, Makai JP, Lukács IE: „Makyoh-topográfia: egy optikai módszer a felületi simaság ellenorzésére", *Anyagvizsgálók Lapja 21: (1-2)39-44 (2011)*
129. **Riesz F**: „Coherence effects in Makyoh topography", *In: Lehmann PH, Osten W, Gastinger K(szerk.) Optical Measurement Systems for Industrial Inspection VII, Bellingham: SPIE, 2011, 80882I-1 (ISBN:9780819486783)*
130. **Riesz F**: „Effects of speckle in Makyoh topography for the studies of extended defects", *J Phys Conf Ser 281: (1)012006 (2011)*
131. **Riesz F**: „General spectral properties of Makyoh imaging of quasi-periodic surfaces", *Opt Laser Technol 43: (1)245-247 (2011)*
132. **Riesz F**: „Sensitivity and detectability in Makyoh imaging", *Optik 122: (11)1005-1009 (2011)*
133. **Schmidt S**, Greczynski G, Goyenola C, Gueorguiev GK, Czigány Zs, Jensen J, Ivanov IG, Hultman L: „CF(x) Thin Solid Films deposited by high power impulse magnetron sputtering: Synthesis and characterization", *Surf Coat Tech 206: (4)646-653 (2011)*
134. **Schulz H**, Ódor G, Ódor Gergely, Nagy MF: „Simulation of 1+1 dimensional surface growth and lattices gases using GPUs", *Comput Phys Commun 182: 1467 (2011)*

135. **Sipos P**, Márton E, Németh T, Kovács-Kis V, May Z, Szalai Z: „Potenitally toxic metal bearing mineral phases in total suspended particles from Budapest, Hungary", *Mineral Mag 75: (3)1884 (2011)*

136. **Solis-Fernandez P**, Paredes JI, Villar-Rodil S, Guardia L, Fernandez-Merino MJ, Dobrik G, Biró LP, Martinez-Alonso A, Tascon JMD: „Global and Local Oxidation Behavior of Reduced Graphene Oxide", *J Phys Chem C 115: (16)7956-7966 (2011)*

137. **Szabó V**, Muskotál A, Tóth B, Mihovilovic MD, Vonderviszt F: „Construction of a Xylanase A Variant Capable of Polymerization", *Plos One 6: (9) (2011)*

138. **Szabó V**, Muskotál A, Tóth B, Vonderviszt F: „Az 1,4-b-xilanáz enzim flagellinnel való fúziós konstrukciójának előállítása", *In: Nagy E, Bokrossy-Csiba M, Törcsváryné Kovács Zs (szerk.) Műszaki Kémiai Napok 2011, Pannon Egyetem, 2011. pp.172-175 (ISBN:978-615-5044-07-6)*

139. **Szabó V**, Muskotál A, Tóth B, Vonderviszt F: „Development of a xylanase A variant capable of forming filamentous assemblies", *Eur Biophys J 40: 240-241 (2011)*

140. **Szabó Z**, Erdélyi R, Makai J, Balázs J, Volk J: „Highly ordered three-dimensional ZnO nanorods for novel photonic devices", *Phys Status Solidi C, 8: (9)2895-2898 (2011)*

141. **Szekeres A**, Fogarassy Zs, Petrik P, Vlaikova E, Cziraki A, Socol G, Ristoscu C, Grigorescu S, Mihailescu IN: „Structural characterization of AlN films synthesized by pulsed laser deposition", *Appl Surf Sci 257: (12)5370-5374 (2011)*

142. **Szentpáli B**, Fürjes P, Bársony I: „THz Detection by Thermopile Antenna", *Abstract on the European Future Technologies Conf and Exhibition 2011, pp.156-157, Selection and peer-review under responsibility of FET11 conference organizers and published by Elsevier B.V.Procedia Computer Science 7doi:10.1016/j.procs.2011.09.029 (2011)*

143. **Szentpáli B**, Fürjes P, Bársony I: „THz Detection by Thermopile Antenna", *In: Giacobino E, Pfeifer R (Ed.) 2nd Europ. Future Techn. Conf. Exh. (FET) Location 2011. pp.156-157*

144. **Szentpáli B**, Matyi G, Fürjes P, László E, Battistig G, Bársony I, Károlyi G, Berceli T: „Thermopile-Based THz Antenna", *Microsyst Technol, pp. (2011)*

145. **Szentpáli B**, Matyi G, Fürjes P, László E, Battistig G, Bársony I, Károlyi G, Berceli T: „THz detection by modified thermopile", *In: Proc. of SPIE Vol. 8066 Smart Sensors, Actuators and MEMS 2011. pp.1-6*

146. **Szentpáli B**, Matyi G, Fürjes P, László E, Battistig G, Bársony I, Károlyi G, Berceli T: „THz detection by modified thermopile", *In: Smart Sensors, Actuators, and MEMS V: Proceedings of SPIESPIE, 2011. pp. (Proc of SPIE; 8066.)(ISBN:978-0-81948-655-4)*

147. **Szolnoki A**, Perc M: „Group-size effects on the evolution of cooperation in the spatial public goods game", *Phys Rev E Stat Nonlin 84: (4) (2011)*

148. **Szolnoki A**, Szabó Gy, Czakó L: „Competition of individual and institutional punishments in spatial public goods games", *Phys Rev E Stat Nonlin 84: (4) (2011) 046106*

149. **Szolnoki A**, Szabó Gy, Perc M: „Phase diagrams for the spatial public goods game with pool punishment", *Phys Rev E Stat Nonlin 83: (3) (2011) 036101*

150. **Szolnoki A**, Xie NG, Wang C, Perc M: „Imitating emotions instead of strategies in spatial games elevates social welfare", *Europhys Lett 96: (3) (2011) 38002*

151. **Tamáska I**, Dobrik G, Nemes-Incze P, Kertész K, Horváth E, Márk GI, Jászi T, Neumann P, Horváth ZE, Biró LP: „Bioinspired photonic nanoarchitectures from graphitic thin films", *RID C-2298-2008 RID A-3057-2010, Thin Solid Films 519: (12)4078-4081 (2011)*

152. **Tamáska I**, Kertész K, Vértesy Z, Bálint Z, Kun A, Yen SH, Biró LP: „Colour changes on cooling of lepidoptera scales containing photonic nanoarchitectures", *Int. Workshop, Advanced Materials & Technologies, MTA MFA, Budapest2011 márc. 23-25 (2011)*

153. **Tapasztó O**, Kun P, Wéber F, Gergely G, Balázsi K, Pfeifer J, Arató P, Kidari A, Hampshire S, Balázsi Cs: „Silicon nitride based nanocomposites produced by two different sintering methods", *Ceram Int 37: (8)3457-3461 (2011)*

154. **Tapasztó O**, Tapasztó L, Markó M, Kern F, Gadow R, Balázsi Cs: „Dispersion patterns of graphene and carbon nanotubes in ceramic matrix composites", *Chem Phys Lett 511: (4-6)340-343 (2011)*

155. **Tikhonov A**, Malin T, Zhuravlev K, Dobos L, Pécz B: „Compare of dislocations behavior in AlxGa1-xN layers with different polarity", *9th International Conference on Nitride Semiconductors, Glasgow 10th - 15th July 2011 (2011)*

156. **Tóth L**, Barna Á, Pécz B, Alomari M, Rossi S, Kohn E: „Electron microscopy of diamond layers grown over InAlN/GaN HEMT structures", *In: 10th Multinational Congress on Microscopy 2011, 2011. pp.557-558*

157. **Tóth L**, Basa P, Jászi T, Dobos L, Pécz B, Horváth ZsJ: „Development of Si nanocrystal layers embedded in Si_3N_4", *In: 10th Multinational Congress on Microscopy 2011, 2011. pp.559-560*

158. **Tsiaoussis I**, Khranovskyy V, Dimitrakopulos GP, Stoemenos J, Yakimova R, Pécz B: „Structural characterization of ZnO nanopillars grown by atmospheric-pressure metalorganic chemical vapor deposition on vicinal 4H-SiC and SiO_2/Si substrates", *J Appl Phys 109: (4) (2011)*

159. **Uglov VV**, Astashynskaya MV, Kuleshov AK, Samtsov MP, Barna PB: „Structure of thin-film nickel-carbon composites formed by microwave plasma-enhanced chemical vapor deposition", *J Surf Investig-X-RA 5: (4)791-795 (2011)*

160. **Vértesy G**, Ueda S, Uchimoto T, Takagi T, Tomáš I, Vértesy Z: „Evaluation of plastic deformation in steels by magnetic hysteresis measurements", *In: Chady T, Gratkowski S, Takagi T, Udpa S S (szerk.) Electromagnetic Nondestructive Evaluation XIV, Amsterdam: IOS Press, 2011. pp.371-378.*

161. **Voigt F**, Sivakov V, Gerliz V, Bauer GH, Hoffmann B, Radnóczi GyZ, Pécz B, Christiansen S: „Photoluminescence of samples produced by electroless wet chemical etching: Between silicon nanowires and porous structures", *Phys Status Solidi A-Appl Mat Sci 208: (4)893-899 (2011)*

162. **Watts BE**, Attolini G, Besagni T, Bosi M, Ferrari C, Rossi F, Riesz F, Jiang L: „Evaluation of curvature and stress in 3C-SiC grown on differently oriented Si substrates", *Mater Sci Forum 679-680: 137-140 (2011)*

163. **Zolnai Z**, Nagy N, Deák A, Battistig G, Kótai E: „Three-dimensional view of the shape, size, and atomic composition of ordered nanostructures by Rutherford backscattering spectrometry", *Phys Rev B Condens Matter Mater Phys 83:* 233302 *(2011)*

Directors of the MFA and its predecessors, from left: István Bársony (MTA MFA), László Bartha (MTA MFKI), György Zimmer (MTA KFKI MKI), József Gyulai (MTA KFKI ATKI).

From 2012. January 1 the institute is officially part of Research Centre for Natural Sciences of the Hungarian Academy of Sciences, but our short name MFA remains the same...